

The NETmix Reactor

Application to High Added-Value Products

Ph.D. Dissertation
in
Chemical and Biological Engineering
by

Carlos Manuel Pereira da Fonte

Supervisors

Madalena Maria Gomes de Queiroz Dias

José Carlos Brito Lopes



Laboratory of Separation and Reaction Engineering
Departamento de Engenharia Química
Faculdade de Engenharia
Universidade do Porto

March 2013

To my family and friends

Da minha aldeia vejo quanto da terra se pode ver do universo...
Por isso a minha aldeia é tão grande como outra terra qualquer,
Porque eu sou do tamanho do que vejo
E não do tamanho da minha altura...

Alberto Caeiro

O Guardador de Rebanhos, Poema VII

Agradecimentos/Acknowledgments

Aproveito para expressar o meu sincero agradecimento a todos os que me apoiaram e tornaram possível a realização deste trabalho.

Em primeiro lugar gostaria de agradecer aos meus orientadores, a Professora Madalena Dias e o Professor José Carlos Lopes, pela orientação, ensinamentos e desafios que permitiram a minha evolução pessoal e pelo qual estarei sempre grato. Por me terem proporcionado as condições para a realização deste trabalho. Pelo apoio, disponibilidade, paciência e amizade.

Ao Professor Alírio Rodrigues, director do LSRE – Laboratório de Processos de Reação e Separação, durante o período em que este trabalho foi desenvolvido.

À Fundação para a Ciência e Tecnologia pelo apoio financeiro através da bolsa de Doutoramento com a referencia SFRH/BD/39040/2007.

Ao Professor Joaquim Faria, Professor Pedro Tavares (UTAD), à Eng. Liliana Pereira, à Doutora Patricia Horcajada (Instituto Lavoisier) e ao Doutor Thomas Devic (Instituto Lavoisier), pela ajuda imprescindível na caracterização físico-química dos materiais e pelo pronto esclarecimento de dúvidas de caracterização que foram surgindo ao longo do trabalho.

À malta da Fluidinova, meus colegas e amigos. Ao Filipe Madureira, António Gouveia, Cássia Almeida, Hugo Campelo, Joana Cardoso, Alexandre Beirão, Renato Sousa, Daniela Correia, Marisa Rodrigues, Pedro Afonso, Erdem Demir, Tiago Marujo, Rui Faria, André Assembleia, Paulo Quadros e António Azevedo.

Aos meus colegas e amigos do LSRE, em especial ao Enis Leblebici e ao Marcelo Costa pela amizade, boa disposição, troca de ideias e por todo o apoio necessário na realização da parte experimental desta trabalho. Ao Ricardo Santos, Ashar Sultan, Marina Torres, Anna Portela, Joana Pereira, Telmo Santos, Nuno Gomes, Kateryna

Krupa, Ângela Novais e Rómulo Oliveira. À Carla Pereira e à Fátima Mota pela simpatia, boa disposição e amizade.

À Susana Cruz por toda ajuda e paciência com os processos burocráticos.

A todos os meus amigos pelos momentos partilhados. Ao Nuno Marques Garrido pelo apoio incondicional, paciência e incentivo. Ao Bruno Gonçalves e Filipe Dias pelo companheirismo e sincera amizade. À Ângela Dias e à Raquel Sousa pelo apoio e bom humor. Ao Paulo Gomes pela amizade, disponibilidade, ensinamentos e por todo o apoio. À Filipa Azevedo pela amizade e boa disposição.

À minha família pela paciência, apoio e amor incondicional. Em especial à minha mãe por sempre me ter motivado e incentivado a escolher o meu caminho e ao meu irmão, Cláudio Fonte, pela amizade, cumplicidade e companheirismo de uma vida.

לחיים

Abstract

The present work concerns the further investigation of the capabilities of the NETmix reactor, including its numerical modelling, characterisation and product development of high added-value products that require fine-tuning of the operational conditions.

Experimental work is used to develop a simple mechanistic model to predict the pressure drop throughout the NETmix reactor. A new 3D CFD model is introduced that enables the computation of transport properties of a more realistic representation of the NETmix geometry. The NETmix performance is studied and proven to be competitive when compared with commercially available mixers and demonstrates new benefits in the enhancement of heat and mass transfer.

The application of the NETmix reactor is extended to heterogeneous liquid-liquid reactions. The adiabatic heterogeneous reaction of nitration of benzene was chosen as a case study due to its relevance as a high added-value material in the polymer industry. A mathematical model is developed and it is capable to predict the formation of nitrobenzene and the raise of temperature inside the NETmix reactor for operational conditions in the range of interest of industrial operation.

The NETmix reactor is tested to produce MIL-88A, a Metal-Organic Framework designed by the Institut Lavoisier. A precipitation model for the prediction of the precipitation of secondary species is developed. From this work, a water based chemical precipitation method at room temperature and atmospheric pressure is developed and used for the production of small monodispersed nanoparticles of 120 × 25 nm of MIL-88A with short reaction times, free of toxic solvents or surfactants and high space-time yields.

Resumo

A presente dissertação concentra-se no aprofundamento da investigação das capacidades do reator NETmix, incluindo a sua modelação numérica, caracterização e desenvolvimento de produtos de alto valor acrescentado que requerem um ajustamento preciso das condições operatórias.

Trabalho experimental é usado no desenvolvimento de um modelo mecanicista simples para a previsão da perda de carga no reator NETmix. Um novo modelo de CFD 3D é introduzido que permite a computação de propriedades de transporte de uma representação da geometria do NETmix mais realista. A performance do reator NETmix é estudada e prova-se ser competitiva quando comparada com outros misturadores comercialmente disponíveis e demonstram-se benefícios no aumento da transferência de calor e de massa.

A aplicação do reator NETmix é alargada a reações heterogéneas liquido-liquido. A reação heterogénea adiabática de nitração do benzeno foi escolhida como caso de estudo devido à sua relevância como um produto de alto valor acrescentado na indústria de polímeros. Um modelo matemático é desenvolvido e é capaz de prever a formação de nitrobenzeno e o aumento de temperatura dentro do reactor NETmix para condições operatórias na gama de interesse de operação industrial.

O reator NETmix é testado na produção de MIL-88A, um *Metal-Organic Framework* desenvolvido pelo instituto Lavoisier. Um modelo de precipitação para a previsão da precipitação de espécies secundarias é desenvolvido. Desde trabalho, um método de precipitação em meio aquoso à temperatura ambiente e pressão atmosférica é desenvolvido e usado para a produção de nanopartículas monodispersas de MIL-88A com 120×25 nm e tempos de reação curtos, livre de solventes tóxicos ou surfactantes e com elevadas produtividades.

Table of Contents

Page

1 Introduction 1
1.1 The NETmix Reactor 2
1.1.1 Existing Reactors 4
1.1.2 Industrial Application of the NETmix Reactor 5
1.2 Previous Work 7
1.3 Thesis Objectives and Layout 10
1.4 References 11

2 Transport Phenomena Studies in the NETmix Reactor 14
2.1 Introduction 14
2.2 Transport Phenomena in NETmix Reactor 20
2.2.1 NETmix Pressure Drop Assessment 20
2.2.1.1 Mechanistic Pressure Drop Model 20
2.2.1.2 NETmix Power Number and Z Factor 23
2.2.2 Heat Transfer 24
2.2.2.1 Energy Balance to a Unit Cell 25
2.2.2.2 Nusselt Number for Flow Between Parallel Plates 27
2.2.2.3 The Analogy with the NETmix Geometry 30
2.2.3 Mass Transfer 32
2.2.3.1 Mass Balance to a Unit Cell 33
2.2.3.2 Sherwood Number Comparison 34
2.3 Pressure Dynamic Experiments 36
2.3.1 Experimental Setup 36
2.3.2 Experimental Fluids 37
2.3.3 Data Acquisition 38
2.3.3.1 Pressure Drop 38
2.3.3.2 Pressure Difference 38
2.3.4 Results 39
2.3.4.1 Pressure Drop Data 39
2.3.4.2 Flow Oscillation Frequency Data 41
2.3.4.3 Benchmarking With Other Mixers 43
2.4 3D CFD Dynamic Simulations 44
2.4.1 NUB Physical Domain 45
2.4.2 Governing Equations and Boundary Conditions 45
2.4.2.1 Hydrodynamic Simulations 45
2.4.2.2 Heat Transfer Simulations 47
2.4.2.3 Mass Transfer Simulations 49
2.4.3 Domain Discretization 50

2.4.3.1 Hydrodynamic Simulations 50
2.4.3.2 Heat Transfer Simulations 50
2.4.3.3 Mass Transfer Simulations 51
2.4.4 Numerical Solution at Steady State 53
2.4.5 Numerical Solution at Transient State 53
2.4.6 Results 54
2.4.6.1 Hydrodynamic Simulations 54
2.4.6.2 Dynamic Tracer Transport 55
2.4.6.3 Heat Transfer Simulations 56
2.4.6.4 Mass transfer Simulations 66
2.5 Conclusions 68
2.6 References 69

3 NETmix Technology Applied to Liquid-Liquid Heterogeneous Reactions 73
3.1 Introduction 73
3.2 Heterogeneous Benzene Nitration Mechanism 77
3.3 NETmix Model Description 80
3.3.1 Reaction Rate Model 81
3.3.2 Heat of Reaction and Dilution of the Mixed Acid 84
3.4 Phase Equilibrium 87
3.4.1.1 Benzene Solubility in the Aqueous Phase 87
3.4.1.2 Nitric Acid Solubility in the Organic Phase 92
3.4.2 Physical Properties 93
3.4.2.1 Molar mass 93
3.4.2.2 Density 94
3.4.2.3 Heat Capacity 95
3.4.2.4 Viscosity 96
3.4.3 Unit Cell Mass Balance 97
3.4.4 Unit Cell Energy Balance 99
3.4.5 Numerical Implementation 99
3.5 Model Validity 108
3.5.1 Comparison with Published Data 108
3.5.2 Power Number Comparison 112
3.6 NETmix Case Study Simulation 115
3.7 Conclusions 122
3.8 References 123

4 Product Development in the NETmix Reactor: Metal-Organic Frameworks 127
4.1 Introduction 127
4.2 MIL-88A 129
4.3 Experimental Setup and Techniques 133
4.3.1 Experimental Setup 133
4.3.1.1 Batch Reactor 134
4.3.1.2 NETmix Reactor 134
4.3.2 Reactants 136
4.3.3 Product Characterization 136

4.3.3.1 Scanning Electron Microscopy (SEM) 136
4.3.3.2 Dynamic Light Scattering (DLS) 136
4.3.3.3 Atomic Absorption Spectroscopy (AAS) 137
4.3.3.4 X-Ray Diffraction (XRD) 137
4.3.3.5 Differential Scanning Calorimetry (DSC) and Thermogravimetric Analysis (TGA) 137
4.3.3.6 Nitrogen Adsorption 138
4.4 Formulation 1 138
4.4.1 Experimental Description 138
4.4.2 Results and Discussion 141
4.4.2.1 Iron (III) Conversion 143
4.4.2.2 XRD Analysis 145
4.4.2.3 SEM Analysis 146
4.4.2.4 Particle Size Distribution 149
4.4.2.5 Specific Surface Area 155
4.4.2.6 Thermal Analysis 156
4.5 Formulation 2 158
4.5.1 Precipitation Model of the Instantaneous Equilibrium without Reaction 159
4.5.1.1 Equilibrium of Fumaric Acid in Aqueous Solutions 159
4.5.1.2 Equilibrium of Iron(III) Hydroxide in Aqueous Solutions 163
4.5.1.3 Instantaneous Equilibrium without Formation of MIL-88A 167
4.5.2 Experimental Description 170
4.5.3 Results and Discussion 171
4.5.3.1 Iron(III) Conversion 173
4.5.3.2 XRD Analysis 173
4.5.3.3 Particle Size Distribution 175
4.5.3.4 Thermal Analysis 177
4.6 Space-Time Yield Consideration 182
4.7 Conclusions 184
4.8 References 185

5 Final Remarks 189
5.1 Conclusions 189
5.2 Future Work 192
5.3 References 193

A Logarithm Mean Temperature Difference 194
A.1 Logarithm Mean Temperature Difference 194

B Size, Surface and Distribution Calculations for MOF Particles 196
B.1 Mean Free Distance Between Particles 196
B.2 Specific External Surface Area 197
B.3 Distribution of Dispersant 198
B.4 Hydrodynamic Diameter 199
B.5 References 200

C Rheological Analysis in MOF Production 201
C.1 Experimental Techniques 201
C.2 Experimental Results 201
C.3 NETmix operation 203

D Modelling of the Equilibrium of Fumaric Acid and Iron(III) Hydroxide in Aqueous Solutions 205
D.1 Equilibrium of Fumaric Acid in Aqueous Solutions 205
D.1.1 Fumaric Acid Dissociation Without Precipitation 206
D.1.2 Fumaric Acid Dissociation With Precipitation 207
D.2 Equilibrium of Iron(III) Hydroxide in Aqueous Solutions 208
D.2.1 Iron(III) Hydroxide Dissociation Without Precipitation 209
D.2.2 Iron(III) Hydroxide Dissociation With Precipitation 210
D.3 Instantaneous Equilibrium after Mixing 211
D.3.1 Case 1: Fumaric acid and Iron(III) Hydroxide Dissociation 212
D.3.2 Case 2: Fumaric acid and Iron(III) Hydroxide Dissociation with Fumaric acid Precipitation 213
D.3.3 Case 3: Fumaric acid and Iron(III) Hydroxide Dissociation with Iron(III) Hydroxide Precipitation 214
D.3.4 Case 4: Fumaric acid and Iron(III) Hydroxide Dissociation with Fumaric Acid and Iron (III) Hydroxide Precipitation 215

Table of Figures

Page

Figure 1.1. Representation of the NETmix network. 2
Figure 1.2. NETmix unit cell: a) 2D unit cell; b) 3D unit cell. 3
Figure 1.3. NETmix prototypes: a) NETmix 3D; b) Lab-scale NETmix 2D; c) Multi-Inlet NETmix 2D. 5
Figure 1.4. nanoXIM industrial production site: a) NETmix industrial reactor; b) reactants storage tanks; c) centrifuge unit; d) spray-dry unit; e) synoptic (adapted from Gomes (2011)). 6
Figure 2.1. Commercially available heat exchangers with static mixing elements: a) Kenics Heat Exchanger; b) Sulzer Monotube Heat Exchanger Type SMXL ; c) Sulzer Multitube Heat Exchanger Type SMXL; d) Statiflo STX Heat Exchange Motionless Mixer STLX. 18
Figure 2.2. Shortest path for calculating the total pressure drop in the system. 22
Figure 2.3. Development of the thermal boundary layer between parallel plates for the cooling of a fluid (adapted from Çengel (2003)) 27
Figure 2.4. Nusselt number for fully developed laminar flow of Newtonian fluids in parallel plates (Bird et al., 2002) 29
Figure 2.5. Sherwood number for fully developed laminar flow of Newtonian fluids in parallel plates. 36
Figure 2.6. Experimental setup for pressure drop measurements 37
Figure 2.7. Flow oscillation measurements setup: (a) drilled channels, (b) system connected to the experimental setup. 39
Figure 2.8. Pressure drop obtained experimentally and model fitting for NETmix 3D 40
Figure 2.9. Pressure drop obtained experimentally and model fitting for Lab-scale NETmix 2D. 40
Figure 2.10. Pressure drop obtained experimentally and model fitting for Multi-Inlet NETmix 2D. 41
Figure 2.11. Power spectra for pressure difference signal for Re=400. 42
Figure 2.12. Frequency of oscillation in the Lab-scale NETmix 2D chambers as a function of the Reynolds number. 42
Figure 2.13. Power number plot for the three NETmix prototypes and for several stirred tanks with different impellers. 43
Figure 2.14. Z factor for the NETmix prototypes as a function of Reynolds number. The grey area corresponds to a typical range of Z factors for some commercial mixers (Thakur et al., 2003) 44
Figure 2.15. NUB showing the imposed boundary conditions. 45
Figure 2.16. Tracer species molar flow rate deviation as a function of Reynolds number. 52

Figure 2.17. Number of elements as a function of the edge length. 52
Figure 2.18. Pressure drop as a function of the Reynolds number obtained experimentally and from CFD simulations, for the Lab-scale NETmix 2D. 54
Figure 2.19. Tracer fraction for Re=300 at different moments after injection at the middle plane of the geometry. 55
Figure 2.20. Tracer fractions for Re=300 at different moments after injection at the middle plane of the geometry. 56
Figure 2.21. Nusselt number results as a function of the thermal entrance length for the wall constant temperature simulation. 57
Figure 2.22. Temperature contour maps at the middle plane of the domain for Re=100 and Re=350 for constant wall temperature simulations. 58
Figure 2.23. Nusselt number results as a function of the thermal entrance length for the wall constant temperature simulation. 58
Figure 2.24. Temperature contour maps at the middle plane of the domain for Re=100 and Re=300 for constant wall heat flux simulations. 59
Figure 2.25. Nusselt number results as a function of the thermal entrance length for the wall constant heat flux simulation for Re=10. 60
Figure 2.26. Ratio between the asymptotic values for thermally developing flows of unit cell Nusselt number and Nusselt number for parallel plates with constant wall temperature. 61
Figure 2.27. Ratio between the asymptotic values for thermally developing flows of the unit cell Nusselt number and Nusselt number for parallel plates with constant wall heat flux. 62
Figure 2.28. Nusselt number as a function of the thermal entrance length for the wall constant temperature simulation for Re=100. 64
Figure 2.29. Nusselt number as a function of the thermal entrance length for the constant wall heat flux simulation for Re=100. 64
Figure 2.30. Area for heat transfer 65
Figure 2.31. Ratio between the asymptotic values for developing concentration boundary layers of unit cell Sherwood number and Sherwood number for parallel plates with constant wall concentration. 67
Figure 3.1 Nitronium ion formation mechanism. 78
Figure 3.2 Mechanism for the reaction of nitration of benzene. 79
Figure 3.3 Global mechanism of benzene nitration. 80
Figure 3.4 Reaction rate model fitting using experimental data from Biggs and White (1956). 84
Figure 3.5 Experimental and calculated distribution coefficients for benzene in sulfuric acid solutions at 313 K. Experimental data from Hanson and Ismail (1975). 89
Figure 3.6 Experimental and calculated distribution coefficients for benzene in nitric acid solutions at 295 K. Experimental data from Hanson and Ismail (1975). 90
Figure 3.7 Experimental and calculated distribution coefficients for benzene in sulfuric acid solutions at 303 K. Experimental data from Hanson and Ismail (1975). 91

Figure 3.8 Experimental and calculated distribution coefficients for benzene in mixed acid solutions at 303 K. Experimental data from Hanson and Ismail (1975). 91
Figure 3.9 Ration between nitric acid and nitrobenzene molar fraction in the organic phase as a function of the nitric acid molar fraction in the aqueous phase. Experimental data from Biggs and White (1956) and Schiefferle et al. (1976). 93
Figure 3.10. Scheme of the interconnection of unit cells. 100
Figure 3.11 Pre-mixed flow in the inlet of each unit cell and flow splitting. 101
Figure 3.12 Algorithm used to solve the benzene nitration reaction for each unit cell. 107
Figure 3.13 Comparison of experimental data (Biggs and White, 1956) and simulation results using the isothermal solver of conversion of benzene. 109
Figure 3.14 Comparison of experimental data (Santos, 2005) and simulation results of mass fraction of nitric acid in the aqueous phase with increasing impeller speed.....110
Figure 3.15 Comparison of experimental data (Santos, 2005) and simulation results of mass fraction of nitric nitrobenzene in the organic phase. 111
Figure 3.16 Comparison of experimental data (Santos, 2005) and simulation results of temperature of nitration. 111
Figure 3.17 Dissipated power per unit volume.....114
Figure 3.18. Conceptual experimental setup used in the simulations. 116
Figure 3.19. Inlet scheme 1. 116
Figure 3.20. Isolines of conversion and outlet temperature as a function of the mass fraction of sulfuric acid and inlet temperature. 117
Figure 3.21. Map of the ratio of molar flow rate of nitrobenzene and the limiting reactant inside both reactors for Inlet Scheme 1. 119
Figure 3.22. Map of nitration temperature inside both reactors for Inlet Scheme 1. 119
Figure 3.23. Inlet scheme 2. 120
Figure 3.24. Map of the ratio of molar flow rate of nitrobenzene and the limiting reactant inside both reactors for inlet scheme 2. 121
Figure 3.25. Map of nitration temperature inside both reactors for inlet scheme 2. .121
Figure 3.26. Conversion along the rows of the NETmix reactors using inlet scheme 1 and inlet scheme 2. 122
Figure 4.1. (a) Trimer and (b) framework of MIL-88A (Serre et al., 2004). 130
Figure 4.2. Molecular structure of MIL-88A trimer. Yellow: iron atoms, red: oxygen atoms, black: carbon atoms. 130
Figure 4.3. Simulated crystalline structures of MIL-88A in its open and closed framework shapes (Serre et al., 2007) 131
Figure 4.4. Batch reaction experimental apparatus. 134
Figure 4.5. NETmix pre-mixed inlet scheme. 135
Figure 4.6. NETmix reactor experimental apparatus. 135
Figure 4.7. Obtained product coloration immediately after reaction (on the left) and after 72h of ageing (on the right). 141

Figure 4.8. N02 samples spray-dried immediately after reaction (on the left) and after 72h of ageing (on the right). 142
Figure 4.9. pH as a function of ageing time for samples N02, B02 and N03. 142
Figure 4.10. Iron conversion as a function of ageing time for samples N01, N02, B02 and B03. 144
Figure 4.11. Iron conversion as a function of ageing time for samples B02, B04 and B06. 144
Figure 4.12. Simulated and experimental XRD patterns for samples B02, N02 and B05. 146
Figure 4.13. SEM images of samples (a) N02 (0 hours), (b) N02 (72 hours), (c) B02 (0 hours) and (d) B02 (72 hours) 147
Figure 4.14. SEM images of sample N01. 147
Figure 4.15. SEM images of samples (a) N03 (0 hours) and (b) N03 (72 hours). 148
Figure 4.16. SEM images of samples (a) N04 (0 hours) and (b) B04 (0 hours). 148
Figure 4.17. SEM image of sample B05 (72 hours). 149
Figure 4.18. SEM image of sample N07: (a) 4300× magnification and (b) 17000× magnification. 149
Figure 4.19. Number particle size distribution for N01, N02 and B02 experiments. ..151
Figure 4.20. Number particle size distribution for B02, B04 and B06 experiments. ..151
Figure 4.21. Mean hydrodynamic diameter as a function of temperature for reactants concentration of 0.4 M. 152
Figure 4.22. Number particle size distribution for N02, N04 and B04 experiments. ..152
Figure 4.23. Number particle size distribution for N02 and N03 experiments. 153
Figure 4.24. Number particle size distribution for N07 and B07 experiments. 153
Figure 4.25. Mean hydrodynamic diameter as a function of the reactants concentration at 25°C (grey dot was estimated from SEM imaging results) 154
Figure 4.26. Number particle size distribution for B02 and B05 experiments. 154
Figure 4.27. Adsorption and desorption isotherm of nitrogen. 155
Figure 4.28. TGA and DSC results for sample N01. 157
Figure 4.29. TGA results for sample N01 and results from Serre et al. (2004). 158
Figure 4.30. Titration of a solution of fumaric acid 0.04 M with a solution of sodium hydroxide. 162
Figure 4.31. Fumaric acid dissociation as a function of pH. 163
Figure 4.32. pH of solution of iron(III) chloride as a function of concentration. 165
Figure 4.33. Titration of iron(III) Chloride solution with sodium hydroxide. 166
Figure 4.34. Effect of temperature on the solubility of iron(III) hydroxide in a solution of iron(III) chloride with concentration 0.008 M. 167
Figure 4.35. Map of fumaric acid and iron(III) hydroxide precipitation regions. 168
Figure 4.36. Solutions after addition of both reactants: (a) immediate addition and (b) after 10 minutes of reaction. 172
Figure 4.37. MIL-88A particles suspension after dilution. 172
Figure 4.38. Gel obtained from centrifugation. 173
Figure 4.39. Simulated and experimental XRD patterns for Batch, NETmix without recirculation and NETmix with recirculation, operation modes. 174

Figure 4.40. Simulated XRD patterns of closed and open frameworks and experimental XRD pattern. 175
Figure 4.41. Number particle size distribution for the Batch operation mode after dilution, 72 hours after dilution and 2 weeks after dilution. 175
Figure 4.42. Number particle size distribution for the NETmix without recirculation operation mode after dilution, 72 hours after dilution and 2 weeks after dilution. 176
Figure 4.43. Number particle size distribution for the NETmix with recirculation operation mode after dilution, 72 hours after dilution and 2 weeks after dilution. 176
Figure 4.44. Number particle size distribution for the experiment in batch, NETmix without recirculation and NETmix with recirculation 72 hours after dilution. 177
Figure 4.45. TGA and DSC results for a sample of wet gel. 178
Figure 4.46. TGA and DSC results for a sample of dry gel. 180
Figure 4.47. TGA and DSC results for a sample of spray-dried powder. 181
Figure 4.48. TGA results of publish data and samples of wet gel, dry gel and spray-dried powder. 181
Figure B.1 Approximate geometry of the particles. 196
Figure B.2. Division of the surface area of a particle. 198
Figure C.1. Viscosity as a function of time for a reactants concentration of 0.4 M and a shear rate of 366 Hz. 202
Figure C.2. Maximum viscosity of the mixture of reactants as a function of shear rate. 202

Table of Tables

Page

Table 1.1. NETmix reactor prototypes geometrical characteristics 5
Table 2.1. NETmix reactor prototypes geometrical characteristics. 36
Table 2.2. Density and viscosity of water and aqueous solutions of glycerol. 38
Table 2.3. Thermal conductivity and heat flux for different thermal entrance lengths. 60
Table 2.4. Thermal conductivity for different thermal entrance lengths. 63
Table 3.1 $a_{o,j}^{(W)}$ parameters for calculation of the partial molar enthalpy of water (Zaldívar et al., 1992). 86
Table 3.2 $a_{o,j}^{(N)}$ parameters for calculation of the partial molar enthalpy of nitric acid (Zaldívar et al., 1992). 86
Table 3.3 $a_{o,j}^{(S)}$ parameters for calculation of the partial molar enthalpy of sulfuric acid (Zaldívar et al., 1992). 86
Table 3.4 Fitting constants for the determination of the partition coefficient of benzene between the two phases. 89
Table 3.5. Molar mass of nitration compounds. 93
Table 3.6. Coefficients to estimate the density of nitration compounds 94
Table 3.7. Coefficients to estimate the liquid heat capacity of nitration compounds. 95
Table 3.8. Coefficients to estimate the liquid viscosity of nitration compounds. 96
Table 3.9. Operating conditions used by Biggs and White (1956). 108
Table 3.10. Operating conditions used by Santos (2005). 110
Table 3.11. Mixing conditions for the experimental data of Biggs and White (1956) and Santos (2005) 113
Table 3.12. Geometrical characteristics of the Lab-Scale NETmix 2D. 114
Table 3.13. Operational conditions used for simulation. 115
Table 3.14. Operational conditions used for simulation. 118
Table 4.1. Lab-Scale NETmix 2D geometrical characteristics. 135
Table 4.2. Series of experiments and respective conditions. 139
Table 4.3. Average hydrodynamic diameters and approximated average particle length. 155
Table 4.4. Dissociation constants of fumaric acid for different temperatures. 160
Table 4.5. Solubility and solubility product of fumaric acid for different temperatures 161
Table 4.6. Average hydrodynamic diameters and approximated particle length. 177

Notation

A	Area $[\mathrm{m}^2]$
a	Activity $[\mathrm{M}]$
$A_{channel}$	Channel cross sectional area $[\mathrm{m}^2]$
$A_{external}$	External NETmix area $[\mathrm{m}^2]$
$A_{lateral}$	Lateral NETmix area $[\mathrm{m}^2]$
A_{part}	Surface area of a particle $[\mathrm{m}^2]$
A_{PP}	Parallel plate heat/mass transfer area $[\mathrm{m}^2]$
A_{transf}	Transfer area $[\mathrm{m}^2]$
c	Concentration $[\mathrm{M}]$
c_b	Bulk concentration $[\mathrm{M}]$
c_{MOF}	Concentration of MOF $[\mathrm{M}]$
c_P	Heat capacity $[\mathrm{J/kg\,K}]$
Δc_{P_r}	Heat capacity difference $[\mathrm{J/kg\,K}]$
Δc_{uc}	Unit cell average concentration difference $[\mathrm{M}]$
c_{wall}	Wall concentration $[\mathrm{M}]$
d	Channel diameter $[\mathrm{m}]$
$\mathcal{D}$	Molecular diffusivity $[\mathrm{m}^2/\mathrm{s}]$
D_{disp}	Dispersant molecule diameter $[\mathrm{m}]$
d_h	Channel hydraulic diameter $[\mathrm{m}]$
$\overline{D}_{h_{\mathrm{part}}}$	Average hydrodynamic diameter $[\mathrm{m}]$
$D_{impeller}$	Impeller diameter $[\mathrm{m}]$
D_{part}	Particle diameter $[\mathrm{m}]$
E_a	Energy of Activation $[\mathrm{J/mol}]$
f	Channel friction factor
F	Molar flow rate $[\mathrm{mol/s}]$
f_{osc}	Natural frequency of oscillation $[\mathrm{Hz}]$
F_{shape}	Shape factor
ΔG_B	Free Gibbs energy $[\mathrm{J/K}]$
$\overline{h}$	Average convective heat transfer coefficient $[\mathrm{W/m^2K}]$
H	Partial molar enthalpy $[\mathrm{J/mol}]$

$\Delta\dot{H}_d$	Heat flow rate of dilution [W]
h_{loc}	Local convective heat transfer coefficient [W/m^2K]
h_{PP}	Parallel plates convective heat transfer coefficient [W/m^2K]
ΔH_r	Heat of reaction [J/mol]
h_{uc}	Unit cell convective heat transfer coefficient [W/m^2K]
$\dot{H}$	Enthalpy convective flow rate [J/s]
i_x	Number of the row
K	Loss coefficient
k	Reaction rate constant [$m^3mol^{-1}s^{-1}$]
k_0	Pre-exponential factor [$m^3mol^{-1}s^{-1}$]
$K_{d,\,Fe(OH)_3}$	Equilibrium solubility constant of $Fe(OH)_3$ [M]
$K_{Fum^{2-}}$	Equilibrium dissociation constant for Fum^{2-} [M]
$K_{Fe(OH)^{2+}}$	Equilibrium dissociation constant of $Fe(OH)^{2+}$ [M]
$K_{Fe(OH)_2^+}$	Equilibrium dissociation constant of $Fe(OH)_2^+$ [M]
$K_{Fe(OH)_4^-}$	Equilibrium dissociation constant of $Fe(OH)_4^-$
K_{HFum^-}	Equilibrium dissociation constant of $HFum^-$ [M]
$k_{m,uc}$	Convective mass transfer coefficient [m/s]
k_r	Apparent reaction rate constant [$m^3mol^{-1}s^{-1}$]
$K_{s,\,Fe(OH)_3}$	Solubility product of $Fe(OH)_3$ [M^4]
$K_{s,\,H_2Fum}$	Solubility product for H_2Fum [M^3]
l	Channel length [m]
L_{part}	Particle length [m]
l^*	Length of the jet inside the chamber [m]
M	Molar mass [kg/mol]
m_B	Partition coefficient
m_{MOF}	Mass of MOF [kg]
m_{part}	Mass of the particle [kg]
N	Impeller rotational speed [s^{-1}]
$\dot{N}_{\mathcal{A}}$	Molar flow rate of species $\mathcal{A}$ transferred from the solid surface [mol/s]
N_A	Avogadro constant
$N_{disp,ads}$	Adsorbed dispersant molecules number
$N_{disp,free}$	Free dispersant molecules number
$N_{disp,total}$	Total dispersant molecules number

$N_{\text{disp},\Delta x}$	Number of dispersant molecules between particles
N_P	Power number
N_{part}	Number of particles
n_x	Number of rows
n_y	Number of columns
Nu_{PP}	Parallel plates Nusselt number
Nu_{uc}	Unit cell Nusselt number
p	Pressure [Pa]
P	Power [W]
p_0	Reference pressure [Pa]
$\Delta p_{friction}$	Friction pressure drop [Pa]
Δp_{mixing}	Mixing pressure drop [Pa]
Δp_{mixer}	Mixer pressure drop [Pa]
Δp_{NETmix}	Total pressure drop [Pa]
Δp_{uc}	Unit cell pressure drop [Pa]
Pr	Prandtl number
$\dot{Q}$	Heat flow rate [W]
Q	Volumetric flow rate [m^3/s]
$q_{channel}$	Channel flow rate [m^3/s]
Q_{inlet}	NETmix inlet volumetric flow rate [m^3/s]
$\dot{q}_{wall}$	Wall heat flux [W/m^2]
r	Ratio of Nu/Sh for the unit cell and parallel plates
R	Universal gas constant [$\text{J}/\text{mol}\,\text{K}$]
R_{nit}	Nitration reaction rate [mol/m^3]
R_{uc}	Total hydraulic resistance [$\text{kg}/\text{m}^4\text{s}$]
R^F	Friction resistance [$\text{kg}/\text{m}^4\text{s}$]
R^{LF}	Linear flow resistance [$\text{kg}/\text{m}^4\text{s}$]
R^{NLF}	Non-linear flow resistance [$\text{kg}/\text{m}^4\text{s}$]
Re	Reynolds number
Re_c	Critical Reynolds number
Re_{PP}	Parallel plate Reynolds number
S_{ext}	Specific external surface area [m^2/kg]
$S_{\text{H}_2\text{Fum}}$	Solubility of H_2Fum [M]
x_{tracer}	Molar fraction of tracer
Sc	Schmidt number

$\mathrm{Sh}_{\mathrm{PP}}$	Parallel plate Sherwood number
Sh_{uc}	Unit cell Sherwood number
T	Temperature [K]
t	Time [s]
T_b	Bulk temperature [K]
$T_{\max}$	Maximum temperature [K]
ΔT_{uc}	Unit cell average temperature difference [K]
T_{wall}	Wall temperature [K]
$\vec{v}$	Velocity vector field [m/s]
V	Volume [m^3]
V_{ads}	Adsorbed volume of nitrogen [m^3]
$\overline{v}_{channel}$	Average channel velocity [m/s]
$v_{max,channel}$	Maximum velocity in the channel [m/s]
V_{NaOH}	Volume of NaOH [m^3]
V_{part}	Particle volume [m^3]
V_{sol}	Volume of solution [m^3]
V_{uc}	Unit cell volume [m^3]
v_x	Velocity in the x direction [m/s]
v_y	Velocity in the y direction [m/s]
v_z	Velocity in the z direction [m/s]
w	Mass molar fraction
Δx	Numerical grid element length [m]
x	Molar fraction
X	Conversion
Δx_{part}	Mean free distance between particles [m]
x_{PP}	Parallel plates entrance length [m]
x^*_{PP}	Parallel plate dimensionless thermal/concentration entrance length
x_{uc}	Unit cell entrance length [m]
x^*_{uc}	Unit cell dimensionless thermal/concentration entrance length
x^*	Dimensionless thermal/concentration entrance length
Z	Z factor

Greek letters

α	Thermal difusivity
Γ	Gamma function
γ	Activity coefficient
$\dot{\gamma}$	Shear rate [Hz]

ε	Volume fraction of the organic phase
θ	Angle [°]
κ	Thermal conductivity [W/m K]
μ	Viscosity [Pa·s]
μ_{corr}	Corrected viscosity [Pa·s]
ρ	Density [kg/m^3]
ρ_{mix}	Average density of the mixture
ρ_{MOF}	MOF density
τ_{uc}	Chamber space time [s]
τ_{ub}	Passage time in the NUB [s]
τ_{total}	Total passage time [s]
φ_F	Initial condition parameter for molar flow rate
φ_T	Initial condition parameter for temperature
φ_{x_N}	Initial condition parameter for nitric acid molar fraction
φ_{iter}	Under-relaxation parameter
χ	Difference of concentration of acid and base [M]
ω	Depth [m]

Mathematical operations

$\frac{\partial}{\partial i}(\cdot)$	Partial derivative with respect to i
$\nabla(\cdot)$	Gradient operator
$\nabla^2(\cdot)$	Laplacian operator

Subscripts

$\mathcal{A}$	Secondary tracer species
B	Benzene
in	Inlet
in_1	Inlet 1
in_2	Inlet 2
N	Nitric acid
NB	Nitrobenzene
out	Outlet
out_1	Outlet 1
out_2	Outlet 2
S	Sulfuric acid
W	Water
L.R.	Limiting reactant

Superscripts

A	Aqueous phase
O	Organic phase

Abbreviations

2D	Two-dimensional
3D	Three-dimensional
AAS	Atomic Absorption Spectroscopy
BET	Braunauer-Emmet-Teller theory
CFD	Computational Fluid Dynamics
DLS	Dynamic Light Scattering
DSC	Differential Scanning Calorimetry
MIL	Materials from Institut Lavoisier
MOFs	Metal-Organic Frameworks
NUB	NETmix Unit Block
STY	Space-Time Yield
TGA	Termogravimetric Analysis
XRD	X-Ray Diffraction

1 Introduction

Mixing is an essential component in the process industries when mixing of fluids of differing compositions or temperatures is required. Mixing becomes crucial for complex chemical reactions that strongly depend on the mixing efficiency for the achievement of high yields and selectivity. Static mixers have become standard equipment in the process industries as an alternative to mechanical mixers since the 1970s for the mixing of miscible or immiscible fluids, homogenization of solid particles, and for the enhancement heat and mass transfer (Szalai and Muzzio, 2003; Thakur et al., 2003). The main advantages of these mixing devices are the small space required, low equipment cost with no moving parts and no power consumption except for pumping (Thakur et al., 2003). Several static mixers of different types have become commercially available and offer a wide range of applications in different industrial processes in the pharmaceutical, petrochemical, food, cosmetics, biotechnology, water/wastewater and polymer/plastics industries (Meijer et al., 2012; Thakur et al., 2003). Due to their range of application and flexibility, the development of mathematically well defined and simple models capable of describing the performance of a given static mixer is of great importance.

The present work focuses on the NETmix reactor, a newly developed static-mixer reactor. The mixing of a NETmix reactor has been measured experimentally, and characterized through intensity of segregation CFD calculations (Gomes et al., 2010; Laranjeira et al., 2009), showing that mixing can be controlled effectively and efficiently, making this type of reactor particularly suited for complex and fast kinetics reactions where mixing quality and intensity are critical (Silva et al., 2008). Yet, the full potential of the NETmix reactor is yet to be understood and this work introduces new knowledge concerning its performance. Furthermore, the full range of applicability of the NETmix reactor is far from being covered. This dissertation aims to expand the application of NETmix as a new innovative device for the production of high added-value products.

In Section 1.1 the NETmix reactor concept is described. Existing prototypes and a current industrial application of the NETmix reactor are also presented and described. In Section 1.2 previous works having NETmix as the core technology and that are the starting point to this dissertation are reviewed. In Section 1.3 the thesis objectives and layout are presented.

1.1 The NETmix Reactor

The NETmix reactor is a new mixing technology consisting of a network of static mixing chambers interconnected by transport channels (see Figure 1.1).

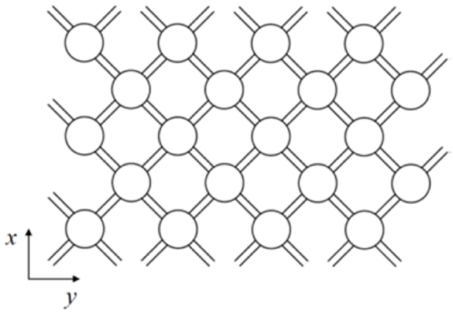


Figure 1.1. Representation of the NETmix network.

Networks are generated by the repetition of unit cells, where each unit cell consists of one chamber and two inlet and two outlet half-channels and can either be constructed from cylindrical chambers and rectangular cross section area channels

(2D unit cell, Figure 1.2a) or from spherical chambers and cylindrical channels (3D unit cell, Figure 1.2b).

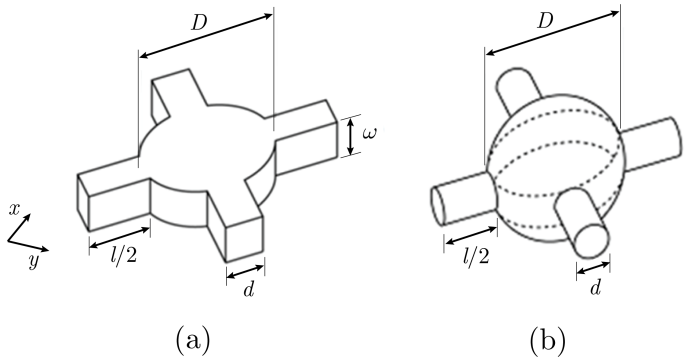


Figure 1.2. NETmix unit cell: a) 2D unit cell; b) 3D unit cell.

The characteristic dimensions of each unit cell are the chamber diameter, D, the channel width or diameter, d, and in the case of 2D unit cells is the depth, ω. L is the distance that separates the centres of two adjacent chambers and l is the length of each channel. The network size is given by the number of rows, n_x, and the number of columns, n_y.

Mixing in the NETmix reactor can only be achieved above a critical channel's Reynolds number, where the flow inside the mixing chambers evolves to a self-sustained oscillatory laminar flow regime inducing strong local laminar mixing (Gomes, 2011; Laranjeira et al., 2009). This occurs due to the geometric characteristics of the NETmix network and the local hydrodynamic instabilities induced by the immerging jets interactions at the chambers and therefore, no mechanical mixing equipment is present.

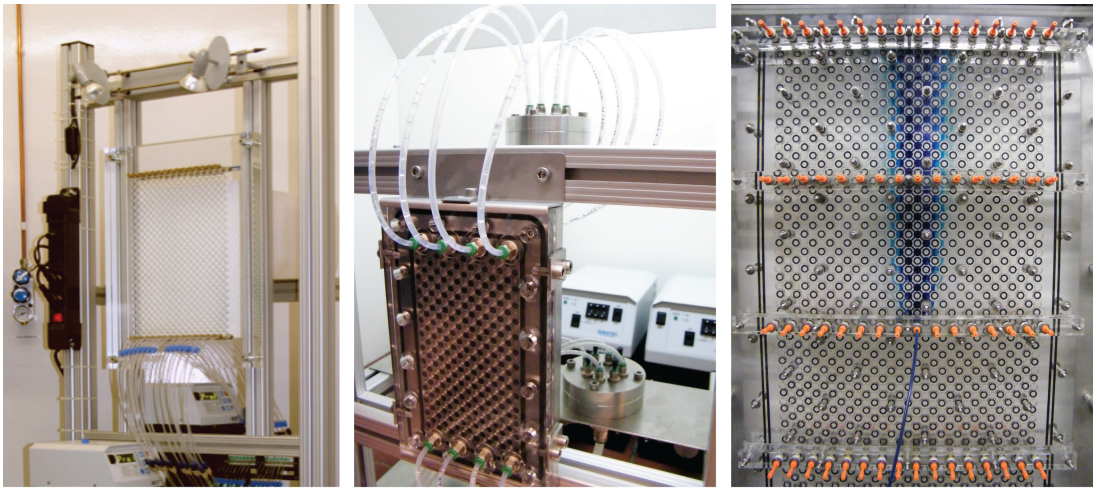
NETmix permits the careful distribution of reactants and flow rate control at the inlet, in accordance to the intended reaction stoichiometry, and product extraction with different properties at different outlets (Laranjeira et al., 2011). The network can be easily scaled-up or numbered-up depending on the process and production objectives.

1.1.1 Existing Reactors

Three different NETmix prototypes currently exist for research and development of new products. The three reactors, shown in Figure 1.3, were built for different purposes.

NETmix 3D was the first prototype ever built (Laranjeira, 2005) and had spherical chambers and cylindrical channels (see Figure 1.3a). The characteristic dimensions of this reactor are presented in Table 1.1. NETmix 3D was constructed from two acrylic slabs where half chambers and channels were imprinted and then glued together. The reactor possesses a total of 30 inlet points, i.e., one inlet point in the front and one inlet point on the back of each of the first row chambers.

The transition to the 2D configuration was introduced by Gomes (2011) and represents a considerable decrease on the construction complexity since only one of the slabs has the chambers and channels imprinted. The two slabs are no longer glued together allowing the fast disassembling and easy cleaning of the reactor, and mechanical sealing is realized by mechanical compression and o-rings. The Lab-scale NETmix 2D is a small lab-scale unit and was built for research projects with small throughputs. The Lab-scale NETmix is composed of a stainless steel plate where the chambers and channels are imprinted and a front cover that can either be made of acrylic (for flow visualization) or stainless steel (for fluids that can chemically attack acrylic or reactions at high temperatures). For larger throughputs, the Multi-Inlet NETmix 2D is used and is built entirely out of acrylic. The Multi-Inlet NETmix 2D has the particularity of incorporating multiple inlet injection points along the reactor. The geometrical characteristics of the two 2D NETmix reactors are summarized in Table 1.1.



(a) (b) (c)

Figure 1.3. NETmix prototypes: a) NETmix 3D; b) Lab-scale NETmix 2D; c) Multi-Inlet NETmix 2D.

Table 1.1. NETmix reactor prototypes geometrical characteristics

Geometry	NETmix 3D	Lab-scale NETmix 2D	Multi-Inlet NETmix 2D
Number of rows, n_x	49	29	65
Number of columns, n_y	15	8	16
Chamber diameter, D (mm)	7	6.5	8.75
Channel diameter, d (mm)	1.5	1	1.5
Geometry depth, ω (mm)	—	3	5.9
Distance between chambers, L (mm)	10	8.5	14
Channel length, l (mm)	3.2	2.1	5.4
Total volume V (mL)	140	23	1500

1.1.2 Industrial Application of the NETmix Reactor

The increasing demand for synthetic nanocrystalline hydroxyapatite material, a biocompatible material that can act as bone or dental fillers, substitutes, or replacements led to the development of an industrial production site. Fluidinova is a spin-off company from LSRE (Laboratory of Separation and Reaction Engineering) at FEUP (Faculdade de Engenharia da Universidade do Porto) and it is a specialized manufacturer of synthetic nanocrystalline hydroxyapatite material, which is

commercialized under the brand name nanoXIM (Fluidinova, 2013). Fluidinova is located at TECMAIA – Parque de Ciência e Tecnologia da Maia.

A production site for nanoXIM was developed at Fluidinova having as core technology the NETmix reactor and a new reactor was developed for the nanoXIM industrial production, the NETmix industrial reactor. It was built in stainless steal and features an o-ring insulation system for easy open-up for fouling clean up. Figure 1.4 shows the nanoXim industrial production site.

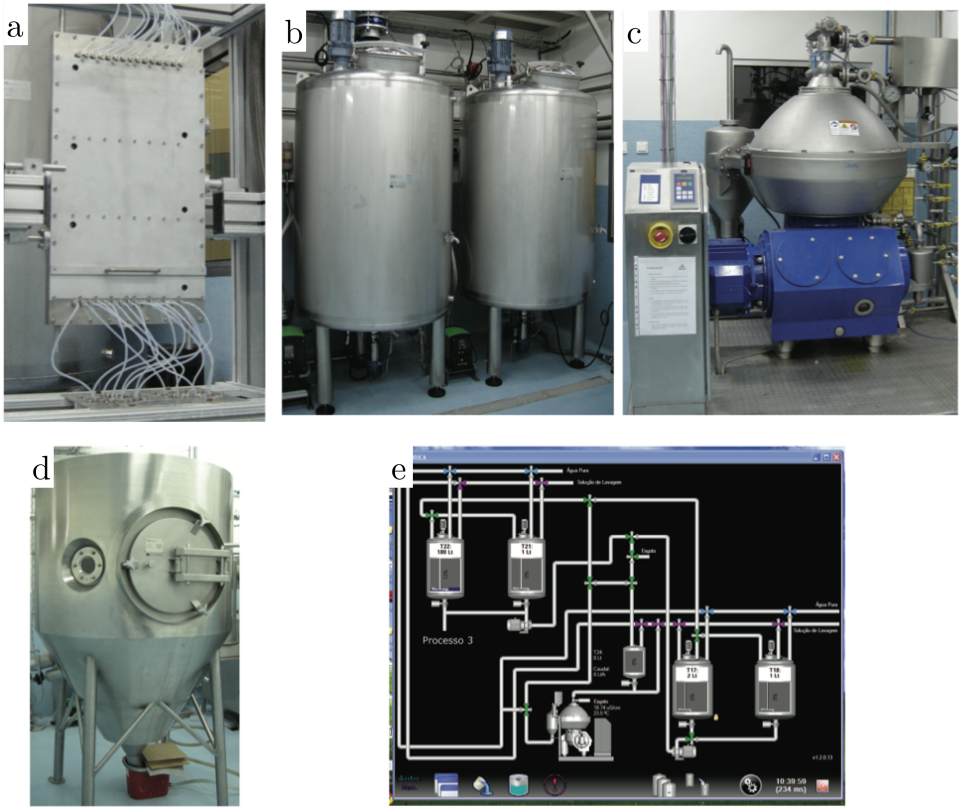


Figure 1.4. nanoXIM industrial production site: a) NETmix industrial reactor; b) reactants storage tanks; c) centrifuge unit; d) spray-dry unit; e) synoptic (adapted from Gomes (2011)).

Currently, nanoXIM production at Fluidinova is divided into three products (Fluidinova, 2013):

- nanoXIM•med, a raw material for medical devices and applications that presents high purity and nano-crystalline structures and is in accordance with the ISO13779 and ASTM F1185 standards requests for medical applications.

- nanoXIM•care, hydroxyapatite nanoparticles for personal care product formulations. It consists of highly dispersed hydroxyapatite paste and is specially conceived for toothpastes, mouthwashes and cream formulations.
- nanoXIM•R&D, hydroxyapatite nanoparticles pastes and microparticles powders for R&D and other applications. This product is suitable for separation/purification processes, other material functionalization, drug delivery systems and other applications and R&D activities.

1.2 Previous Work

This work is the follow up of the studies done by Laranjeira (2005) and Gomes (2011) for their Ph.D thesis. Before the presentation of the objectives and layout of this thesis, it is necessary to situate its departure point and introduce other works having as core technology the NETmix reactor that resulted in master's degree thesis, patents or published papers.

The NETmix concept was initially developed and explored by Laranjeira (2005). The NETmix reactor was first introduced as a general mixing and chemical reaction model based on a network structure of chambers and channels to simulate porous media. The NETmix model was capable of coupling macromixing and micromixing and to predict the steady-state yield and selectivity for different types of reaction schemes. From experimental work, Laranjeira (2005) observed that the flow only stabilized inside the NETmix chambers for low Reynolds numbers and above a certain Reynolds number flow oscillations were detected in every chamber. The transition point was identified as the critical Reynolds number where a self-sustained chaotic dynamic state develops and mixing between the inlets of each chamber occurs. Laranjeira (2005) performed 2D CFD simulations to study the flow field and viability of mixing in network structures of chambers and channels, such as the NETmix reactor. Laranjeira (2005) also performed experimental work for study the pressure drop across the NETmix static mixer. Experimental results were compared with simulations obtained both with the NETmix model and the 2D CFD model. Tracer flow visualisation experiments were also performed to gain further insight on

the Reynolds number influence on the flow field structures and dynamic behaviour of the NETmix static mixer that provided a first validation of the NETmix model as a macromixing model for the NETmix static mixer and further validation of the 2D CFD simulations. The mixing efficiency of the NETmix static mixer was studied using a consecutive competitive reaction system as test reaction. Imaging and mixing-reactions experiments are compared with the computed results from the NETmix model in order to ultimately validate the NETmix model as a macromixing and micromixing and chemical reaction descriptive model for the NETmix static mixer. These enthusiastic and promising results led to the submission of an international patent (Lopes et al., 2005) and the publication of two papers (Laranjeira et al., 2009; Laranjeira et al., 2011).

Many of the existing continuous reactors used for nanoparticles production overcome the difficulty of controlling the mixing conditions by scaling down. The issue with downscaling is the reduction of reactor throughput, and for that reason high volume production of nanoparticles is one of the major challenges for process engineers nowadays. NETmix has been shown to be a promising technology to produce nanoparticles with high reproducibility, mainly in terms of size distribution (Gomes et al., 2009; Silva et al., 2008), where the control of the stoichiometry of the reactants and micro and macromixing are key factors. This line of research resulted in the submission of an international patent (Lopes et al., 2008). A production site for those particles was developed having as core technology the NETmix reactor (Fluidinova, 2013; Gomes, 2011) as mentioned previously in Section 1.1.2 and Faria (2008) worked on the optimization of the process for producing nano-sized hydroxyapatite recurring to the NETmix reactor at Fluidinova facilities.

Correia (2008) studied the maturations steps involved on the hydroxyapatite production by wet chemical reaction using the NETmix reactor. Also, the presence of citrate ions in the reaction system as a surfactant agent was studied and had a positive effect in avoiding particle agglomeration. The final product obtained from this work was characterized as good raw material for medical applications.

Rodrigues (2008) and Constantino (2009) both studied the inclusion of metal ions in the hydroxyapatite crystalline structure. Rodrigues (2008) focused on the inclusion of iron to confer magnetic properties to nano-sized hydroxyapatite. The iron-doped hydroxyapatite showed a superparamagnetic behaviour while maintaining the characteristic distribution and particle size of nanoXIM. The main objective of the work from Constantino (2009) was the synthesis of zinc-doped hydroxyapatite for the applications in transesterfication reactions. The material produced using the NETmix reactor showed higher catalytic activity when compared to other catalysts.

Gomes (2011) first introduced the 2D NETmix geometry consisting of cylindrical chambers and rectangular cross section area channels. Along with the 2D NETmix geometry, Gomes (2011) also introduced a new flow distributor that evenly distributes the flow rate through all the inlets of the NETmix reactor. Experimental work was performed for the description of the flow field developed within the NETmix prototype by using a coloured tracer. Similarly to Laranjeira (2005), two states of the flow inside the mixing chambers were identified for the 2D NETmix geometry: a segregated pseudo-steady state and a self-sustained chaotic dynamic state where mixing between the inlets of each chamber occurs. Gomes (2011) also developed a 2D CFD model for the determination of the intensity of segregation by measuring the amount of interfacial area generated on several unit cells.

Leblebici (2011) performed experimental work for the measurement of pressure drop in two different static mixers, one of them the NETmix reactor, and further comparison with commercially available static mixers.

Costa (2012) studied the capabilities of the NETmix reactor for the production of MIL-88A, a metal-organic framework built up from iron(III) trimmers linked to fumarate ligands, creating a three-dimensional flexible crystal. The influence of concentration, temperature, addition of dispersant and the maturation step on the particle size and shape were studied. Nevertheless, no significant differences were verified between the production in the NETmix reactor and the production in a stirred vessel.

1.3 Thesis Objectives and Layout

The general objective of this work is the further investigation of the capabilities of the NETmix reactor, including its numerical modelling, characterisation and product development. Although a considerably amount of work has been previously done on the characterization of NETmix reactor, the full potential of the NETmix reactor is yet to be understood. The present work shows the role that more realistic 3D CFD modelling can play in the design of new configurations, enabling a more fundamental understanding of the NETmix reactor operation process and further application to new geometries and products. This work also proves the NETmix performance to be competitive when compared with commercially available mixers and demonstrates new benefits in the enhancement of heat and mass transfer. The NETmix technology was also used for the development of high added-value products that require fine-tuning of the operational conditions from the development of strategies and tools that can lead to the achievement of high yields and shorter reactions times.

The state of the art is presented according to its relevance in the beginning of each chapter. The thesis is divided as follows:

- In Chapter 2 a simple mechanistic model is developed for the estimation of the pressure drop for any NETmix reactor design. This model is validated with experimental data. From this pressure drop model, it is possible to make comparisons with other type of mixers by estimating two benchmarking mixing devices properties, the power number and the Z factor. The concept of the *NETmix Unit Block* (NUB) model, a simplified three-dimensional CFD simulation strategy, is introduced to reduce the computational domain for CFD simulation of the whole NETmix reactor. This simulation tool can be applied to any particular geometry of the NETmix reactor and overcomes the need of experimental data each time a new configuration is designed. Furthermore, the capability of NETmix to enhance heat and mass transfer is studied, recurring to the NETmix Unit Block model.

- In Chapter 3 a simulation tool for a multiphase liquid-liquid heterogeneous reaction is developed and the nitration of benzene is chosen as a case study. The model takes into account the mass and energy balances for each NETmix unit cell and the distribution of species between phases. The numerical implementation of the model is presented and simulation results are compared and validated with published experimental data. Moreover, considerations are made for the NETmix operational conditions.
- Chapter 4 focus on the production of MIL-88A, a metal-organic framework built up from iron(III) trimmers linked to fumarate ligands, creating a three-dimensional flexible network, from a water based chemical precipitation method. Two different types of reactors and two formulations are used and the effect of concentration, temperature and pH of the medium are studied. A precipitation model for the prediction of the precipitation of secondary species is developed. From this work, a water based chemical precipitation method at room temperature and atmospheric pressure is developed and used for the production of nanoparticles of MIL-88A with short reaction times, free of toxic solvents or surfactants and high space-time yields.
- Final remarks and suggestions for future work are presented in Chapter 5.

1.4 References

Constantino, D.S.M., 2009. Produção de Hidroxiapatite Funcionalizada com Propriedades Catalíticas [M.Sc], Departamento de Engenharia Química. Universidade do Porto, Porto.

Correia, D.F.M., 2008. Production of Hydroxyapatite Nanoparticles for Cosmetic and Orthopaedic Applications: Effect of Chelants and Dispersants [M.Sc], Departamento de Engenharia Química. Universidade do Porto, Porto.

Costa, M.F.S., 2012. Development of Nanomaterials using the NETmix® Technology: Application to Production of MOFs [M.Sc], Departamento de Engenharia Química. Universidade do Porto, Porto.

Faria, R.P.V., 2008. Estudo e Optimização do Processo industrial de Produção de Hidroxiapatite Recorrendo à Tecnologia NETmix [M.Sc], Departamento de Engenharia Química. Universidade do Porto, Porto.

Fluidinova, 2013. Fluidinova, S.A. - Hydroxyapatite Supplier, http://www.fluidinova.com/home/hydroxyapatite-supplier/4/.

Gomes, P.J., Fonte, C.P., Santos, R.J., Dias, M.M., Lopes, J.C.B., 2010. Experimental and numerical characterization and quantification of mixing in a NETmix® reactor, ECCE 7 - 7th European Congress of Chemical Engineering & CHISA 2010- 19th internation Congress and Process Engineering. Process Engineerig Publisher, Prahe, Prague, Czech Republic.

Gomes, P.J., Silva, V.M., Quadros, P.A., Dias, M.M., Lopes, J.C.B., 2009. A Highly Reproducible Continuous Process for Hydroxyapatite Nanoparticles Synthesis. Journal of Nanoscience and Nanotechnology 9, 3387-3395.

Gomes, P.J.G., 2011. The NETmix Reactor - Strategies for Optimizing Mixing and Development fo New Reactor Designs [Ph.D], Departamento de Engenharia Química. Universidade do Porto, Porto.

Laranjeira, P.E., 2005. NETmix® Static Mixer Modelling, CFD Simulation and Experimental Characterisation [Ph.D], Departamento de Engenharia Química. Universidade do Porto, Porto.

Laranjeira, P.E., Martins, A.A., Lopes, J.C.B., Dias, M.M., 2009. NETmix®, a new type of static mixer: Modeling, simulation, macromixing, and micromixing characterization. AIChE Journal 55, 2226-2243.

Laranjeira, P.E., Martins, A.A., Nunes, M.I., Lopes, J.C.B., Dias, M.M., 2011. NETmix®, a new type of static mixer: Experimental characterization and model validation. AIChE Journal 57, 1020-1032.

Leblebici, M.E., 2011. Comparative Study of NETmix® and T-jets Reactors Based on Pressure Dynamics [M.Sc], Departamento de Engenharia Química. Universidade do Porto, Porto.

Lopes, J.C.B., Dias, M.M.G.Q., Silva, V.M.T.M., Quadros, P.A., Monteiro, F.J.M., Cunha, P.J.G., Mateus, A.Y.P., 2008. Production method for calcium phosphate nano-particles with high purity and their use. PPCT/PT2007/000031. European Patent EP 2007793968.

Lopes, J.C.B., Laranjeira, P.E., Dias, M.M., Martins, A.A., 2005. Network mixer and related mixing process. PCT/IB2005/000647, February 2005. European Patent EP172643 B1, October 2008.

Meijer, H.E.H., Singh, M.K., Anderson, P.D., 2012. On the performance of static mixers: A quantitative comparison. Progress in Polymer Science 37, 1333-1349.

Rodrigues, M.F.B., 2008. Doping of Hydroxyapatite Nanoparticles with Metal Ions for Biomedical, Orthopedic and Dentistry Applications [M.Sc], Departamento de Engenharia Química. Universidade do Porto, Porto.

Silva, V.M., Quadros, P.A., Laranjeira, P.E., Dias, M.M., Lopes, J.C.B., 2008. A Novel Continuous Industrial Process for Producing Hydroxyapatite Nanoparticles. Journal of Dispersion Science and Technology 29, 542-547.

Szalai, E.S., Muzzio, F.J., 2003. Fundamental approach to the design and optimization of static mixers. AIChE Journal 49, 2687-2699.

Thakur, R.K., Vial, C., Nigam, K.D.P., Nauman, E.B., Djelveh, G., 2003. Static Mixers in the Process Industries—A Review. Chemical Engineering Research and Design 81, 787-826.

2 Transport Phenomena Studies in the NETmix Reactor

2.1 Introduction

Static mixers are nowadays used in several industrial applications to perform continuous operations and have become standard equipment since the 1970s for the mixing of miscible or immiscible fluids, homogenization of solid particles, and for the enhancement heat and mass transfer (Szalai and Muzzio, 2003; Thakur et al., 2003). as an alternative to mechanical mixers. The effectiveness of static mixers to deliver good mixing of miscible fluids or to enhance heat and mass transfer comes from their capacity to induce radial mixing and to bring fluid elements into close proximity (Thakur et al., 2003). In these devices, products are mixed by flow energy alone. Thus they do not require external power except the required power for pumping the fluids through the mixer. Coupled with the small space required, low equipment cost and no moving parts (Thakur et al., 2003). Static mixers are applied in a wide range of different industrial processes in the pharmaceutical, petrochemical, food, cosmetics, biotechnology, water/wastewater, paper and polymer/plastics industries (Meijer et al., 2012; Thakur et al., 2003). Several static mixers have become commercially available and can be of different types:

- Twisted static mixers constructed of right and left twisted plates such as Kenics mixer from Chemineer Inc. (Chemineer Inc., 2013), or the combination of individual segments positioned to divide and rotate the flow alternately such as the Statiflo static mixer series from Statiflo International (Statiflo Iternational, 2013) and the Inliner series from SPX-Lightnin (SPX-Lightnin, 2013).
- Structured static mixers made of stacked lamella elements positioned to create intricate network of flow channels such as the SMV, SMX, SMXL static mixers from Sulzer (Sulzer, 2013), the KMX static mixer from Chemineer Inc. (Chemineer Inc., 2013) and the Konax static mixer from Konax Systems Inc. (Konax Systems Inc., 2013).
- Vortex generating static mixers, where mixing is accomplished by controlled vortex structures generated by elements that suddenly change the cross section of the tubing, such as the High Efficiency Vortex Mixer (HEV) from Chemineer Inc. (Chemineer Inc., 2013) and the compacX, SMI and SMF from Sulzer (Sulzer, 2013).
- Interfacial surface generator (ISG) static mixer that consists of individual mixing elements that are stacked in a tubular housing from Ross Mixers (Ross Mixers, 2013).

The main drawback on using static mixers is the extra pressure drop inserted in the system as well as greater potential for fouling, relative difficulty for cleaning and greater cost (Thakur et al., 2003). The selection of a static mixer is not straightforward and until recently only a few studies have been reported that compare the performance of static mixers in terms of the Z factor.

The characterization and comparison of performance of static mixers started with the work of Pahl and Muschelknautz (1980) and Cybulski and Werner (1986).

Rauline et al. (1998) used 3D numerical simulations in laminar creeping flow regime to study and compare the performance of six different static mixers (Kenics, Inliner, LPD, Cleveland, SMX and ISG) providing the first compilation of dimensionless

pressure drop. Numerical pressure drop results were compared against experimental data, showing overall a good agreement.

The review paper of Thakur et al. (2003) gives an extensive review on the energy efficiency of different static mixers for a wide range of flow conditions and provides a good summary, discussing in which applications static mixers are beneficial and are to be preferred above stirred vessels and other conventionally agitated vessels.

More recently, Meijer et al. (2012) also provided a detailed study for the performance of industrially relevant static mixers that work via chaotic advection in the Stokes regime for highly viscous fluids, flowing at low Reynolds numbers and the different static mixers were compared using as criteria the energy consumption, measured in terms of the dimensionless pressure drop.

The fact that static mixers can enhance heat transfer is not a new topic and several authors have already observed the beneficial effect on the heat transfer and tried to find Nusselt number correlations for different static mixing elements to be used in the design of heat transfer equipment. Grace (1971) and Nauman (1979) presented the first studies on the enhancement of heat transfer and thermal homogeneity using static mixers and assess the heat transfer performance with the Nusselt number.

Lammers and Beenackers (1994), Joshi et al. (1995), determined and proposed correlations of the Nusselt number for the Kenics static mixer for the operation in laminar regime. Myers et al. (1997) determined a correlation for the Nusselt number for the operation in the turbulent regime. In general, the heat transfer coefficient can be enhanced 2-3 times in these static mixing devices.

Manglik and Bergles (1993) determined laminar flow correlations for the Nusselt number for twisted-tape inserts in isothermal tubes and conclude that enhancement in heat transfer is due to the tube partitioning and flow blockage, longer flow path, and secondary fluid circulation.

Li et al. (1996) studied the Sulzer SMX static mixer and observed that the heat transfer coefficient is enhanced by a factor of about 5 in the Sulzer SMX static mixer compared with that in an empty tube.

Thakur et al. (2003) delivered the first compilation on correlations for the Nusselt number obtained experimentally in tubes containing commercially available static mixers.

Computational fluid dynamics (CFD) is nowadays seen as an increasingly effective alternative to speed up equipment design (Szalai and Muzzio, 2003) and to be used as a fundamental tool for optimizing heat transfer enhancement using static mixers (Thakur et al., 2003). The use of this computational tool can be found in the literature in, for example, Visser et al. (1999) that used CFD simulations to predict pressures, velocities and temperatures in SMX elements and in the work of Lisboa et al. (2010) that performed a CFD simulation study of a Kenics static mixer to be used as a heat exchanger for supercritical carbon dioxide.

Heat exchangers that include static mixing elements are currently used in the industry and have become commercially available. Some examples of such devices are:

- Kenics Heat Exchanger from Chemineer Inc. (Chemineer Inc., 2013);
- Heat Exchanger Type SMR, Monotube Heat Exchanger Type SMXL and the Multitube Heat Exchanger Type SMXL from Sulzer (Sulzer, 2013);
- STX Heat Exchange Motionless Mixer series from Statiflo International (Statiflo Iternational, 2013);
- Klean-Wall Heat Exchanger from Konax Systems Inc (Konax Systems Inc., 2013).

These manufactures claim to enhance the heat transfer by the improved radial mixing and flow division for elimination of boundary layers that form the major resistance to heat transfer in laminar flow. Figure 2.1 shows some of the referred heat exchangers.

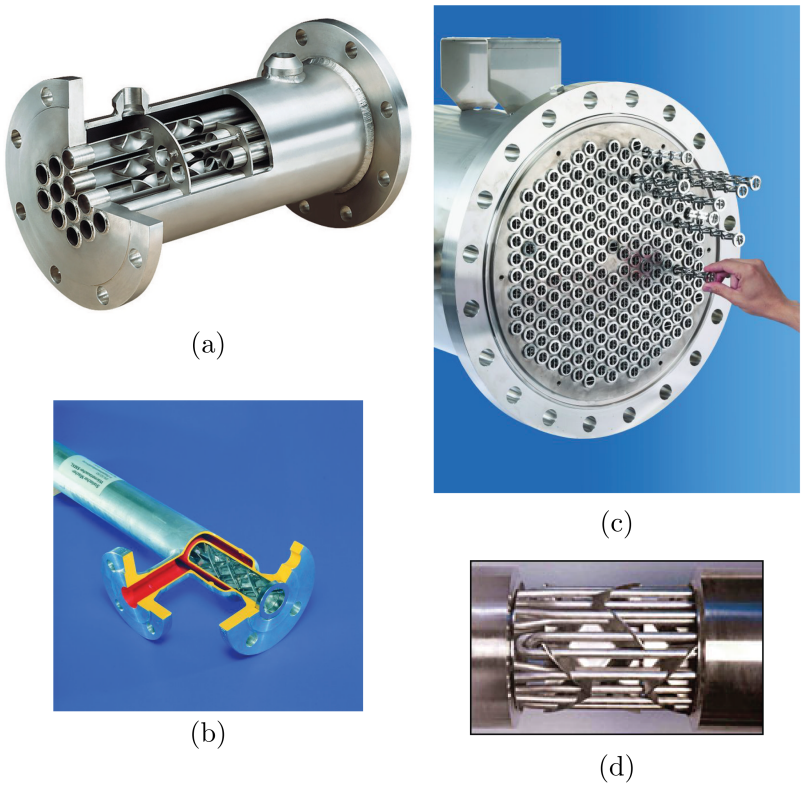


Figure 2.1. Commercially available heat exchangers with static mixing elements: a) Kenics Heat Exchanger; b) Sulzer Monotube Heat Exchanger Type SMXL ; c) Sulzer Multitube Heat Exchanger Type SMXL; d) Statiflo STX Heat Exchange Motionless Mixer STLX.

Mass transfer enhancement from the inclusion of static mixing devices is also a subject of great study in the literature. Static mixers are usually used as interface generators in multiphase flows to improve radial mixing (Cavatorta et al., 1999; Chisti and Moo-Young, 1996; Joshi et al., 1995; Munter, 2010) and it was observed that the mass transfer coefficients in static mixers can be 2 orders of magnitude higher than that in conventional stirred tanks and bubble columns (Munter, 2010) .

Few works can be found in the literature concerning the application of static mixing elements for the mass transfer enhancement in wall-coated reactors.

Morris and Misson (1974) and Morris and Benyon (1976) cited by Joshi et al. (1995) presented details of local and mean mass transfer from the surface of a tube fitted with Kenics type elements. Experimental measurements on the mass transfer coefficient were made on the transfer of naphthalene from the tube surface to the air flowing down the tube to find Sherwood number correlations.

Khinast et al. (2003) induced chaotic laminar flow mixing by introducing a Kenics static mixer into a ceramic wall-coated reactor tube and observed that the effective Sherwood number is 1.5 to 3 times higher than that for an empty tube.

Li et al. (2011) used a Kenics static mixer to intensify heterogeneous photocatalysis in the degradation of different compounds. Li et al. (2011) observed that the degradation rates increased from 20% to 150% with the installation of the Kenics static mixer. This area of catalysis is still dominated by microstructured reactors (MSRs) due to their high surface to volume ratio of the order of $10^4\ m^2/m^3$ compared to more traditional devices with a surface to volume ratio of usually $10^2\ m^2/m^3$ that seldom exceeds $10^3\ m^2/m^3$ (Kiwi-Minsker and Renken, 2005). Nevertheless, Khinast et al. (2003) and Li et al. (2011) demonstrated that static mixers can introduce significant advantages in this area.

In this chapter, transport phenomena will be studied in the NETmix reactor. Mixing in a NETmix reactor has been evaluated and characterized both through experimental measures and intensity of segregation CFD calculations (Gomes et al., 2010; Laranjeira et al., 2009), showing that mixing can be controlled effectively and efficiently, making this type of reactor particularly suited for complex and fast kinetics reactions where mixing quality and intensity are critical (Silva et al., 2008). However, the performance of the NETmix reactor, in terms of energy performance, was yet to be evaluated and compared with other mixing devices.

In this chapter, a simple mechanistic model is developed, that can estimate the pressure drop for any NETmix reactor design, and its validation with experimental data and CFD simulations is presented. From this pressure drop model, it is then possible to make comparisons with other type of mixers by estimating two benchmarking mixing devices properties, the power number and the Z factor.

The capability of NETmix to enhance heat and mass transfer was also studied. NETmix can be seen as a good candidate device for heat and mass transfer due to its high surface to volume ratio of the order of $\sim 10^3\ m^2/m^3$, one or two orders of

magnitude higher when compared to conventional heat exchanger/reactors (Anxionnaz et al., 2008) and conventional reactors for catalytic reactions (Keil, 2004; Kiwi-Minsker and Renken, 2005) and although the surface to volume ratio is one order of magnitude smaller than for MSRs (Kashid and Kiwi-Minsker, 2009; Kiwi-Minsker and Renken, 2005), the heat and mass transfer coefficients are expected to be enhanced by the induced laminar mixing in the NETmix chambers (Khinast et al., 2003; Li et al., 2011) associated with lower pressure drops.

This chapter is organized into five sections. In Section 2.2, a mechanistic model for the pressure drop with a single adjustable parameter is presented. The mathematical foundations for the estimation of heat and mass transfer coefficients in the NETmix geometry are also presented. In Section 2.3 experimental setup is described and results are presented and discussed. In section 2.4 CFD models are described and simulation results are shown and discussed. Conclusions are presented in Section 2.5.

2.2 Transport Phenomena in NETmix Reactor

2.2.1 NETmix Pressure Drop Assessment

2.2.1.1 Mechanistic Pressure Drop Model

A mechanistic model has been developed following the general strategy of network modelling for flow in packed beds proposed by Martins et al. (2007). The pressure drop in each mixing unit cell, Δp_{uc}, is modelled using an analogy with an equivalent pure resistive electric circuit (Dias and Payatakes, 1986), where the flow rate across the channels resembles the current through resistive branches and the pressure drop between chambers corresponds to the voltage between nodes and is expressed by

$$\Delta p_{uc} = R_{uc} q_{channel} \tag{2.1}$$

where R_{uc} is the total hydraulic resistance from the inlet to the outlet of the unit cell and $q_{channel}$ is the flow rate through the channel. This hydrodynamic model assumes

the flow to be isothermal, incompressible, laminar and steady state. The total hydraulic resistance can be expressed as the sum of three terms,

$$R_{uc} = R^{F} + R^{LF} + R^{NLF} \tag{2.2}$$

where R^{F} is the friction resistance in the channels, and R^{LF} and R^{NLF} are hydraulic inertial resistances related to the contractions and expansions in the chambers. Friction resistance in the chambers is considered negligible.

The friction resistance in the channels in laminar regime is obtained from Haegen-Poiseuille equation as,

$$R^{F} = \frac{1}{2} f \rho \frac{l}{d_h} \frac{q_{channel}}{A_{channel}^2} = 32\mu \frac{l}{d_h^2 A_{channel}} \tag{2.3}$$

where f is the channel friction factor, ρ is the fluid density, l is the channel length, d_h is the channel hydraulic diameter and $A_{channel}$ is the channel cross sectional area. The hydraulic diameter is equal to the diameter of the cylindrical channels or to

$$d_h = 2\omega d / \left(\omega + d\right) \tag{2.4}$$

for rectangular cross section area channels.

The linear flow hydraulic resistance, R^{LF}, in the chamber for laminar regime was defined by Koplik (1982) as

$$R^{LF} = 32\mu \frac{l^*}{d_h^2 A_{channel}} \tag{2.5}$$

where $l^* = 2d_h / \pi$ for this kind of geometry. This resistance exists whenever an unbounded jet flow has to be considered. When the fluid leaves the channel, the canonical friction term cannot model the energy transfer in the chamber, as the flow is not bounded by the channel walls. Instead, the fluid's solid channel is replaced with a viscous surrounding as long as the jet keeps its form. The nonlinear flow

hydraulic resistance, R^{NLF}, that takes into account the energy dissipation due to accelerations/decelerations in the mixing chambers, and is modelled as,

$$R^{NLF} = \frac{1}{2}\rho K \frac{q_{channel}}{A^2_{channel}} \tag{2.6}$$

where K is a coefficient equivalent to the loss coefficients for sudden contractions and expansions in piping systems. The value of K depends on the particular geometrical characteristics of NETmix, and can be determined from experimental data for particular designs, or in general from CFD laminar simulations for any NETmix design.

The total pressure drop in the NETmix device, Δp_{NETmix}, will then be determined by summing the pressure drop for each unit cell, along the shortest path (see Figure 2.2), that is

$$\Delta p_{\mathrm{NETmix}} = \sum_{i=1}^{n_x} \Delta p_{uc} = n_x \Delta p_{uc}. \tag{2.7}$$

where n_x is the number of rows in the main flow direction.

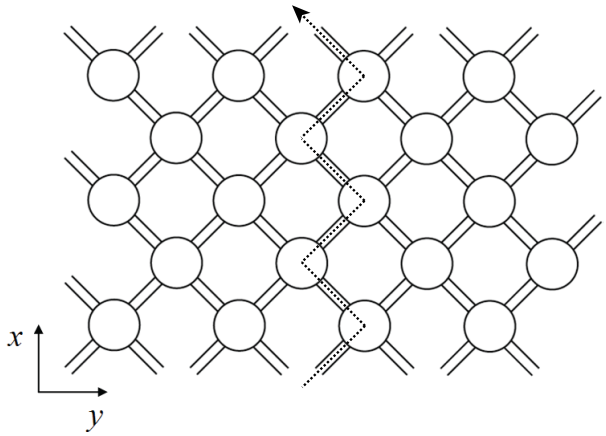


Figure 2.2. Shortest path for calculating the total pressure drop in the system.

Above a certain value of Reynolds number (critical Reynolds number, $\mathrm{Re}_c = 150$) the flow inside the mixing chambers, diverges from a simple stationary wavy flow to a self-sustained oscillatory flow regime inducing locally at the chamber scale, and over

the whole reactor, a strong laminar chamber mixing (Laranjeira, 2005). These oscillations are intrinsic to the nature of the flow and not determined by external factors. The natural frequency of these oscillations, f_{osc}, was proposed to be simply determined to the space-time inside the unit cell (Laranjeira, 2005), which can be expressed as

$$f_{osc} = \frac{1}{\tau_{uc}} = 2\frac{V_{uc}}{d_h A_{channel}}\frac{\mu}{\rho}\mathrm{Re} \tag{2.8}$$

in which τ_{uc} is the chamber space-time equal to $V_{uc}/2q_{channel}$, V_{uc} is the volume of the unit cell, and Re is the Reynolds number calculated with the channels hydraulic diameter,

$$\mathrm{Re} = \frac{\rho d_h \overline{v}_{channel}}{\mu} \tag{2.9}$$

where $\overline{v}_{channel}$ is the average velocity through the channel. The unit cell space-time, τ_{uc}, can also be viewed as the local mixing time scale, solely determined from geometrical parameters and fluid velocity (Equation (2.8)). Experimental measurement of the dynamics of pressure drop oscillations will be presented in Section 2.3.4.2 for comparison with predicted values from Equation (2.8), useful in evaluating the mixing time scales in the NETmix.

2.2.1.2 NETmix Power Number and Z Factor

A common approach in the analysis of the power consumption in mixing devices, such as stirred tanks, is to plot the dimensionless power number versus the impeller Reynolds number. The dimensionless power number, N_p, is defined as the ratio between the total energy power supplied to the mixing device, and the energy that is needed to cause the fluid motion necessary for mixing, i.e, the total energy input minus the energy losses by friction. For a static mixing device, Laranjeira (2005) has shown that a similar power number can be defined as,

$$N_P = \frac{\Delta p_{\text{mixer}}}{\Delta p_{\text{mixer}} - \Delta p_{\text{friction}}} \tag{2.10}$$

where Δp_{mixer} is the total pressure drop in the mixer and $\Delta p_{\text{friction}}$ is the pressure drop due to friction. For the NETmix operating in laminar regime, with the previously derived mechanistic model (Equations (2.1) through (2.6)), the power number can now be calculated as,

$$N_P = 1 + \frac{1}{K}\frac{\left(l + 2d_h/\pi\right)}{d_h}\frac{64}{\text{Re}} \tag{2.11}$$

Another common way of comparing the pressure drop for different static mixers is by using the Z factor defined as the ratio between the pressure drop through the static mixer, $\Delta p_{\text{static mixer}}$, and the equivalent pressure drop through an empty tube of equal length and diameter, $\Delta p_{\text{empty tube}}$. For the NETmix geometry, the Z factor can be derived similarly, and

$$Z = \frac{\Delta p_{\text{static mixer}}}{\Delta p_{\text{empty tube}}} = \frac{\left(l + 2d_h/\pi\right)}{L} + \frac{d_h K}{64L}\text{Re} \tag{2.12}$$

where L is the distance between the centres of interconnected chambers. As can be seen in Equations (2.11) and (2.12), for the same Reynolds number, both the power number and the Z factor, are not dependent on the fluid properties, and are only dependent on the geometrical design configuration of the NETmix reactor.

2.2.2 Heat Transfer

In this section, the convective heat transfer coefficient for the NETmix is defined. Results of convective heat transfer coefficient will be presented in the dimensionless form as Nusselt number. The fluid flow with heat transfer through the walls of a 2D NETmix geometry resembles to plate heat exchanger equipment. Therefore, an analogy of Nusselt numbers in the NETmix reactor and the Nusselt number for the

flow between parallel plates is made for known analytic solutions in the laminar regime of two different reference heat transfer conditions: constant wall temperature and constant wall heat flux.

2.2.2.1 Energy Balance to a Unit Cell

The heat flow rate transferred across the solid interface in a unit cell, $\dot{Q}_{uc}$, can be estimated by performing an energy balance to the unit cell domain (see Figure 1.2),

$$\dot{Q}_{uc} - \oiint_{CS} T\rho c_P \left(\vec{v}\cdot\vec{n}\right)\mathrm{d}S = 0 \tag{2.13}$$

where c_P is the heat capacity of the fluid , T is temperature and $\vec{v}$ is the fluid velocity vector field. The vector $\vec{n}$ represents here the normal unitary vector pointing outwards the control surface that delimits the boundaries of the domain, CS.

Since the unit cell only has two inlets and two outlets (Figure 1.2), the transferred heat flow rate across the solid interface is given by the sum of the enthalpy flow rate at the inlets and outlets,

$$\dot{Q}_{uc} = \dot{H}_{out_1} + \dot{H}_{out_2} + \dot{H}_{in_1} + \dot{H}_{in_2} \tag{2.14}$$

where $\dot{H}_{in_1}$ and $\dot{H}_{in_2}$ are the enthalpy flow rates in inlet 1 and inlet 2 of the unit cell, respectively, and $\dot{H}_{out_1}$ and $\dot{H}_{out_2}$ are the enthalpy flow rates in outlet 1 and outlet 2, respectively. For this geometry, the enthalpy flow rate from each inlet/outlet can be calculated as

$$\dot{H}_{in_i/out_i} = \iint_{A_i} T\rho c_P \left(\vec{v}\cdot\vec{n}\right)\mathrm{d}A \tag{2.15}$$

where $\dot{H}_{in_i/out_i}$ takes a positive value when evaluated at the outlets and a negative value when evaluated at the inlets. Once calculated the rate of heat flow across the solid interface, the average convective heat transfer coefficient, h_{uc}, can be

determined by considering the solid area for heat transfer, A_{transf}, and the temperature difference from the walls to the bulk of the fluid flow,

$$h_{uc} = \frac{A_{transf} \Delta T_{uc}}{\dot{Q}_{uc}} \tag{2.16}$$

where ΔT_{uc} is a characteristic temperature difference in the unit cell and estimated by the logarithm mean temperature difference,

$$\Delta T_{uc} = \frac{T_{b,\,out} - T_{b,\,in}}{\ln\left[\left(T_{wall,\,in} - T_{b,\,in}\right) / \left(T_{wall,\,out} - T_{b,\,out}\right)\right]} \tag{2.17}$$

where $T_{b,in}$ and $T_{b,out}$ are the average bulk temperatures at the inlet and the outlet of the unit cell, respectively, and $T_{wall,in}$ and $T_{wall,out}$ are the average wall temperatures at the inlet and outlet of the unit cell, respectively (Çengel, 2003). In Appendix A the derivation of ΔT_{uc} for a unit cell was made. The bulk temperature is the average temperature weighted by the mass flow rate of the fluid in the channel,

$$T_b = \frac{\iint_A \rho\left(\vec{v} \cdot \vec{n}\right) T \, \mathrm{d}A}{\iint_A \rho\left(\vec{v} \cdot \vec{n}\right) \mathrm{d}A}. \tag{2.18}$$

The computed values of convective heat transfer coefficient will be reported as unit cell Nusselt number, defined as

$$\mathrm{Nu}_{uc} = \frac{h_{uc} d_h}{\kappa} \tag{2.19}$$

where κ is the thermal conductivity of the fluid and d_h is the channel's hydraulic diameter defined in Equation (2.4).

2.2.2.2 Nusselt Number for Flow Between Parallel Plates

When a given fluid with a uniform temperature flows between parallel plates whose temperature is kept at different temperatures, the fluid particles in contact with the wall will assume the surface temperature. This initiates convective heat transfer and the development of a thermal boundary layer. The thickness of the thermal boundary layer increases in the flow direction until it reaches the centre of the gap between the parallel plates. The region over which the thermal boundary layer is still developing is called thermally developing region. The region beyond the thermally developing region in which the dimensionless temperature profile expressed as $\left(T_{wall}-T\right)/\left(T_{wall}-T_b\right)$ remains unchanged, where T_{wall} is the temperature at the wall of the parallel plates and T_b is the bulk temperature of the fluid flow, is called the thermally fully developed region. Figure 2.3 shows a representation of the development of the thermal boundary layer for the cooling of a fluid flowing between parallel plates where can be seen the change of the temperature profile along the flow direction. Here x_{PP} is distance from the entrance in the flow direction and ω is the clearance between the two parallel plates,

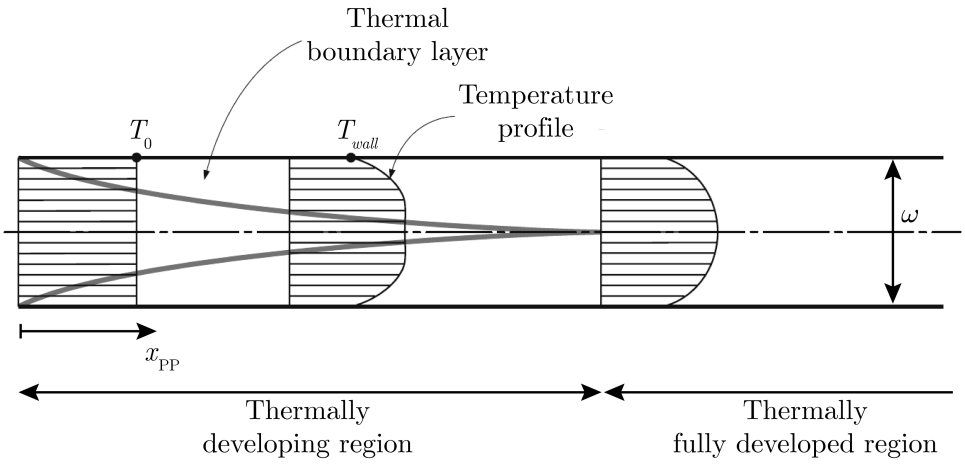


Figure 2.3. Development of the thermal boundary layer between parallel plates for the cooling of a fluid (adapted from Çengel (2003)).

The asymptotic results for flow between parallel plates with constant wall temperatures have been derived for Newtonian fluids with constant physical

properties and fully developed velocity profiles (Bird et al., 2002; Shah and London, 1978).

For the flow region of the domain where the thermal boundary layer is still developing, the parallel plate local Nusselt number, $\mathrm{Nu}_{\mathrm{PP}}$, is a function of the dimensionless thermal entrance length and is given by

$$\mathrm{Nu}_{\mathrm{PP}} = \frac{4}{3^{1/3}\Gamma\left(3/4\right)}\left(x^{*}_{\mathrm{PP}}\right)^{-1/3} \tag{2.20}$$

where Γ is the gamma function and x^{*}_{PP} is the dimensionless thermal entrance length for flow between parallel plates, defined as

$$x^{*}_{\mathrm{PP}} = \frac{1}{\mathrm{Re}_{\mathrm{PP}}\,\mathrm{Pr}}\frac{x_{\mathrm{PP}}}{2\omega}. \tag{2.21}$$

$\mathrm{Pr} = c_{P}\mu/\kappa$ is the Prandtl number and $\mathrm{Re}_{\mathrm{PP}} = 2\omega\rho\overline{v}/\mu$ is the parallel plates Reynolds number. The local Nusselt number is here defined as $\mathrm{Nu}_{\mathrm{PP}} = 2h_{\mathrm{PP}}\omega/\kappa$ (Bird et al., 2002) where h_{PP} is the parallel plates local convective heat transfer coefficient.

The value of the Nusselt number decreases with the thermal entrance length while the thermal boundary layer is still developing. Finally, for the thermally fully developed region where the thermal boundary layer is fully developed, the Nusselt number is found to be a constant value,

$$\mathrm{Nu}_{\mathrm{PP}} = 7.54. \tag{2.22}$$

Between the two asymptotic regions, the Nusselt number curve as a function of dimensionless thermal entrance lengths can be well approximated by

$$\mathrm{Nu}_{\mathrm{PP}} = \left[\left(\frac{4}{3^{1/3}\Gamma\left(3/4\right)}\left(x^{*}_{\mathrm{PP}}\right)^{-1/3}\right)^{n} + 7.54^{n}\right]^{1/n} \tag{2.23}$$

where $n = 8$ gives a good approximation to the values of Bird et al. (2002) (see Figure 2.4).

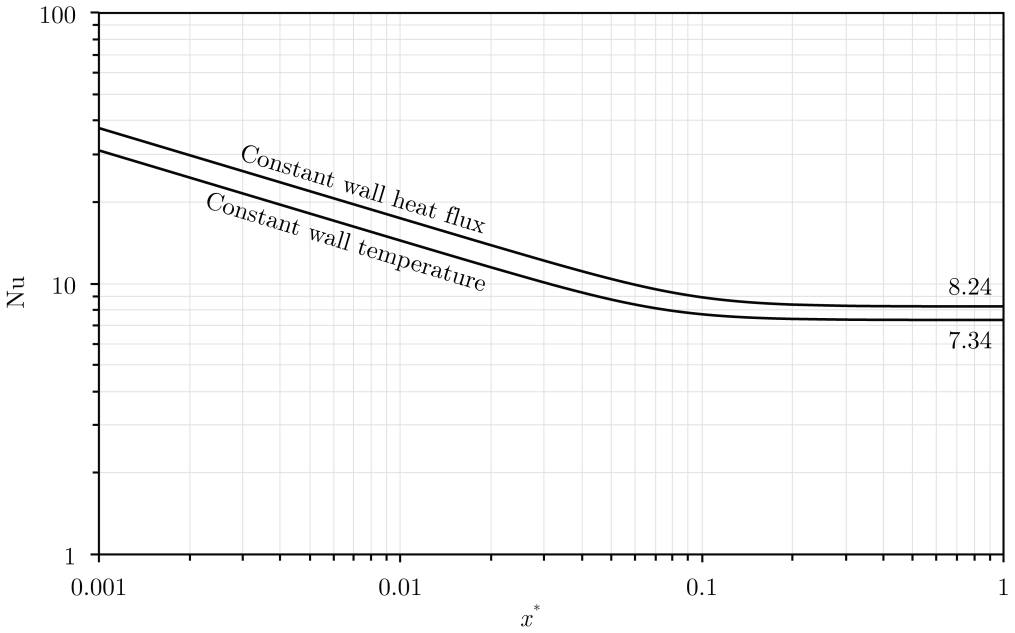


Figure 2.4. Nusselt number for fully developed laminar flow of Newtonian fluids in parallel plates (Bird et al., 2002).

A similar derivation was made for the flow between parallel plates with constant heat flux on the walls for Newtonian fluids with constant physical properties and for fully developed velocity profiles (Bird et al., 2002; Shah and London, 1978). For thermally developing region, the Nusselt number is given by

$$\mathrm{Nu}_{\mathrm{PP}} = \frac{4\Gamma\left(2/3\right)}{3^{1/3}}\left(x^*_{\mathrm{PP}}\right)^{-1/3} \tag{2.24}$$

and for the thermally fully developed flow, the Nusselt number is found to be a constant value,

$$\mathrm{Nu}_{\mathrm{PP}} = 8.24. \tag{2.25}$$

The same approximation used in Equation (2.23) can be used for the estimation of the Nusselt number for the whole range of dimensionless thermal entrance length,

$$\mathrm{Nu}_{\mathrm{PP}} = \left[\left(\frac{4\Gamma\left(2/3\right)}{3^{1/3}} \left(x^{*}_{\mathrm{PP}} \right)^{-1/3} \right)^{n} + 8.24^{n} \right]^{1/n} \tag{2.26}$$

where $n = 8$ gives a good approximation (see Figure 2.4).

2.2.2.3 The Analogy with the NETmix Geometry

For the NETmix geometry, the thermal entrance length at a given unit cell can be defined, similarly, as

$$x^{*}_{uc} = \frac{1}{\mathrm{Re}\,\mathrm{Pr}} \frac{x_{uc}}{\omega} \tag{2.27}$$

where x_{uc} is the distance between the entrance of the NETmix reactor and the middle position of the unit cell and can be expressed as

$$x_{uc} = \left(i_{x} - \frac{1}{2} \right) \frac{L}{\sqrt{2}} \tag{2.28}$$

where i_{x} is the number of the row where the unit cell is positioned and L is the distance between the centres of interconnected chambers.

Therefore, taking into consideration the different definitions of the Reynolds and Nusselt numbers for the NETmix geometry and for flow between parallel plates (Bird et al., 2002), the following analogue definitions have to be established:

- For the thermal entrance length

$$x_{uc} = \frac{\omega}{4 d_{h}} x_{\mathrm{PP}}; \tag{2.29}$$

- For the unit cell Nusselt number

$$\mathrm{Nu}_{uc} = \frac{d_h}{2\omega}\mathrm{Nu}_{\mathrm{PP}}. \tag{2.30}$$

The unit cell Nusselt number, in Equation (2.19), is the average value over the unit cell, evaluated between the inlet and outlet of the unit cell while the mathematical expressions of Equations (2.23) and (2.26) provided by Bird et al. (2002) give the local Nusselt number, and consequently the local convective heat transfer coefficient, at a given thermal entrance length for flow between parallel plates. For the comparison between both results of Nusselt numbers for the unit cell and parallel plates, it is necessary to examine if the average convective heat transfer coefficient calculated between two positions that correspond to the inlet and outlet positions of a unit cell can be directly compared with the local heat transfer coefficient estimated to a position equal to the middle position of a unit cell or if it deviates from local convective heat transfer coefficient value.

The average convective heat transfer coefficient, $\overline{h}$, between the dimensionless thermal entrance points x_{in}^* to x_{out}^* for thermally developing flows is given by

$$\overline{h} = \frac{\int_{x_{in}^*}^{x_{out}^*} h_{loc}\left(x^*\right)\mathrm{d}x^*}{x_{out}^* - x_{in}^*} \tag{2.31}$$

where h_{loc} is a function of the type

$$h_{loc} = C'\left(x^*\right)^{-1/3} \tag{2.32}$$

and C' is a constant value. Integrating Equation (2.31), the average convective heat transfer coefficient comes

$$\overline{h} = \frac{3}{2}C'\frac{\left[\left(x_{out}^*\right)^{2/3} - \left(x_{in}^*\right)^{2/3}\right]}{x_{out}^* - x_{in}^*}. \tag{2.33}$$

The dimensionless thermal entrance points x_{in}^{*} and x_{out}^{*} can be related to x_{uc}^{*} by

$$\begin{cases} x_{out}^{*} = \left(\dfrac{i_x}{i_x - 1/2} \right) x_{uc}^{*} \\ x_{in}^{*} = \left(\dfrac{i_x - 1}{i_x - 1/2} \right) x_{uc}^{*} \end{cases} \tag{2.34}$$

Combining Equation (2.32) and Equation (2.33), the ratio between the average and local convective heat transfer coefficient is given by

$$\left. \frac{\overline{h}}{h_{loc}} \right|_{x^{*}=x_{uc}^{*}} = \frac{3}{2} \frac{\left(\dfrac{i_x}{i_x - 1/2} \right)^{2/3} - \left(\dfrac{i_x - 1}{i_x - 1/2} \right)^{2/3}}{\left(\dfrac{1}{i_x - 1/2} \right)}. \tag{2.35}$$

Except for the first chamber, the average convective heat transfer coefficient calculated between two positions that correspond to the inlet and outlet of a unit cell do not differ more than 0.5% with respect to the local heat transfer coefficient estimated at the position that corresponds to the middle position of a unit cell. Therefore, the direct comparison of the overall unit cell heat coefficient and the local heat transfer coefficient analytical solution derived by Bird et al. (2002) can be made.

2.2.3 Mass Transfer

In this section, the convective mass transfer coefficient for the NETmix is defined. Results of convective mass transfer coefficient will be presented in the dimensionless form as Sherwood number. Mass transfer studies are made for a NETmix reactor with a coated external wall with a secondary species $\mathcal{A}$ that dissolves and is transferred from the solid interface to the bulk of the fluid flow. The analogy of Sherwood number in the NETmix reactor is made with the Sherwood number for the flow between parallel plates for the known analytic solution in the laminar regime for mass transfer with imposed constant wall concentration.

2.2.3.1 Mass Balance to a Unit Cell

The mass of a secondary species $\mathcal{A}$ transferred from the solid interface in a unit cell can be estimated by a mass balance to the unit cell domain,

$$\dot{N}_{\mathcal{A}} - \frac{1}{M_{\mathcal{A}}} \oiint_{CS} \rho w_{\mathcal{A}} \left(\vec{v} \cdot \vec{n}\right) \mathrm{d}S = 0 \tag{2.36}$$

where $M_{\mathcal{A}}$ is the molar mass of the species $\mathcal{A}$ and $\dot{N}_{\mathcal{A}}$ is the molar flow rate of species $\mathcal{A}$ transferred from the solid interface. For the particular geometry of the unit cell with two inlets and two outlets, the transferred molar flow rate of species $\mathcal{A}$ from the solid interface is given by the sum of the molar flow rate at the inlets and outlets,

$$\dot{N}_{\mathcal{A}} = F_{\mathcal{A},out_1} + F_{\mathcal{A},out_2} + F_{\mathcal{A},in_1} + F_{\mathcal{A},in_2} \tag{2.37}$$

where the $F_{\mathcal{A},in_1}$ and $F_{\mathcal{A},in_2}$ are the molar flow rate of species $\mathcal{A}$ in inlet 1 and inlet 2 of the unit cell, respectively, and $F_{\mathcal{A},out_1}$ and $F_{\mathcal{A},out_2}$ are the molar flow rate of species $\mathcal{A}$ in outlet 1 and outlet 2, respectively. For this geometry, the molar flow rate of species $\mathcal{A}$ from each inlet/outlet can be calculated as

$$F_{\mathcal{A},in_i/out_i} = \frac{1}{M_{\mathcal{A}}} \iint_{A} \rho w_{\mathcal{A}} \left(\vec{v} \cdot \vec{n}\right) \mathrm{d}A \tag{2.38}$$

where $w_{\mathcal{A}}$ is the mass fraction of the species secondary species $\mathcal{A}$ and $F_{\mathcal{A},in_i/out_i}$ takes a positive value when evaluated at the outlets and a negative value when evaluated at the inlets. Once calculated the flow rate of the secondary species $\mathcal{A}$, the convective mass transfer coefficient, $k_{m,uc}$, can be determined by knowing the area for mass transfer, A_{transf}, and the concentration difference from the walls to the bulk of the flow,

$$k_{\mathrm{m},uc} = \frac{A_{transf}\Delta c_{uc}}{\dot{N}_{\mathcal{A}}} \tag{2.39}$$

where Δc_{uc} is the is a characteristic concentration difference in the unit cell. Similarly to Equation (2.17), the logarithm mean concentration difference in the unit cell is given by

$$\Delta c_{uc} = \frac{c_{b,\,out} - c_{b,\,in}}{\ln\left[\left(c_{wall,\,in} - c_{b,\,in}\right)/\left(c_{wall,\,out} - c_{b,\,out}\right)\right]}. \tag{2.40}$$

The bulk concentration is the concentration average weighted by the mass flow rate of the fluid in the channel,

$$c_{\mathcal{A},b} = \frac{\iint_A \rho\left(\vec{v}\cdot\vec{n}\right)c_{\mathcal{A}}\,\mathrm{d}A}{\iint_A \rho\left(\vec{v}\cdot\vec{n}\right)\mathrm{d}A} \tag{2.41}$$

The computed values of convective mass transfer coefficient will be reported as unit cell Sherwood number, defined as

$$\mathrm{Sh}_{uc} = \frac{k_{\mathrm{m},uc}d_h}{\mathcal{D}_{\mathcal{A}}} \tag{2.42}$$

where $\mathcal{D}_{\mathcal{A}}$ is the molecular diffusivity of species $\mathcal{A}$ in the continuous phase.

2.2.3.2 Sherwood Number Comparison

By analogy with the heat transfer calculations, the Sherwood number can be estimated by choosing the appropriate analogous Nusselt number relationship for the given geometry and analogous boundary conditions, replacing the Nusselt number by the Sherwood number and the Prandtl number by the Schmidt number (Çengel, 2003).

For the case of the transport of a secondary species in a continuous phase with constant concentration of the secondary species on the wall, the Sherwood number, $\mathrm{Sh}_{\mathrm{PP}} = 2k_{m,\mathrm{PP}}\omega \big/ \mathcal{D}_{\mathcal{A}}$, as a function of the concentration entrance length for developing concentration boundary layers can be estimated as

$$\mathrm{Sh}_{\mathrm{PP}} = \frac{4}{3^{1/3}\Gamma\left(3/4\right)}\left(x^{*}_{\mathrm{PP}}\right)^{-1/3} \tag{2.43}$$

where x^{*}_{PP} is the dimensionless concentration entrance length for the flow between parallel plates and is defined as

$$x^{*}_{\mathrm{PP}} = \frac{1}{\mathrm{Re}_{\mathrm{PP}}\,\mathrm{Sc}}\frac{x_{\mathrm{PP}}}{2\omega}. \tag{2.44}$$

The Schmidt number, $\mathrm{Sc} = \mu / \rho\mathcal{D}_{\mathcal{A}}$, and the Reynolds number, $\mathrm{Re}_{\mathrm{PP}} = 2\omega\rho\overline{v} / \mu$, are evaluated for flow between parallel plates.

For the fully developed concentration boundary layer, the Sherwood number was found to be

$$\mathrm{Sh}_{\mathrm{PP}} = 7.54. \tag{2.45}$$

Between the two asymptotic regions, the Sherwood number curve as a function of dimensionless thermal entrance lengths can be well approximated by

$$\mathrm{Sh}_{\mathrm{PP}} = \left[\left(\frac{4}{3^{1/3}\Gamma\left(3/4\right)}\left(x^{*}_{PP}\right)^{-1/3}\right)^{n} + 7.54^{n}\right]^{1/n} \tag{2.46}$$

with $n = 8$ (see Figure 2.5).

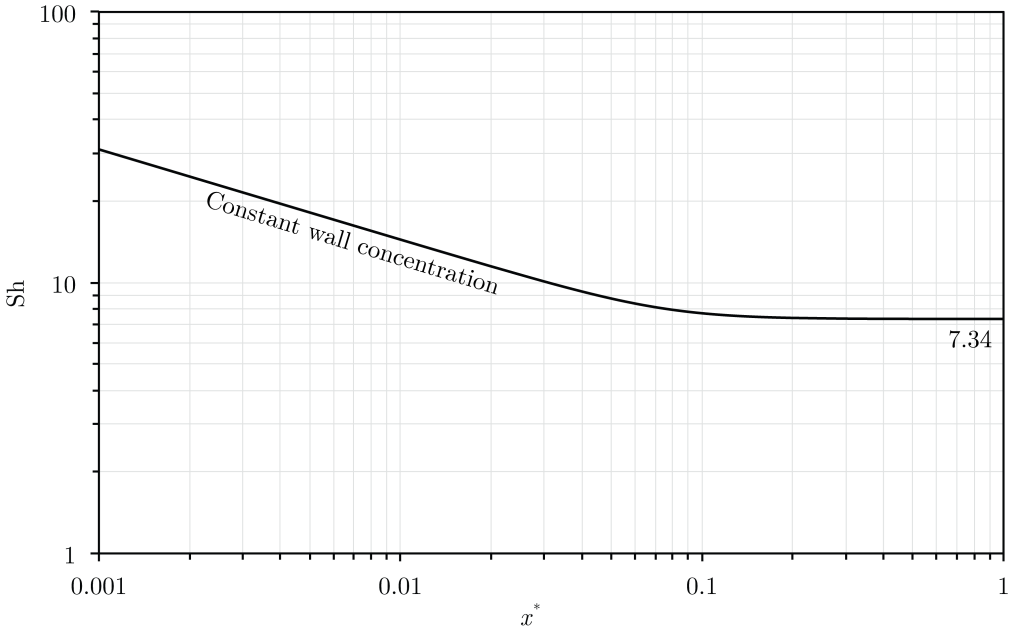


Figure 2.5. Sherwood number for fully developed laminar flow of Newtonian fluids in parallel plates.

2.3 Pressure Dynamic Experiments

2.3.1 Experimental Setup

The three different NETmix reactors designs described in Chapter 1 were used for the pressure drop experiments: the NETmix 3D, with spherical chambers and cylindrical channels and the Lab-scale NETmix 2D and the Multi-Inlet NETmix 2D, with cylindrical chambers and rectangular cross section area channels. The geometrical characteristics of the three reactors are summarized in Table 2.1.

Table 2.1. NETmix reactor prototypes geometrical characteristics.

Geometry	NETmix 3D	Lab-scale NETmix 2D	Multi-Inlet NETmix 2D
Number of rows, n_x	49	29	65
Number of columns, n_y	15	8	16
Chamber diameter, D (mm)	7	6.5	8.75
Channel diameter, d (mm)	1.5	1	1.5
Geometry depth, ω (mm)	—	3	5.9
Channel length, l (mm)	3	2	5.4
Total volume V (mL)	140	23	1500

Figure 2.6 shows a schematic drawing of the experimental set-ups used.

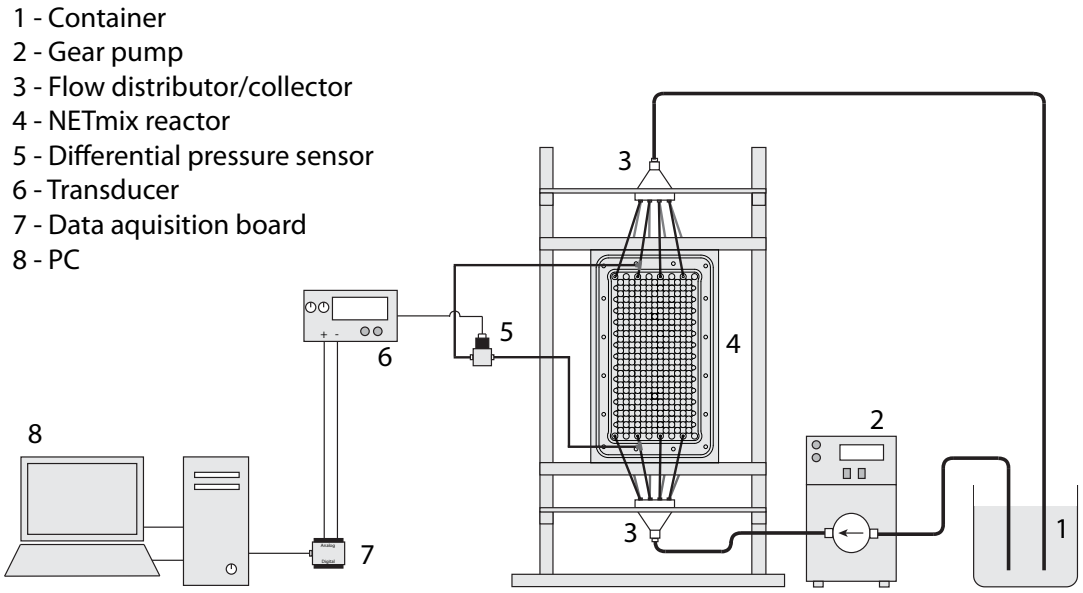


Figure 2.6. Experimental setup for pressure drop measurements.

All experimental setups are composed of the NETmix reactor itself, manufactured out of acrylic and/or stainless steal, the feeding and discharging reservoirs, a pumping system and tubing with all the necessary fittings and support structure. An ISMATEC gear pump was used to convey fluids, and the pump was calibrated to obtain the flowrate value from gear rotation speeds. A flow distributor, developed by Gomes (2011), was used to evenly distribute the fluid through the all NETmix reactor inlets. A similar distributor was used as a collector of all the outlet streams of the NETmix reactor.

2.3.2 Experimental Fluids

Water as well as aqueous solutions of glycerol with 10%, 20% and 60% in mass, were used in the measurements in order to vary the physical properties of the fluid. The density and viscosity of water and aqueous solution of glycerol are shown in Table 2.2. The experiments were all carried out at room temperature.

Table 2.2. Density and viscosity of water and aqueous solutions of glycerol.

% wt. glycerol	$\rho\left(\mathrm{kg/m^3}\right)$	$\mu\left(\mathrm{Pa\cdot s}\right)$
0	998	8.90×10^{-4}
10	1.02×10^{3}	1.19×10^{-3}
20	1.04×10^{3}	1.35×10^{-3}
60	1.15×10^{3}	9.30×10^{-3}

2.3.3 Data Acquisition

2.3.3.1 Pressure Drop

The pressure drop along the reactor was measured from the inlet to the outlet of each NETmix reactor with a Validyne DP 215 differential pressure sensor as shown in Figure 2.6. The pressure drop signal from the pressure sensor was converted to voltage data via a transducer and sent to the computer via a NIDAQ data acquisition board from National Instruments, and digitally processed with a LabView interface. A 10 Hz sampling rate was used for average pressure drop measurements. The pressure sensor was calibrated with a water column for each set of experiments so the voltage signal acquired from the transducer could be converted to differential pressure.

2.3.3.2 Pressure Difference

For measurements of frequency of the self-sustained flow oscillations in the chambers, the Lab-scale NETmix 2D front cover was drilled to measure the pressure difference between two outlet channels from the same unit cell as shown in Figure 2.7. The same differential pressure transducer was connected to the outlets to monitor the flow imbalances with time. The digital sampling rate of pressure difference for this study was $500\,\mathrm{Hz}$. The final dataset for each flow condition was processed using MATLAB interface, and Fast Fourier Transform was applied to determine the pressure difference power spectra. Acquisition time for each dataset was $100\,\mathrm{s}$ to ensure a resolution in the frequency of $0.01\,\mathrm{Hz}$.

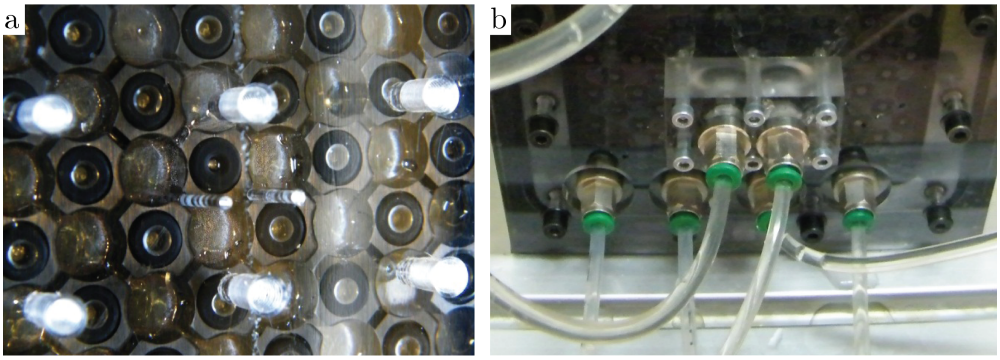


Figure 2.7. Flow oscillation measurements setup: (a) drilled channels, (b) system connected to the experimental setup.

2.3.4 Results

2.3.4.1 Pressure Drop Data

Pressure drop data was obtained for the three NETmix reactors, with three fluids with different viscosities, varying the Reynolds numbers in the range of 100 to 1400. The solid lines show the best fit obtained from the mechanistic model (Equation (2.1)). The best fit value of K, was obtained by the least squares method and the following K values were obtained: NETmix 3D, $K = 0.94$; Lab-scale NETmix 2D, $K = 1.2$; Multi-Inlet NETmix 2D, $K = 1.3$. The mechanistic model fitted quite well the experimental data with a maximum deviation of 15%, and with K values varying in a short range for all the 3 different NETmix designs.

Figure 2.8, Figure 2.9 and Figure 2.10 show the pressure drop obtained experimentally and model fitting for the three NETmix prototypes.

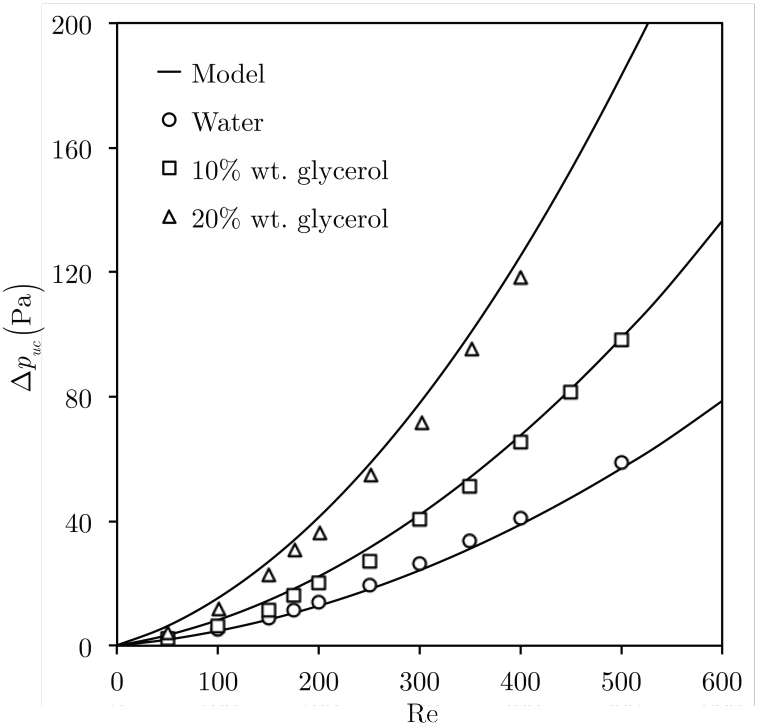


Figure 2.8. Pressure drop obtained experimentally and model fitting for NETmix 3D.

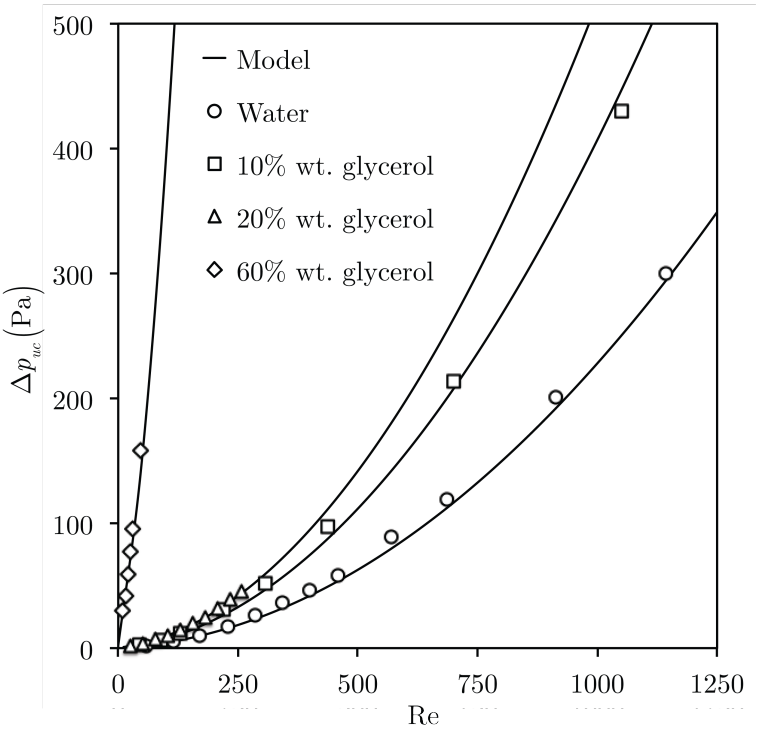


Figure 2.9. Pressure drop obtained experimentally and model fitting for Lab-scale NETmix 2D.

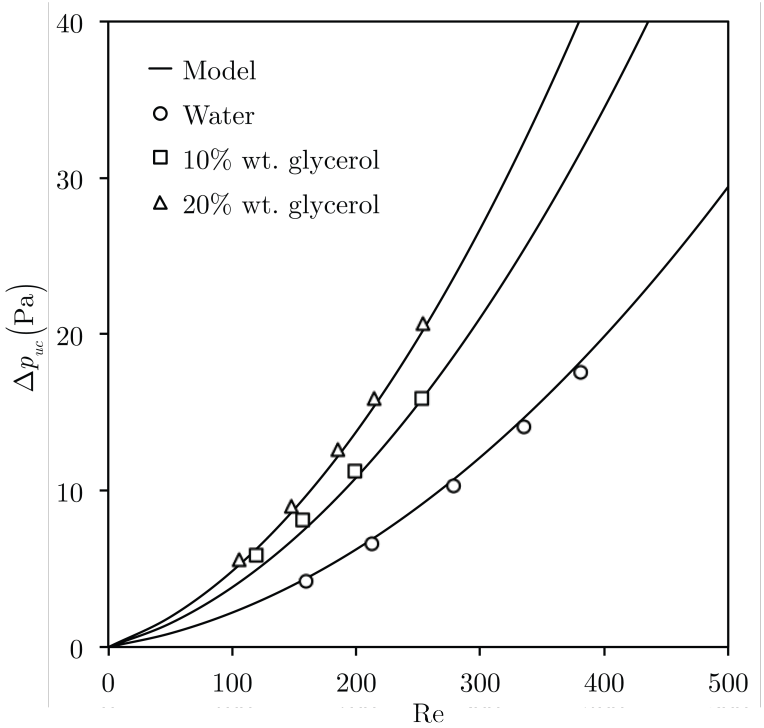


Figure 2.10. Pressure drop obtained experimentally and model fitting for Multi-Inlet NETmix 2D.

2.3.4.2 Flow Oscillation Frequency Data

For flow conditions above the critical Reynolds number, i.e. $\mathrm{Re} > 150$, the dynamics of the local flow oscillations within the unit cell were characterized by determining characteristic frequencies using power spectral analysis. The power spectral analysis was performed on the fluctuation of the pressure difference signal with time obtained with the pressure transducer for the Lab-scale NETmix 2D reactor. The signal was obtained from two measuring points at two outlets of a single chamber located in the middle region of the NETmix reactor. For each Reynolds number tested, a dominant peak indicating the natural frequency of oscillation inside the chambers was observed as exemplified in Figure 2.11.

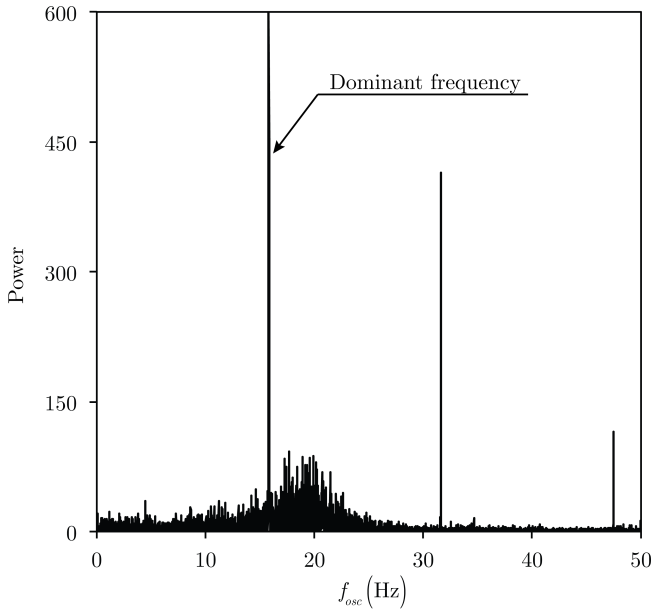


Figure 2.11. Power spectra for pressure difference signal for Re=400.

The frequency of the dominant oscillation, for the three different fluids and for flow rates above the critical Reynolds number, $\mathrm{Re} > 150$, was fitted to the proposed frequency model, Equation (2.10). Figure 2.12 shows quite good agreement between the measured and fitted oscillating frequencies with a maximum deviation of 10%. Smaller number of flow rate conditions for larger viscosities were used due to pump pressure limitations.

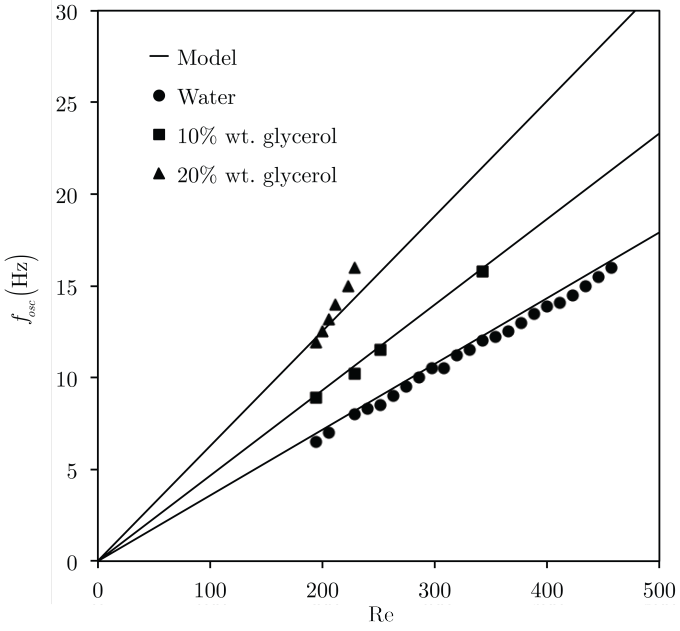


Figure 2.12. Frequency of oscillation in the Lab-scale NETmix 2D chambers as a function of the Reynolds number.

2.3.4.3 Benchmarking With Other Mixers

Power number results for the three NETmix reactors are shown in Figure 2.13. These results are compared with power number data of stirred tank mixers with different impeller designs obtained in the literature (Bates et al., 1963; Hemrajani and Tatterson, 2003). Results show that the power number for NETmix decreases with increasing Reynolds number, and for Reynolds numbers within the self-sustainable flow regime, the power number is significantly lower than the corresponding values for stirred tanks, and levels off at $\mathrm{Re} \approx 1000$.

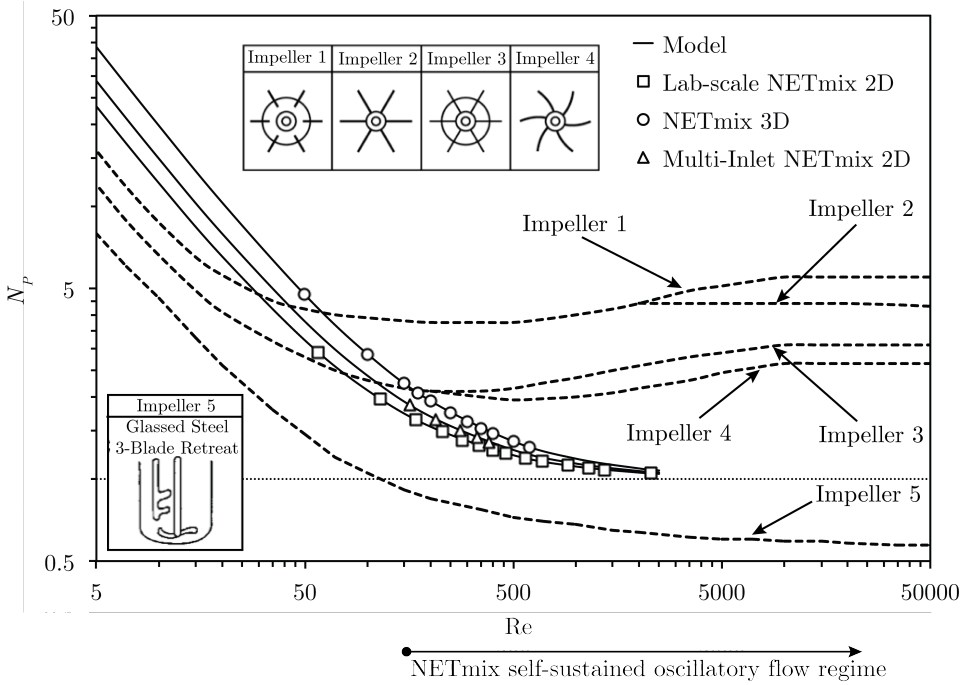


Figure 2.13. Power number plot for the three NETmix prototypes and for several stirred tanks with different impellers.

Figure 2.14 shows the Z factor values for the three NETmix reactors as a function of the Reynolds number. In this range of Reynolds numbers, all the NETmix reactors exhibit Z factor values one order of magnitude lower than the commercial static mixers data found in the literature (Thakur et al., 2003). Therefore, the NETmix reactors can be operated with much smaller pressure drops than other commercially available static mixers, and thus showing considerably higher energy efficiencies for mixing.

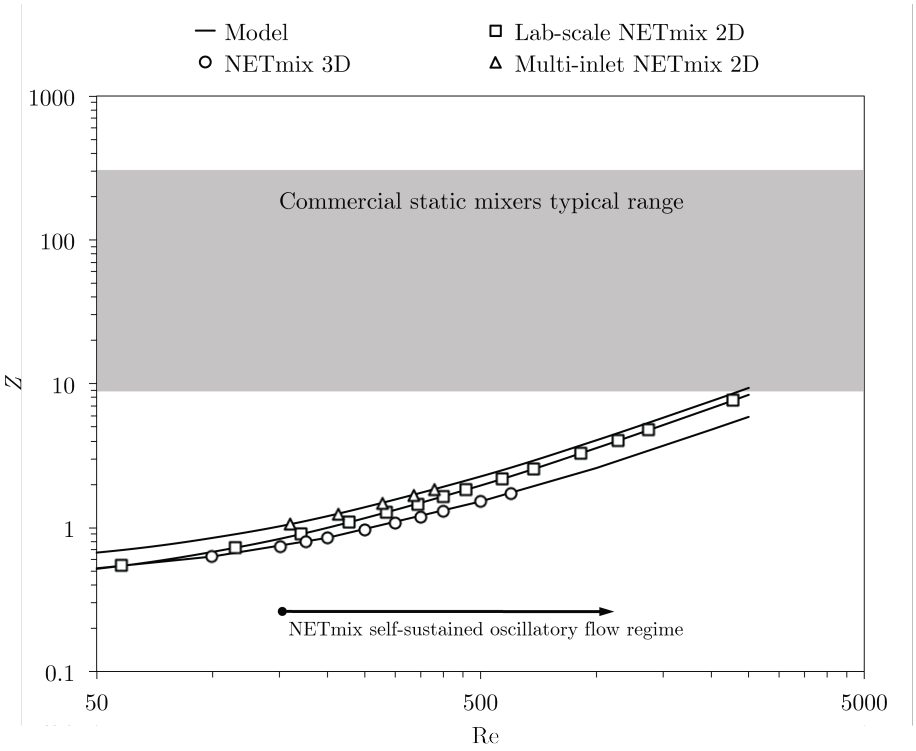


Figure 2.14. Z factor for the NETmix prototypes as a function of Reynolds number. The grey area corresponds to a typical range of Z factors for some commercial mixers (Thakur et al., 2003).

2.4 3D CFD Dynamic Simulations

In order to obtain a computational tool for prediction of accurate values of K and Z factors, for any particular geometry of the NETmix reactor, a simplified CFD simulation strategy has been developed and validated with existing experimental data, based on the concept of the *NETmix Unit Block* (NUB) model here introduced. The experimental visualization dynamic studies of Gomes (2011), and the consistent measurements of quasi-periodic pressure power spectra, shown in Section 2.3.4.2, suggested the application of dynamic periodic spatial boundary conditions in order to reduce the computational domain for CFD simulation of the whole NETmix reactor, reducing it to the dynamic simulation of a few mixing units cells, as it is explained next.

The NUB model was also used for the determination of the convective heat and mass transfer coefficients in the unit cells of the NETmix reactor. The results were compared with the results for flow between parallel plates.

2.4.1 NUB Physical Domain

Due to computer memory limitations, it is not feasible to simulate, with the necessary grid refinement, the whole NETmix flow domain. Since both the geometry and the expected flow pattern have a periodically repetitive nature, it is possible to simulate a larger system by modelling a small representative part of its flow domain, the NUB model, consisting on a representative section of the lab-scale NETmix 2D reactor comprised of 5 rows and 3 columns, see Figure 2.15, where the chambers of the first and third columns are half chambers.

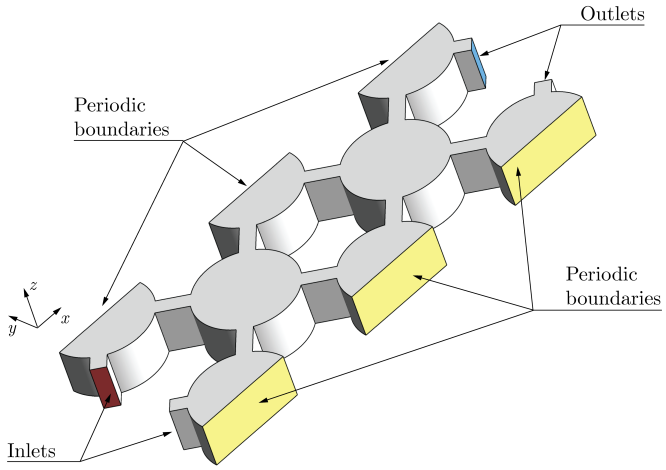


Figure 2.15. NUB showing the imposed boundary conditions.

A translational periodic boundary condition was applied to these cut surfaces, as can also be seen in Figure 2.15. The flow at a periodic boundary is treated as if the coupled periodic plane is a direct neighbour to the cells adjacent to the periodic boundary it is connected to. Thus, when calculating the flow through the periodic boundary adjacent to a fluid cell, the flow conditions at the fluid cell adjacent to the opposite periodic plane are used.

2.4.2 Governing Equations and Boundary Conditions

2.4.2.1 Hydrodynamic Simulations

The flow field simulation is achieved by numerical integration of the continuity and Navier-Stokes equations. For incompressible flow, the continuity equation (conservation of mass), assumes the form

$$\nabla \cdot \vec{v} = 0 \tag{2.47}$$

where $\vec{v}$ is the velocity field. The Navier-stokes equation describes the conservation of momentum as is expressed as

$$\rho\left(\frac{\partial \vec{v}}{\partial t} + \vec{v} \cdot \nabla \vec{v}\right) = -\nabla p + \mu \nabla^2 \vec{v} \tag{2.48}$$

where t is time.

At the chamber and channel walls a no-slip condition was assumed, $\vec{v} = 0$. A uniform velocity profile was applied to the network inlet channels and a constant and uniform pressure value was set at the network outlet channels, $p = p_0$.

To obtain an initial segregated flow condition for the transient simulations, steady-state simulations were performed beforehand, where shear-free walls were placed in the middle of the chambers to keep the flow segregated/symmetric, similarly to the strategy adopted by Gomes (2011). The shear-free condition at the middle plane of the chambers imposed by setting $v_y = 0$, $v_z = 0$ and $\frac{\partial v_x}{\partial y} = \frac{\partial v_z}{\partial y} = 0$.

The fluid used in the simulation was water with constant physical properties at room temperature, with a density of $\rho = 998\ \mathrm{kg/m^3}$ and a viscosity of $\mu = 8.9 \times 10^{-4}\ \mathrm{Pa \cdot s}$.

A dynamic tracer transport simulation with the NUB model was also used to inspect the dynamic behaviour of the flow inside the mixing chambers.

The conservation equation for the transport of a the tracer species $\mathcal{A}$ is given by

$$\frac{\partial c_{\mathcal{A}}}{\partial t} + \vec{v} \cdot \nabla c_{\mathcal{A}} = \mathcal{D}_{\mathcal{A}} \nabla^2 c_{\mathcal{A}} \tag{2.49}$$

where $c_{\mathcal{A}}$ is the concentration of the secondary species. A molecular diffusivity of $\mathcal{D}_{\mathcal{A}} = 10^{-9}\ \mathrm{m^2/s}$, characteristic of liquids, was used in the simulation. At one of the

inlets, a molar fraction of the tracer species $\mathcal{A}$ of $x_{\mathcal{A}} = 1$ was imposed while for the other inlet, a molar fraction of the tracer species $\mathcal{A}$ of $x_{\mathcal{A}} = 0$ was defined. The tracer species was defined with the same physical properties of water.

2.4.2.2 Heat Transfer Simulations

To describe the flow field and temperature distribution, the governing equations of continuity, momentum conservation and energy conservation are expressed as

$$\frac{\partial \rho}{\partial t} + \nabla \cdot \left(\rho \vec{v}\right) = 0\,, \tag{2.50}$$

$$\frac{\partial \left(\rho \vec{v}\right)}{\partial t} + \vec{v} \cdot \nabla \left(\rho \vec{v}\right) = -\nabla p + \nabla \cdot \left(\mu \nabla \vec{v}\right) \text{ and} \tag{2.51}$$

$$\frac{\partial \left(\rho c_P T\right)}{\partial t} + \nabla \cdot \left(\rho c_P \vec{v} T\right) = \nabla \cdot \left(\kappa \nabla T\right), \tag{2.52}$$

respectively.

The equations are to be solved for the following boundary conditions: no-slip condition was assumed in the walls of the domain, $\vec{v} = 0$; a uniform velocity profile was applied to the network inlet channels; and a constant and uniform pressure value was set at the network outlet channels, $p = p_0$.

Initial segregated flow conditions for the transient simulations was obtained from steady-state simulations, where shear-free walls were placed in the middle of the chambers to keep the flow separated. The shear-free condition at the middle of the chambers imposed by setting $v_y = 0$, $v_z = 0$ and $\frac{\partial v_x}{\partial y} = \frac{\partial v_z}{\partial y} = 0$.

A uniform temperature of $293\,\mathrm{K}$ was imposed at the network inlet channels. For the simulations with constant wall temperature, a constant temperature $T_{wall} = 373\,\mathrm{K}$ was imposed to the external walls of the geometry. For the simulations with constant

heat flux, a constant average heat flux was imposed to the external walls of the NETmix. For each simulation, the heat flux value was chosen for a maximum increase of $60\,\mathrm{K}$ from the inlet to the outlet of the domain and is given by a function of the flow rate in the channels and was estimated by

$$\dot{q}_{wall} \approx \frac{2\rho q_{channel} c_P \left(T_{out} - T_{in}\right)}{A_{transf}}. \tag{2.53}$$

The physical properties of the working fluid were fitted to polynomial expressions from published data (Lide, 2004) for a range of temperatures from $273\,\mathrm{K}$ to $373\,\mathrm{K}$ and are listed next:

- Density:

$$\rho\left(\mathrm{kg/m^3}\right) = -250 + 11.5T - 3.45\times10^{-2}T^2 + 3.28\times10^{-5}T^3; \tag{2.54}$$

- Viscosity:

$$\begin{aligned}\mu\left(\mathrm{Pa\cdot s}\right) = 1.57\times10^{-1} - 1.65\times10^{-3}T + 6.60\times10^{-6}T^2 - \\ -1.18\times10^{-8}T^3 + 7.95\times10^{-12}T^4;\end{aligned} \tag{2.55}$$

- Specific heat capacity:

$$\begin{aligned}c_P\left(\mathrm{J/kg\ K}\right) = 1.53\times10^{4} - 116\,T + 4.51\times10^{-1}T^2 - \\ -7.84\times10^{-4}T^3 + 5.20\times10^{-7}T^4;\end{aligned} \tag{2.56}$$

- Thermal conductivity:

$$\kappa\left(\mathrm{W/m\ K}\right) = -4.32\times10^{-1} + 5.73\times10^{-3}T - 8.08\times10^{-6}T^2 - 1.86\times10^{-9}T^3. \tag{2.57}$$

If, in the course of a simulation, the temperature assumes local above $373\,\mathrm{K}$, the physical properties were assumed to take a constant value equal to the value calculated for $373\,\mathrm{K}$.

2.4.2.3 Mass Transfer Simulations

The isothermal flow of an incompressible fluid inside the Unit Block geometrical domain was simulated by solving the Navier-Stokes equations:

$$\nabla \cdot \vec{v} = 0 \tag{2.58}$$

for mass conservation and

$$\rho\left(\frac{\partial \vec{v}}{\partial t} + \vec{v} \cdot \nabla \vec{v}\right) = -\nabla p + \mu \nabla^2 \vec{v} \tag{2.59}$$

for momentum conservation. The conservation equation for the transport of a secondary species $\mathcal{A}$ is given by

$$\frac{\partial c_{\mathcal{A}}}{\partial t} + \vec{v} \cdot \nabla c_{\mathcal{A}} = \mathcal{D}_{\mathcal{A}} \nabla^2 c_{\mathcal{A}} \tag{2.60}$$

where $c_{\mathcal{A}}$ is the concentration of the secondary species.

The following boundary conditions were used: No-slip condition was assumed in the walls, $\vec{v} = 0$. A uniform velocity profile was applied to the network inlet channels and a constant and uniform pressure value was set at the network outlet channels, $p = p_0$. Steady-state simulations were performed to obtain an initial segregated flow condition for the transient simulations. A shear-free walls were placed in the middle of the chambers to keep the flow separated and was imposed by setting $v_y = 0$, $v_z = 0$ and $\frac{\partial v_x}{\partial y} = \frac{\partial v_z}{\partial y} = 0$.

The working fluids used in the simulation were water and a tracer fluid, both with equal constant physical properties at room temperature, with a density of $\rho = 998\ \mathrm{kg/m^3}$ and a viscosity of $\mu = 8.9 \times 10^{-4}\ \mathrm{Pa \cdot s}$. A molecular diffusivity of $\mathcal{D}_{\mathcal{A}} = 10^{-9}\ \mathrm{m^2/s}$, characteristic of liquids, was used in the simulation.

A molar fraction of the tracer species $\mathcal{A}$ of $x_{\mathcal{A}} = 0$ was imposed to the inlet of the network. A constant molar fraction $x_{\mathcal{A}} = 1$ was imposed to the external walls of the NUB.

2.4.3 Domain Discretization

The geometrical domain and simulation grid were generated with the software packages *DesignModeler* and *Meshing* included in Ansys® 13 suit.

2.4.3.1 Hydrodynamic Simulations

Grid refinement tests were performed to the model by evaluating the pressure drop and average velocity value for different grid refinements and three different Reynolds numbers in the channels of 50, 100 and 150. A simulation domain with uniform hexahedral finite volumes with maximum edge length of $\Delta x = 0.0625\,\text{mm}$ was observed to be sufficiently refined, since the pressure drop measured along the model did not vary more than 1% with a further increase on the number of finite elements. The number of elements in the z direction of the geometry was reduced to half by doubling their size without significant changes on the accuracy of the solution, thus reducing to half the number of elements and a computational grid with approximately 1.3 million elements was used.

2.4.3.2 Heat Transfer Simulations

For the heat transfer simulations, the grid refinement used for the pressure drop simulations was not sufficient to accurately simulate the temperature distribution inside the NUB domain. The heat flow rate and average temperature measured along the model were measured for different grid refinements and three different Reynolds numbers in the channels of 50, 100 and 150. A simulation domain with uniform hexahedral finite volumes with maximum edge length of $\Delta x = 0.05\,\text{mm}$ was necessary so that the heat flow rate and average temperature measured along the model did not vary more than 1% with the further increase on the number of finite elements. In order to reduce the total amount of elements, the number of elements in

the z direction was reduced to half. The computational mesh was more refined next to the walls. A proportional size growth was applied and the first element next to the walls had the dimension of 0.05 mm growing to 0.1 mm in the centre position of the geometry. A computational grid with approximately 2.5 million elements was used.

2.4.3.3 Mass Transfer Simulations

For the tracer species mass transfer simulations, the grid refinement of $\Delta x = 0.05$ mm was not sufficient to accurately simulate the transport of the secondary species inside the NUB domain. The mass flow rate measured along the model was measured for different grid refinements and three different Reynolds numbers in the channels of 50, 100 and 150.

For simulations of flows with high Schmidt numbers (convection dominant) the numerical diffusion may not be negligible and the system appears to have a higher diffusivity than the true medium. Numerical diffusion occurs due to the insufficient spatial discretization of the convective term in the Navier-Stokes equations (Patankar, 1980) and is magnified for multidimensional problems (Ferziger and Perić, 2002).

The effect of numerical diffusivity becomes higher with the increase of the Reynolds number. Figure 2.16 shows the maximum deviation of mass flow rate of tracer species $\mathcal{A}$ with the increase on the Reynolds number for a total number of finite elements of 5.2 million ($\Delta x = 0.05$ mm). The dashed curve is an extrapolation of the obtained results.

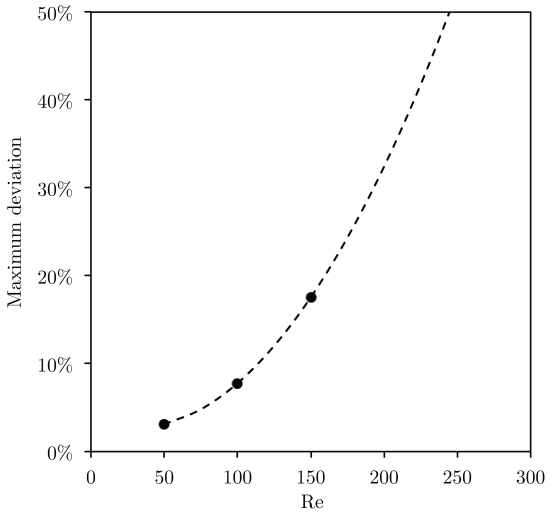


Figure 2.16. Tracer species molar flow rate deviation as a function of Reynolds number.

The accuracy of the solution can be increased by further refinement of the computational grid (Ferziger and Perić, 2002; Patankar, 1980). The main drawback is the rapid increase of the total number of elements for three-dimensional grids. Figure 2.17 shows the increase of the number of elements with the edge length of the finite volume elements. Due to computer memory limitations, a higher refinement is not feasible to simulate.

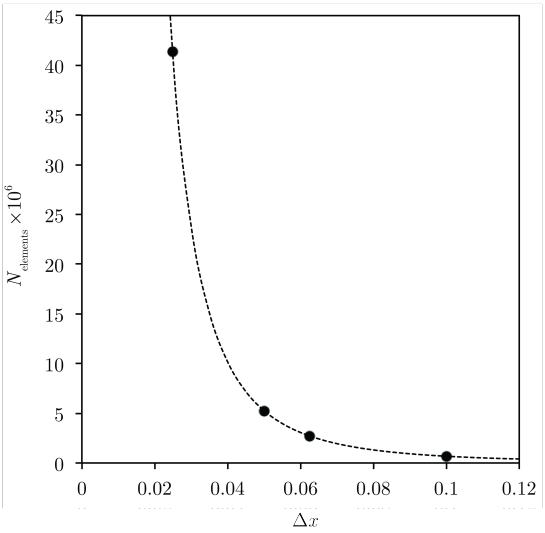


Figure 2.17. Number of elements as a function of the edge length.

To overcome this numerical diffusion problem, studies of mass transfer in the NETmix reactor were performed by increasing the molecular diffusivity. For working fluids with physical properties similar to water, the thermal diffusivity, $\alpha = \kappa / \rho c_P$,

is of the order of $\alpha \sim 10^{-7}$ while the molecular diffusivity of the tracer species is of the order of $\mathcal{D}_{\mathcal{A}} \sim 10^{-9}$.

2.4.4 Numerical Solution at Steady State

The flow equations solutions were obtained using an Intel® Xeon® 3GHz 8-core machine running the finite-volume commercial CFD software ANSYS Fluent™ 13.0. The initial segregated flow condition for the transient simulations was obtained from steady-state simulations where non-frictional walls were placed in the middle of the chambers to keep the flow separated. The SIMPLEC scheme was used for the pressure-velocity coupling and the Standard and Third-Order MUSCL schemes were used for pressure and momentum discretization, respectively. For simulations with heat transfer, Third-Order MUSCL scheme was used for the discretization of the convective term of the energy conservation equation. For simulations with mass transfer, Third-Order MUSCL scheme was used for the discretization of the convective term of the conservation equation for the transport of a secondary species. Higher order numerical methods were used for the discretization of the convective terms because they tend to have less numerical diffusion than low order methods (Ferziger and Perić, 2002; Patankar, 1980). Simulations were considered to have converged when a stable and constant value of the normalized residues of the governing equations was reached. In all simulations, these values were lower than 10^{-6}.

2.4.5 Numerical Solution at Transient State

For the transient simulations, a second order explicit scheme was used for time discretization. For each time step, the solution was considered to have converged when a normalized value of 10^{-4} for the residues of all variables was reached. The time step size for the transient simulations, Δt, was defined as

$$\Delta t = \frac{\Delta x}{v_{max,\,channel}} \tag{2.61}$$

where Δx is the minimum dimension of a fluid element in the channel, where the highest velocities occur, and $v_{max,\,channel} = 3/2\,\overline{v}_{chamber}$. All simulations were performed for a total flow time of $15\tau_{uc}$.

2.4.6 Results

2.4.6.1 Hydrodynamic Simulations

The pressure drop in the unit cell was estimated from CFD simulations. For transient simulations, the pressure drop was estimated as the average pressure drop along time. The CFD simulation results were compared to the experimental pressure drop data, and to the model fitting, for the Lab-scale NETmix 2D prototype, as shown in Figure 2.18.

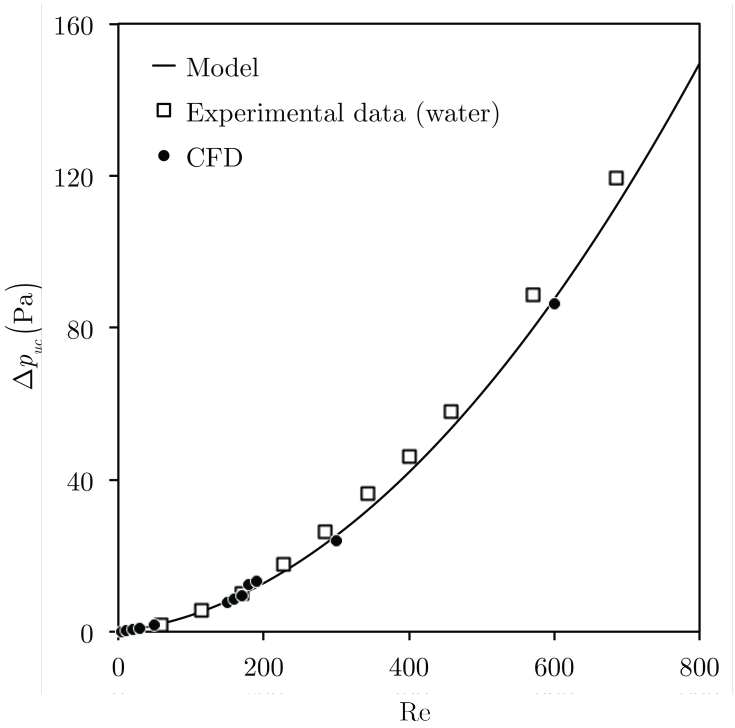


Figure 2.18. Pressure drop as a function of the Reynolds number obtained experimentally and from CFD simulations, for the Lab-scale NETmix 2D.

The experimental data and the CFD results are in good agreement within a maximum deviation of 15%.

The dynamic behaviour of the flow inside the mixing chambers can also be well described by calculating the pressure difference along the time between two outlets of

the same chamber. The frequency of oscillation of the flow obtained from CFD simulation for $\mathrm{Re} = 300$ is $f_{osc} = 11.8\,\mathrm{Hz}$ within a 10% deviation from the model value, $f_{osc} = 10.7\,\mathrm{Hz}$. It is thus expected that CFD simulations can be used to evaluate the pressure drop and dynamics throughout the NETmix reactor, and in this way overcome the need of experimental data each time a new configuration is designed.

2.4.6.2 Dynamic Tracer Transport

The dynamic tracer transport simulation with the NUB model can also be used to inspect the dynamic behaviour of the flow inside the mixing chambers. At one of the inlets, tracer with the same physical properties of water was injected. The simulation was performed for $\mathrm{Re} = 300$. Figure 2.19 shows the contours of tracer fraction at the middle plane of the domain for eight different instants after injection $(0 \le t/\tau_{ub} \le 1.5)$, with τ_{ub} being the unit block passage time, where it can be observed the dynamics of mixing along the unit block, with almost total mixing of the initially segregated two feed currents, only after just two mixing unit cells, as reported by Laranjeira (2005) and Gomes (2011), and also observed in the present work.

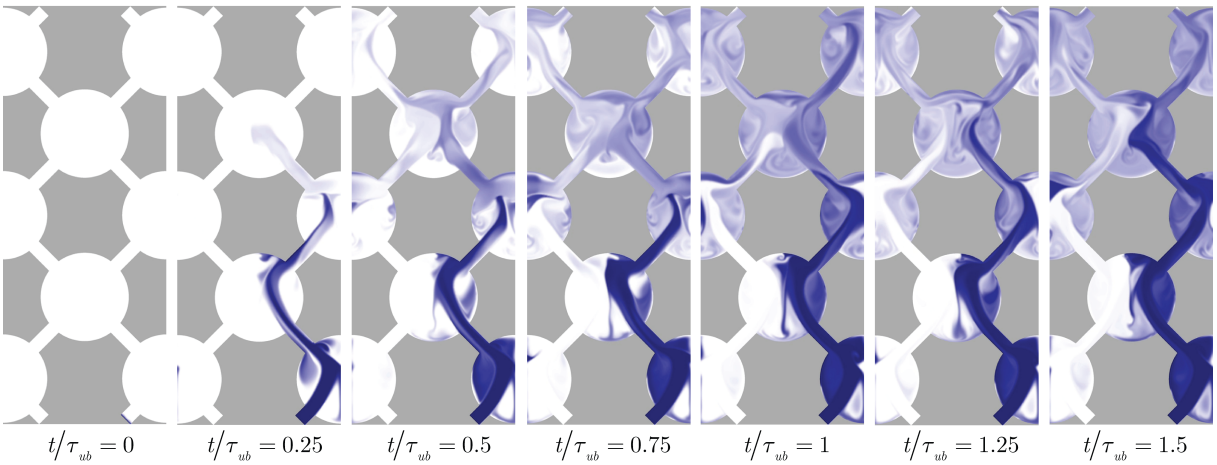


Figure 2.19. Tracer fraction for Re=300 at different moments after injection at the middle plane of the geometry.

The flow oscillations inside the mixing cells, are shown on Figure 2.20 for 5 instants in a full period of oscillation of the unit cell $(8.25 \le t/\tau_{uc} \le 9.25)$, where it can be

observed that each inlet stream produces into the opposite outlet stream during 50% of the unit cell period, or characteristic cell mixing time, corresponding to a dilution of each inlet current by a factor of two on the outlet streams.

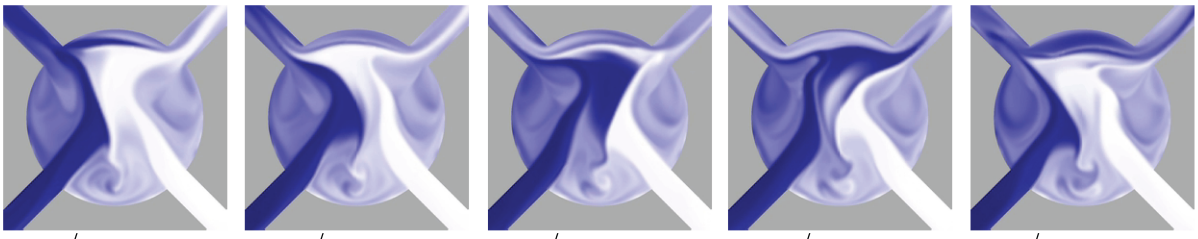


Figure 2.20. Tracer fractions for Re=300 at different moments after injection at the middle plane of the geometry.

This is repeated on every mixing cell, and promoting in this way a very rapid dilution of each inlet current of the NETmix reactor, that evolves in a geometric fashion as 2^{n_x}, along n_x rows of the reactor in the main flow direction.

2.4.6.3 Heat Transfer Simulations

The average unit cell Nusselt number was estimated from CFD simulations. Heat is transferred across the solid-fluid interface of the external heated walls of the NUB domain, thus heating the working fluid flowing along the geometry. Two different sets of simulations were performed, one with constant wall temperature and another one with constant wall heat flux.

The average unit cell Nusselt number was estimated for the unit cell in the fourth row of the NUB model from the CFD simulation results for different flow conditions and compared with the analytical solution for the flow between parallel plates.

Figure 2.21 shows the Nusselt number for different dimensionless thermal entrance lengths, for the simulation with constant wall temperature. With increasing flow rate, and consequently increase of Reynolds number in the channels, the dimensionless thermal entrance length value decreases for the same position in the NETmix reactor. Simulations were performed for Reynolds numbers from 5 to 600 at the NUB inlet.

Interestingly, with the increasing Reynolds number in the channels, the Nusselt number values start to deviate from the expected value for the Nusselt number for the flow between parallel plates, tending to a considerably higher asymptotic value.

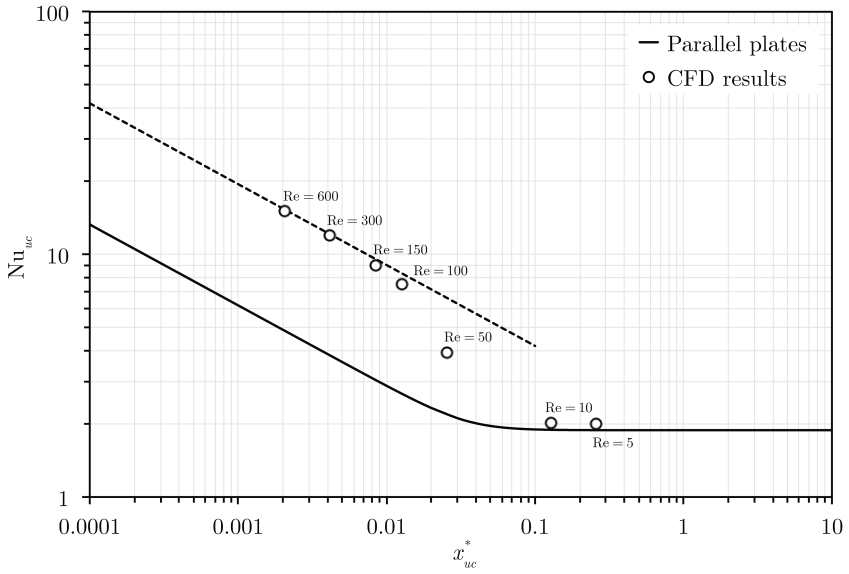


Figure 2.21. Nusselt number results as a function of the thermal entrance length for the wall constant temperature simulation.

With the increase of Reynolds number, the characteristic of the flow changes inside the unit cells. Above the critical Reynolds number, flow oscillations start to occur inside the chambers, leading to a more uniform temperature distribution. This can be seen in Figure 2.22 that shows the temperature contour maps at the middle plane of the NUB geometry for $\mathrm{Re} = 100$, where no oscillations occur, and for $\mathrm{Re} = 300$, above the critical Reynolds number, where the flow inside the mixing chambers evolved to a self-sustained oscillatory laminar flow regime inducing strong local laminar mixing.

Permanent hot spots are observed when no local laminar mixing occurs in the mixing chamber. Although the presence of hot spots is also observed for $\mathrm{Re} = 300$, the hot-spots position is renewed along time by the local hydrodynamic instabilities induced by the immerging jets interactions at the chambers and promoting the reduction of the thermal boundary layers due to fluid motion perpendicular to the flow direction.

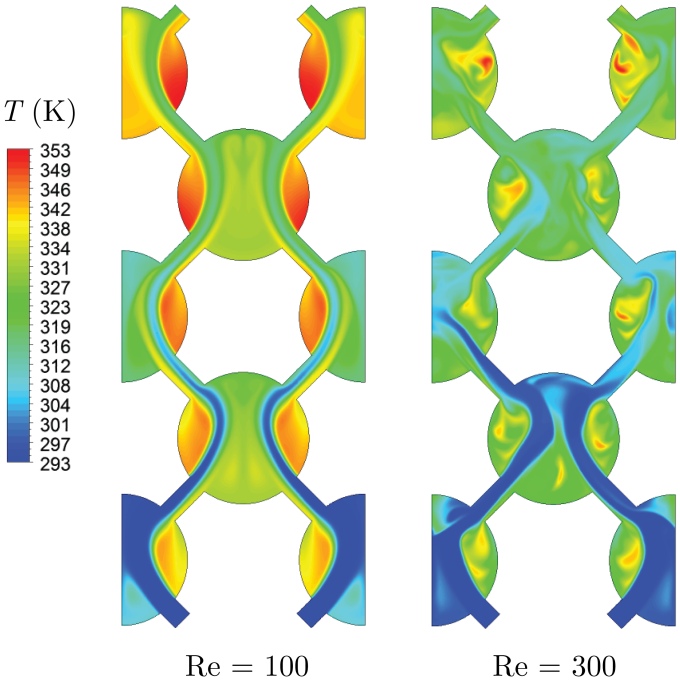


Figure 2.22. Temperature contour maps at the middle plane of the domain for Re=100 and Re=350 for constant wall temperature simulations.

The same behaviour is observed for the simulations with constant heat flux on the external walls of the unit cell as shown in Figure 2.23. Simulations were performed for Reynolds numbers from 10 to 600 at the inlet of the NUB.

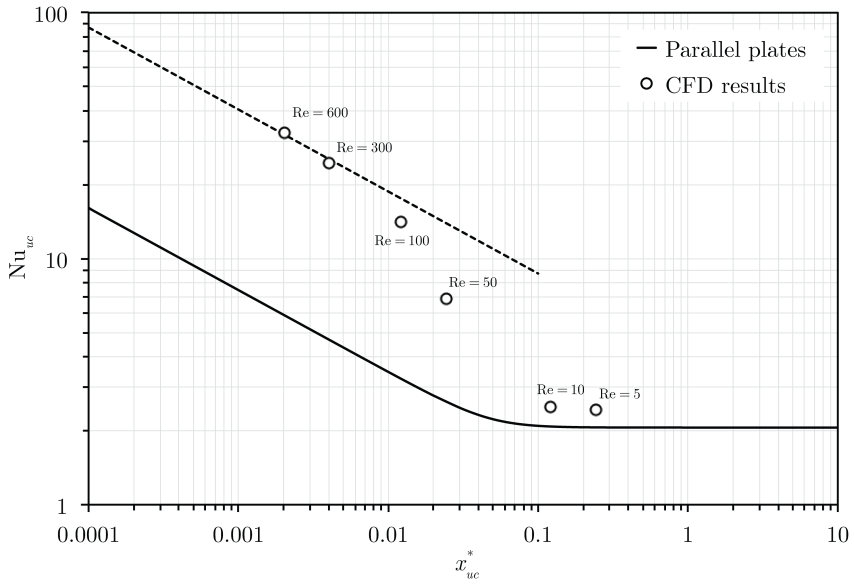


Figure 2.23. Nusselt number results as a function of the thermal entrance length for the wall constant temperature simulation.

Figure 2.24 shows the temperature contour maps at the middle plane of the domain for $\mathrm{Re} = 100$ and $\mathrm{Re} = 300$ for constant wall heat flux simulations. Similarly to the

results obtained for the constant wall temperature simulations, the hot spot position is renewed along time by the local hydrodynamic instabilities.

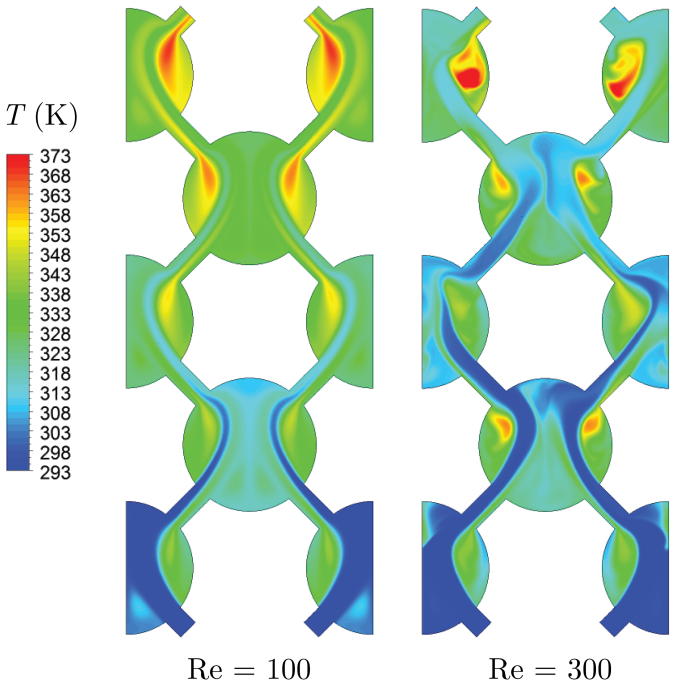


Figure 2.24. Temperature contour maps at the middle plane of the domain for Re=100 and Re=300 for constant wall heat flux simulations.

Although the increase of the average Nusselt number in the unit cell with the increase of Reynolds number, the asymptotic result of Nusselt number for thermally fully developed flows remains the same as the expected value for the flow between parallel plates, even for higher Reynolds numbers. To observe that, a simulation was performed with a conceptual fluid with constant physical properties, with a density of $\rho = 1000\ \mathrm{kg/m^3}$, a viscosity of $\mu = 10^{-3}\ \mathrm{Pa \cdot s}$, a heat capacity of $c_P = 10\ \mathrm{J/kg\ K}$ and a thermal conductivity of $\kappa = 1\ \mathrm{W/m\ K}$. The simulation was run for $\mathrm{Re} = 300$ and $x^*_{uc} = 2.6$ and a value of $\mathrm{Nu}_{uc} = 2.4$ is obtained, similar to the asymptotic value of $\mathrm{Nu}_{\mathrm{PP}} = 2.1$ for the flow between parallel plates.

Furthermore, to verify that the increase of Nusselt number is due to the change of the characteristics of the flow by the increase of Reynolds number, a simulation was performed with constant physical properties and a fixed low $\mathrm{Re} = 10$.

The heat capacity and the heat flux on the walls were set accordingly to the dimensionless thermal entrance length as shown in Table 2.3.

Table 2.3. Thermal conductivity and heat flux for different thermal entrance lengths.

x^*_{uc}	$c_P\left(\mathrm{J/kg\ K}\right)$	$\dot{q}_{wall}\left(\mathrm{kW/m^2}\right)$
0.001	7.01×10^5	4×10^3
0.01	7.01×10^4	400
0.1	7.01×10^3	40
1	701	4
10	70.1	0.4

A density of $\rho = 1000\ \mathrm{kg/m^3}$, a viscosity of $\mu = 10^{-3}\ \mathrm{Pa\cdot s}$ and a thermal conductivity of $\kappa = 1\ \mathrm{W/m\ K}$ were used in the simulation.

Figure 2.26 shows that, if $\mathrm{Re} = 10$, for different simulated dimensionless thermal entrance lengths the Nusselt values agrees with the Nusselt value for flow between parallel plates.

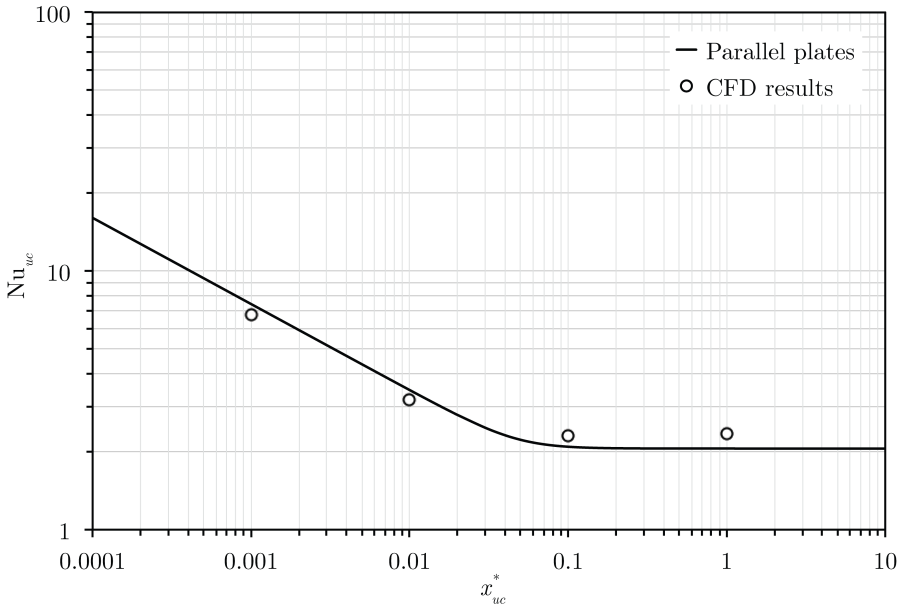


Figure 2.25. Nusselt number results as a function of the thermal entrance length for the wall constant heat flux simulation for Re=10.

Increasing the Reynolds number in the channels shifts the asymptotical value for the thermally developing flow region but the Nusselt number asymptotically tends to the Nusselt number value estimated for the flow between parallel plates. For the thermally developing flow region, the ratio between the Nusselt number in the unit

cell and the expected value for the flow between parallel plates were fitted to an expression that is dependent on the Reynolds number,

$$r\left(\mathrm{Re}\right)=\frac{\mathrm{Nu}_{uc}}{\mathrm{Nu}_{\mathrm{PP}}}=r_{\max}-\left(r_{\max}-r_{\min}\right)\exp\left(\frac{-\mathrm{Re}}{\beta}\right) \tag{2.62}$$

where $r_{\max}$, $r_{\min}$ and β are the fitting parameters.

Figure 2.26 shows the ratio between the asymptotic values for thermally developing flows of Nusselt number in the unit cell and Nusselt number for parallel plates with constant wall temperature. The best fit values of the three fitting parameters were obtained by the least squares method: $r_{\max}=3.17$, $r_{\min}=0.650$ and $\beta=85.7$. The correlation can fit the CFD simulation values with a maximum deviation of 15%. It can be seen that the Nusselt number ratio tends to a fixed value for $\mathrm{Re}>400$ and a maximum convective heat transfer coefficient is achieved when the flow inside the mixing chambers evolves to a self-sustained oscillatory laminar flow regime.

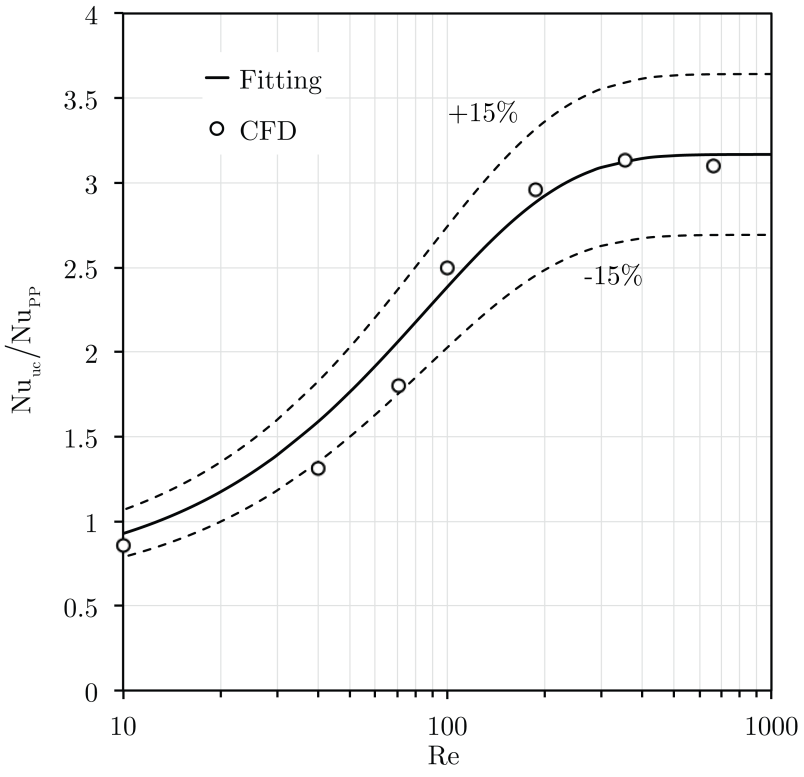


Figure 2.26. Ratio between the asymptotic values for thermally developing flows of unit cell Nusselt number and Nusselt number for parallel plates with constant wall temperature.

Figure 2.27 shows the ratio between the asymptotic values for thermally developing flows of the unit cell Nusselt number and the Nusselt number for parallel plates with constant wall heat flux. The best fit values for the fitting parameters obtained by the least squares method were: $r_{max} = 5.51$, $r_{min} = 0.686$ and $\beta = 127$. The obtained simulation values can also be well predicted with a maximum deviation of 15%. For this case, the Nusselt number ratio tends to a constant value for $\mathrm{Re} > 600$.

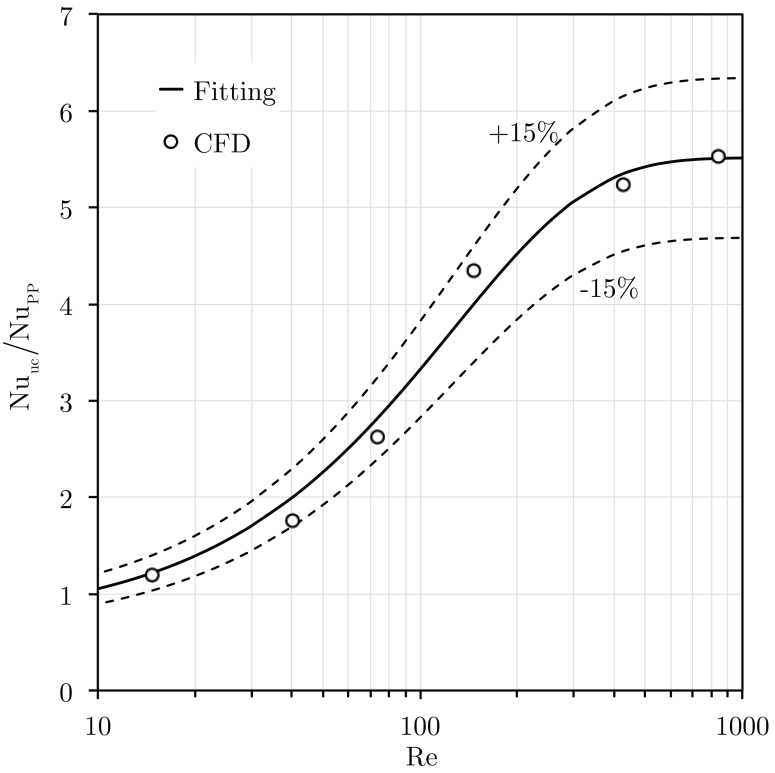


Figure 2.27. Ratio between the asymptotic values for thermally developing flows of the unit cell Nusselt number and Nusselt number for parallel plates with constant wall heat flux.

From the fitting to Equation (2.62) obtained for both cases with constant wall temperature and constant wall heat flux, it is possible to determine the expressions for the asymptotic results for thermally developing flows and fully thermally developed flows.

For constant wall temperature, the unit cell Nusselt number is given by

$$\mathrm{Nu}_{uc} = \begin{cases} \left[1.95 - 1.55\exp\left(\dfrac{-\mathrm{Re}}{85.7}\right)\right]\left(\dfrac{d_h}{2\omega}\right)^{2/3}\left(x^*_{uc}\right)^{-1/3} \;\; ; \;\; x^*_{uc} << 1 \\ 7.34\,\dfrac{d_h}{2\omega} \;\; ; \;\; x^*_{uc} >> 1 \end{cases} \tag{2.63}$$

and for constant heat flux is given by

$$\mathrm{Nu}_{uc} = \begin{cases} \left[4.11 - 3.60\exp\left(\dfrac{-\mathrm{Re}}{127}\right)\right]\left(\dfrac{d_h}{2\omega}\right)^{2/3}\left(x^*_{uc}\right)^{-1/3} \;\; ; \;\; x^*_{uc} << 1 \\ 8.24\,\dfrac{d_h}{2\omega} \;\; ; \;\; x^*_{uc} >> 1 \end{cases} \tag{2.64}$$

The correlations of Equations (2.63) and (2.64) were tested for flow at $\mathrm{Re} = 100$ for different thermal entrance lengths. Different thermal entrance lengths for a constant Reynolds number value were achieved by changing the physical properties of a conceptual fluid with constant density of $\rho = 1000\ \mathrm{kg/m^3}$, viscosity of $\mu = 10^{-3}\ \mathrm{Pa \cdot s}$, heat capacity of $c_P = 4200\ \mathrm{J/kg\ K}$ and variable thermal conductivities as shown in Table 2.4.

Table 2.4. Thermal conductivity for different thermal entrance lengths.

x^*_{uc}	$\kappa\left(\mathrm{W/m\ K}\right)$
0.001	0.06
0.005	0.30
0.01	0.60
0.02	1.2

Figure 2.28 shows the unit cell Nusselt number as a function of the thermal entrance length for the wall constant temperature simulation for $\mathrm{Re} = 100$. It can be seen that the simulation points are well predicted by Equation (2.63).

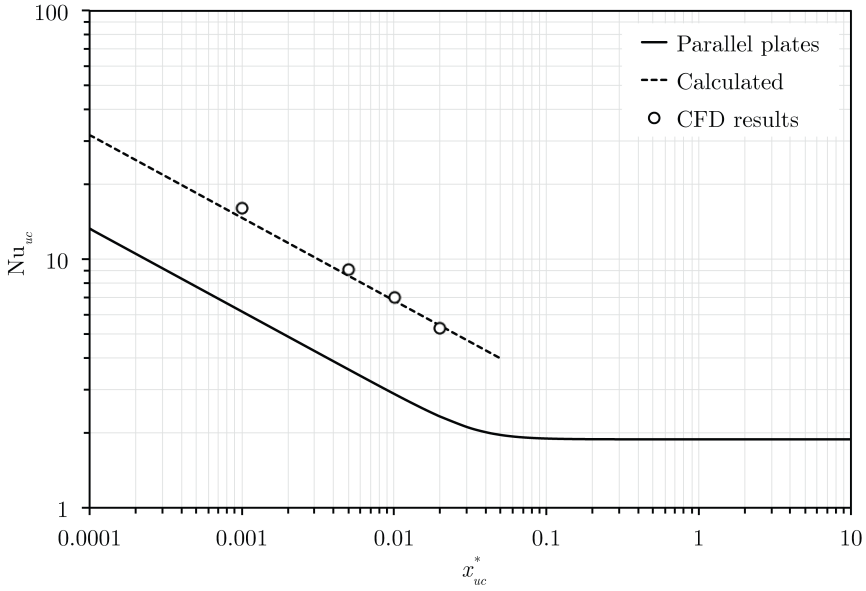


Figure 2.28. Nusselt number as a function of the thermal entrance length for the wall constant temperature simulation for Re=100.

Figure 2.29 shows the unit cell Nusselt number as a function of the thermal entrance length for the constant wall heat flux simulation for $\mathrm{Re} = 100$. It can be also seen that the simulation points are well predicted by Equation (2.64).

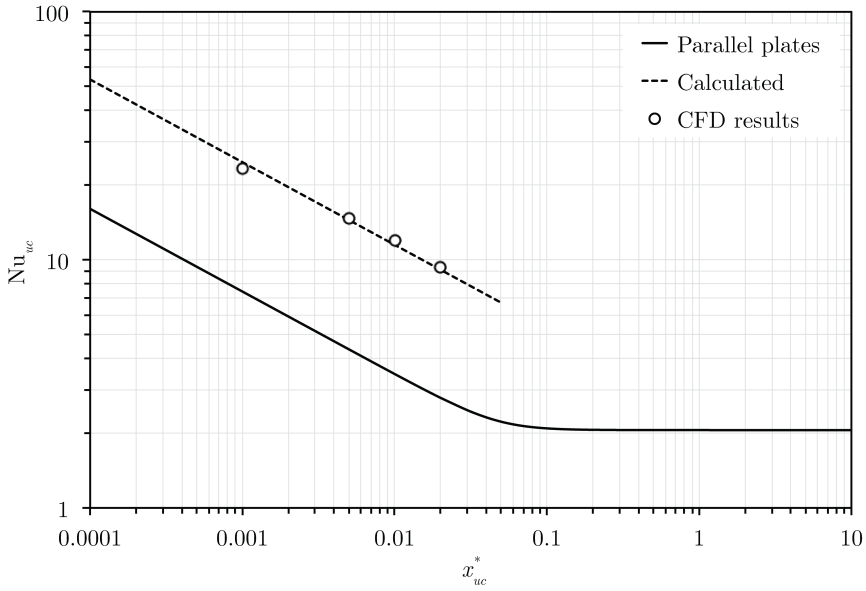


Figure 2.29. Nusselt number as a function of the thermal entrance length for the constant wall heat flux simulation for Re=100.

Although the heat transfer coefficient can increase up to 5.5 times the heat transfer coefficient for parallel plates, it is necessary to take into account the reduction of available area for heat transfer by using the NETmix reactor instead of parallel

plates. Figure 2.30 shows the corresponding area for heat transfer in the NETmix reactor against the correspondent area for the flow between parallel plates.

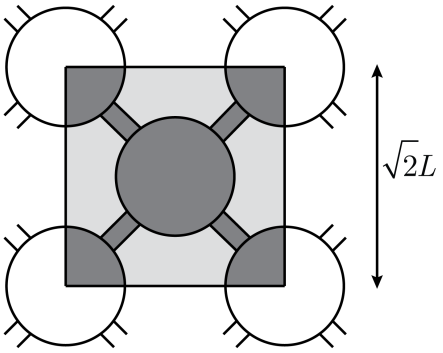


Figure 2.30. Area for heat transfer.

The reduction of available area for heat transfer is given by

$$\frac{A_{external}}{A_{PP}} \approx \frac{\pi D^2 + 8dl}{4L^2} \tag{2.65}$$

and for this particular geometry, $A_{external} = 0.52 A_{PP}$.

For the same temperature gradient in a unit cell and an equivalent portion of parallel plates, the effective increase of heat flow rate transferred is given by,

$$\frac{\dot{Q}_{uc}}{\dot{Q}_{PP}} = \frac{A_{external}}{A_{PP}} \frac{h_{uc}}{h_{PP}} = 0.52 \frac{h_{uc}}{h_{PP}} \tag{2.66}$$

For constant wall temperature $\dot{Q}_{uc}$ is 1.7 times higher than $\dot{Q}_{PP}$ and 2.9 times higher for constant wall heat flux. It can be concluded that the increase of the convective heat transfer coefficient is higher than the required value to compensate the reduction of the area.

Nevertheless, these calculations do not take into account the lateral area of the unit cell that can also be used for heat transfer and represent 45% of the total wall surface area,

$$\frac{A_{lateral}}{A_{external}+A_{lateral}} \approx \frac{\omega\left(2\pi D-8d+4l\right)}{\pi D^2+8dl+\omega\left(2\pi D-8d+4l\right)} = 0.45. \tag{2.67}$$

Moreover, it is desirable to operate in the zone of developing thermal boundary layer for the convective heat transfer coefficient to be higher than the asymptotical value for fully thermally developed flows. The total number of unit cells to achieve a certain dimensionless thermal entrance length is given by

$$n_x = \sqrt{2}x_{uc}^{*}\frac{\omega}{L}\mathrm{Re}\,\mathrm{Pr}+\frac{1}{2} \tag{2.68}$$

For this geometrical configuration and $\mathrm{Re}=300$, it is necessary more than 10^3 unit unit cells in the flow direction for the flow to be thermally fully developed, assuming a fluid with the physical properties of water.

2.4.6.4 Mass transfer Simulations

The average unit cell Sherwood number was estimated from CFD simulations. A secondary tracer species was placed on the external walls of the NUB domain with molar fraction $x_{\mathcal{A}}=1$, which dissolves in the continuous phase along the reactor.

The ratio of the simulation results of Sherwood number for the developing concentration boundary layer region and the analytical expression for parallel plates was expected to follow the value found for the analogous heat transfer problem,

$$r\left(\mathrm{Re}\right)=\frac{\mathrm{Sh}_{uc}}{\mathrm{Sh}_{\mathrm{PP}}}=3.17-2.52\exp\left(\frac{-\mathrm{Re}}{85.7}\right) \tag{2.69}$$

As shown in Section 2.4.3.3, the computational grid could not be sufficiently refined for the numerical diffusion not to affect the simulation results for working fluids with molecular diffusivities characteristic of liquids. For the numerical diffusivity to be negligible, as observed for the heat transfer simulations, the molecular diffusivity of the working fluid was increased up to 10^{-7}.

With the increading molecular diffusivity, and decreasing Schmidt number, the unit cell Sherwood number starts to deviate from the correlated values, increasing more rapidly with the increase of the Reynolds number (see Figure 2.31). Nevertheless, for molecular diffusivities of the same order of magnitude as the thermal diffusivity ($D \sim 10^{-7}$; Sc=10), the results are well described with the equivalent expression for mass transfer of Equation (2.63).

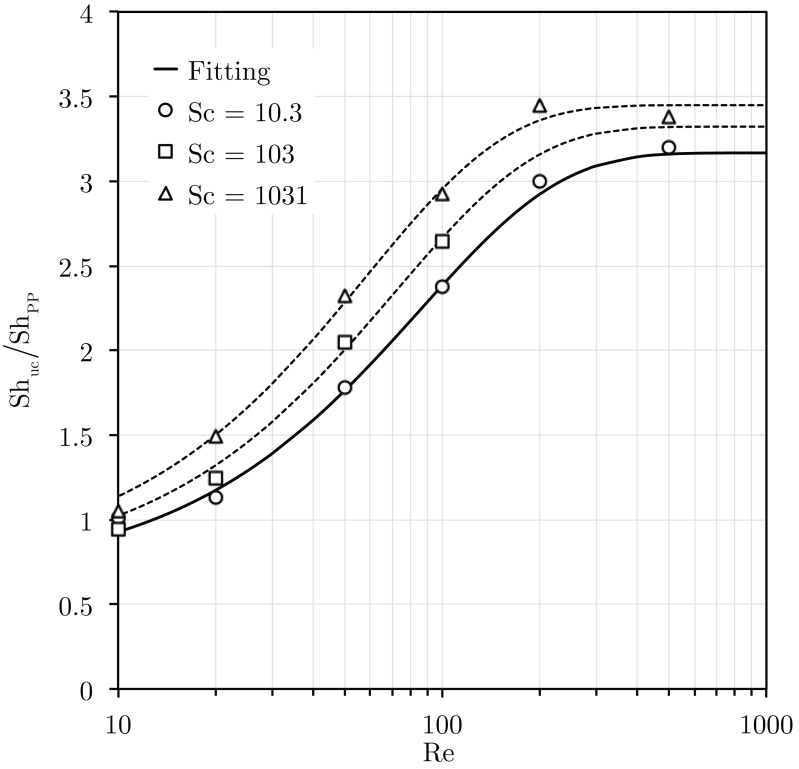


Figure 2.31. Ratio between the asymptotic values for developing concentration boundary layers of unit cell Sherwood number and Sherwood number for parallel plates with constant wall concentration.

Therefore, it can be assumed that a direct analogy with heat transfer can be made and the asymptotic results of unit cell Sherwood number can be estimated by

$$\mathrm{Sh}_{uc} = \begin{cases} \left[1.95 - 1.55\exp\left(\dfrac{-\mathrm{Re}}{85.7}\right)\right]\left(\dfrac{d_h}{2\omega}\right)^{2/3}\left(x^*_{uc}\right)^{-1/3} \;\; ; \;\; x^*_{uc} << 1 \\ 7.34\,\dfrac{d_h}{2\omega} \;\; ; \;\; x^*_{uc} >> 1 \end{cases} . \qquad (2.70)$$

2.5 Conclusions

In this chapter, experimental data of pressure drop obtained from three different NETmix reactor prototypes was successfully used to develop a model for prediction of the pressure drop with a single adjustable parameter that is only dependent on the geometric configuration of the network. Dynamic pressure measurements were also used to assess mixing dynamics in NETmix reactor and to confirm and extend a previously proposed model by Laranjeira (2005) for the frequency of oscillation in the chambers.

The mixing efficiency in NETmix was previously estimated (Gomes et al., 2010; Laranjeira et al., 2009). However from this work, its energy performance was quantified and shown to be competitive with existing mixers by evaluating N_P and Z factor for the three NETmix reactor prototypes. The power number is significantly lower (2-4 times) than the corresponding values for stirred tanks and the Z factor is one order of magnitude lower than the corresponding values for other existing commercial static mixers published by Thakur et al. (2003).

Due to computer memory limitations, it is not feasible to simulate, with the necessary grid refinement, the whole NETmix flow domain. The concept of the NUB model was introduced to reduce the computational domain for CFD simulation of the whole NETmix reactor. The NUB model is a simplified CFD simulation strategy that takes advantage of the periodically repetitive nature of the geometry and the expected flow pattern.

The pressure drop along the simulation domain and the dynamic behaviour of the flow inside the mixing chambers are in good agreement with existing experimental data, thus validating the NUB model. This simulation tool can be applied to any particular geometry of the NETmix reactor and overcomes the need of experimental data each time a new configuration is designed.

The NUB model was also used on the computation of other transport properties. CFD simulations were performed to study heat and mass transfer in the NETmix reactor and correlations of average unit cell Nusselt and Sherwood numbers were developed. The present study suggests that 3-5 times higher heat/mass transfer rate is achieved with the increasing Reynolds number in the channels when compared to the flow between parallel plates. Maximum convective heat and mass transfer coefficients are achieved when the flow inside the mixing chambers evolves to a self-sustained oscillatory laminar flow regime inducing strong local laminar mixing.

2.6 References

Anxionnaz, Z., Cabassud, M., Gourdon, C., Tochon, P., 2008. Heat exchanger/reactors (HEX reactors): Concepts, technologies: State-of-the-art. Chemical Engineering and Processing: Process Intensification 47, 2029-2050.

Bates, R.L., Fondy, P.L., Corpstein, R.R., 1963. Examination of Some Geometric Parameters of Impeller Power. Industrial & Engineering Chemistry Process Design and Development 2, 310-314.

Bird, R.B., Stewart, W.E., Lightfoot, E.N., 2002. Transport Phenomena, 2nd ed. John Wiley & Sons, Inc., USA.

Cavatorta, O.N., Böhm, U., de del Giorgio, A.M.C., 1999. Fluid-dynamic and mass-transfer behavior of static mixers and regular packings. AIChE Journal 45, 938-948.

Çengel, Y.A., 2003. Heat Transfer: A Practical Approach. McGraw-Hill.

Chemineer Inc., 2013. Chemineer - Reliability & Technology in Mixing, http://www.chemineer.com/products/kenics.html.

Chisti, Y., Moo-Young, M., 1996. Bioprocess intensification through bioreactor engineering. Chemical Engineering Research & Design, 575-583.

Cybulski, A., Werner, K., 1986. Static Mixers - Criteria for Application and Selections. International Chemical Engineering 26, 171-180.

Dias, M.M., Payatakes, A.C., 1986. Network models for 2-phase flow in porous-media. 1. Immiscible microdisplacement of nonwetting fluids. Journal of Fluid Mechanics 164, 305-336.

Ferziger, J.H., Perić, M., 2002. Computational Methods for Fluid Dynamics. Springer-Verlag GmbH.

Gomes, P.J., Fonte, C.P., Santos, R.J., Dias, M.M., Lopes, J.C.B., 2010. Experimental and numerical characterization and quantification of mixing in a NETmix® reactor, ECCE 7 - 7th European Congress of Chemical Engineering & CHISA 2010- 19th internation Congress and Process Engineering. Process Engineerig Publisher, Prahe, Prague, Czech Republic.

Gomes, P.J.G., 2011. The NETmix Reactor - Strategies for Optimizing Mixing and Development fo New Reactor Designs [Ph.D], Departamento de Engenharia Química. Universidade do Porto, Porto.

Grace, C.D., 1971. Static mixing and heat transfer. Chemical Processing & Engineering 52, 57-59.

Hemrajani, R.R., Tatterson, G.B., 2003. Mechanically Stirred Vessels, in: Paul, E.L., Atiemo-Obeng, V.A., Kresta, S.M. (Eds.), Handbook of Industrial Mixing - Science and Practice. John Wiley & Sons, New Jersey, pp. 345-390.

Joshi, P., Nigam, K.D.P., Nauman, E.B., 1995. The Kenics Static Mixer: New Data and Proposed Correlations. The Chemical Engineering Journal 59, 265-271.

Kashid, M.N., Kiwi-Minsker, L., 2009. Microstructured Reactors for Multiphase Reactions: State of the Art. Industrial & Engineering Chemistry Research 48, 6465-6485.

Keil, F.J., 2004. Catalytic reactions and reactors. Chemical Engineering Science 59, 5473-5478.

Khinast, J.G., Bauer, A., Bolz, D., Panarello, A., 2003. Mass-transfer enhancement by static mixers in a wall-coated catalytic reactor. Chemical Engineering Science 58, 1063-1070.

Kiwi-Minsker, L., Renken, A., 2005. Microstructured reactors for catalytic reactions. Catalysis Today 110, 2-14.

Konax Systems Inc., 2013. Konax Systems Inc. - Mixing by design, http://www.komax.com.

Koplik, J., 1982. Creeping flow in two-dimensional networks. Journal of Fluid Mechanics 119, 219-247.

Lammers, G., Beenackers, A.A.C.M., 1994. Heat transfer and the continuous production of hydroxypropyl starch in a static mixer reactor. Chemical Engineering Science 49, 5097-5107.

Laranjeira, P.E., 2005. NETmix® Static Mixer Modelling, CFD Simulation and Experimental Characterisation [Ph.D], Departamento de Engenharia Química. Universidade do Porto, Porto.

Laranjeira, P.E., Martins, A.A., Lopes, J.C.B., Dias, M.M., 2009. NETmix®, a new type of static mixer: Modeling, simulation, macromixing, and micromixing characterization. AIChE Journal 55, 2226-2243.

Li, D., Xiong, K., Yang, Z., Liu, C., Feng, X., Lu, X., 2011. Process intensification of heterogeneous photocatalysis with static mixer: Enhanced mass transfer of reactive species. Catalysis Today 175, 322-327.

Li, H.Z., Fasol, C., Choplin, L., 1996. Hydrodynamics and heat transfer of rheologically complex fluids in a Sulzer SMX static mixer. Chemical Engineering Science 51, 1947-1955.

Lide, D.R., 2004. CRC Handbook of Chemistry and Physics.: A Ready-Reference Book of Chemical and Physical Data. CRC Press.

Lisboa, P.F., Fernandes, J., Simões, P.C., Mota, J.P.B., Saatdjian, E., 2010. Computational-fluid-dynamics study of a Kenics static mixer as a heat exchanger for supercritical carbon dioxide. The Journal of Supercritical Fluids 55, 107-115.

Manglik, R.M., Bergles, A.E., 1993. Heat Transfer and Pressure Drop Correlations for Twisted-Tape Inserts in Isothermal Tubes: Part I---Laminar Flows. Journal of Heat Transfer 115, 881-889.

Martins, A.A., Laranjeira, P.E., Lopes, J.C.B., Dias, M.M., 2007. Network modeling of flow in a packed bed. AIChE Journal 53, 91-107.

Meijer, H.E.H., Singh, M.K., Anderson, P.D., 2012. On the performance of static mixers: A quantitative comparison. Progress in Polymer Science 37, 1333-1349.

Munter, R., 2010. Comparison of Mass Transfer Efficiency and Energy Consumption in Static Mixers. Ozone: Science & Engineering 32, 399-407.

Myers, K.J., Bakker, A., Ryan, D., 1997. Avoid Agitation by Selecting Static Mixers. Chemical Engineering Progress 93, 28-38.

Nauman, E.B., 1979. Enhancement of heat transfer and thermal homogenity with motionless mixers. AIChE Journal 25, 246-258.

Pahl, M.H., Muschelknautz, E., 1980. Static Mixers and their applications. Chemie Ingenieur Technik 52, 285-291.

Patankar, S.V., 1980. Numerical Heat Transfer and Fluid Flow. Taylor & Francis.

Rauline, D., Tanguy, P.A., Le Blévec, J.-M., Bousquet, J., 1998. Numerical investigation of the performance of several static mixers. The Canadian Journal of Chemical Engineering 76, 527-535.

Ross Mixers, 2013. Ross - Industrial Mixers and Blenders, http://www.mixers.com/static-mixers.asp.

Shah, R.K., London, A.L., 1978. Laminar flow forced convection in ducts: a source book for compact heat exchanger analytical data. Academic Press.

Silva, V.M., Quadros, P.A., Laranjeira, P.E., Dias, M.M., Lopes, J.C.B., 2008. A Novel Continuous Industrial Process for Producing Hydroxyapatite Nanoparticles. Journal of Dispersion Science and Technology 29, 542-547.

SPX-Lightnin, 2013. SPX - Where Ideas Meet industry, http://www.spx.com/en/lightnin/pc-mixers/.

Statiflo Iternational, 2013. Statiflo Static and Montionless Mixers, Pipe Mixers and Channel Mixers, http://www.statiflo.net.

Sulzer, 2013. Sulzer, http://www.sulzer.com/en/Products-and-Services/Agitators-Mixers-and-Dispensers/Static-Mixers/General-Purpose-Mixers.

Szalai, E.S., Muzzio, F.J., 2003. Fundamental approach to the design and optimization of static mixers. AIChE Journal 49, 2687-2699.

Thakur, R.K., Vial, C., Nigam, K.D.P., Nauman, E.B., Djelveh, G., 2003. Static Mixers in the Process Industries—A Review. Chemical Engineering Research and Design 81, 787-826.

Visser, J.E., Rozendal, P.F., Hoogstraten, H.W., Beenackers, A.A.C.M., 1999. Three-dimensional numerical simulation of flow and heat transfer in the Sulzer SMX static mixer. Chemical Engineering Science 54, 2491-2500.

3 NETmix Technology Applied to Liquid-Liquid Heterogeneous Reactions

3.1 Introduction

Two-phase liquid-liquid reactions represent important chemical processes but their operation and control can be problematic. Several operating parameters must be taken into consideration such as the difference in the physical properties of both phases, the inherent reaction rate nature (stoichiometry of reactants, intrinsic reaction rate, isothermal/adiabatic conditions), the separation of the reaction product, the residence time required and characteristics of the reactor to promote mass and heat transfer. Often batch or semi-batch processing with sub-optimal operation of the process is performed and thereby, the process is often run to the limitations of existing equipment. Continuous processing using structured equipment has the potential to overcome such limitations and focus on process intensification and safety (Burns and Ramshaw, 1999; Kashid and Kiwi-Minsker, 2009).

The use of the NETmix reactor for this type of reactions, has the aim to improve selectivity and yield and provide better mixing performance in bulk chemical production with liquid-liquid reactions by generating high interfacial area, optimizing the process conditions and controlling micromixing and temperature.

The reaction of nitration of benzene with a mixture of concentrated nitric acid and sulfuric acid, also called mixed acid, was selected as a case study. The nitration of benzene is an electrophilic aromatic substitution reaction between benzene and nitric acid to produce nitrobenzene. Given the importance of nitrobenzene and its derivatives, it is crucial to understand the interaction of all the involved phenomena to correctly understand and model the nitration reaction.

About 97% of the world's production of nitrobenzene is used to obtain aniline which itself is intrinsically related to the production of methylene diphenyl diisocyanate, MDI. MDI is an aromatic diisocyanate that can react with several polyols for the manufacture of polyurethanes, widely used as insulation materials in construction and car industries, elastomers and resins (Nexant, 2012; Six and Richter, 2000). Nitrobenzene can also be used for other applications such as explosives, dyes and pigments, pesticides, drugs, solvents and synthetic rubbers (Booth, 2000; Nexant, 2012).

The most widespread technological process to produce nitrobenzene consists on the adiabatic benzene nitration with a mixture of nitric and sulfuric acid. Due to the complexity of the heterogeneous mixture, the kinetics is often controlled by diffusional limitations between both phases and different type of reactors can be used to perform the reaction. Castner (1941) first patented a process for adiabatic nitration of aromatic compounds. This method admits batch or continuous operation using one or a series of CSTRs. Years later, Alexanderson et al. (1978) suggested an improvement to the process. This method is still widely used for industrial production. Other traditional patented processes make use of plug flow reactors in turbulent regime (Evans, 1990; Humphrey and Smoak, 1963).

More recently, alternative configurations to the adiabatic nitration in CSTRs were patented. Rae and Hauptmann (1991) and Guenkel et al. (1994) adopted a jet impingement reactor where a nearly total conversion for small reactions times can be achieved. Konig et al. (1997) developed a system of plug flow reactors with static mixers coupled to the coalescence zones. The patent of Hermann and Gebauer (1998)

uses a system of two concentric jets where 80% of conversion is immediately achieved in the interface of the jets. Gillis et al. (2003) patented a method that uses a tubular reactor with perforated plates alternated with coalescence zones.

Western Europe, with Bayer, Huntsman and BASF, and the USA, with Rubicon, First Chemical and BASF, are the main manufactures of nitrobenzene (Nexant, 2012). Portugal, through Quimigal, has a nitrobenzene production capacity of around 10% of the total Western Europe production capacity (Santos, 2005). The main suppliers of nitration technology worldwide nowadays are the Canadian company Noram with the adiabatic process and the Swiss company Biazzi with the isothermal process (Biazzi, 2013; Noram, 2013). Quimigal, First Chemical Corp., Bayer, Huntsman and Rubicon are the main operators of the Noram Technology (Noram, 2013).

Being a reaction of great interest, several studies were made to determine the nitration reaction rate. These studies of reaction rate are divided into two main areas, homogeneous and heterogeneous nitration processes.

Studies of homogenous nitration are processed only in the aqueous phase by dissolving the aromatic species into the aqueous phase in an amount equal or smaller to the saturation concentration. In this way, it is possible to study the nitration mechanism and kinetic parameters without mass transfer limitation interferences. (Coombes et al., 1968; Deno and Stein, 1956; Field and Strachan, 1982; Hughes et al., 1950; Marziano et al., 1998; Marziano et al., 1980; Sheats and Strachan, 1978). However, in these experiments of homogeneous nitration, industrial conditions are not covered, since the molar fraction of nitric acid used is orders of magnitude smaller than the actual fraction used in heterogeneous nitration in industrial conditions due to the small amount of benzene that can be dissolved.

Measurements of reaction rate in heterogeneous nitration are difficult to obtain due to the mass transfer limitation between phases. Lewis and Suen (1940) were pioneers in heterogeneous nitration of benzene studies. Measurements of nitration rate were

performed using a continuous stirred tank with high impeller speed so that increase in agitation and dispersion had no further effect on the nitration rate.

Biggs and White (1956) made a crucial contribution by studying the rate of nitration of benzene with mixed acid and sulfuric acid over ranges of phase ratio that are of interest in industrial nitration. Furthermore, the resistance terms to mass transfer were made sufficiently small to eliminate the stirrer speed as a variable affecting the reaction rate. Biggs and White (1956) proposed a reaction rate model that assumes reaction takes place in both phases but years later it was verified that the reaction rate in the organic phase can be neglected (Cox and Strachan, 1971; Giles et al., 1976).

Santos (2005) proposed a model for the heterogeneous liquid-liquid reaction of benzene nitration by applying the film and Dankwerts penetration model, that take into account the diffusional resistances. Both models were confronted with experimental results showing good predictions in an intermediate regime where chemical reactions and diffusional processes compete. Santos (2005) also used multivariable linear regression techniques to develop empirical models which are able to predict the formation of nitrobenzene as a function of the main operating conditions, the interfacial area, concentration of nitric and sulfuric acid and nitration temperature. Nevertheless, no energy balance is considered and all the models developed assume that the nitration temperature and interfacial area are known.

In this chapter, a simulation tool for a multiphase liquid-liquid heterogeneous reaction was developed. Generation of interfacial area is considered high enough so that a kinetically controlled regime is assumed, and thus, no calculations of interfacial area are required. This assumption is sustained by the work of Gomes (2011) that employed Computational Fluid Dynamic simulations to evaluate the generation of high interfacial area in the NETmix reactor. Furthermore, considerations will be presented, based on experimental published date, for the NETmix operation conditions that have to be set to ensure that diffusional

limitations can be neglected. The energy balance was solved to estimate the nitration temperature along the NETmix reactor.

This chapter is organized into six sections. In Section 3.2, a description of the benzene nitration mechanism is presented. In Section 3.3, the mathematical formulation to model the heterogeneous nitration reaction in a NETmix reactor is described. This model takes into account the mass and energy balances for each NETmix unit cell and the distribution of species between phases resulting in a system of non-linear equations. The numerical implementation to solve a system of equations is also presented. In Section 3.5, simulation results are compared and validated with published experimental data. Moreover, considerations are made for the NETmix operation conditions that have to be set to ensure that no diffusional limitations exist. In Section 3.6, a case study is selected and simulations performed to demonstrate the applicability of the model on predicting the final conversion and temperature raise. Additionally, results are discussed and an analysis to the operational conditions is presented. Conclusion are presented in Section 3.7.

3.2 Heterogeneous Benzene Nitration Mechanism

Nitration of benzene is an electrophilic aromatic substitution reaction between benzene and nitric acid to yield nitrobenzene. Benzene reacts slowly with concentrated nitric acid and the reaction is faster if carried out by using a mixture of concentrated nitric sulfuric acids. Sulfuric acid acts as a catalyst and increases the rate of nitration by increasing the concentration of the electrophile, the nitronium ion (NO_2^+), involved in the reaction (Solomons and Fryhle, 2000).

Nitric acid in solution is involved in two different equilibria. When in water, nitric acid dissociates in its conjugate base, the nitrate ion, NO_3^-,

$$HNO_3 \rightleftarrows H^+ + NO_3^-. \tag{3.1}$$

However, since nitric acid in solution has both acidic and basic properties it can undergo an autoprotolysis reaction to form the nitronium ion, which is the active reactant in aromatic nitration reactions. When sulfuric acid is also in solution, nitric acid accepts a proton from the stronger acid to form nitronium ion and water,

$$H^+ + HNO_3 \rightleftarrows H_2O + NO_2^+. \tag{3.2}$$

Figure 3.1 synthesizes the two steps of the mechanism of nitronium ion formation.

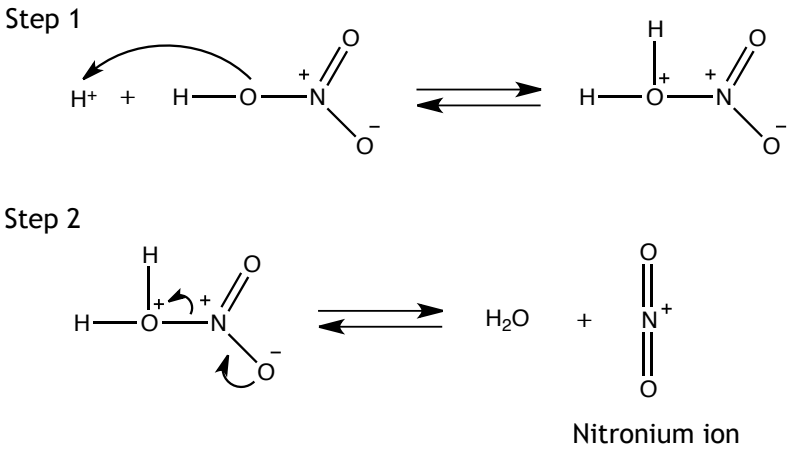


Figure 3.1 Nitronium ion formation mechanism.

The presence of high concentrations of sulfuric acid in solution favours the formation of the nitronium ion. The evidence of that can be found in the experimental results from Sampoli et al. (1985) and Hanson et al. (1976).

The nitration of benzene occurs in a two-step reaction mechanism (Figure 3.2). In the first step, the nitronium ion acting as the electrophile in the nitration reacts with benzene to form a resonance-stabilized arenium ion. In a second step, the arenium ion loses a proton to a Lewis base and becomes nitrobenzene (Solomons and Fryhle, 2000).

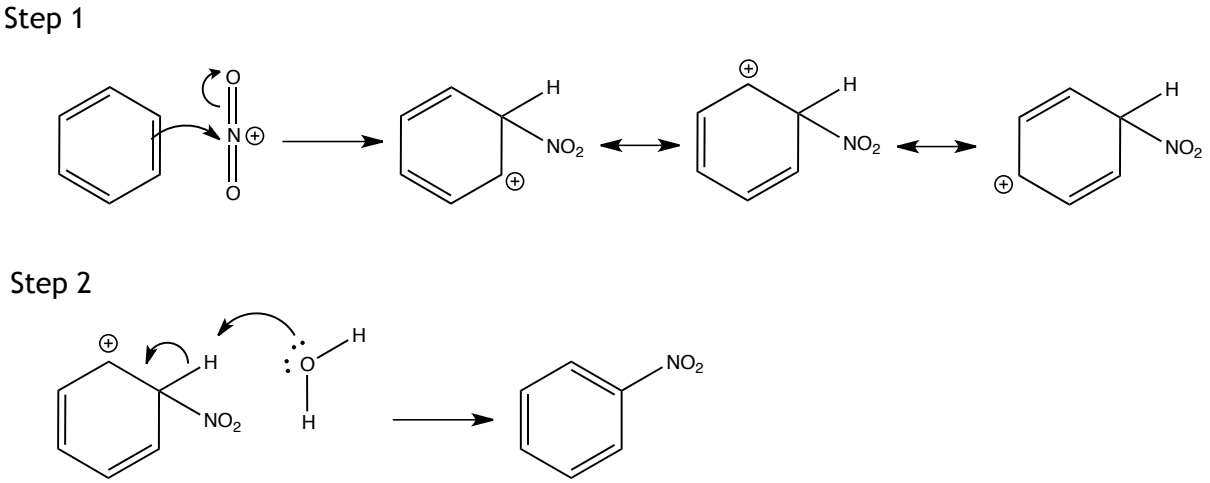


Figure 3.2 Mechanism for the reaction of nitration of benzene.

Reaction in the organic phase can also happen. However the reaction rate is several orders of magnitude lower than the reaction rate in the aqueous phase and therefore can be neglected (Cox and Strachan, 1971; Giles et al., 1976). Based on the work of Lewis and Suen (1940) the reaction in the organic phase is negligible at low organic phase volume fraction values and although nitric acid is present in the organic phase, the nitration rate is negligible due to the fact that the concentration of H^+ in the organic phase is too low for the nitronium ion to be generated to an appreciable extent (Modak and Juvekar, 1995).

The global conceptual mechanism that was considered for modelling purposes, similar to the mechanism proposed by Giles et al. (1976), is shown in Figure 3.3. The steps involved are:

- benzene is transferred through the interface and diffuses in the aqueous phase;
- benzene reacts with the nitronium ion in equilibrium with the other nitric species to form nitrobenzene;
- nitrobenzene diffuses through the aqueous phase and is transferred to the organic phase when it reaches the interface.

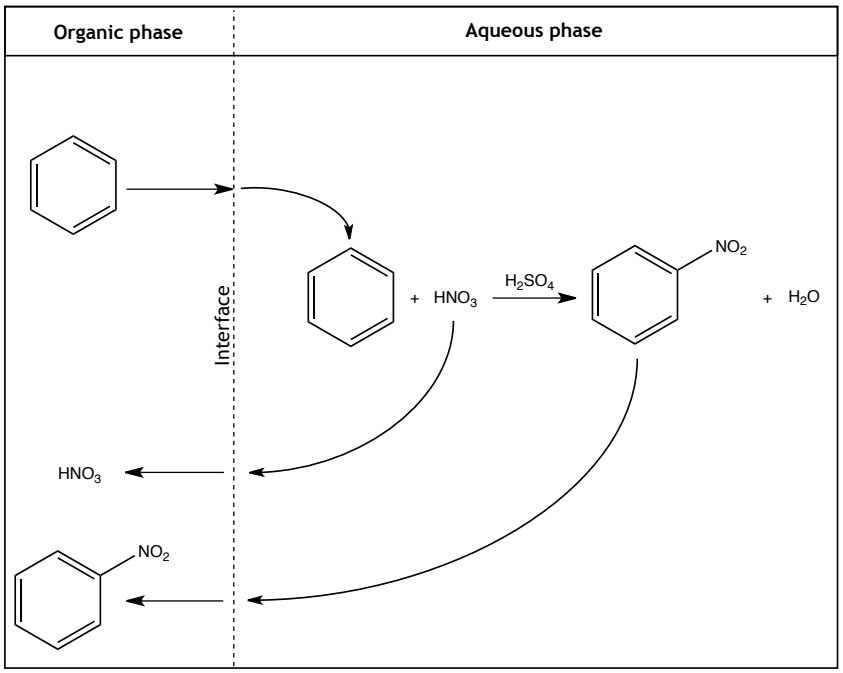


Figure 3.3 Global mechanism of benzene nitration.

3.3 NETmix Model Description

In this section, the mathematical description of all the phenomena involved in the aromatic nitration of benzene is provided. A correlation for the reaction rate is developed and the physical properties change with temperature of all the species involved in the reaction are presented. The heat of reaction, the heat of dilution of the mixed acid solution and the equilibrium of species between phases are also considered. Finally, mass balance and energy balances are performed for each unit cell and the numerical implementation to solve the nitration of benzene reaction throughout the NETmix reactor is described.

Superscript characters A and O are used to represent the aqueous and the organic phase, respectively. Subscripts characters were used to represent each species where B is benzene, NB is nitrobenzene, N is nitric acid, S is sulfuric acid and W is water.

3.3.1 Reaction Rate Model

As reported by several authors (Biggs and White, 1956; Lewis and Suen, 1940), the overall nitration reaction rate, R_{nit}, is defined as the sum of the parallel reaction rates in both organic and aqueous phases.

$$R_{nit} = R_{nit}^{A} + R_{nit}^{O} \tag{3.3}$$

where R_{nit}^{A} is the reaction rate in the aqueous phase and R_{nit}^{O} is the reaction rate in the organic phase. As stated in Section 3.2, the nitration rate is negligible in the organic phase and the overall reaction can be written as a function of the activities of benzene and nitric acid in the aqueous phase,

$$R_{nit} \approx R_{nit}^{A} = k a_N^A a_B^A \left(1-\varepsilon\right) \tag{3.4}$$

where k is the reaction rate constant in the aqueous phase, ε is the hold-up fraction of the organic phase, a_N^A is the activity of nitric acid in the aqueous phase and a_B^A is the activity of benzene in the aqueous phase. The hold-up fraction is defined as the ratio of the organic phase volume and the total volume,

$$\varepsilon = \frac{V^O}{V^O + V^A} \tag{3.5}$$

where V^A is the volume of aqueous phase and V^O is the volume of organic phase. For continuous reactors, with similar average velocities of both phases, the hold-up fraction can be approximated by

$$\varepsilon = \frac{Q^O}{Q^O + Q^A} \tag{3.6}$$

where Q^A is the volume of aqueous phase and Q^O is the volume of organic phase.

Under steady state conditions, it is assumed that benzene is transferred into the aqueous phase at the same rate as it is consumed by the reaction, so the reaction rate can be equated to the mass transfer rate of benzene between both phases,

$$R_{nit}^{A} = K_B\left(a_B^O - a_B^A\right) \tag{3.7}$$

where K_B is the mass transfer coefficient for benzene between phases.

Replacing the activity a_B^A from Equation (3.7) in Equation (3.4), the reaction rate comes

$$R_{nit} = \frac{a_N^A a_B^O\left(1-\varepsilon\right)}{\left(\frac{1}{k} - \frac{a_N^A\left(1-\varepsilon\right)}{K_B}\right)} \tag{3.8}$$

If it is assumed that NETmix provides a high degree of mixing in each unit cell, mass transfer limitations can be considered negligible. Increasing the degree of agitation will decrease the resistance terms of mass transfer by increasing the transfer coefficient K_B and Equation (3.8) can be simplified, in the limit, to

$$R_{nit} = k a_N^A a_B^O\left(1-\varepsilon\right) \tag{3.9}$$

The activity coefficient of the organic component, γ_B^O, was considered equal to unity as assumed by Barduhn and Kobe (1956) and shown by McKinley and White (1944) (cited by Barduhn and Kobe (1956)). Equation (3.8) simplifies to

$$R_{nit} = k\gamma_N^A c_N^A c_B^O\left(1-\varepsilon\right) \tag{3.10}$$

where γ_N^A is the activity coefficient of nitric acid in the aqueous phase, c_N^A is the nitric acid concentration in the aqueous phase and c_B^O is the benzene concentration in the organic phase.

The unknown terms of the reaction rate constant, k and γ_N^A, can be grouped in a single variable, the apparent kinetic rate, k_r,

$$k_r = k\gamma_N^A = k_r\left(c_N^A, c_S^A, T\right) \tag{3.11}$$

that is a function of temperature and the composition of the aqueous phase, either in terms of the change on the catalyst strength and the change of the activity coefficient of nitric acid.

Published experimental data by Biggs and White (1956) was used for the development of a correlation for the predict the reaction rate constant. This set of data was selected because it comprises a detailed study concerning the effect of temperature, mixed acid composition and hold-up fraction on the reaction rate. Furthermore, the stirring speed was high enough to ensure that a fine emulsion was maintained and that increasing the speed of the impeller would not affect the reaction rate. Operational conditions used by Biggs and White (1956) are explained in more detail in section 3.5.1. The correlation chosen for the prediction of the reaction rate constant features four fitting parameters and is given by

$$k_r = k_0 \exp\left(\frac{-E_a}{RT}\right)\exp\left[\alpha_1\left(x_N^A + \alpha_2 x_S^A\right)\right] \tag{3.12}$$

where k_0 is a pre-exponential factor, E_a is the energy of activation, R is the universal gas constant, T is temperature, x_N^A is the nitric acid molar fraction in the aqueous phase, x_S^A is the sulfuric acid molar fraction in the aqueous phase and α_1 and α_2 are fitting parameters. The values of $E_a = 1.19\times10^5$ J/mol, $k_0 = 0.210$ m^{3}mol^{-1}s^{-1}, $\alpha_1 = 80.3$ and $\alpha_2 = 1.44$ were found to best fit the experimental data using the least square method. Finally, the reaction rate is given by

$$R_{nit} = k_0 \exp\left(\frac{-E_a}{RT}\right)\exp\left[\alpha_1\left(x_N^A + \alpha_2 x_S^A\right)\right]c_N^A c_B^O\left(1-\varepsilon\right). \tag{3.13}$$

Figure 3.4 shows the plot of $\ln\left(\frac{R_{nit}}{c_N^A c_B^O\left(1-\varepsilon\right)}\right)$ as a function of $\alpha_1\left(x_N^A + \alpha_2 x_S^A\right)$, where it can be seen the fitting of experimental results for three different temperatures.

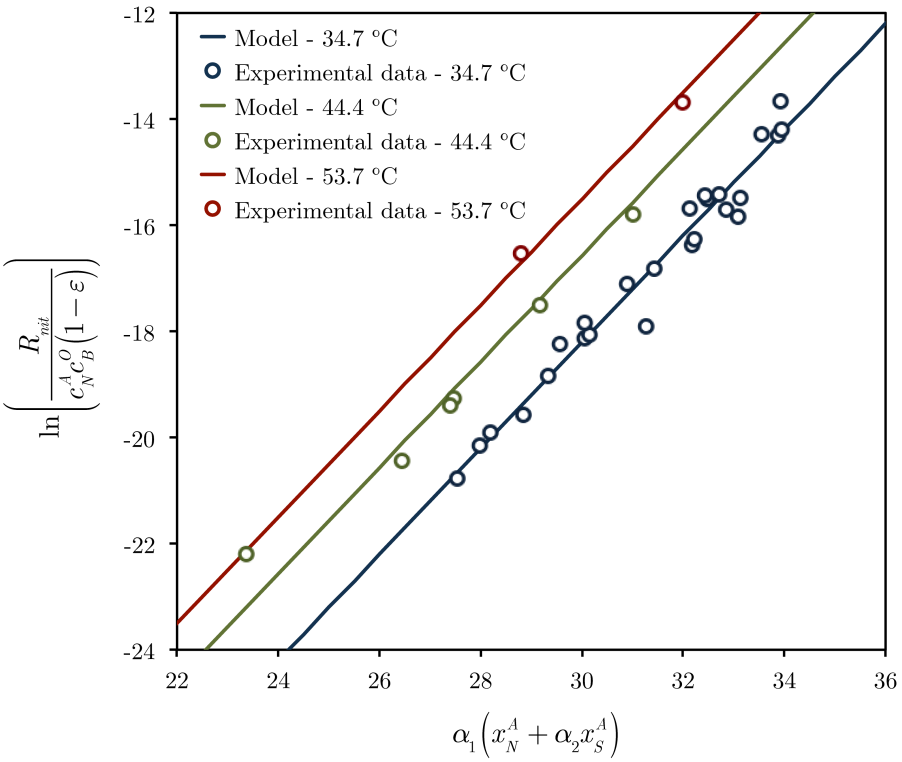


Figure 3.4 Reaction rate model fitting using experimental data from Biggs and White (1956).

3.3.2 Heat of Reaction and Dilution of the Mixed Acid

Benzene nitration is a highly exothermic reaction with a heat of reaction, ΔH_r, of -145 kJ/mol at the reference temperature of 298 K (Burns and Ramshaw, 1999). Enthalpy of reaction can be determined for other temperatures using the Kirchhoff's equation for enthalpy change (Smith et al., 2001),

$$\Delta H_r\left(T\right) = \Delta H_r\left(T_0\right) + \int_{T_0}^{T} \Delta c_{P_r}\left(T\right)\mathrm{d}T \tag{3.14}$$

where Δc_{P_r} is the difference of heat capacities between products and reactants and is given by

$$\Delta c_{P_r} = \sum_{i}^{NB,W} c_{P_i} - \sum_{i}^{B,N} c_{P_i} \tag{3.15}$$

where c_{P_i} is the heat capacity of reactant or product i.

As mentioned in Section 3.2 during the nitration of an aromatic compound, by means of a mixture of concentrated nitric and sulfuric acids, water is formed as a product of nitration. This dilution causes extra heat release.

In continuous processes, the heat flow rate resulting from dilution effects, $\Delta \dot{H}_d$, is calculated from the change between the final and the initial state of the sum of the relative partial molar enthalpies times the molar flow rate of each component (Zaldívar et al., 1992),

$$\Delta \dot{H}_d = \sum_{i=1}^{N,S,W} \Delta\left(F_i H_i\right) = \sum_{k=1}^{N,S,W} F_i H_i \Big|_{out} - \sum_{i=1}^{N,S,W} F_i H_i \Big|_{in} \tag{3.16}$$

where F_i is the molar flow rate of component i and H_i is the partial molar enthalpy.

The partial molar enthalpy of each component was correlated by Zaldívar et al. (1992) as a function of the molar fractions of the three components using a polynomial equation of type,

$$H_i = \prod_{o=1}^{N,S,W} \left(\sum_{j=1}^{3} a_{o,j}^{(i)} \left(100 x_o\right)^{j-1} \right) \tag{3.17}$$

where $a_{o,j}^{(i)}$ are the polynomial parameters of the fitting and x is the molar fraction.

In Table 3.1 to

Table 3.3 are listed the $a_{o,j}^{(i)}$ parameters for the estimation of the partial molar enthalpy at $273\,\mathrm{K}$. Partial molar enthalpy is given in $\mathrm{kJ/mol}$.

Table 3.1 $a_{o,j}^{(W)}$ parameters for calculation of the partial molar enthalpy of water (Zaldívar et al., 1992).

$o \setminus j$	1	2	3
W	-23.6	3.86×10^{-1}	-1.49×10^{-3}
N	430	-13.7	1.39×10^{-1}
S	1.36×10^{-3}	9.87×10^{-5}	-9.67×10^{-7}

Table 3.2 $a_{o,j}^{(N)}$ parameters for calculation of the partial molar enthalpy of nitric acid (Zaldívar et al., 1992).

$o \setminus j$	1	2	3
W	-26.7	-2.66×10^{-1}	-1.95×10^{-2}
N	-214	-3.16	4.92×10^{-2}
S	-5.50×10^{-4}	-8.86×10^{-5}	-9.49×10^{-8}

Table 3.3 $a_{o,j}^{(S)}$ parameters for calculation of the partial molar enthalpy of sulfuric acid (Zaldívar et al., 1992).

$o \setminus j$	1	2	3
W	-24.1	-5.77×10^{-1}	-1.53×10^{-2}
N	-284	3.19	-1.92×10^{-2}
S	-1.11×10^{-3}	1.15×10^{-5}	-7.32×10^{-9}

The partial enthalpy of each component i can be estimated for other temperatures than the reference temperature using the Kirchhoff's equation for enthalpy change,

$$H_i(T) = H_i(T_0) + \int_{T_0}^{T} c_{P_i}(T)\,\mathrm{d}T. \tag{3.18}$$

In industrial nitration conditions, the heat released due to dilution is only around 1 to 5% of the total heat release during the benzene reaction. Nevertheless, it can be now understood that the formation of water has opposite effects on the reaction rate. The catalyst's effect decreases by reducing the concentration of sulfuric acid. On the contrary, the heat released by dilution of the mixed acid solution favours the reaction rate.

3.4 Phase Equilibrium

For modelling two-phase reactions, it is required to take into account the solubility of species and equilibrium between phases. In this model, only the solubility of benzene in the aqueous phase and the distribution of nitric acid between the aqueous and organic phase are taken into account. Sulfuric acid and water are considered immiscible in the organic phase, since the solubility of nitric acid in the organic phase is at least one order of magnitude higher than the solubility of sulfuric acid and water (Albright et al., 1976; Ismail, 1973). Although nitrobenzene is more soluble than benzene in the aqueous phase (Schiefferle et al., 1976), the solubility of nitrobenzene was not considered due to the lack of published data or correlations for the prediction of the solubility of nitrobenzene in mixed acid as a function of concentration and temperature.

3.4.1.1 Benzene Solubility in the Aqueous Phase

When the organic phase contacts with the aqueous phase, benzene is partially soluble in the mixed acid. Based on the work of Zaldivar et al. (1995), the distribution or partition coefficient of benzene, m_B, in mixed acid defined as the ratio between the concentrations of benzene in the aqueous phase and in the organic phase can be correlated as a function of the Gibbs free energy change, ΔG_B, and temperature, T,

$$m_B = \frac{c_B^A}{c_B^A} = \exp\left(-\frac{\Delta G_B}{RT}\right) \tag{3.19}$$

The Gibbs energy free change is a function of the sulfuric acid strength, the difference in internal pressure of the two immiscible solvents and the molar volume of the aromatic compounds. The effect of the nitric acid concentration on the total solubility has also to be taken into account while estimating the Gibbs-energy free change of mixing for this component's system (Ismail, 1973). ΔG_B was empirically correlated by Zaldivar et al. (1995) as

$$\Delta G_B = \lambda_1 \psi_S \psi_N + \lambda_2 - \lambda_3 T \tag{3.20}$$

where λ_1, λ_2 and λ_3 are fitting constants and ψ_S and ψ_N are functions of the molar fraction of sulfuric acid and nitric acid respectively. ψ_S is a polynomial function that results from the fitting to the experimental data from Hanson and Ismail (1975),

$$\psi_S = \sum_{i=1}^{7} a_i \left(x_S^A\right)^{i-1} \tag{3.21}$$

where a_1 to a_7 are the fitting constants (Zaldivar et al., 1995). ψ_N is an exponential function that results from the fitting to the experimental data from Hanson and Ismail (1975),

$$\psi_N = b_1 \exp\left(-b_2 \left(x_N^A\right)^{b_3}\right) \tag{3.22}$$

where b_1, b_2 and b_3 are the fitting constants. This fitting was preferred to the fitting proposed by Zaldivar et al. (1995) since it shows better accuracy while predicting the solubility change of benzene with varying nitric acid concentration.

The numerical values of the fitting constants of equations (3.20), (3.21) and (3.22) are listed in Table 3.4. The fitting is valid in the range of $0 \leq x_S^A \leq 0.3$ and $0 \leq x_N^A \leq 0.15$.

Table 3.4 Fitting constants for the determination of the partition coefficient of benzene between the two phases.

i	λ_i	a_i	b_i
1	57.1	167	1.60
2	-1.38×10^3	606	0.212
3	-5.20	-4.46×10^3	0.617
4	—	1.34×10^4	—
5	—	-1.38×10^4	—
6	—	-5.97×10^3	—
7	—	1.29×10^4	—

Figure 3.5 shows the comparison between the calculated data and the experimental data from Hanson and Ismail (1975) of the distribution coefficient of benzene in sulfuric acid solutions. Equation (3.19) can predict well the solubility of benzene in sulphuric acid solutions, in the range of molar fractions of sulphuric acid from 0 to 0.3, with a maximum deviation of 15% relative to the experimental data.

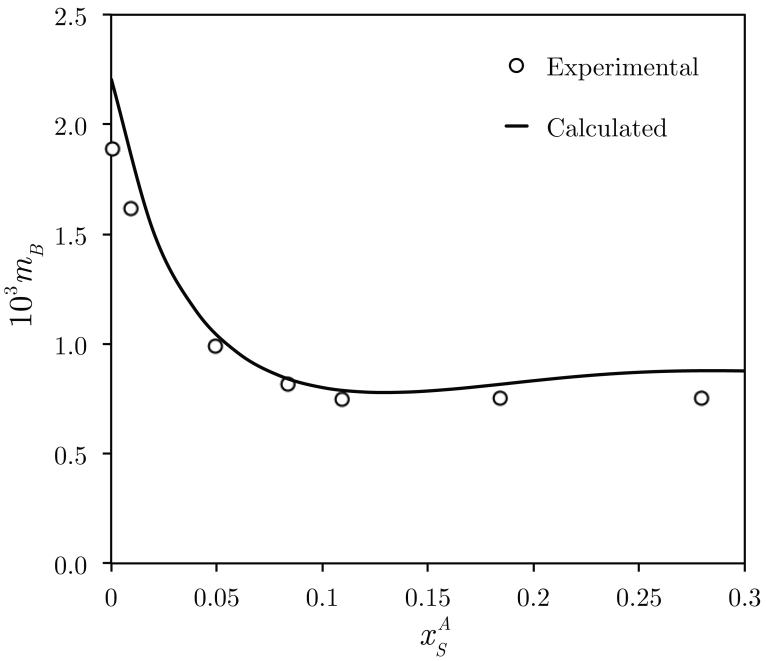


Figure 3.5 Experimental and calculated distribution coefficients for benzene in sulfuric acid solutions at 313 K. Experimental data from Hanson and Ismail (1975).

Figure 3.6 shows the experimental data from Hanson and Ismail (1975) of the partition coefficient of benzene in nitric acid solutions. A comparison is made

between the experimental data and the calculated values. Equation (3.19) can also predict well the solubility of benzene in nitric acid solutions, in the range of molar fraction of nitric acid from 0 to 0.15, with a maximum deviation of less than 1% relatively to the experimental data

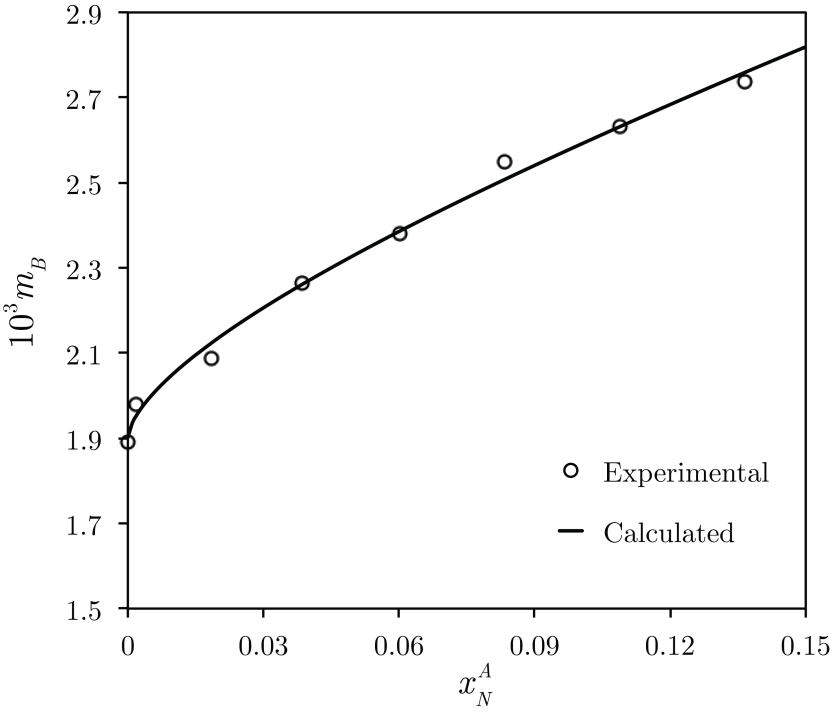


Figure 3.6 Experimental and calculated distribution coefficients for benzene in nitric acid solutions at 295 K. Experimental data from Hanson and Ismail (1975).

Equation (3.19) was also compared to experimental data from Hanson and Ismail (1975) for the partition coefficient of benzene in mixed acid solution with different ratios of nitric acid and sulfuric acid combined. In each set, nitrobenzene was also present in the organic phase in different proportions.

Figure 3.7 shows the comparison between the experimental data and the calculated values from Equation (3.19) for $c_N^A = 0\,\mathrm{M}$. The presence of nitrobenzene in the organic phase seems not to influence the distribution coefficient of benzene between the two phases as predicted by Equation (3.19).

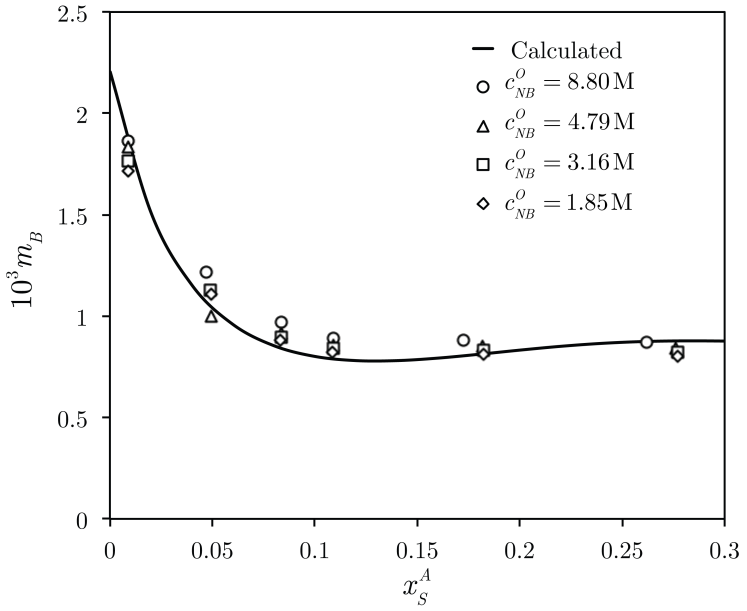


Figure 3.7 Experimental and calculated distribution coefficients for benzene in sulfuric acid solutions at 303 K. Experimental data from Hanson and Ismail (1975).

Figure 3.8 shows the comparison between the experimental distribution coefficient and the calculated distribution for benzene. Equation (3.19) can be used to predict the distribution of benzene in mixed acid solutions with the presence of not of nitric acid with a deviation of 15%.

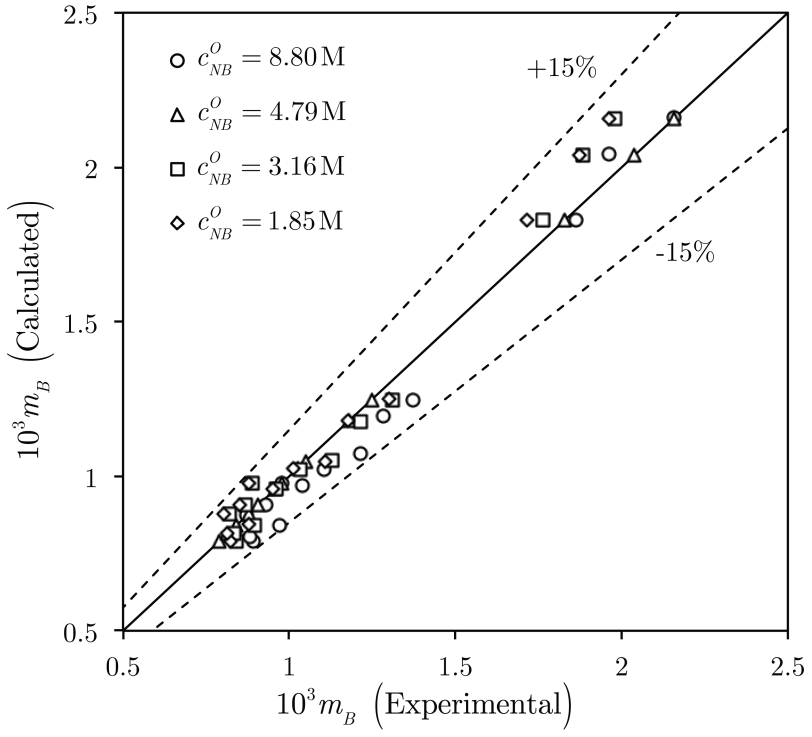


Figure 3.8 Experimental and calculated distribution coefficients for benzene in mixed acid solutions at 303 K. Experimental data from Hanson and Ismail (1975).

3.4.1.2 Nitric Acid Solubility in the Organic Phase

Nitric acid is partially soluble in the organic phase. While in the organic phase nitric acid does not form the nitronium ion $\left(NO_2^+\right)$ and therefore it will not take part in the reaction. Biggs and White (1956) reported experimental data for the distribution of nitric acid in the aqueous and organic phases. Nitric acid distribution was correlated as a function of the nitric acid molar fraction on the aqueous phase and nitrobenzene molar fraction in the organic phase,

$$\frac{x_N^O}{x_{NB}^O} = 4.25 x_N^A \tag{3.23}$$

According to this expression, nitric acid is only soluble in the organic phase if nitrobenzene exists in solution which agrees with experimental data from Schiefferle et al. (1976).

Schiefferle et al. (1976) only observed a slight increase (less than 10%) of the solubility of nitric acid in the organic phase with increasing of temperature from 5 °C to 55 °C. Therefore, for simulation purposes, it will be assumed that the distribution of nitric acid between both phases is independent on temperature.

Figure 3.9 shows the calculated ratio between nitric acid and nitrobenzene molar fraction in the organic phase as a function of the nitric acid molar fraction in the aqueous phase (Equation (3.23)). Experimental data of Schiefferle et al. (1976) were also plotted and are in good agreement with the expression proposed by Biggs and White (1956).

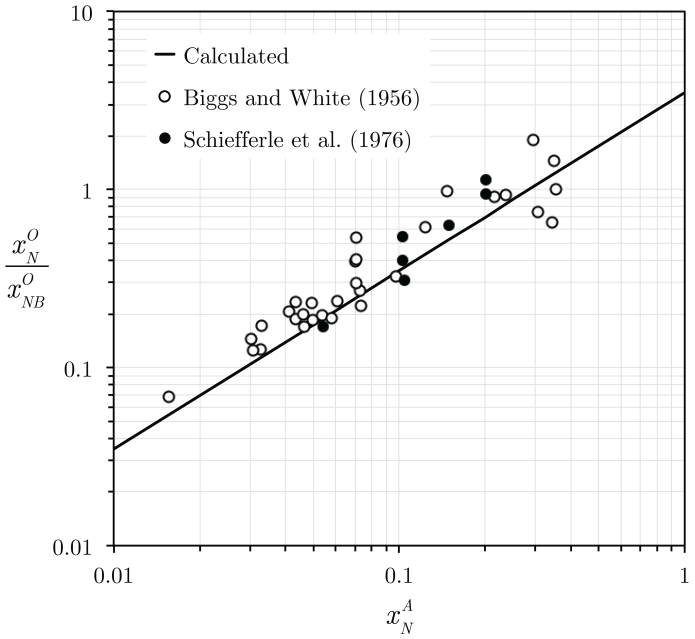


Figure 3.9 Ration between nitric acid and nitrobenzene molar fraction in the organic phase as a function of the nitric acid molar fraction in the aqueous phase. Experimental data from Biggs and White (1956) and Schiefferle et al. (1976).

Biggs and White (1956) state that the accuracy of the data upon which Figure 3.8 is based is not high, but that the correlation in Equation (3.23) should be useful for the purposes of estimating the influence of both the nitric acid and the nitrobenzene molar fraction.

3.4.2 Physical Properties

3.4.2.1 Molar mass

Table 3.5 lists the molar mass of all the components involved in the benzene nitration (Daubert and Danner, 1994).

Table 3.5. Molar mass of nitration compounds.

Compound	$M\left(\mathrm{g/mol}\right)$
Nitric Acid	63.0
Sulfuric Acid	98.1
Water	18.0
Benzene	78.1
Nitrobenzene	123.1

3.4.2.2 Density

The density, ρ in $\mathrm{kg/m^3}$, of each nitration compound was calculated using

$$\rho = ab^{-\left(1+\left(1-\frac{T}{c}\right)^d\right)}M \tag{3.24}$$

where the coefficients a, b, c and d are data fitting coefficients of the fitting, T is the temperature in K and M is the molar mass in mol/kg.

Table 3.6 shows the coefficients used to estimate the density of the nitration species. Predictions from DIPPR (2009).

Table 3.6. Coefficients to estimate the density of nitration compounds

Compound	$T_{\min}(\mathrm{K})$	$T_{\max}(\mathrm{K})$	a	b	c	d
Nitric Acid	231.6	373.2	1.59	0.230	520	0.193
Sulfuric Acid	284.5	610.0	1.45	0.265	924	0.271
Water	273.2	647.1	4.97	0.278	647	0.187
Benzene	278.7	562.1	1.03	0.267	562	0.284
Nitrobenzene	278.9	719.0	0.691	0.241	719	0.281

The density for each phase can be calculated by

$$\rho^O = \left(\sum_i^{B,N,NB} \frac{w_i}{\rho_i}\right)^{-1} \tag{3.25}$$

and

$$\rho^A = \left(\sum_i^{B,N,S,W} \frac{w_i}{\rho_i}\right)^{-1} \tag{3.26}$$

where ρ^O is the density of the organic phase, ρ^A is the density of the aqueous phase and w_i and ρ_i are the mass fraction and density of compound i, respectively. The average density of the mixture, ρ_{mix} can be estimated by

$$\rho_{mix} = \varepsilon\rho^O + \left(1-\varepsilon\right)\rho^A \tag{3.27}$$

where ε is the volume fraction of the organic phase (Santos, 2005).

3.4.2.3 Heat Capacity

The molar heat capacity, c_P in $\mathrm{J/kmol\cdot K}$, of each nitration compound was calculated using

$$c_P = a + bT + cT^2 + dT^3 + eT^4 \tag{3.28}$$

where T is the temperature in K and a, b, c, d and e are data fitting coefficients.

Table 3.7 shows the coefficients used to estimate the liquid heat capacity of all the nitration compounds (DIPPR, 2009).

Table 3.7. Coefficients to estimate the liquid heat capacity of nitration compounds.

Compound	$T_{\min}\left(\mathrm{K}\right)$	$T_{\max}\left(\mathrm{K}\right)$	a	b	c	d	e
Nitric Acid	238.6	302.9	1.31×10^{5}	-122	0.170	0	0
Sulfuric Acid	298.0	610.0	5.98×10^{4}	395	-0.521	3.12×10^{4}	-7.06×10^{-8}
Water	273.2	533.2	2.76×10^{5}	-2090	8.13	-1.41×10^{-2}	9.37×10^{-6}
Benzene	278.7	500.0	1.63×10^{5}	-345	0.856	0	0
Nitrobenzene	278.9	484.0	2.95×10^{5}	-891	1.71	0	0

3.4.2.4 Viscosity

The viscosity, μ in $\mathrm{Pa \cdot s}$, of each nitration compound can be determined by

$$\mu = \exp\left(a + \frac{b}{T} + c \ln T\right) \tag{3.29}$$

where a, b and c are data fitting coefficients, T is the temperature in K.

Table 3.8 shows the coefficients used to estimate the density of the nitration species. Predictions from DIPPR (2009).

Table 3.8. Coefficients to estimate the liquid viscosity of nitration compounds.

Compound	$T_{\min}(\mathrm{K})$	$T_{\max}(\mathrm{K})$	a	b	c
Nitric Acid	273.2	367.9	-28.9	1.94×10^3	2.68
Sulfuric Acid	273.1	610.0	-13.3	2.86×10^3	0
Water	273.2	646.2	-52.8	3.70×10^3	5.87
Benzene	278.7	545.0	7.51	2.48×10^3	-2.79
Nitrobenzene	273.2	480.8	-34.6	294	3.42

The viscosity for each phase, can be determined by

$$\log \mu^O = \sum_i^{B,N,NB} w_i \log \mu_i \tag{3.30}$$

and

$$\log \mu^A = \sum_i^{B,N,S,W} w_i \log \mu_i \tag{3.31}$$

where μ^O is the density of the organic phase, μ^A is the density of the aqueous phase and w_i and μ_i are the mass fraction and viscosity of compound i, respectively.

Zaldivar et al. (1995) proposes a correction for the viscosity of the aqueous phase with a polynomial expression obtained from experimental data,

$$\mu_{corr}^{A} = 9.68\times10^{-3} - 2.52\mu^{A} + 3.15\times10^{-10}\left(\mu^{A}\right)^{2} \tag{3.32}$$

3.4.3 Unit Cell Mass Balance

Each unit cell is assumed to behave as a perfectly mixed continuous stirred tank in steady state conditions. The two inlet streams are joined in a single pre-mixed inlet stream to reduce the number of variables in the system of equations as explained further in Section 3.4.5. Molar balance equations of each component are solved individually for each unit cell of NETmix. At the same time, the distribution of benzene and nitric acid between both phases is estimated. It is considered that the volumetric flow rate in the network is constantly and equally divided between the outlets of each the unit cell.

The molar balance equations for each unit cell are given by

$$F_{B,in}^{O} - F_{B,out}^{O} = F_{B,out}^{A} - F_{B,in}^{A} + k_{r}\frac{F_{B,out}^{O}}{Q^{O}}\frac{F_{N,out}^{A}}{Q^{A}}\left(1-\varepsilon\right)V_{uc} \tag{3.33}$$

$$F_{N,in}^{O} - F_{N,out}^{O} = F_{N,out}^{A} - F_{N,in}^{A} + k_{r}\frac{F_{B,out}^{O}}{Q^{O}}\frac{F_{N,out}^{A}}{Q^{A}}\left(1-\varepsilon\right)V_{uc} \tag{3.34}$$

$$F_{W,in}^{A} = F_{W,out}^{A} - k_{r}\frac{F_{B,out}^{O}}{Q^{O}}\frac{F_{N,out}^{A}}{Q^{A}}\left(1-\varepsilon\right)V_{uc} \tag{3.35}$$

$$F_{NB,in}^{O} = F_{NB,out}^{O} - k_{r}\frac{F_{B,out}^{O}}{Q^{O}}\frac{F_{N,out}^{A}}{Q^{A}}\left(1-\varepsilon\right)V_{uc} \tag{3.36}$$

where F refers to the molar flow rate of each species, Q refers to the volumetric flow rate, and V_{uc} is the volume of the unit cell where the reaction occurs. Subscript in represents the inlet stream and subscript out the outlet.

Since sulfuric acid only acts as the catalyst, its molar flow rate remains unchanged during reaction,

$$F^{A}_{S,out} = F^{A}_{S,in}. \tag{3.37}$$

Mass transfer limitations between the organic and the aqueous phase are assumed to be negligible, since the degree of mixing is considered to be high enough to overcome the existence of a stagnant film near the interface. Consequently, immediate equilibrium between phases is assumed.

The solubility of benzene in the aqueous phase is calculated, as shown in Section 3.4.1.1 throughout Equations (3.19) to (3.22), by

$$\frac{F^{A}_{B,out}}{Q^{A}} = m_{B}\left(x^{A}_{N}, x^{A}_{S}, T_{out}\right)\frac{F^{O}_{B,out}}{Q^{O}} \tag{3.38}$$

where m_B is the partition coefficient of benzene in each phase and is a function of the temperature and of the molar fractions of nitric and sulfuric acid in the aqueous phase.

The distribution of nitric acid is estimated as shown in Section 3.4.1.2 by

$$F^{O}_{N,out} = 4.25 x^{A}_{N} F^{O}_{NB,out} \tag{3.39}$$

Since the temperature changes along the reactor as well as the composition of the phases due to the progress of the reaction, for each unit cell, the change of flow rates in both phases must be taken into account,

$$Q^{O} = F^{O}_{B,out}\frac{M_B}{\rho_B} + F^{O}_{N,out}\frac{M_N}{\rho_N} + F^{O}_{NB,out}\frac{M_{NB}}{\rho_{NB}} \tag{3.40}$$

and

$$Q^{A} = F^{A}_{B,out}\frac{M_B}{\rho_B} + F^{A}_{N,out}\frac{M_N}{\rho_N} + F^{A}_{S,out}\frac{M_S}{\rho_S} + F^{A}_{W,out}\frac{M_W}{\rho_W}. \tag{3.41}$$

3.4.4 Unit Cell Energy Balance

The energy balance for adiabatic operation takes into account the enthalpy flow rate change from the inlet to the outlet of the unit cell caused by the temperature rise due to reaction and effects of dilution. The energy balance is given by

$$\dot{H}_{in}^{O} + \dot{H}_{in}^{A} = \dot{H}_{out}^{A} + \dot{H}_{out}^{O} + \Delta H_{r}\left(T_{out}\right) k_{r}\left(T_{out}\right) \frac{F_{B,out}^{O}}{Q^{O}} \frac{F_{N,out}^{A}}{Q^{A}} \left(1-\varepsilon\right) V_{uc} + \Delta \dot{H}_{d} \tag{3.42}$$

where ΔH_{r} is the enthalpy of reaction and $\Delta \dot{H}_{d}$ is the heat flow rate due to dilution. $\dot{H}_{in}^{O}$ and $\dot{H}_{in}^{A}$ are the hentalpy flow rate of the organic and aqueous phase at the inlet, respectively, and $\dot{H}_{out}^{O}$ and $\dot{H}_{out}^{A}$ are the hentalpy flow rate of the organic and aqueous phase at the outlet, respectively, and are defined as

$$\dot{H}_{in}^{O} = \sum_{i}^{B,NB,N} F_{i,in}^{O} c_{P_i}\left(T_{in}\right) T_{in} \tag{3.43}$$

$$\dot{H}_{out}^{O} = \sum_{i}^{B,NB,N} F_{i,out}^{O} c_{P_i}\left(T_{out}\right) T_{out} \tag{3.44}$$

$$\dot{H}_{in}^{A} = \sum_{i}^{B,N,S,W} F_{i,in}^{O} c_{P_i}\left(T_{in}\right) T_{in} \tag{3.45}$$

$$\dot{H}_{out}^{A} = \sum_{i}^{B,N,S,W} F_{i,out}^{O} c_{P_i}\left(T_{out}\right) T_{out} \tag{3.46}$$

3.4.5 Numerical Implementation

In this section is shown the numerical implementation of the mass and energy balance system of equations to solve the nitration of benzene throughout the all NETmix reactor network. The mathematical formulation to model the heterogeneous nitration reaction in a NETmix Reactor was implemented in VBA language code. The input and output of data is done through a Microsoft® Excel worksheet.

The mass and energy balances result in a system of non-linear equations to be solved for each unit cell. Since it is considered that the volumetric flow rate in the network is constantly and equally divided between the outlets of each the unit cell, each row can be solved recursively in the flow direction by knowing the information of the previous rows. Figure 3.10 shows a scheme of the interconnection of generic unit cells. Unit cell $\left[i,j\right]$ is fed by the two interconnected unit cells in the previous row: unit cell $\left[i-1,j\right]$ through the Inlet 1 channel; and unit cell $\left[i-1,j+1\right]$ through the Inlet 2 channel.

The total flow of unit cell $\left[i,j\right]$ is equally divided between the Outlet 1 channel and the Outlet 2 channel. Outlet 1 is fed to unit cell $\left[i+1,j\right]$ and Outlet 2 to unit cell $\left[i+1,j+1\right]$.

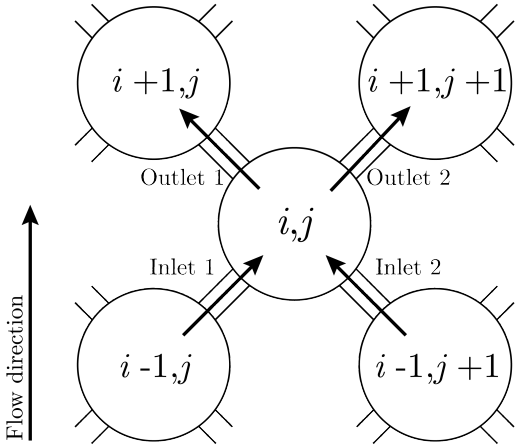


Figure 3.10. Scheme of the interconnection of unit cells.

To reduce the number of variables in the molar and energy balance equations, a pre-mixed flow is fed to each unit cell resulting from the junction of the flow of the two inlets. The molar flow rate in the outlet is then equally divided between the outlets of the unit cell (Figure 3.11).

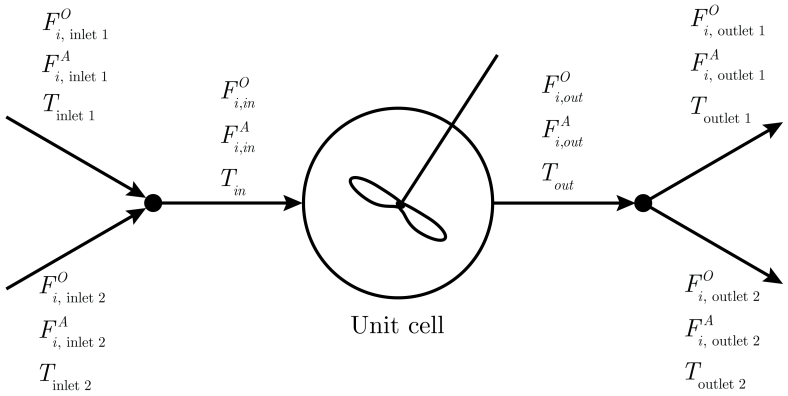


Figure 3.11 Pre-mixed flow in the inlet of each unit cell and flow splitting.

For each component i, the inlet molar flow rate in each phase is given by

$$F^O_{i,in} = F^O_{i,\text{ inlet 1}} + F^O_{i,\text{ inlet 2}} \tag{3.47}$$

and

$$F^A_{i,in} = F^A_{i,\text{ inlet 1}} + F^A_{i,\text{ inlet 2}}. \tag{3.48}$$

The energy balance of the combination of both streams is given by

$$\dot{H}^O_{\text{inlet 1}} + \dot{H}^O_{\text{inlet 2}} + \dot{H}^A_{\text{inlet 1}} + \dot{H}^A_{\text{inlet 2}} = \dot{H}^O_{in} + \dot{H}^A_{in} \tag{3.49}$$

or expanding the enthalpy flow rate terms,

$$\begin{aligned}
&\sum_i^{B,NB,N} F^O_{i,\text{ inlet 1}} c_{P_i}\left(T_{\text{inlet 1}}\right)T_{\text{inlet 1}} + \sum_i^{B,N,S,W} F^A_{i,\text{ inlet 1}} c_{P_i}\left(T_{\text{inlet 1}}\right)T_{\text{inlet 1}} + \\
&\sum_i^{B,NB,N} F^O_{i,\text{ inlet 2}} c_{P_i}\left(T_{\text{inlet 2}}\right)T_{\text{inlet 2}} + \sum_i^{B,N,S,W} F^A_{i,\text{ inlet 2}} c_{P_i}\left(T_{\text{inlet 2}}\right)T_{\text{inlet 2}} = \\
&\sum_i^{B,NB,N} F^O_{i,in} c_{P_i}\left(T_{in}\right)T_{in} + \sum_i^{B,N,S,W} F^A_{i,in} c_{P_i}\left(T_{in}\right)T_{in}
\end{aligned} \tag{3.50}$$

Equation (3.49) is solved iteratively to find T_{in}.

At the outlet, the total stream is divided evenly for each outlet stream of the unit cell,

$$F^{O}_{i,\,\text{outlet 1}} = F^{O}_{i,\,\text{outlet 2}} = F^{O}_{i,out} / 2 \tag{3.51}$$

and

$$F^{A}_{i,\,\text{outlet 1}} = F^{A}_{i,\,\text{outlet 2}} = F^{A}_{i,out} / 2. \tag{3.52}$$

The temperature of the two outlet streams is equal to the temperature of the unit cell,

$$T_{\text{outlet 1}} = T_{\text{outlet 2}} = T_{out}. \tag{3.53}$$

The necessary inlet parameters to solve the non-linear system of equations for each unit cell are $F^{O}_{B,in}$, $F^{A}_{B,in}$, $F^{O}_{N,in}$, $F^{A}_{N,in}$, $F^{A}_{S,in}$, $F^{A}_{W,in}$, $F^{O}_{NB,in}$ and T_{in} and the system unknowns are $F^{O}_{B,out}$, $F^{A}_{B,out}$, $F^{O}_{N,out}$, $F^{A}_{N,out}$, $F^{A}_{S,out}$, $F^{A}_{W,out}$, $F^{O}_{NB,out}$ and T_{out}.

Since the system of non-linear equations is solved iteratively, it is necessary to estimate an initial guess for the solution of the system. The initial guess for the molar flow rates unknowns is given by

$$\begin{cases} F^{O}_{B,out} = F^{O}_{B,in} - \varphi_F F_{L.R.} \\ F^{A}_{B,out} = 10^{-2} F^{O}_{B,out} \\ F^{O}_{N,out} = 0 \\ F^{A}_{N,out} = F^{A}_{N,in} - \varphi_F F_{L.R.} \\ F^{A}_{S,out} = F^{A}_{S,in} \\ F^{A}_{W,out} = F^{A}_{W,in} + \varphi_F F_{L.R.} \\ F^{O}_{NB,out} = F^{O}_{NB,in} + \varphi_F F_{L.R.} \end{cases} \tag{3.54}$$

where φ_F is the initial condition parameter for the molar flow rates and $F_{L.R.}$ is the molar flow rate of the limiting reactant and is defined as

$$F_{L.R.} = \begin{cases} F^{A}_{N,in}, & F^{O}_{B,in} \Big/ F^{A}_{N,in} > 1 \\ F^{O}_{B,in}, & F^{O}_{B,in} \Big/ F^{A}_{N,in} < 1 \end{cases} \tag{3.55}$$

An estimative of the outlet temperature is obtained by

$$T_{out} = T_{in} + \varphi_{T}\left(T_{\max} - T_{in}\right) \tag{3.56}$$

where φ_{T} is the initial condition parameter for the temperature and $T_{\max}$ is the maximum temperature that can be achieved at the outlet of the unit cell assuming total conversion.

To estimate $T_{\max}$, the energy balance for the unit cell is solved assuming total conversion of the limiting reactant. Effects of dilution are neglected and constant heat capacities and heat of reaction evaluated for the inlet temperature are considered. The energy balance is given by

$$\dot{H}^{O}_{in} + \dot{H}^{A}_{in} \approx \dot{H}^{O}_{in} + \dot{H}^{A}_{in} - \Delta H_{r}\left(T_{in}\right) F_{L.R.}. \tag{3.57}$$

The enthalpy flow rate at the inlet can outlet for each phase is given by

$$\dot{H}^{O}_{in} = F^{O}_{B,in} c_{P_B}\left(T_{in}\right) T_{in} + F^{O}_{N,in} c_{P_N}\left(T_{in}\right) T_{in} + F^{O}_{NB,in} c_{P_{NB}}\left(T_{in}\right) T_{in} \tag{3.58}$$

$$\dot{H}^{A}_{in} = F^{A}_{B,in} c_{P_B}\left(T_{in}\right) T_{in} + F^{A}_{N,in} c_{P_N}\left(T_{in}\right) T_{in} + F^{A}_{S,in} c_{P_S}\left(T_{in}\right) T_{in} + F^{A}_{W,in} c_{P_W}\left(T_{in}\right) T_{in} \tag{3.59}$$

$$\dot{H}^{O}_{out} \approx \left[\left(F^{O}_{B,in} - F_{L.R.}\right) c_{P_B}\left(T_{in}\right) + \left(F^{O}_{NB,in} + F_{L.R.}\right) c_{P_{NB}}\left(T_{in}\right)\right] T_{\max} \tag{3.60}$$

$$\dot{H}^{A}_{out} \approx \left[\left(F^{A}_{N,in} - F_{L.R.}\right) c_{P_N}\left(T_{in}\right) + F^{A}_{S} c_{P_S}\left(T_{in}\right) + \left(F^{A}_{W,in} + F_{L.R.}\right) c_{P_W}\left(T_{in}\right)\right] T_{\max} \tag{3.61}$$

Rearranging Equation (3.57), the maximum temperature can be approximately calculated by

$$T_{\max} \approx \frac{\dot{H}_{in}^{O} + \dot{H}_{in}^{A} + \Delta H_r F_{L.R.}}{\zeta_{out}^{O} + \zeta_{out}^{A}} \tag{3.62}$$

where ζ_{out}^{O} and ζ_{out}^{A} are defined as

$$\zeta_{out}^{O} = \left(F_{B,in}^{O} - F_{L.R.}\right) c_{P_B}\left(T_{in}\right) + \left(F_{NB,in}^{O} + F_{L.R.}\right) c_{P_{NB}}\left(T_{in}\right) \tag{3.63}$$

and

$$\zeta_{out}^{A} = \left(F_{N,in}^{A} - F_{L.R.}\right) c_{P_N}\left(T_{in}\right) + F_S^A c_{P_S}\left(T_{in}\right) + \left(F_{W,in}^{A} + F_{L.R.}\right) c_{P_W}\left(T_{in}\right). \tag{3.64}$$

It was verified that the system is extremely sensitive to the molar fraction of nitric acid that is used in the kinetic rate constant. Large variations on this value while solving the system of equations may cause the solution to diverge. To overcome that, a strategy of maintaining the value of molar fraction of nitric acid constant while solving the system of equations was used. When a solution to the system of equations is found, a new estimative for the nitric acid molar fraction is used and the system is continuously solved iteratively until the convergence of the nitric acid molar fraction, which will give the true kinetic rate constant.

The final solution is found when the relative deviation of molar fraction of nitric acid, $x_{N,est}$, from two consecutive iterations is lower than 10^{-6},

$$\left| \frac{x_{N,est}^{(i)} - x_{N,est}^{(i-1)}}{x_{N,est}^{(i)}} \right| < 10^{-6} \tag{3.65}$$

where i is the number of the iteration. The first guess for the molar mass fraction of nitric acid is given by

$$x_{N,est}^{(0)} = \varphi_{x_N} x_{N,in}^{A} \tag{3.66}$$

where φ_{x_N} is the initial condition parameter for the nitric acid molar fraction. The new guess for the molar fraction of nitric acid is given by

$$x_{N,est}^{(i)} = \varphi_{iter} x_{N,est}^{(i-1)} + \left(1-\varphi_{iter}\right) x_N^A \tag{3.67}$$

where φ_{iter} is an under-relaxation parameter used to avoid divergence of the solution by sudden change of the molar fraction of nitric acid. If possible, $\varphi_{iter} = 0$ is used to accelerate convergence.

Following this methodology, the kinetic rate constant is determined as

$$k_r = k_0 \exp\left(\frac{-E_a}{RT}\right) \exp\left[\alpha_1 \left(x_{N,est}^{(i)} + \alpha_2 x_S^A\right)\right]. \tag{3.68}$$

The values of $\varphi_F = 0.7$, $\varphi_T = 0.5$ and $\varphi_{x_N} = 0.5$ were observed to provide a good initial guess to solve the system of equations for most of the runs.

The complete non-linear system of equations to be solved is

$$\begin{cases} \dfrac{F_{B,out}^A}{Q^A} - m_B\left(x_N^A, x_S^A, T_{out}\right)\dfrac{F_{B,out}^O}{Q^O} = 0 \\ F_{N,out}^O - 4.25 x_N^A F_{NB,out}^O = 0 \\ F_{B,out}^O + F_{B,out}^A - F_{B,in}^O - F_{B,in}^A + k_r\left(x_{N,est}^{(i)}, x_S^A, T_{out}\right)\dfrac{F_{B,out}^O}{Q^O}\dfrac{F_{N,out}^A}{Q^A}\left(1-\varepsilon\right)V_{uc} = 0 \\ F_{N,out}^O + F_{N,out}^A - F_{N,in}^O - F_{N,in}^A + k_r\left(x_{N,est}^{(i)}, x_S^A, T_{out}\right)\dfrac{F_{B,out}^O}{Q^O}\dfrac{F_{N,out}^A}{Q^A}\left(1-\varepsilon\right)V_{uc} = 0 \\ F_{S,out}^A = F_{S,in}^A \\ F_{W,out}^A - F_{W,in}^A - k_r\left(x_{N,est}^{(i)}, x_S^A, T_{out}\right)\dfrac{F_{B,out}^O}{Q^O}\dfrac{F_{N,out}^A}{Q^A}\left(1-\varepsilon\right)V_{uc} = 0 \\ F_{NB,out}^O - F_{NB,in}^O - k_r\left(x_{N,est}^{(i)}, x_S^A, T_{out}\right)\dfrac{F_{B,out}^O}{Q^O}\dfrac{F_{N,out}^A}{Q^A}\left(1-\varepsilon\right)V_{uc} = 0 \\ \dot{H}_{out}^A + \dot{H}_{out}^O - \dot{H}_{in}^A - \dot{H}_{in}^O + \Delta H_r k_r\left(x_{N,est}^{(i)}, x_S^A, T_{out}\right)\dfrac{F_{B,out}^O}{Q^O}\dfrac{F_{N,out}^A}{Q^A}\left(1-\varepsilon\right)V_{uc} + \Delta\dot{H}_d = 0 \end{cases} \tag{3.69}$$

where the enthalpy flow rate terms, heat of reaction, heat flow rate of dilution, kinetic rate constant, partition coefficients, hold-up fraction and flow rates are all function of the composition of the stream and temperature.

The system is solved by using the Newton method for non-linear equations incorporating Gaussian elimination to solve the approximated linearized system.

Figure 3.12 summarizes the algorithm used to solve the benzene nitration reaction for each unit cell.

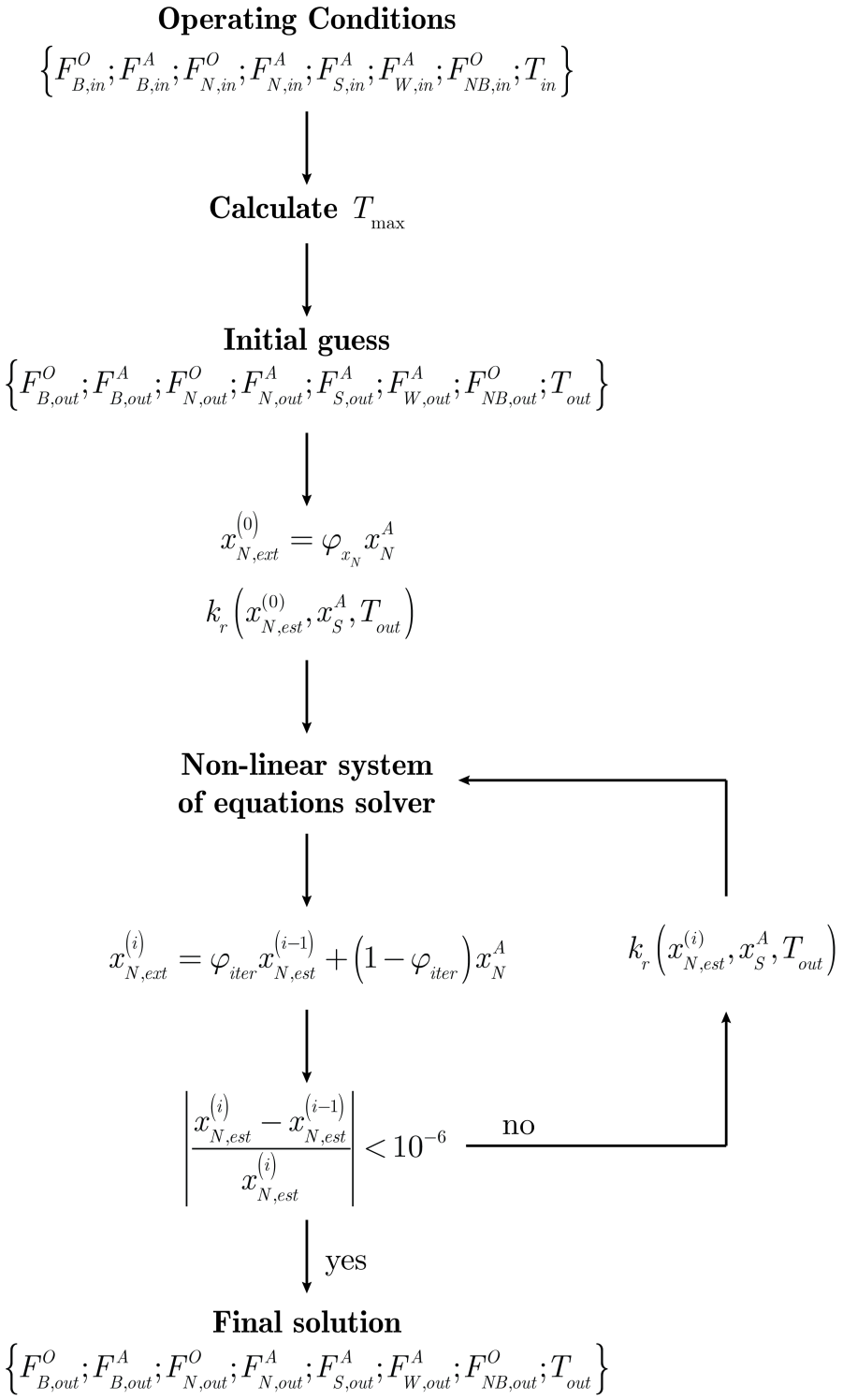


Figure 3.12 Algorithm used to solve the benzene nitration reaction for each unit cell.

3.5 Model Validity

3.5.1 Comparison with Published Data

The simulator was adapted to calculate the nitrobenzene conversion in a single CSTR and compared to the experimental results of Biggs and White (1956) and Santos (2005). Both works study the effects of agitation, phase composition, phase ratio and temperature on the rate of nitration of benzene.

Biggs and White (1956) used a cylindrical Pyrex glass reactor that was designed to maintain a uniform emulsion of the aqueous and organic phases and a high degree of circulation of the contents. A 316 stainless steel stirrer shaft with three propellers equally spaced of four blades where used. With exception of the stirrer assembly in the reactor, all the apparatus was constructed of glass. This study comprises a wide range of mass fraction of nitric and sulfuric acid, hold up fractions and molar ratios of benzene and nitric acid and temperature was kept constant. Also, the resistance terms to the mass transfer were made sufficiently small to eliminate the stirrer speed as a variable affecting the reaction rate, which was observed for impeller speeds higher than 2200 rpm. The experimental conditions used are summarized in Table 3.9.

Table 3.9. Operating conditions used by Biggs and White (1956).

Temperature of nitration	$34.7 - 53.7$ °C
Impeller speed	$2200 - 2810$ rpm
Holdup fraction	$0.21 - 0.75$
Molar ratio of benzene and nitric acid	$0.37 - 6.1$
Residence time	$19 - 40$ min
Mass fraction of sulfuric acid	$0 - 0.60$
Mass fraction of nitric acid	$0.09 - 0.69$
Volume	$300 - 400\,\mathrm{cm}^3$

Results from experimental data and simulation were compared in terms of total conversion of the limiting reactant into nitrobenzene,

$$X = \frac{F_{NB,out}^{O}}{F_{L.R.}} \tag{3.70}$$

where $F_{L.R.}$ is the molar flow rate of the limiting reactant. The conversion obtained experimentally is well predicted with 15% of deviation as can be seen in Figure 3.13.

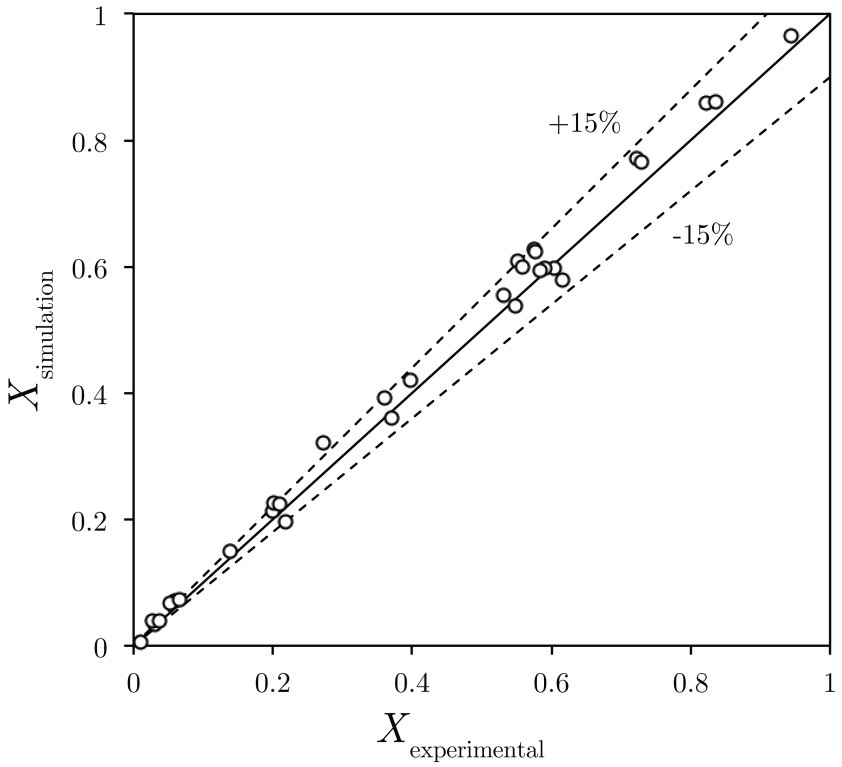


Figure 3.13 Comparison of experimental data (Biggs and White, 1956) and simulation results using the isothermal solver of conversion of benzene.

Santos (2005) used a glass reactor with 95 mm of diameter and 151 mm in height and with a total volume of 1060 cm^3. The reactor was kept insulated to ensure adiabatic operation. Four baffles were placed inside the reactor and two types of impellers were used with two or four blades. Both the baffles as the impellers were made of tantalum to avoid corrosion.

The operating conditions used by Santos (2005) are summarized in Table 3.10.

Table 3.10. Operating conditions used by Santos (2005).

Temperature of nitration	$80-135$ °C
Mixed acid flow temperature	$58-103$ °C
Impeller speed	$390-1700$ rpm
Holdup fraction	$0.13-0.18$
Molar ratio of benzene and nitric acid	$0.9-1.15$
Residence time	$2-6$ min
Mass fraction of sulfuric acid	$0.57-0.69$
Mass fraction of nitric acid	$0.026-0.064$
Volume	1060 cm^3

Experimental results are divided into two groups. Group 1 includes experimental results where the impeller speed was varied. Experimental results from Group 2 were run at a constant impeller speed of approximately 1200 rpm while changing the other operating conditions.

When experimental results from Group 1 are compared to the simulation results, it is observed that better predictions are achieved with increasing impeller speeds (see Figure 3.14). This is due to the reduction of the mass transfer limitations that are not considered in this simulator.

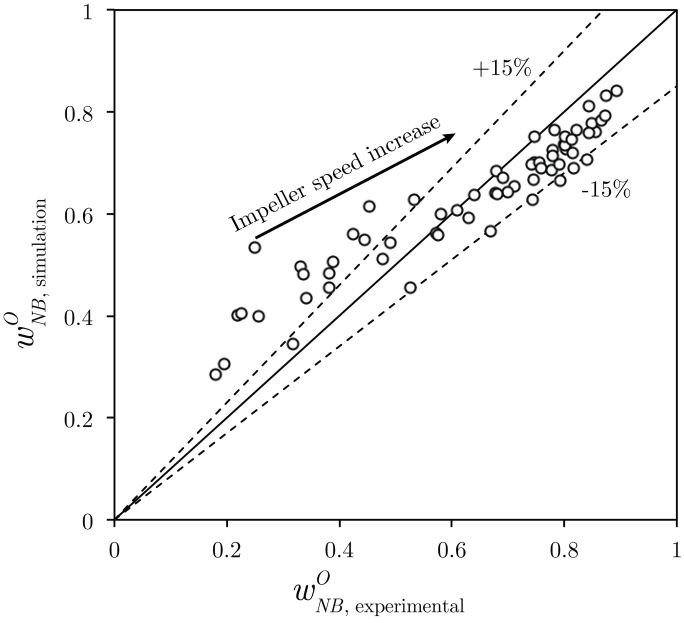


Figure 3.14 Comparison of experimental data (Santos, 2005) and simulation results of mass fraction of nitric acid in the aqueous phase with increasing impeller speed.

If experimental results from Group 2 are compared to the simulation results, the majority of the experimental data presents deviations lower than 15% as can be seen in Figure 3.15.

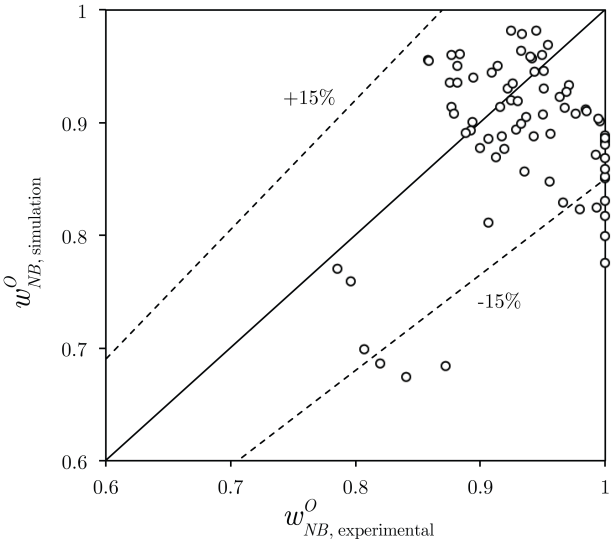


Figure 3.15 Comparison of experimental data (Santos, 2005) and simulation results of mass fraction of nitric nitrobenzene in the organic phase.

The temperature of nitration can also be predicted with a maximum deviation of 15% as shown in Figure 3.16.

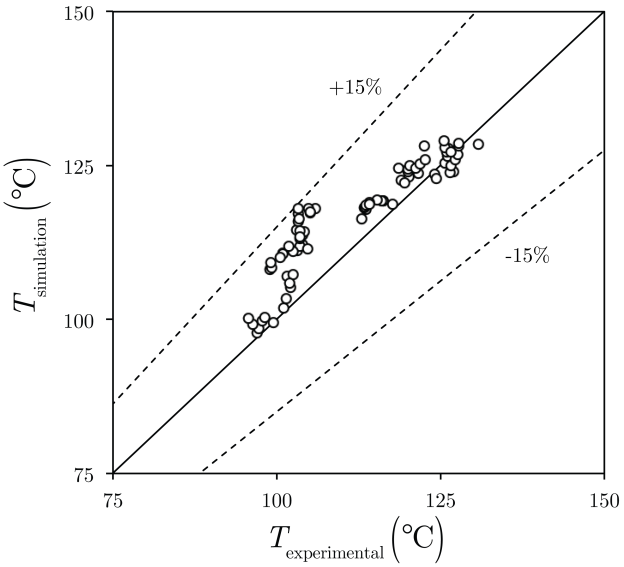


Figure 3.16 Comparison of experimental data (Santos, 2005) and simulation results of temperature of nitration.

It can be concluded that the developed model for the nitration reaction that comprises four fitting parameters and considers no diffusional limitations is also capable to predict the formation of nitrobenzene and the outlet temperature in

adiabatic operation within 15% of deviation for the operational conditions used Santos (2005), operational conditions in the range of interest in industrial operation, if stirring speed is high enough so diffusional limitation can be neglected.

3.5.2 Power Number Comparison

The experimental works of Biggs and White (1956) and Santos (2005) used different reactors and impeller speeds meaning that the mixing conditions were probably not the same in both situations. To compare them, the power dissipated by the impeller per unit volume was calculated.

The power used by the impeller, P, in these two experimental sets was estimated by

$$P = N_P \rho N^3 D_{impeller}^5 \tag{3.71}$$

where N_P is the power number, N is the rotational speed and $D_{impeller}$ is the impeller diameter (Hemrajani and Tatterson, 2003).

For these calculations, it was considered a fluid with density of $1400\,\mathrm{kg/m^3}$ and viscosity of $0.006\,\mathrm{Pa \cdot s}$, characteristic of a mixed acid stream.

Table 3.11 summarizes the mixing conditions used by Biggs and White (1956) and Santos (2005) and the calculated value of dissipated power per unit volume.

Table 3.11. Mixing conditions for the experimental data of Biggs and White (1956) and Santos (2005).

	Biggs and White (1956)	Santos (2005)
$D_{impeller}$ (m)	0.046	0.054
$N_{\max}$ $\left(\mathrm{s}^{-1}\right)$	37	28
Re	2.7×10^{4}	1.8×10^{4}
N_P	4.6	5
P (W)	65	68
P/V $\left(\mathrm{kW/m}^3\right)$	187	64

Calculating the power per unit volume, Santos (2005) employs a 64 $\mathrm{kW/m}^3$ against 187 $\mathrm{kW/m}^3$ achieved by Biggs and White (1956). The fact that the Santos (2005) can not achieve the same power per unit volume with his setup as Biggs and White (1956), can explain the higher deviation of the experimental results to the simulation predictions. For the maximum impeller speed used by Santos (2005), the reaction regime achieved is still in an intermediate regime where chemical reactions and diffusional processes compete.

For the operation in NETmix reactor, the power used for mixing can be estimated from the pressure drop model developed in Section 2.2.1.1 of Chapter 2. In each unit cell, the power per unit volume was derived and is given by

$$\frac{P}{V_{uc}} = 2\frac{q_{channel}}{V_{uc}}\Delta p_{mixing} = \frac{\rho K A_{channel}}{V_{uc}}\overline{v}^{3}_{channel} \tag{3.72}$$

where V_{uc} is the volume of each unit cell of NETmix, Δp_{mixing} is the pressure drop caused by fluid motion inside the unit cell necessary for mixing , $q_{channel}$ is the flow rate in the channels, ρ is the density of the fluid, $A_{channel}$ is the cross-sectional area of the channel, $\overline{v}_{channel}$ is the average velocity in the channel and K is a coefficient equivalent to the loss coefficients for sudden contractions and expansions in piping systems and can vary in a range of 0.9 to 1.3 for the three studied NETmix reactors.

From this analysis it is possible to estimate the flow conditions that have to be set to ensure the same mixing conditions in NETmix as the experimental results of Biggs and White (1956), thus ensuring that mass transfer limitations can be neglected.

Assuming the same physical properties and a NETmix geometry with the dimensions of the Lab-Scale NETmix prototype (Table 3.12), the power used for mixing per unit volume was determined as a function the Reynolds number.

Table 3.12. Geometrical characteristics of the Lab-Scale NETmix 2D.

Geometry	Lab-Scale NETmix 2D
Number of rows, n_x	29
Number of columns, n_y	8
Chamber diameter, D (mm)	6.5
Channel diameter, d (mm)	1
Geometry depth, ω (mm)	3
Channel length, l (mm)	2
Total volume, V (mm)	23

This specific NETmix geometry has to operate at a Reynolds number around 570 to deliver the same power per unit volume inside each unit cell comparable to the experimental setup of Biggs and White (1956) (see Figure 3.17).

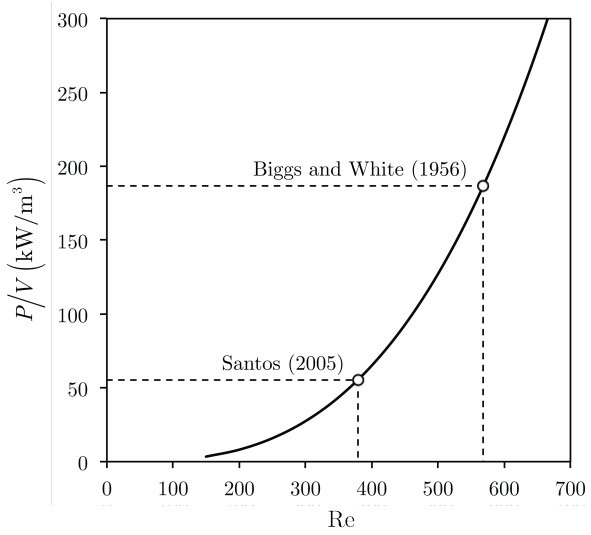


Figure 3.17 Dissipated power per unit volume.

3.6 NETmix Case Study Simulation

The study of the influence of the operating parameters was made considering a setup with lab scale dimensions. A study of the influence of the initial temperature of the reactants and the amount of sulfuric acid to the aqueous phase was performed.

Operational conditions of typical values used in industry where chosen (Barretta, 2011; Guenkel et al., 1994; Santos, 2005) and are shown in Table 3.13. Guenkel et al. (1994) suggest that a range of mass fractions of sulfuric acid between $64-72.5\%$ and a maximum mass fraction of nitric acid of 3% to be selected to increase the selectivity of the reaction by reducing the formation of by-products.

Table 3.13. Operational conditions used for simulation.

	Operational conditions
$T_{in}\left(^{\circ}\mathrm{C}\right)$	50–80
$F_B^O \,/\, F_N^A$	1.15
$\tau_{total}(\mathrm{s})$	1
ε	0.07
w_N^A	0.03
w_S^A	0.6–0.7

To ensure sufficient power per unit volume to overcome diffusional limitations and to have a reaction time inside the reactor of at least one second to ensure high conversion of benzene, two NETmix reactors with the Lab-scale NETmix 2D dimensions (see Table 3.12) must be coupled in series. Figure 3.18 shows a conceptual experimental setup used for simulations.

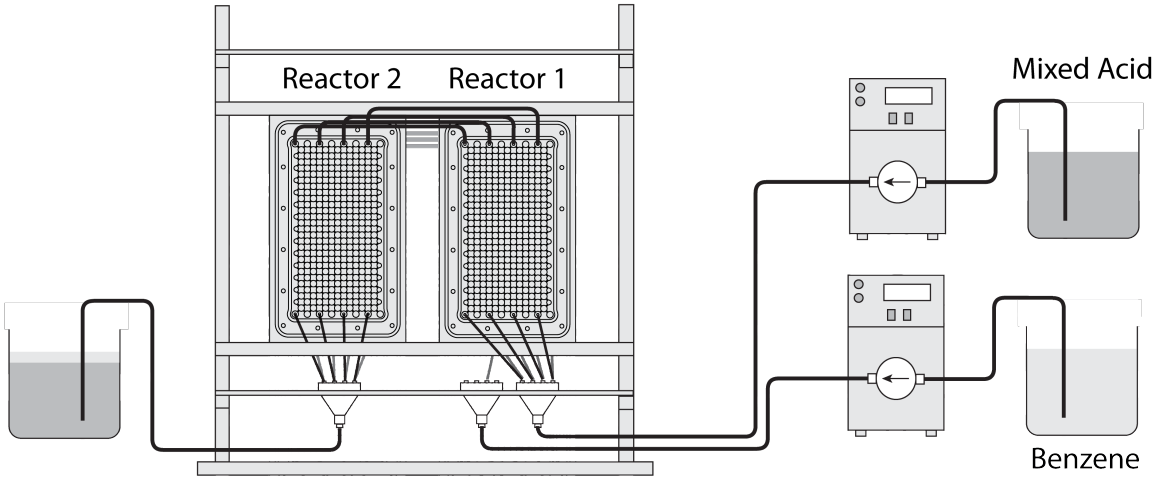


Figure 3.18. Conceptual experimental setup used in the simulations.

Inlet scheme 1 uses 1 inlet of organic phase and 7 inlets of aqueous phase as shown in Figure 3.19. Since the hold-up fraction, ε, is small, this inlet scheme keeps the flow rates more evenly distributed at each inlet of the reactor, $Q_{inlet}^{A} / Q_{inlet}^{O} = 1.9$.

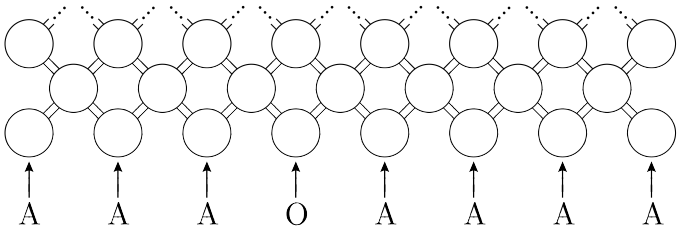


Figure 3.19. Inlet scheme 1.

A map of the results of the average final conversion and nitration temperature for the selected range of inlet temperatures and sulfuric acid mass fractions is shown in Figure 3.20. This analysis provides a way to select, for a given inlet temperature, the optimal amount of catalyst to be added to the aqueous phase to ensure high conversion.

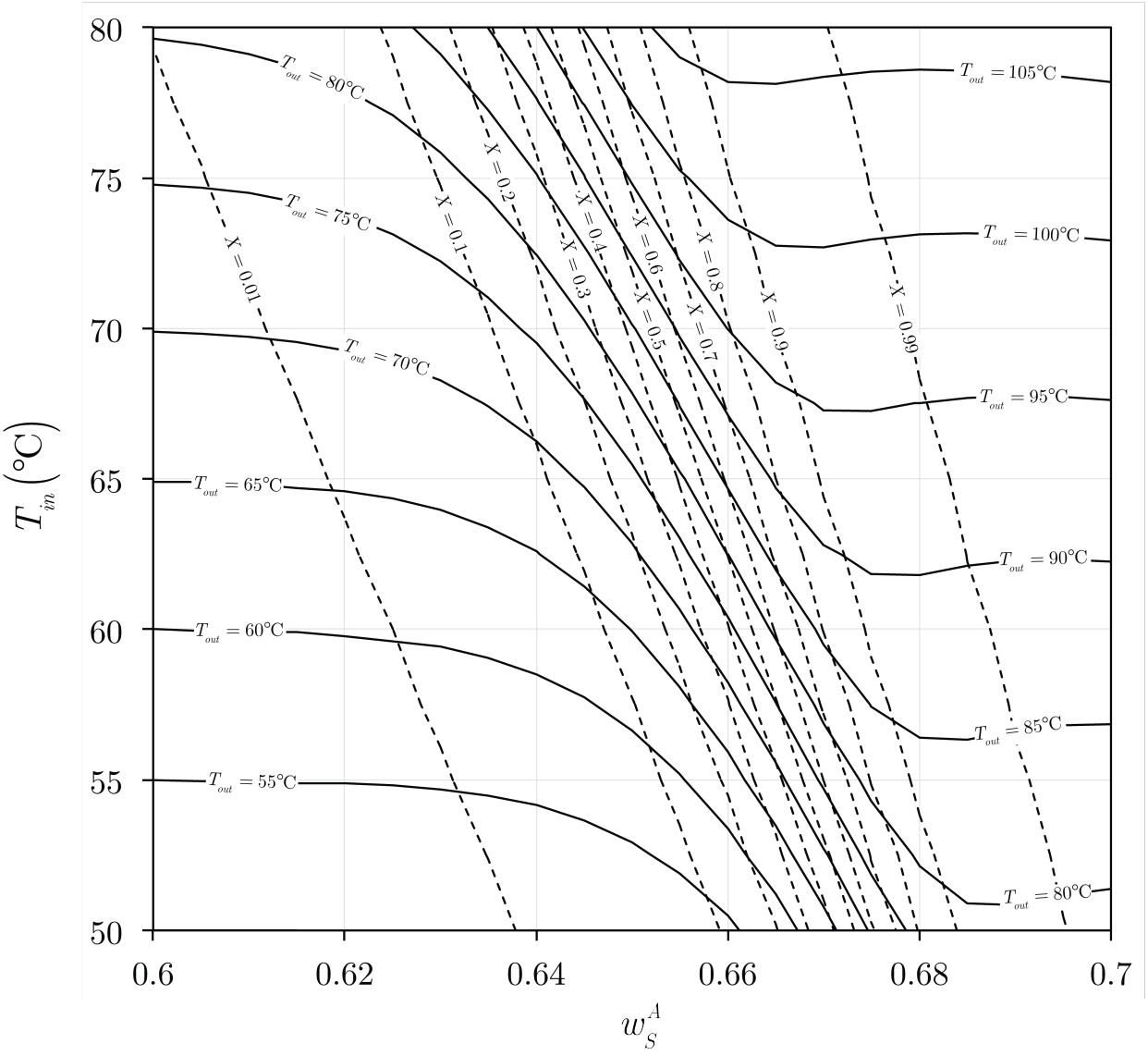


Figure 3.20. Isolines of conversion and outlet temperature as a function of the mass fraction of sulfuric acid and inlet temperature.

An adiabatic rise of temperature in a range of $25-30$°C is expected if conversion is complete. It can also be concluded that small changes in the mass fraction of sulfuric acid can change the final conversion drastically.

Furthermore, simulation results show that the right selection of operation conditions can lead to small reaction times with high conversions. This reduces the probability of formation of secondary products (Santos, 2005).

This simulation tool also allows to inspect the interior of the reactor and to evaluate the progression of the reaction and the temperature rise due to reaction and dilution effects, and in this way, to optimize the operation.

In Figure 3.21 and Figure 3.22 are represented the map of the ratio of molar flow rate of nitrobenzene and the limiting reactant and the map of the nitration temperature inside both reactors, respectively, for a simulation with operational conditions of Table 3.14.

Table 3.14. Operational conditions used for simulation.

	Operational conditions
$T_{in}\left(°C\right)$	70
$F_B^O \,/\, F_N^A$	1.15
$\tau_{total}(s)$	1
ε	0.07
w_N^A	0.03
w_S^A	0.66

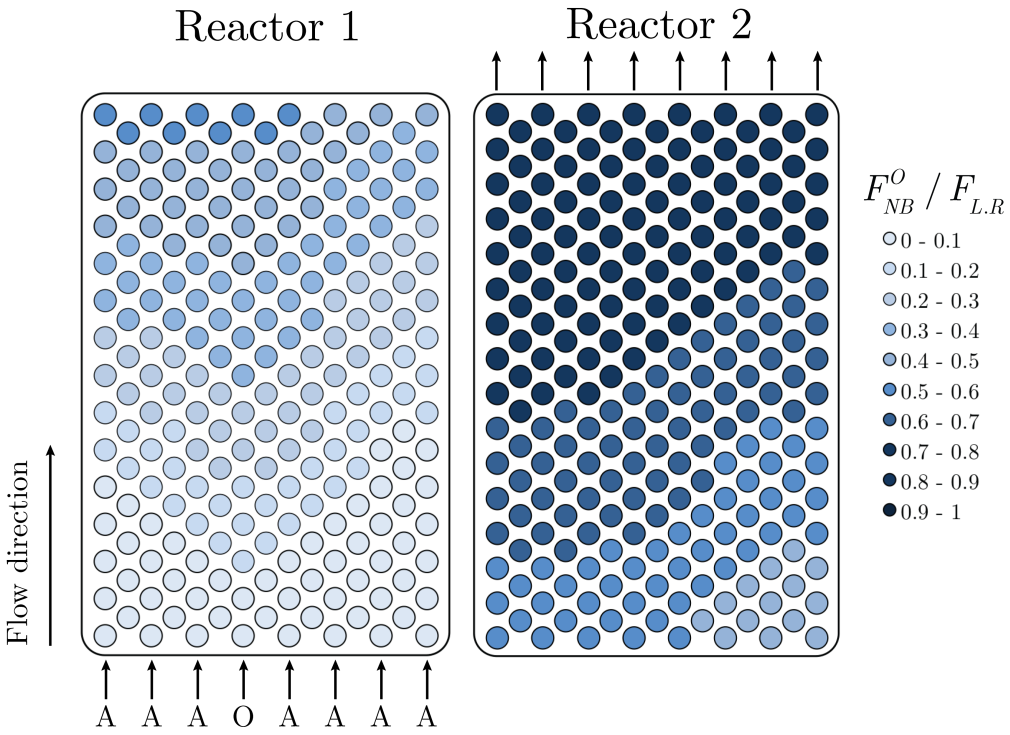


Figure 3.21. Map of the ratio of molar flow rate of nitrobenzene and the limiting reactant inside both reactors for Inlet Scheme 1.

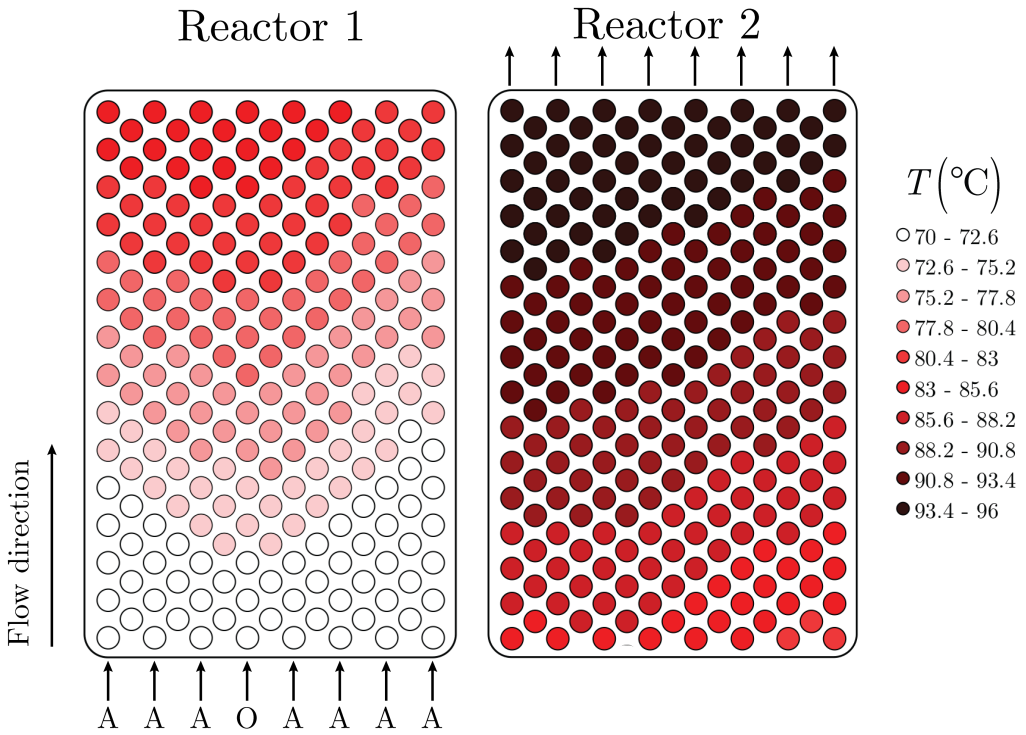


Figure 3.22. Map of nitration temperature inside both reactors for Inlet Scheme 1.

From Figure 3.21 it is possible to immediately detect that the progression of the reaction is faster in the left side of the reactor. This asymmetry happens because of the selected inlet scheme. Since the number of inlets is even, the injection of the organic phase cannot be made in the middle of the reactor. Since the spreading of the material throughout the NETmix reactor is made at a 45º angle from the inlet, by using only one inlet for the injection of the organic phase, there will be a zone at the beginning of the reactor where reaction will not occur.

To overcome this problem, a different inlet scheme was used in the simulations, Inlet Scheme 2, that has 2 inlets of organic phase and 6 inlets of aqueous phase, shown in Figure 3.23. For this inlet scheme $Q^{A}_{inlet} / Q^{O}_{inlet} = 4.4$.

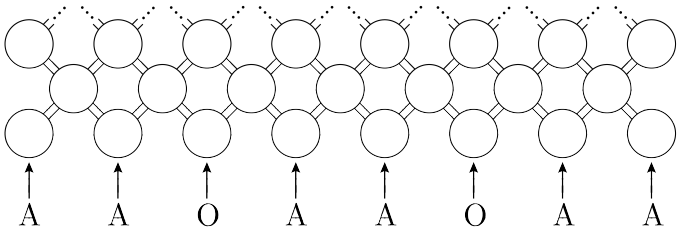


Figure 3.23. Inlet scheme 2.

The impact of the inlet scheme on conversion can be seen from the map of the ratio of molar flow rate of nitrobenzene and the limiting reactant and the map of the nitration temperature inside both reactors (see Figure 3.24 and Figure 3.25).

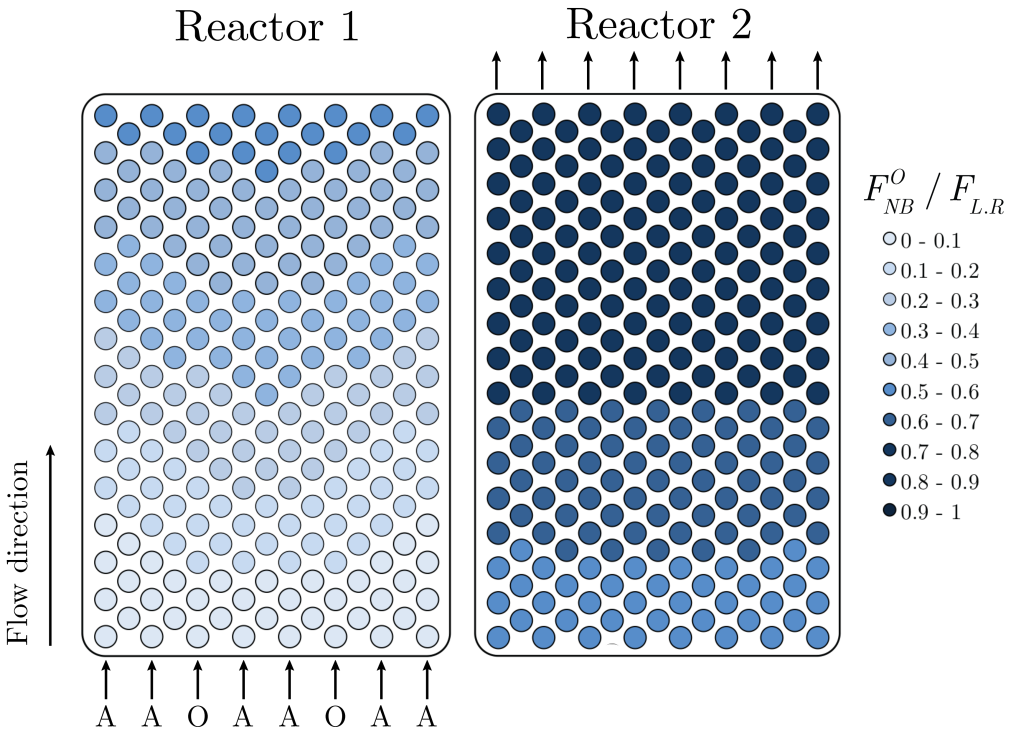


Figure 3.24. Map of the ratio of molar flow rate of nitrobenzene and the limiting reactant inside both reactors for inlet scheme 2.

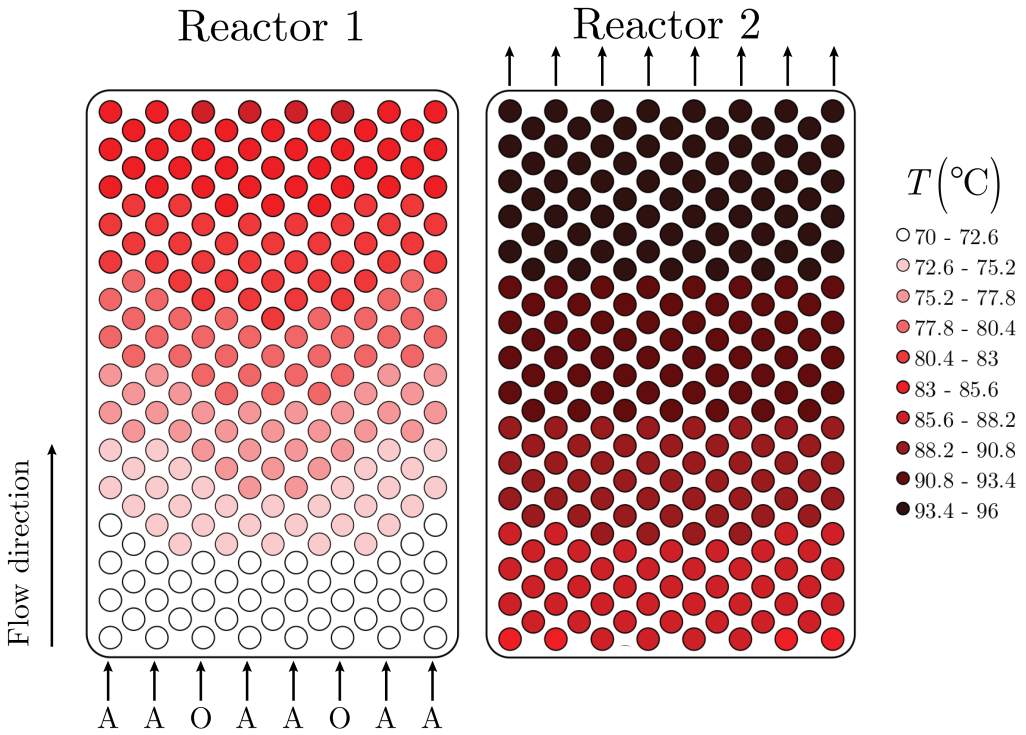


Figure 3.25. Map of nitration temperature inside both reactors for inlet scheme 2.

The even distribution of both phases at the inlets of the reactor avoids a deficit of the organic phase in one side of the reactor. Furthermore, since there are two injection points the spread of the organic phase throughout the rows of the NETmix reactor will be faster and a larger portion of the reactor will be used for the reaction between both phases. The selection of Inlet Scheme 2 will have a favourable effect on the final conversion. Simulation results of average conversion in each row of the two reactors, i_x, using both inlet schemes with the same operational conditions show that higher conversions are in fact achieved using Inlet Scheme 2 (Figure 3.26).

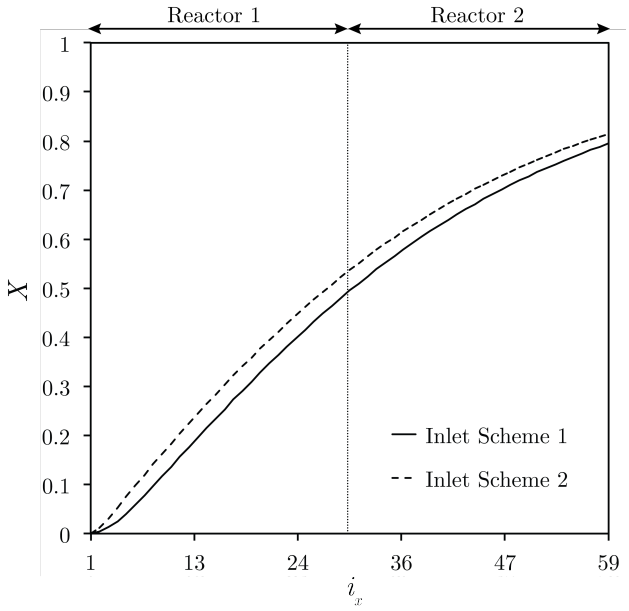


Figure 3.26. Conversion along the rows of the NETmix reactors using inlet scheme 1 and inlet scheme 2.

3.7 Conclusions

A detailed simulation tool for the adiabatic heterogeneous reaction of benzene was developed. In this model, the generation of interfacial area is considered high enough so a kinetically controlled regime is achieved. Therefore, no calculations of interfacial area are required.

The model was capable to predict, for operational conditions in the range of interest in industrial operation, the formation of nitrobenzene and the outlet temperature in

adiabatic operation within 15% of deviation when compared to the published experimental data of Biggs and White (1956) and Santos (2005).

Considerations were made for the NETmix operation conditions that have to be set to ensure that diffusional limitations can be neglected. A mathematical expression was developed to calculate the minimum Reynolds number that ensures that a sufficient power per unit volume is used for mixing.

From simulation it was seen that the right selection of operation conditions could lead to small reaction times with high conversions. It was shown that NETmix can be used to deliver high degree of mixing in laminar regime with large throughputs, suitable for large-scale production, which is difficult to achieve in large in large-scale reactors.

Nonetheless, the simulator lacks further validation with experimental data obtained with the NETmix reactor and although the studied range of operational conditions should, by its own, minimize the formation of bi-products, it would also be interesting to evaluate the selectivity obtained with NETmix and compare it with other methods.

3.8 References

Albright, L.F., Schiefferle, D.F., Hanson, C., 1976. Reactions Occurring in the Organic Phase During Aromatic Nitrations. Journal of Applied Chemistry and Biotechnology 26, 522-525.

Alexanderson, V., Trecek, J.B., Vanderwaart, C.M., 1978. Continuous Adiabatic Process for the Mononitration of Benzene. US Patent 4,091,042.

Barduhn, A., Kobe, K., 1956. Toluene Nitration Kinetics. Industrial & Engineering Chemistry 48, 1305-1315.

Barretta, S., 2011. Adiabatic Process for Making Mononitrobenzene. Noram International Limited, EP2352717 A1.

Biazzi, 2013. Biazzi SA., http://www.biazzi.ch/page/nitration.php.

Biggs, R.D., White, R.R., 1956. Rate of Nitration of Benzene With Mixed Acid. AIChE Journal 2, 26-33.

Booth, G., 2000. Nitro Compounds, Aromatic, Ullmann's Encyclopedia of Industrial Chemistry. Wiley-VCH Verlag GmbH & Co. KGaA.

Burns, J.R., Ramshaw, C., 1999. Development of a Microreactor for Chemical Production. Chemical Engineering Research and Design 77, 206-211.

Castner, J.B., 1941. Nitration of Organic Compounds. US Patent 2,256,999.

Coombes, R.G., Moodie, R.B., Schofield, K., 1968. Electrophilic Aromatic Substitution. Part I. The Nitration of Some Reactive Aromatic Compounds in Concentrated Sulphuric and Perchloric Acids. Journal of the Chemical Society B: Physical Organic, 800-804.

Daubert, T.E., Danner, R.P., 1994. Physical and Thermodynamic Properties of Pure Chemicals - Data Compilation. Taylor & Francis, Pennsylvania.

Deno, N.C., Stein, R., 1956. Carbonium Ions. III. Aromatic Nitration and the C0 Acidity Function1. Journal of the American Chemical Society 78, 578-581.

DIPPR, 2009. Design Institute for Physical Properties, Sponsored by AIChE. DIPPR Project 801 - Full Version. Design Institute for Physical Property Research/AIChE.

Evans, C.M., 1990. Manufacture of Organic Nitro Compounds. US Patent 4,973,770.

Field, J.P., Strachan, A.N., 1982. Dependence of the Rate Constant and Activation Energy of Aromatic Nitration on Mixed Acid Composition. Industrial and Engineering Chemistry Product Research and Development 21, 352-355.

Giles, J., Hanson, C., Ismail H. A, M., 1976. A Model for Rate of Nitration of Toluene Under Heterogeneous Conditions, Industrial and Laboratory Nitrations. American Chemical Society, pp. 190-209.

Gillis, P.A., Braun, H., Schmidt, J., Verwijs, J.W., Velten, H., Platkowski, K., 2003. Process for Conducting Liquid/Liquid Multiphase Reactions in a Tubular Reactor Having Static Mixing Elements Separated by Coalescing Zones. US Patent 6,562,247.

Gomes, P.J.G., 2011. The NETmix Reactor - Strategies for Optimizing Mixing and Development fo New Reactor Designs [Ph.D], Departamento de Engenharia Química. Universidade do Porto, Porto.

Guenkel, A.A., Rae, J.M., Hauptmann, E.G., 1994. Nitration Process. US Patent 5,313,009.

Hanson, C., Ismail, A.M., 1975. Solubility and Distribution Data for Benzene and Toluene Between Aqueous and Organic Phases. Journal of Applied Chemistry and Biotechnology 25, 319-325.

Hanson, C., Pratt M. W, T., Sohrabi, M., 1976. Some Aspects of Aromatic Nitration in Aqueous Systems, Industrial and Laboratory Nitrations. American Chemical Society, pp. 225-242.

Hemrajani, R.R., Tatterson, G.B., 2003. Mechanically Stirred Vessels, in: Paul, E.L., Atiemo-Obeng, V.A., Kresta, S.M. (Eds.), Handbook of Industrial Mixing - Science and Practice. John Wiley & Sons, New Jersey, pp. 345-390.

Hermann, H., Gebauer, J., 1998. Process for the Nitration of Aromatic Coumpunds. US Patent 5,763,697.

Hughes, E.D., Ingold, C.K., Reed, R.I., 1950. Kinetics and Mechanism of Aromatic Nitration. Part II. Nitration by the Nitronium Ion, NO2+, Derived from Nitric Acid. Journal of the Chemical Society (Resumed), 2400-2440.

Humphrey, S.B., Smoak, D.R., 1963. Nitration of Aromatic Hydrocarbons. US Patent 3,092,671.

Ismail, H.A.M., 1973. Macrokinetics of Aromatic Nitrations. Ph.D. Dissertation. Postgraduate School of Studies in Chemical Engineering, University of Bradford, Bradford, United Kingdom.

Kashid, M.N., Kiwi-Minsker, L., 2009. Microstructured Reactors for Multiphase Reactions: State of the Art. Industrial & Engineering Chemistry Research 48, 6465-6485.

Konig, B.M., Judat, H., Blank, H.U., 1997. Process for the Adiabatic Preparation of Mononitrotoluenes. US Patent 5,648,565.

Lewis, W.K., Suen, T.J., 1940. Rate of Nitration of Benzene. Industrial & Engineering Chemistry 32, 1095-1101.

Marziano, N.C., Tomasin, A., Tortato, C., Zaldivar, J.M., 1998. Thermodynamic Nitration Rates of Aromatic Compounds. Part 4. Temperature Dependence in Sulfuric Acid of HNO3→NO2+ Equilibrium, Nitration Rates and Acidic Properties of the Solvent. Journal of the Chemical Society. Perkin Transactions 2, 1973-1982.

Marziano, N.C., Traverso, P.G., Cimino, G.G., 1980. Thermodynamic Nitration Rates of Aromatic Compounds. Part 1. The Nitration of Benzene and Some Benzene Derivatives in Aqueous Sulphuric and Perchloric Acids. A Comparison of the Results Referred to Water as Standard State. Journal of the Chemical Society, Perkin Transactions 2.

Modak, S.Y., Juvekar, V.A., 1995. Role of Interfacial Reaction in Heterogeneous Aromatic Nitration. Industrial & Engineering Chemistry Research 34, 4297-4309.

Nexant, 2012. Nitrobenzene/Aniline/MDI. PERP 2011-4, Nexant Chem Systems, New York, USA.

Noram, 2013. Noram Engineering and Constructors Ltd., http://www.noram-eng.com/groups/nitration-group-technologies.html.

Rae, J.M., Hauptmann, E.G., 1991. Jet Impingment Reactor. US Patent 4,994,242.

Sampoli, M., De Santis, A., Marziano, N.C., Pinna, F., Zingales, A., 1985. Equilibria of nitric acid in sulfuric and perchloric acid at 25°C by Raman and UV spectroscopy. Journal of Physical Chemistry 89, 2864-2869.

Santos, P.A.Q.O., 2005. Nitração de Compostos Aromáticos: Transferência de Massa e Reacção Química. [Ph.D]. Faculdade de Ciências e Tecnologia da Universidade de Coimbra, Coimbra, Portugal.

Schiefferle, D.F., Hanson, C., Albright, L.F., 1976. Heterogeneous Nitration of Benzene, Industrial and Laboratory Nitrations. American Chemical Society, Washington, D. C., USA, pp. 176-189.

Sheats, G.F., Strachan, A.N., 1978. Rates and Activation Energies of Nitronium Ion Formation and Reaction in the Nitration of Toluene in ~ 78% Sulphuric Acid. Canadian Journal of Chemistry 56, 1280-1283.

Six, C., Richter, F., 2000. Isocyanates, Organic, Ullmann's Encyclopedia of Industrial Chemistry. Wiley-VCH Verlag GmbH & Co. KGaA.

Smith, J.M., Van Ness, H.C., Abbott, M.M., 2001. Introduction to Chemical Engineering Thermodynamics, 6th ed. McGraw-Hill, Singapore.

Solomons, T.W.G., Fryhle, C.B., 2000. Organic Chemistry, 7th ed. John Wiley & Sons, New York.

Zaldívar, J.M., Hernández, H., Barcons, C., Nomen, R., 1992. Heat Effects Due to Dilution During Aromatic Nitrations by Mixed Acid in Batch Conditions. Journal of Thermal Analysis 38, 2575-2582.

Zaldivar, J.M., Molga, E., Alós, M.A., Hernández, H., Westerterp, K.R., 1995. Aromatic Nitrations by Mixed Acid. Slow Liquid-Liquid Reaction Regime. Chemical Engineering and Processing: Process Intensification 34, 543-559.

4 Product Development in the NETmix Reactor: Metal-Organic Frameworks

4.1 Introduction

Metal-organic frameworks (MOFs) are a class of organic-inorganic hybrid materials made of metal clusters interconnected through an organic linker (carboxylates, phosphonates, imidazolates) creating crystalline coordination networks.

Since their discovery in 1989 (Hoskins and Robson, 1989), the synthesis of MOFs has been given much attention both in academia and industry due to their highly versatile composition together with exceptionally high surface areas $(500-6000\ \mathrm{m^2/g})$, regular porosities, well-defined crystalline structures and the lack of non-accessible bulk volume, which make them promising candidates for applications in a large number of fields related to porous materials (Furukawa et al., 2010; Stock and Biswas, 2012).

One of their key advantages compared to other porous materials (such as zeolites, silica, polymers, activated carbon) is the possibility of easily tuning the composition through a change of the metal and/or the organic linker. Functionalization of the organic linker represents another advantage of MOFs with the possibility of grafting,

during or after the synthesis, various organic functionalities (polar, apolar, acidic, basic), thus modulating the physicochemical properties of the solid (Kim et al., 2012). Additionally, MOFs possess a high metal content with regular active sites because of the highly crystalline nature of metal-organic frameworks (Stock and Biswas, 2012).

The two most prominent academic research groups in the area of MOFs are the group of Omar M. Yaghi at the Center for Reticular Chemistry of the University of California and the group of Christian Serre at the Institut Lavoisier, a research institute from the University of Versailles in France. Omar M. Yaghi engineered the first MOF structure in 1998 by mixing together two molecular building blocks (Sanderson, 2007; Yaghi et al., 1998). Gérard Férey, a chemist at the Institut Lavoisier, is nowadays credited for having developed the MOF with largest surface area of $5900\,\mathrm{m^2/g}$, an equivalent area of an average-sized American football field (Sanderson, 2007).

Different MOF compounds are currently sold under the trade name Basolite by Sigma-Aldrich® and are manufactured in a BASF pilot plant in Ludwigshafen, Germany, in $10\,\mathrm{kg/day}$ batches (Jacoby, 2008). These products are sold for about $6\,000\,€/\mathrm{kg}$ (Sigma-Aldrich, 2013).

Different synthesis routes can be used in the production of MOFs. MOFs are typically synthesized by combining the organic polycomplexing ligands (carboxylates, phosphonates, imidazolates) and well-soluble metal salts in hydro/solvothermal conditions at relatively low temperatures (below $300°\mathrm{C}$) (Kuppler et al., 2009) with reaction times that can vary within several hours to several days (Czaja et al., 2009). Alternative synthetic routes have been proposed for MOFs preparation such as ball milling, electrochemistry, sonochemistry, microwave-assisted solvothermal synthesis or ambient pressure conditions (Chalati et al., 2011; Stock and Biswas, 2012). Starting from the same reaction mixture, the choice of the synthesis method may have a strong impact on reaction time, yield or particle size and morphology (Chalati et al., 2011).

Potential applications of MOFs include the traditional areas of hydrogen and methane storage, gas separation and catalysis, based on the pore size and shape as well host-guest interactions (Kuppler et al., 2009; Stock and Biswas, 2012). Other potential uses are in biomedical applications such as drug delivery and imaging (Horcajada et al., 2012) or sensor applications (Stock and Biswas, 2012).

The use of MOFs in industrial applications requires their large-scale production, with high yield, purity, and reproducibility. Furthermore, control of particle size is also needed for some applications, such in drug delivery (Horcajada et al., 2012; Stock and Biswas, 2012). Applications in biomedical or cosmetic fields demand the production of monodispersed nanoparticles coupled with synthesis in non-toxic solvents without surfactants, in order to be compatible with the intravenous route of administration (Chalati et al., 2011).

In this chapter, the NETmix reactor is tested to produce MIL-88A (a MOF designed by the Institut Lavoisier) and a method for producing nanoparticles by water based chemical precipitation route is presented. Two different formulations are used. In Section 4.4, Formulation 1 is described and the obtained experimental results and characterization are shown and discussed. In Section 4.5, a precipitation model for the prediction of secondary precipitate phases is introduced. Experimental conditions are chosen according to the precipitation model and are described. Experimental results and characterization are shown and discussed. In Section 4.6, the space-time yield for this method is calculated and compared to industrial space-time yields.

4.2 MIL-88A

In this work, a specific MOF was chosen, the MIL-88A. This MOF was developed and synthesized at the Institut Lavoisier and the acronym MIL stands for Materials from Institut Lavoisier. The production of MIL-88A was chosen due to the simplicity of its synthesis. Reaction occurs simply by mixing a fumarate source and an iron (III) source in non-solvothermal conditions (temperatures under 80°C) and at atmospheric pressure.

MIL-88A structure is based on oxocentered trimers of iron(III) octahedra linked to fumarate dianions, a bidendate dicarboxylate, creating a three-dimensional framework with interconnected pores and cages of $5-7$ Å (see Figure 4.1).

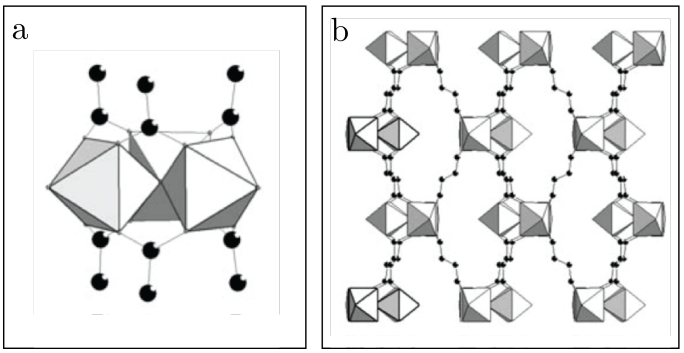


Figure 4.1. (a) Trimer and (b) framework of MIL-88A (Serre et al., 2004).

Each trimer is composed by three iron octahedra bounded to an oxygen bridging ligand, a O^{μ_3} atom. Iron atoms are situated within an octahedral environment of four oxygen atoms from the fumarate dianons, the binding ligand and one oxygen atom from a solvent molecule that bounds to the molecule of MIL-88A during the synthesis. Figure 4.2 shows the molecular structure of each trimer with water used as solvent during the MIL-88A synthesis.

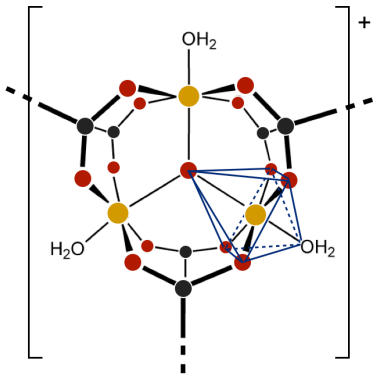


Figure 4.2. Molecular structure of MIL-88A trimer. Yellow: iron atoms, red: oxygen atoms, black: carbon atoms.

The chemical formula of MIL-88A molecule synthesized in water is

$$Fe_3^{III}O^{\mu_3}\left(H_2O\right)_3\left(O_2C-C_2H_2-CO_2\right)_3\cdot Y\cdot nH_2O \tag{4.1}$$

where n is the number of free water molecules placed inside the structure and Y is a counterion to maintain electric neutrality of the molecule. Depending on the

reactants used, Y can either be, for example, hydroxide, chloride or acetate anions. Simulations suggest that $n = 19$ for this molecule (Mellot-Draznieks et al., 2005). A high water content of 42% (36% free water adsorbed, 6% bounded water) can be found in the MIL-88A molecule. Considering this amount of water adsorbed, the molecule of MIL-88A has a molar mass of $940\ \mathrm{g/mol}$. The density of MIL-88A was experimentally measured by Serre et al. (2004) to be $1.55\ \mathrm{g/cm^3}$. Through molecular simulation, Serre et al. (2004) estimated a density value of $1.73\ \mathrm{g/cm^3}$.

The chemical formula that represents the chemical reaction for synthesis in water is

$$3Fe^{3+} + 3C_4H_2O_4^{2-} + 3H_2O \rightarrow Fe_3O\left(H_2O\right)_3\left(C_4H_2O_4\right)_3 \cdot OH^- \cdot nH_2O \qquad (4.2)$$

assuming the counter ion to be the hydroxide anion.

In addition, this solid exhibits a flexible framework and possesses active iron metal sites. MIL-88A can almost double its cell volume (80% of increase) between the anhydrous (closed form) and the open form while fully retaining its open-framework topology (Surble et al., 2006), as shown in Figure 4.3. This behaviour is validated by X-ray diffraction and different crystalline structure patterns are observed for different forms of the molecule (Mellot-Draznieks et al., 2005; Serre et al., 2004).

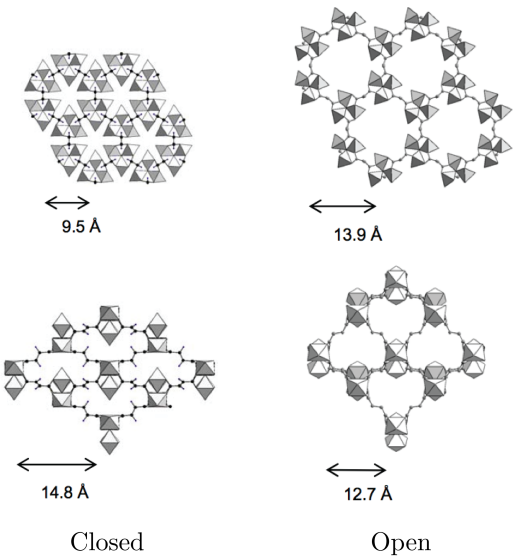


Figure 4.3. Simulated crystalline structures of MIL-88A in its open and closed framework shapes (Serre et al., 2007).

In pharmaceutical products, most of the existing carrier materials show poor drug loading and/or rapid release of the proportion of the drug that is simply adsorbed at the external surface of the nanocarrier (Horcajada et al., 2010). Non-toxic MOF nanoparticles with the ability to tune their structures and porosities for better drug interactions and high loadings, are well suited to serve as nanocarriers for an efficient drug delivery (Horcajada et al., 2012). The cytotoxicity of nanoparticulate MIL-88A was studied by Horcajada et al. (2010) and low values were of observed comparable with cytotoxity values of the currently available nanoparticulate systems. Furthermore, the degradation products of MIL-88A, iron and fumaric acid are endogenous and show low toxicity values making it suitable to be used as non-toxic and biocompatible drug nanocarrier. Furthermore, due to the iron-based cores, MIL-88A was found to be a good candidate as a magnetic resonance imaging contrast agent (Horcajada et al., 2010).

Several synthesis methods and solvents can be used in the production of MIL-88A and were the subject of further development by Chalati et al. (2011). Different hydro/solvothermal synthesis routes were studied and were compared in terms of particle size, polydispersity and yield. The influence of temperature, time, concentration, pH or the use of additives was studied for each synthesis route. Water, methanol and dimethylformamide (DMF) were used as solvents. It was observed that the use of alcohols decreased the reaction kinetics due to the competitive reaction of formation of fumaric acid esters. Only after the addition of sodium hydroxide, the crystallization of MIL-88A occurred. The use of DMF led to smaller particle size than the use of water and ethanol. This is related to higher solubility of fumaric acid and the change of interfacial tension between the solvent and particles. It was also observed that acetic acid worked as an inhibitor while the addition of sodium hydroxide increased the reaction kinetics. This may indicate that the pH of the medium has influence over the crystallization rate of MIL-88A.

Large amounts of MOFs can be easily produced through common hydrothermal synthesis but large size particles with high polydispersity are obtained. The particle

size distribution of MIL-88A was bimodal, probably due to the competition between nucleation and growth during the crystallization process and to an aggregation of the particles (Horcajada et al., 2010). Using sonothermal conditions, small and monodispersed nanoparticles around 100 nm were prepared and were obtained through the use of inhibitors, very high dilutions or low temperatures. However, a small synthesis yield below 3% was achieved and this method led sometimes to metastable or new phases. Hydrothermal microwave-assisted synthesis showed promising results by allowing the control of the size while obtaining high yields close to 60% of monodispersed particles (100 nm) of the porous flexible MIL-88A MOFs with small reaction times (2-10 minutes). No information about the space-time yield (the mass of product formed per volume of the reaction mixture and time) is reported for this method.

In this work, two different types of reactors are used for the production of MIL-88A from a water based chemical precipitation method. Two different formulations and the effect of concentration, temperature and the pH of the medium are studied.

Finally, a water based chemical precipitation method at room temperature and atmospheric pressure is developed and used for the production of nanoparticles of MIL-88A with small and narrow particle size distribution, with short reaction times, free of toxic solvents or surfactants and high space-time yields.

4.3 Experimental Setup and Techniques

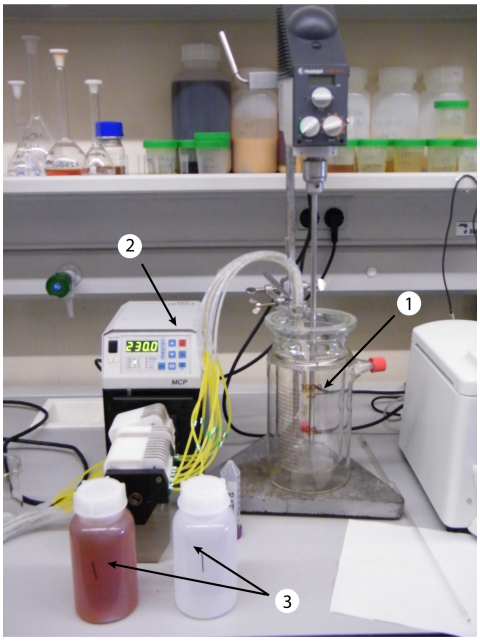
In this section, the experimental setup and techniques for the production and characterization of MIL-88A are described.

4.3.1 Experimental Setup

For comparison purposes, reaction was carried out in two different mixing devices, continuous flow reaction in a NETmix reactor and batch reaction in a stirred vessel.

4.3.1.1 Batch Reactor

In the batch setup (semi-batch to be more accurate), one of the reactants is placed in a batch reaction vessel, with 1 L of capacity, while the other is introduced in the system by a peristaltic pump (ISMATEC MCP). The experimental setup for batch reaction in a stirred vessel is shown in Figure 4.4.



Legend: 1 - Batch reaction vessel
2 - Peristaltic pump
3 - Reactants vessels

Figure 4.4. Batch reaction experimental apparatus.

The injection of reactant was made directly into the liquid on top of the rotating impellers and the flow rate of the peristaltic pump was chosen to feed the reactant to the system during the same amount of time as the experiment in the NETmix reactor. The rotational speed of the impeller was chosen to ensure that no visible stagnant zones occurred.

4.3.1.2 NETmix Reactor

The Lab-Scale NETmix 2D unit was used for these experiments due to its small throughputs; Table 4.1 summarizes the geometrical characteristic of this NETmix reactor.

Table 4.1. Lab-Scale NETmix 2D geometrical characteristics.

Geometry	Lab-Scale NETmix 2D
Number of rows, n_x	29
Number of columns, n_y	8
Chamber diameter, D (mm)	6.5
Channel diameter, d (mm)	1
Geometry depth, ω (mm)	3
Channel length, l (mm)	2
Total volume, V (mL)	23

The reactants were fed to the reactor through a pre-mixed inlet scheme, as shown in Figure 4.5, and two Ismatec BVP-Z Standard pumps were used to convey the reactants to the reactor inlets.

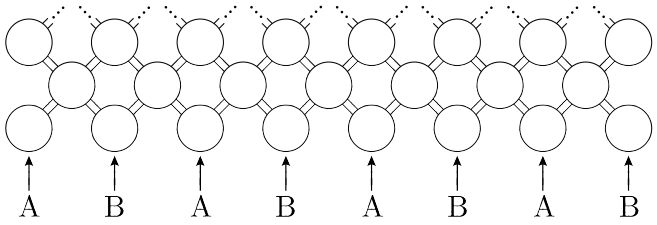
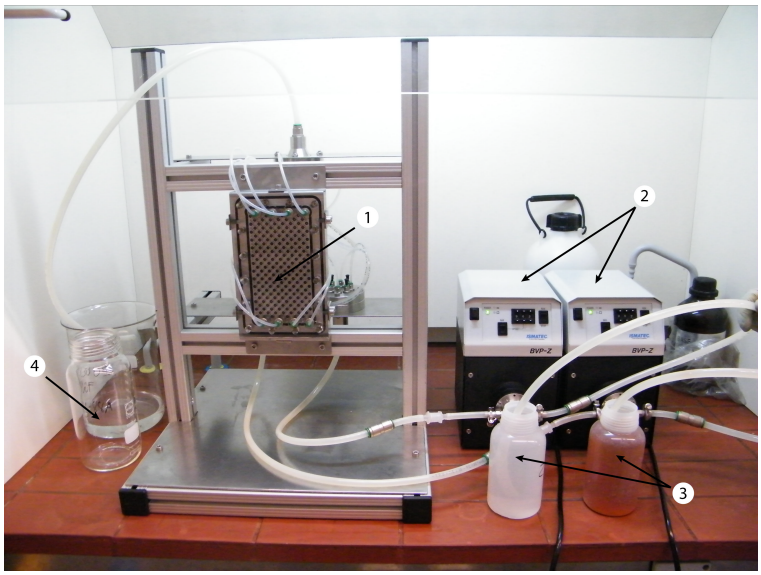


Figure 4.5. NETmix pre-mixed inlet scheme.

The experimental setup for continuous flow reaction in a NETmix reactor is shown in Figure 4.6.



Legend: 1 - NETmix reactor 2 - Feeding pumps
3 - Reactants vessels 4 - Final product flask

Figure 4.6. NETmix reactor experimental apparatus.

4.3.2 Reactants

The solutions used in these experiments were prepared with distilled water. The iron(III) cations necessary for reaction were obtained from a solution of iron(III) chloride hexahydrate, $FeCl_3.6H_2O$, (98% purity from Sigma-Aldrich) and the source of fumarate anions was sodium fumarate dibasic, $NaO_2C-C_2H_2-CO_2Na$, (99% purity from Sigma-Aldrich) or fumaric acid, $HO_2C-C_2H_2-CO_2H$, (99% purity from Sigma-Aldrich), depending on the formulation used.

Solutions of hydrochloric acid (>37% solution from Sigma-Aldrich) and sodium hydroxide (0.8 M solution from Fluka) were used to adjust the pH of the solutions of iron(III) chloride and sodium fumarate if needed.

4.3.3 Product Characterization

The final product was characterized by the experimental techniques described in this section.

4.3.3.1 Scanning Electron Microscopy (SEM)

Scanning electron microscopy (SEM) was used to obtain high-resolution particle image. Additionally energy dispersive spectroscopy (EDS) was used for elemental characterization of the sample. The equipment used for the analysis was a Jeol JSM 6301F microscope with Oxford Inca Energy 350 energy dispersive X-ray system owned by CEMUP – Centro de Materiais da Universidade do Porto. Samples were prepared in a metallic holder and fixed in a carbon tape and were coated with gold for 200 seconds to avoid the accumulation of charge due to their low conductivity.

4.3.3.2 Dynamic Light Scattering (DLS)

Particle size distribution information was obtained by dynamic light scattering. The analysis was performed using a Malvern ZetaSizer Nano ZS ZEN 3600.

Particles suspensions were pre-diluted when needed to ensure that the used concentration is within the working range of particle concentration of the device. A

solution of polyvinylpyrrolidone (PVP) with a concentration of 8 g/L was used as a dispersant to dilute the samples and avoid agglomeration. This concentration of PVP is in excess relatively to the theoretical amount needed to coat all particles and was found to stabilize the suspension during the time of the analysis. The calculation of the amount of surfactant used is explained in Appendix B. The particles suspensions were further dispersed with ultrasounds for 2 minutes using and Hielscher UP50H ultrasound device.

4.3.3.3 Atomic Absorption Spectroscopy (AAS)

Atomic absorption spectroscopy was used to determine the chemical conversion of iron in MIL-88A. This technique makes use of absorption spectrometry to assess the concentration of an analyte in a sample. The equipment used for atomic absorption was a GBC 932 plus. Standard solutions in a range of 2-145 mg/L were used for the calibration curve to relate absorbance with concentration.

4.3.3.4 X-Ray Diffraction (XRD)

Two devices were used for X-ray diffraction analysis, a Bruker D8 equipped with an eye-lynx detector with a copper source from Intitut Lavoisier and a PAN'alytical, X´Pert Pro with s X'Celerator detector and secondary monochromator from Unidade de Microscopia Electrónica (UME) at Universidade de Trás-os-Montes e Alto Douro (UTAD). The obtained XRD patterns were compared with simulated XRD patterns determined by the Institut Lavoisier (Mellot-Draznieks et al., 2005; Serre et al., 2004). Simulated XRD pattern from crystal data and structure refinement parameters for MIL-88A were obtained with PowderCell 2.3, software for powder pattern calculation from single crystal data and refinement of experimental curves.

4.3.3.5 Differential Scanning Calorimetry (DSC) and Thermogravimetric Analysis (TGA)

Thermal characterization of the obtained solid by reaction was obtained with differential scanning calorimetry (DSC). This technique measures the difference in the amount of heat required to increase the temperature of a sample and a reference

sample as a function of temperature. Information about the heat capacity of the sample and phase transitions can be studied by this technique. Furthermore, thermogravimetic analysis (TGA) measurements were performed to investigate changes in physical and chemical properties of materials as a function of increasing temperature.

DSC and TGA measurements were executed with a Netzsch STA 409 PC device with an inert atmosphere of nitrogen at the Laboratory of Catalysis and Materials (LCM) at the University of Porto.

4.3.3.6 Nitrogen Adsorption

The specific surface area is an important property in the characterization of porous materials. A sorption isotherm of nitrogen can be used to calculate the specific surface area using the Braunauer-Emmet-Teller (BET) theory. Specific surface area measurements through BET were performed with a Quantachrome Instruments Autosorb iQ MP at the Laboratory of Catalysis and Materials (LCM) at the University of Porto.

4.4 Formulation 1

4.4.1 Experimental Description

A series of experiments were performed using the NETmix reactor and the stirred tank batch reactor. The influence of three parameters was evaluated: the Reynolds number in the NETmix channels, the reactants concentration; and the temperature. A list of the experiments and respective conditions is given in Table 4.2. Concentration of reactants was similar to the values used by Chalati et al. (2011) for the production of MIL-88A. Equal volumes of 500 mL of each reactant were prepared for all the experiments. For the experiments in the NETmix reactor, a Reynolds number of 600 in the channels was selected to ensure an efficient mixing in the unit cells.

Table 4.2. Series of experiments and respective conditions.

Exp.	Process	Re	$T\left(°C\right)$	$c_{Reac}\left(M\right)$	Objective
N01	NETmix	78	25	0.4	Study of the influence of the Reynolds number
N02	NETmix	600	25	0.4	
B02	Batch	n.a.	25	0.4	Comparison of the batch production with NETmix final product N02
N03	NETmix	600	25	0.02	Study of the reactants concentration
N04	NETmix	600	80	0.4	Study of the effect of temperature
B04	Batch	n.a.	80	0.4	Comparison of the batch production with NETmix final product N04
B05	Batch	n.a.	25	0.4	Study of the effect of the addition of sodium citrate as a dispersant
B06	Batch	n.a.	50	0.4	Study of the effect of temperature
N07	NETmix	600	25	0.008	Study of the reactants concentration
B07	Batch	n.a.	25	0.008	Comparison of the batch production with NETmix final product N07

The first experiment, N01, was performed using the NETmix reactor. Two solutions of iron(III) chloride and sodium fumarate of $0.4\,\mathrm{M}$ were prepared. Assuming water physical properties at $25°C$, a total inlet flow rate of $1.03\,\mathrm{L/min}$ was used to achieve $\mathrm{Re} = 600$ in the NETmix channels. However, a sudden increase of viscosity was observed to approximately 9 times the viscosity of water. This increase of viscosity is related to the rapid generation of particles when the reactants are mixed at this concentration. Consequently, the increase of viscosity decreased the Reynolds number in the channels to $\mathrm{Re} = 78$ and a self-sustainable mixing regime inside the NETmix unit cell was not attained. Segregation of the flow was observed including the blockage of some channels.

A methodology was developed (Costa, 2012) for the proper choice of the flow rate for a desired Reynolds number, based on viscosity measurements as a function of the

reactants concentration and shear rate, described in Appendix C. And thus, experiment N02 was done with the same concentrations and temperature as experiment N01 but a total inlet flow rate of 3.60 L/min that ensures a Reynolds number of 600 in the NETmix channels. Experiment B02 was performed in batch conditions with the same conditions as experiment N02.

In experiment N03, a reactants concentration 20 times lower was used. This ensures that at the mean free distance between the particles is 1.9 times the length of the particles, $\Delta x_{\text{part}} / L_{\text{part}} = 1.9$, while for the concentration of 0.4 M, the value was only 0.08 times the length of the particles. The calculation of $\Delta x_{\text{part}} / L_{\text{part}}$ is described in Appendix B. Two solutions of iron(III) chloride and sodium fumarate of 0.02 M were prepared. Following the methodology described in Appendix C, a total inlet flow rate of 1.80 L/min was used to achieve $\text{Re} = 600$ in the NETmix channels.

For experiments N04 and B04, the reaction was carried at 80°C by heating up both reactants in a thermal bath. Two solutions of iron(III) chloride and sodium fumarate of 0.4 M were prepared. A total inlet flow rate of 1.03 L/min was used to achieve $\text{Re} = 600$ in the NETmix channels. For this temperature, the viscosity increase was not significant.

For experiment B05, sodium citrate was used as a dispersant agent to avoid agglomeration of particles during reaction. The amount of citrate used was 10 times higher than the theoretical amount needed to coat all particles. The calculation the necessary citrate concentration is described in Appendix B.

For experiments B06, the temperature of reaction was set to 50°C by heating up both reactants in a thermal bath. Two solutions of iron(III) chloride and sodium fumarate of 0.4 M were prepared.

In experiments N07 and B07, two solutions of iron(III) chloride and sodium fumarate of 0.008 M were used to increase the mean free distance between particles,

$\Delta x_{\text{part}} / L_{\text{part}} = 3$, to decrease particle interaction and reduce particle agglomeration. A total inlet flow rate of $1.03\,\text{L/min}$ was used to achieve $\text{Re} = 600$ in the NEtmix channels for experiment N07.

All the products went through an ageing process for 72 hours under constant stirring to avoid the deposition of particles. This ageing of 72 hours corresponds to the period where no significant changes in the pH of solution were detected. This way, it can be assumed that no more reaction is taking place during this period.

Samples were collected immediately after reaction and after 72 hours of ageing and dried in a Büchi Mini spray-dryer B-290 to obtain a fine powder to use for SEM imaging, XRD, BET, DSC, TGA analyses.

The suspensions were centrifuged at different periods using a Thermo Fisher Scientific Heraeus Multifuge X1R for 30 minutes at $-5°\text{C}$ at a centrifugal force of 15000g. The supernatant was analysed to ensure that presence of particles was not detected by DLS. The iron content in the supernatant was quantified by atomic absorption spectroscopy.

4.4.2 Results and Discussion

After reaction, a suspension of particles is obtained with brown coloration. Along the ageing time, the coloration changes from brown to pale pink (see Figure 4.7).



Figure 4.7. Obtained product coloration immediately after reaction (on the left) and after 72h of ageing (on the right).

The spray-dried samples for analyses present the same difference in the coloration for samples obtained immediately after reaction and samples obtained after 72 hours of ageing time (see Figure 4.8).



Figure 4.8. N02 samples spray-dried immediately after reaction (on the left) and after 72h of ageing (on the right).

During the production of MIL-88A, the pH of the medium decreases through the release of H^+ cations (Equation (4.2)). When equilibrium is achieved, the change in pH is no longer observed. After 72 hours of ageing, the change in pH value per hour is less than 1% so it can be assumed that the reaction finished during this period (Figure 4.9).

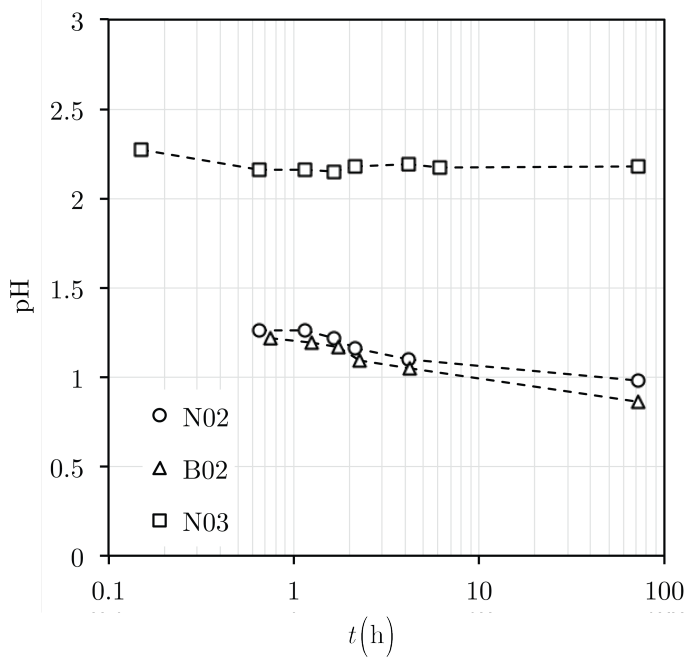


Figure 4.9. pH as a function of ageing time for samples N02, B02 and N03.

4.4.2.1 Iron (III) Conversion

Samples collected along different ageing times were centrifuged. The supernatant resulting from the centrifugation was used to measure the amount of iron yet in solution by atomic absorption.

Knowing the amount of unreacted iron in solution and the volume of the supernatant, it is possible to determine by a simple mass balance the amount of iron consumed by reaction.

The chemical conversion in iron, X_{Fe}, is calculated by

$$X_{\mathrm{Fe}} = 1 - \frac{c_{\mathrm{Fe}}\left(t\right)}{c_{\mathrm{Fe},0}} \tag{4.3}$$

where c_{Fe} is the concentration of consumed iron for a given instant, t , and $c_{Fe,0}$ is the initial concentration of iron in solution before reaction taking place.

Figure 4.10 and Figure 4.11 show the results of iron conversion as a function of the ageing time. High iron conversions of around 90% are achieved after 72 ageing hours for samples N01, N02 and B02. The difference is not enough to state that the initial mixing conditions affect the final conversion. Conversion increase with ageing time is slower for N01 sample and can be related to the lack of mixing in the NETmix chamber by the sudden viscosity increase. N03 sample presents a lower conversion of iron of around 80%.

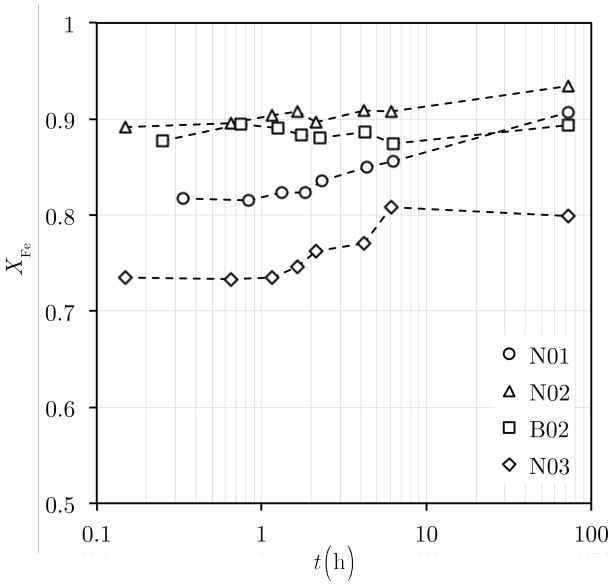


Figure 4.10. Iron conversion as a function of ageing time for samples N01, N02, B02 and B03.

Experimental results obtained at 25°C (B02) and 50°C (B06) do not show any significant difference. The experimental result carried at 80°C (B04) shows higher conversion of iron of about 96%.

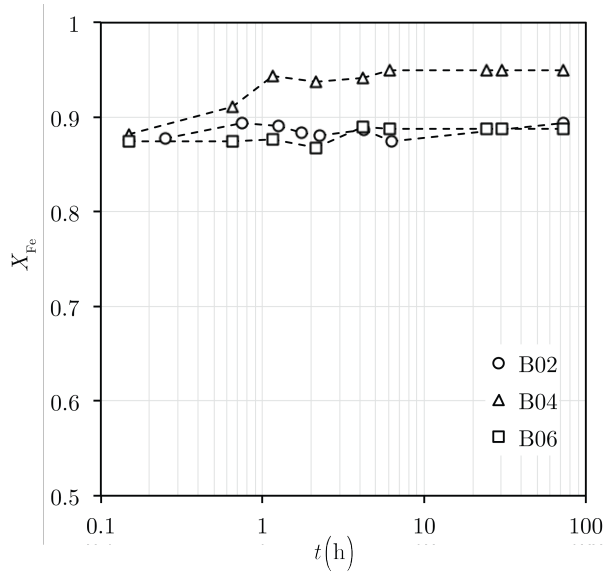


Figure 4.11. Iron conversion as a function of ageing time for samples B02, B04 and B06.

Final conversion after 72 ageing hours seems not to be influenced by the initial mixing conditions. From the experimental results, conversion is dependent on the reactants concentration and lower conversions are achieved for lower concentration of reactants. No definitive conclusion can be made for the influence of temperature on the final conversion. The higher conversion obtained at 80°C can be due the

formation of secondary products related to the chemistry of iron in solution (iron hydroxides and oxides). This topic will be discussed later in this chapter.

Nonetheless, total conversion was not achieved in 72 hours of ageing and several reasons can be pointed out:

- fumarate molecules trapped inside the framework and cannot react with unconverted iron in solution;
- ageing time was not enough to achieve full conversion of iron due to the decrease of reaction rate;
- a chemical equilibrium of all species in solution has been achieved and therefore no higher conversions are possible to attain.

4.4.2.2 XRD Analysis

XRD analysis was performed to determine if the obtained final material was in fact MIL-88A. XRD results for samples N02 (0 h and 72 h of ageing time), B02 (0 h and 72 h of ageing time) and B05 (72 h) are presented in Figure 4.12. Moreover, the experimental results were compared to the simulated XRD patterns of MIL-88A in its expanded form due to water molecules adsorbed as determined by Mellot-Draznieks et al. (2005). The crystalline structure of MIL-88A was observed in all cases after comparison with the simulated XRD patterns. Some slightly differences are observed in the samples with 0 hours of ageing time and may be due to the difference on the crystalline structure as observed from SEM. The main difference is the existence of only one peak at $2\theta = 13 - 14°$.

Samples were analyzed to verify the presence of other phases. The formation or iron hidroxides/oxides could not be validated or the presence of unreacted fumaric acid. Only the presence of sodium chloride was detected by XRD.

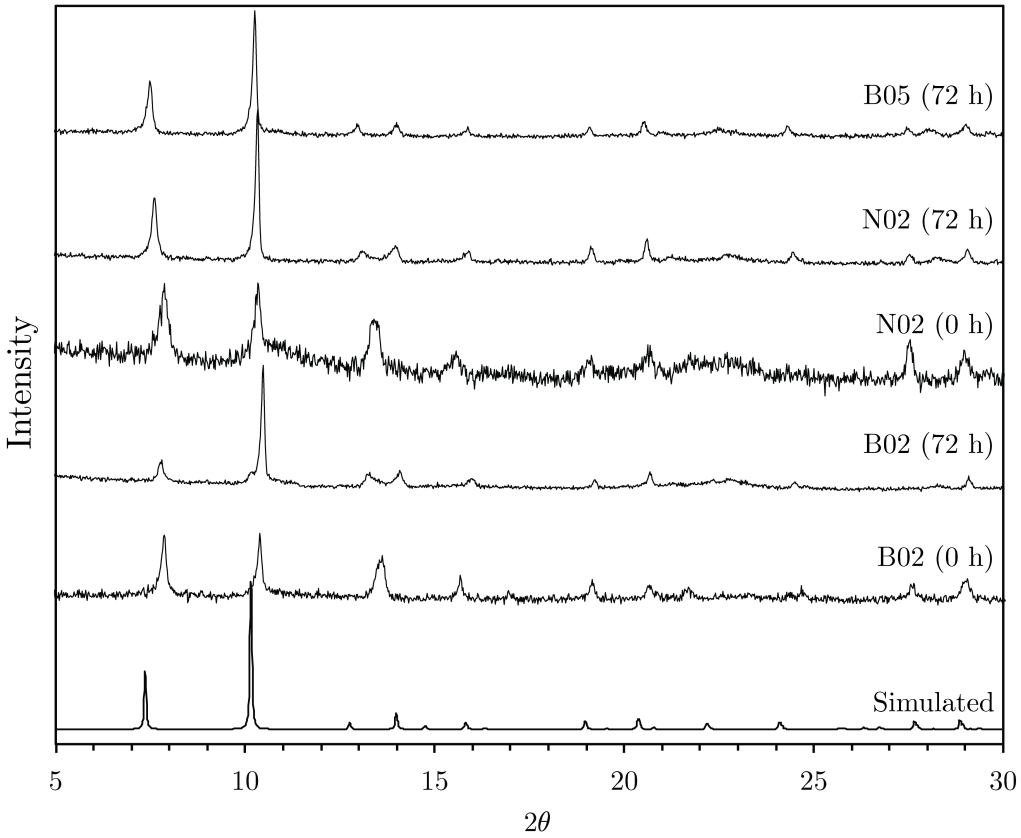


Figure 4.12. Simulated and experimental XRD patterns for samples B02, N02 and B05.

4.4.2.3 SEM Analysis

For samples that were not aged, an amorphous phase is observed instead of MIL-88A crystals (Figure 4.13a and Figure 4.13c). After 72 hours, through dissolution processes, reorganization or growth, crystalline rod-shaped crystals appear (Figure 4.13b and Figure 4.13d).

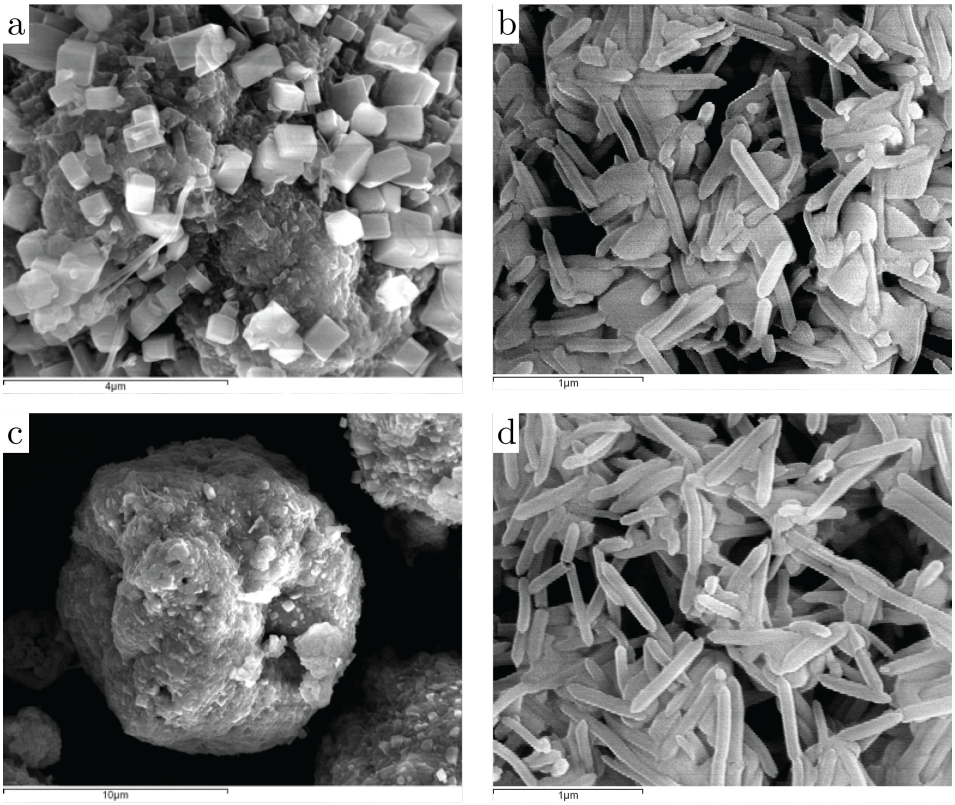


Figure 4.13. SEM images of samples (a) N02 (0 hours), (b) N02 (72 hours), (c) B02 (0 hours) and (d) B02 (72 hours).

For this formulation, the ageing process is important for the formation of crystals of MIL-88A. The same crystal shape with similar size can be observed for N01 sample after 72 hours of ageing. For the selected operational conditions in the NETmix reactor that led to poor mixing performance at the beginning of the reaction, no significant impact can be detected.

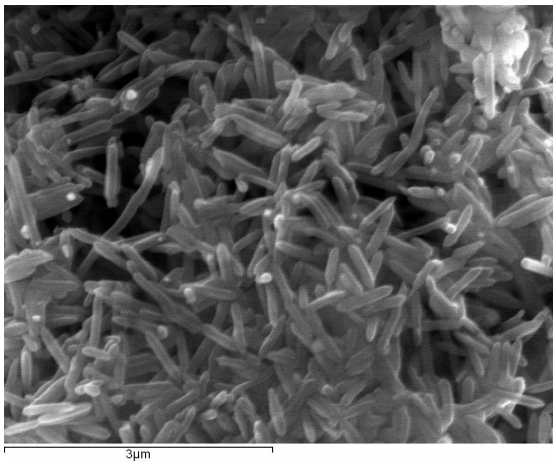


Figure 4.14. SEM images of sample N01.

An amorphous phase is also observed for non-aged N03 samples. After 72 hours of ageing, bigger crystals are observed than the ones observed for N02 and B02 samples (see Figure 4.15).

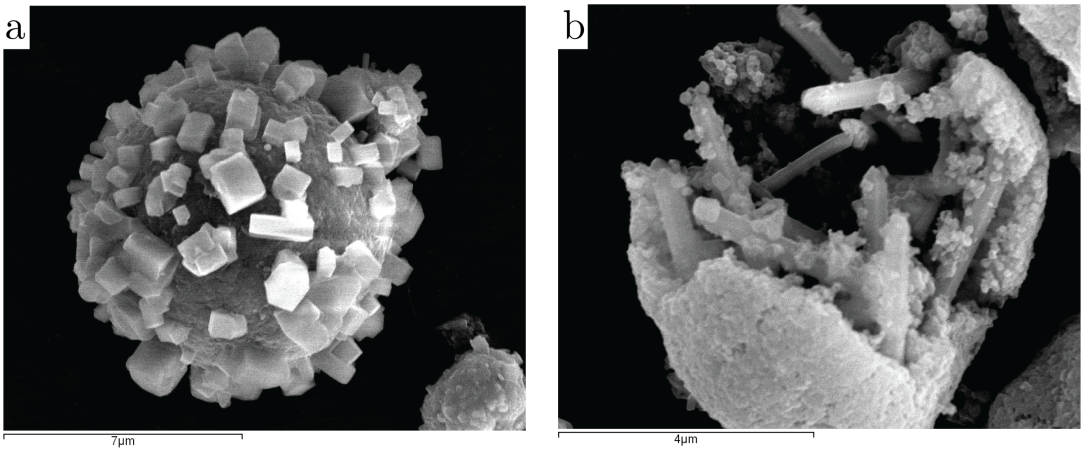


Figure 4.15. SEM images of samples (a) N03 (0 hours) and (b) N03 (72 hours).

When the reaction is held at 80°C, rod-shaped crystals are immediately observed without the need for ageing for samples of experiments N04 and B04 (see Figure 4.16). Nevertheless, the temperature increase promotes the crystal growth rate and the dimensions of the crystals are larger when compared with samples from experiments N02 and B02, with a size of about 1500×300 nm.

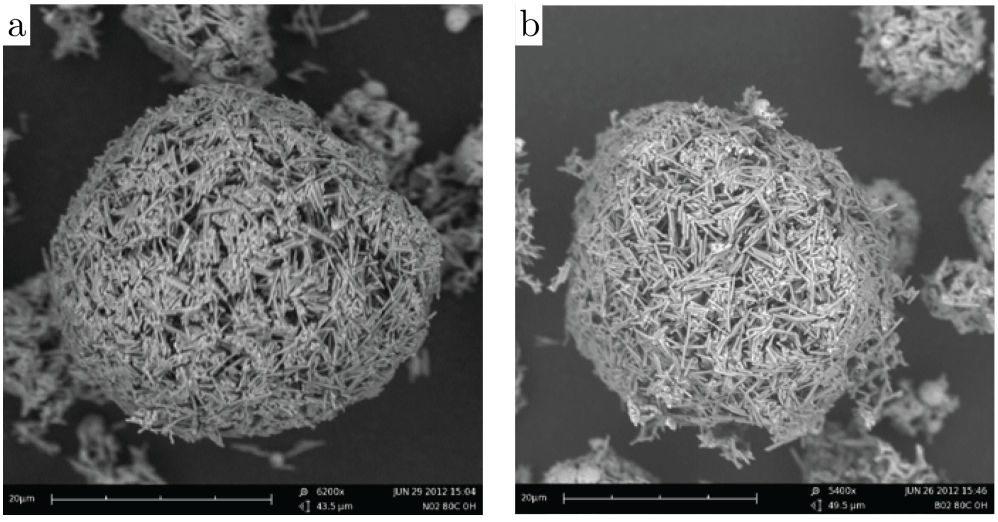


Figure 4.16. SEM images of samples (a) N04 (0 hours) and (b) B04 (0 hours).

Sample B05 appears to essentially have an amorphous arrangement with some visible crystals after 72 hours of ageing (see Figure 4.17). The addition of citrate to the reaction seems to delay the formation of crystals of MIL-88A. This can be due to a

competitive reaction between the sodium citrate and the fumarate chains of MIL-88A.

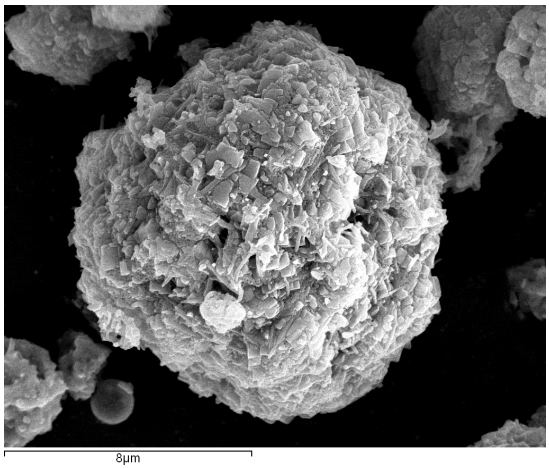


Figure 4.17. SEM image of sample B05 (72 hours).

Big particles of around $20 \times 4\ \mu$m are observed for sample N07. It can be seen that the crystals can easily fracture into smaller pieces (see Figure 4.18). The same observations can be made for sample B07.

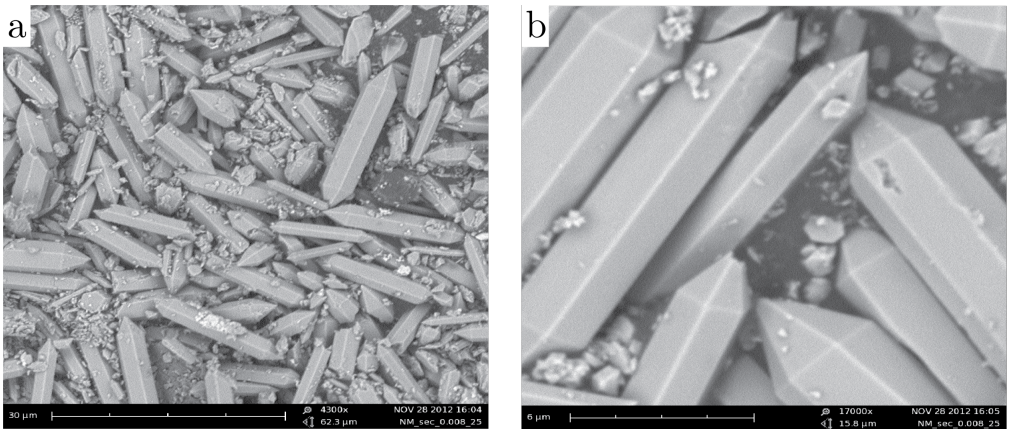


Figure 4.18. SEM image of sample N07: (a) 4300× magnification and (b) 17000× magnification.

4.4.2.4 Particle Size Distribution

From DLS results it is possible to observe the effect of temperature and concentration on the average particle size. DLS analyses were performed to the obtained products after 72h of ageing time.

During the crystallization process of MIL-88A, competition between nucleation and growth processes occurs (Horcajada et al., 2010). Before the crystals develop, the

formation of nuclei, that acts as centres of crystallization, start within the solution. From a global point of view, nucleation of solids is controlled by supersaturation of the solution and the interface energy. To initiate the crystallisation, the supersaturation of the solution is required to overcome the energy barrier for nucleation (Chalati et al., 2011). As soon as stable nuclei have been formed, they begin to grow into larger crystals. Matter is deposited continuously on the crystal face at a rate that is proportional to the difference in concentration between the point of deposition and the bulk of the solution (Mullin, 2001). High supersaturation of the solutions leads to fast nucleation and smaller growth rates. Aggregation of the particles and coalescence processes can also occur with time. Small particles in liquid suspensions have the tendency to cluster together. When particles are small enough, van der Wall forces exceed the gravitational forces and interparticle collision can result in permanent attachment of the particles (Mullin, 2001). Coalescence is a process where the small particles dissolve over time and the solute redeposit onto larger particles. Particles reach a minimum total surface free energy and become thermodynamically more stable (Mullin, 2001).

The particles suspensions were diluted and dispersed in a PVP solution to avoid agglomeration during the period of the DLS analysis. Ultrasounds were also applied to break the particle clusters resulting from the aggregation of particles with time. Results of DLS measurements are presented as number particle size distributions.

Figure 4.19 shows the number particle size distributions for N01, N02 and B02 experiments. It can be observed that the initial mixing conditions are not crucial to obtain smaller particle sizes following this formulation since all experiments present a similar average hydrodynamic diameter.

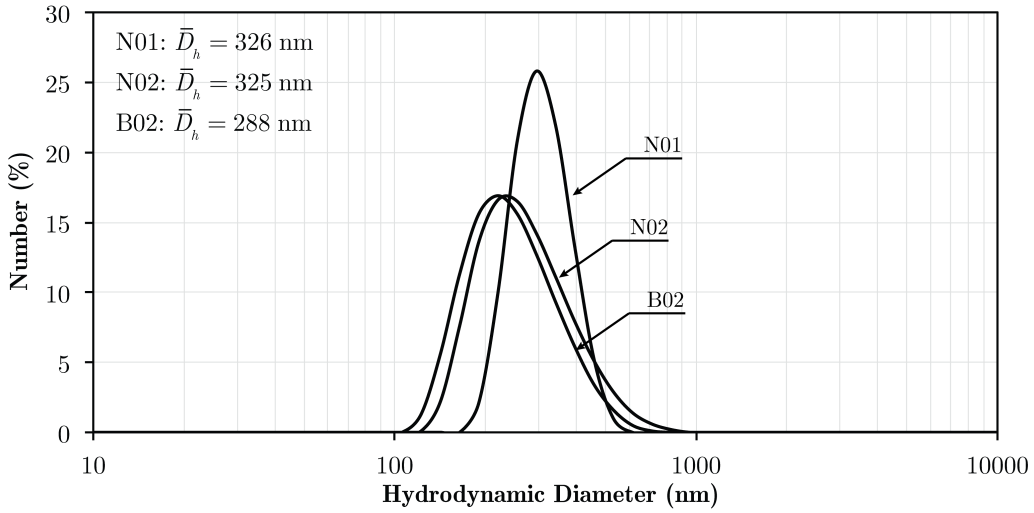


Figure 4.19. Number particle size distribution for N01, N02 and B02 experiments.

Figure 4.20 shows the impact of reaction temperature on experiments conducted at 25°C (B02), 50°C (B06) and 80°C (B04). The increase of temperature promotes both the nucleation and the crystal growth rate (Mullin, 2001). As the temperature of reaction increases, crystal growth rate seems to increase more rapidly and prevail to the nucleation rate and the final dimensions of the crystals are larger.

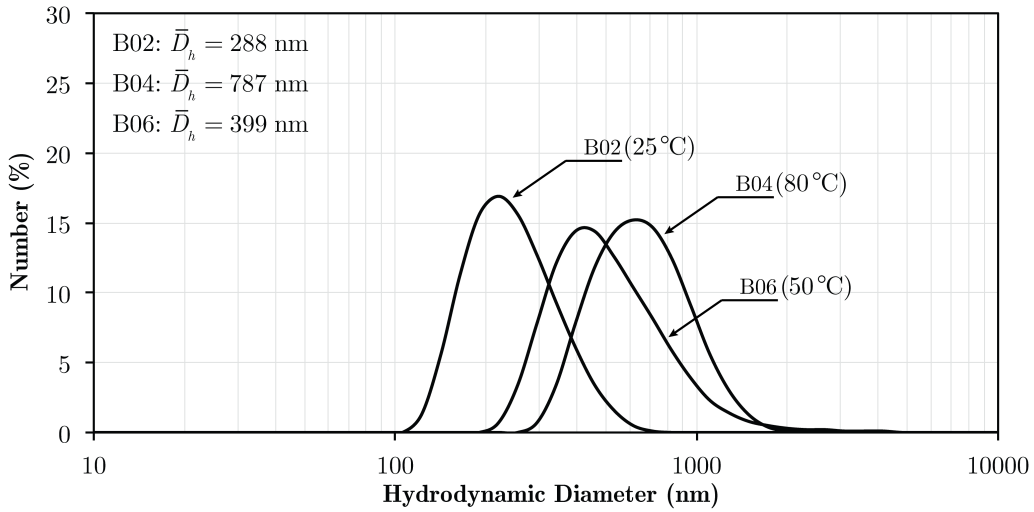


Figure 4.20. Number particle size distribution for B02, B04 and B06 experiments.

Figure 4.21 shows the mean hydrodynamic diameter as a function of temperature determined from the number particle size distribution data of B02, B04 and B06 experiments with a reactants concentration of 0.4 M. The dotted line represents an approximate trend of the results, clearly showing the increase of mean hydrodynamic diameter with the temperature.

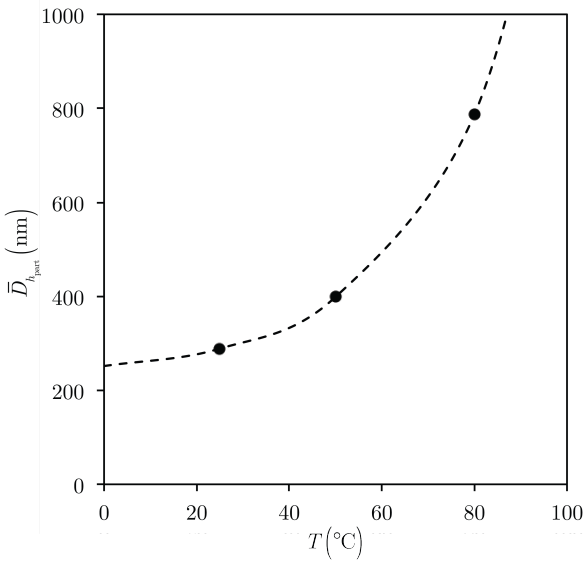


Figure 4.21. Mean hydrodynamic diameter as a function of temperature for reactants concentration of 0.4 M.

Figure 4.22 shows the number particle size distribution for N02, N04 and B04 experiments. From these results it is also possible to conclude that the initial mixing conditions are not crucial to obtain smaller particle sizes for higher temperatures since experiments N04 and B04 present similar average hydrodynamic diameters.

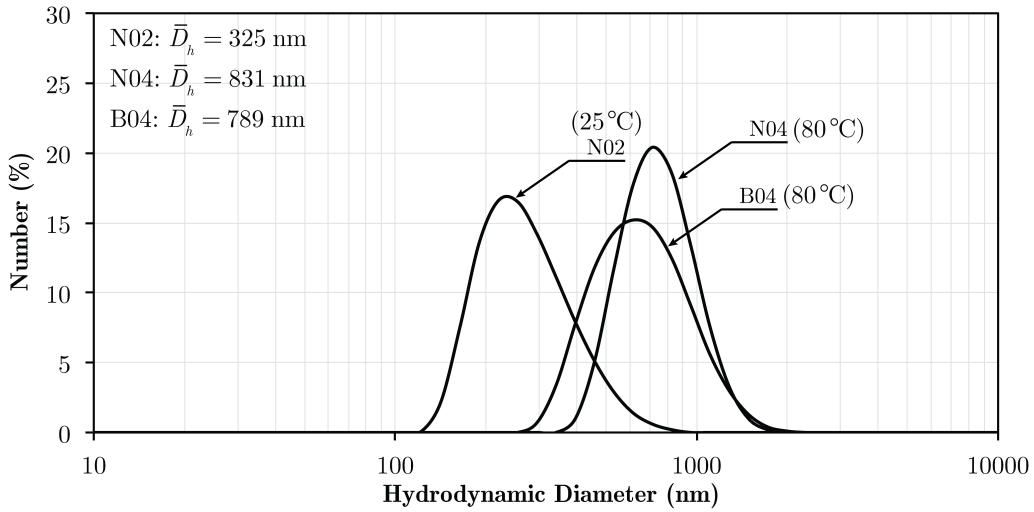


Figure 4.22. Number particle size distribution for N02, N04 and B04 experiments.

The concentration of the reactants affects the particle size distribution as can be seen in Figure 4.23. Although particles have a bigger mean free distance between them and therefore less interaction, nucleation rate is smaller for smaller concentrations. The fewer particles are formed, the larger they can grow from the unreacted species in solution with the ageing process.

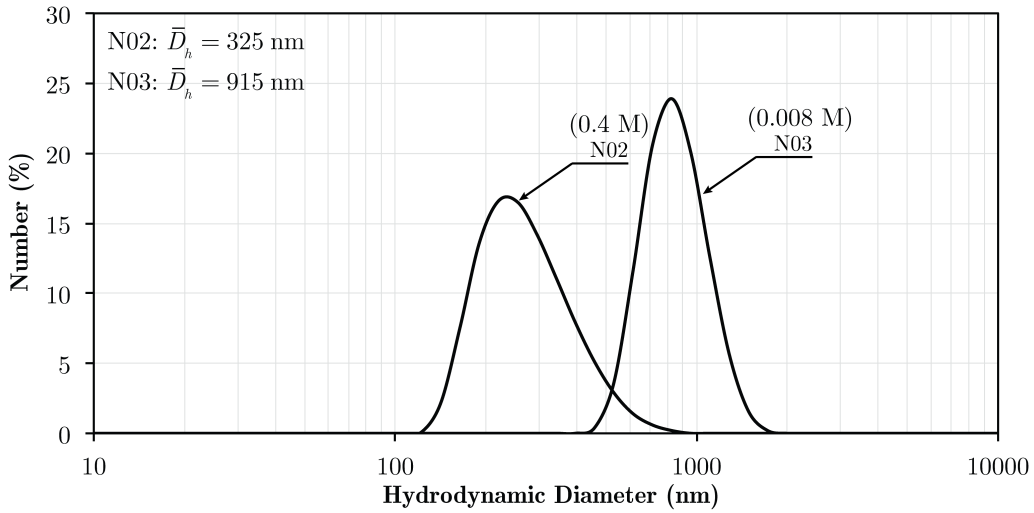


Figure 4.23. Number particle size distribution for N02 and N03 experiments.

For N07 and B07, small hydrodynamic diameters were measured by DLS (see Figure 4.24) but these results are misleading. It was previously shown in Section 4.4.2.3 through SEM imaging that big particles of around $20 \times 4\ \mu$m are formed. Peaks of small hydrodynamic diameter are formed of small pieces that result from the fracture of big crystals due to use of the ultrasound device.

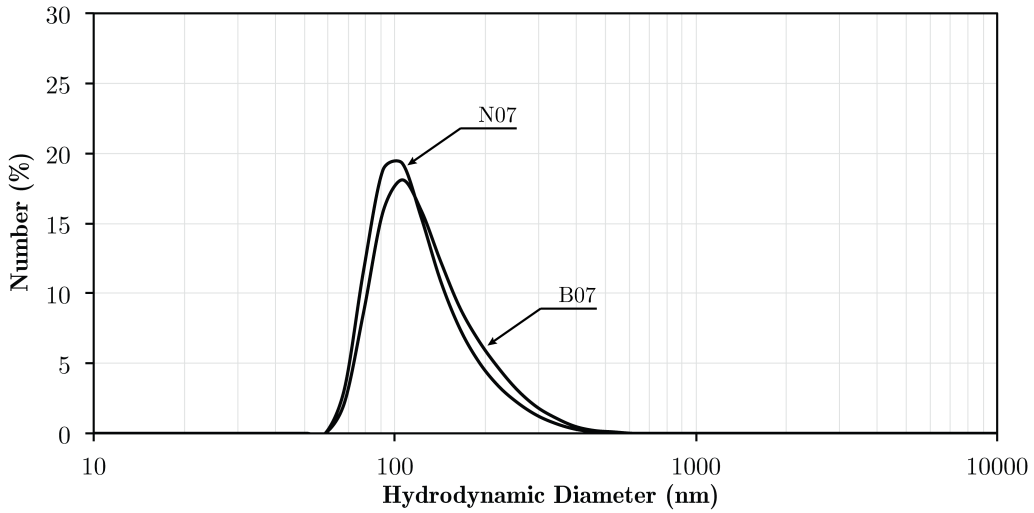


Figure 4.24. Number particle size distribution for N07 and B07 experiments.

Figure 4.25 shows the mean hydrodynamic diameter obtained from DLS as a function of reactants concentration obtained from number particle size distribution data of N02, N03 and N07 experiments performed at 25°C. The grey dot in the figure was estimated from SEM imaging results for N07 sample. The relationship between

hydrodynamic diameter and rod-shaped particles dimensions is described in Appendix B. The dotted line represents an approximate trend of the results.

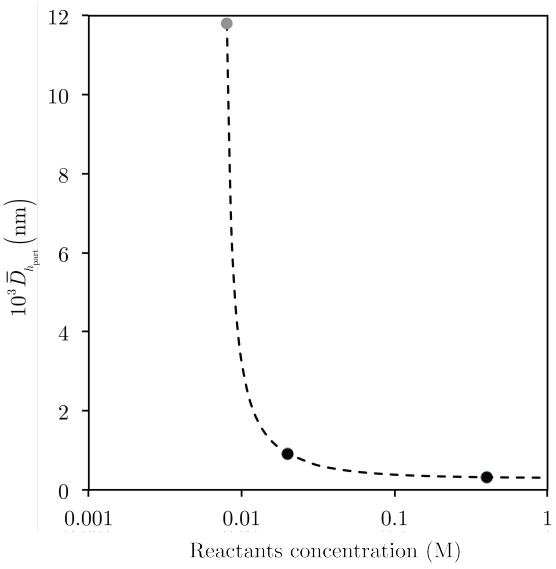


Figure 4.25. Mean hydrodynamic diameter as a function of the reactants concentration at 25°C (grey dot was estimated from SEM imaging results).

The addition of citric acid as a surfactant during the reaction in experiment B05 has a deleterious effect by increasing the particles size and showing no improvements on the suspension stability. Figure 4.26 shows the comparison of the number particle size distribution for B02 and B05 experiments.

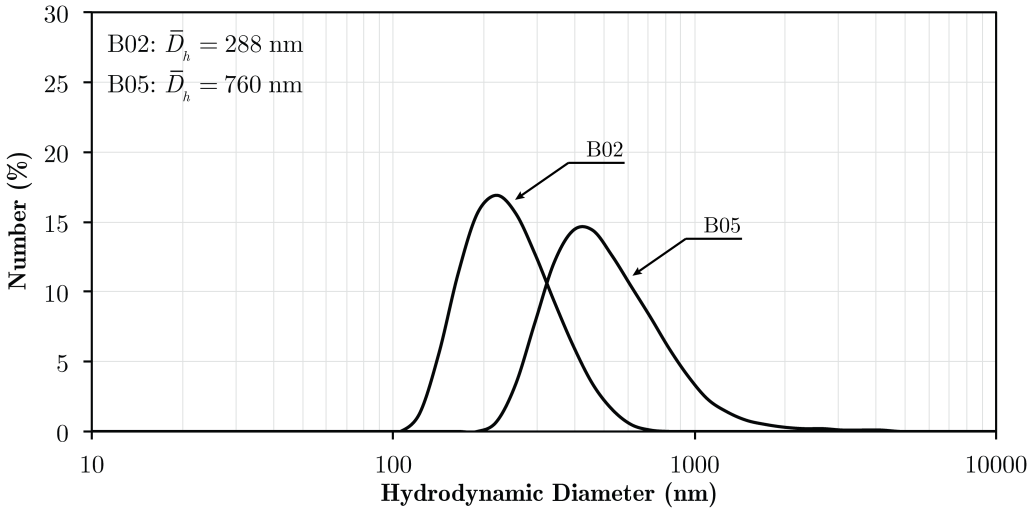


Figure 4.26. Number particle size distribution for B02 and B05 experiments.

Table 4.3 shows the average hydrodynamic diameters and an approximated calculation of the particle length as presented in Appendix B and assuming

$L_{\text{part}} / D_{\text{part}} = 5$ where L_{part} is the length and D_{part} is the diameter of the rod-shaped crystals.

Table 4.3. Average hydrodynamic diameters and approximated average particle length.

Sample	$\overline{D}_{h_{\text{part}}}\left(\text{nm}\right)$	$\overline{L}_{\text{part}}\left(\text{nm}\right)$
N01	326	650
N02	325	650
B02	288	620
N03	915	1800
N04	831	1600
B04	787	1600
B05	760	1500
B06	399	800

These results are in good agreement with the particle sized observed by SEM imaging.

4.4.2.5 Specific Surface Area

The specific surface area of MIL-88A was determined by the BET method. Figure 4.27 shows the nitrogen adsorption isotherm for N01 sample. Degasing was performed at 150°C during 3 hours.

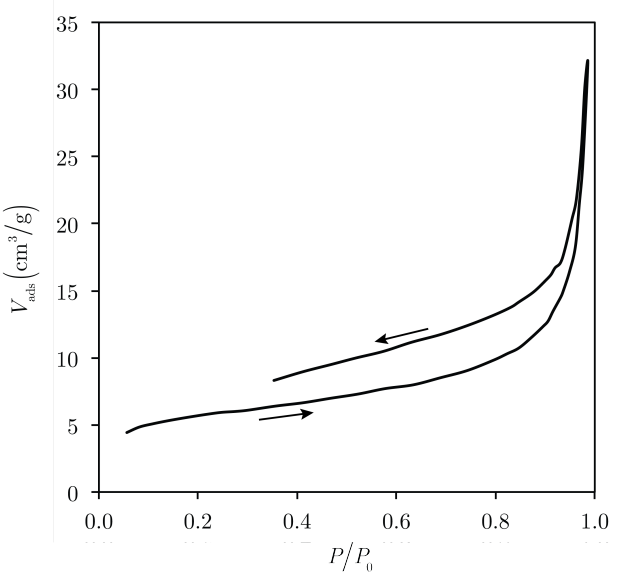


Figure 4.27. Adsorption and desorption isotherm of nitrogen.

Hysteresis is observed in the adsorption/desorption isotherm. The calculated BET specific surface area is 19.6 m^2/g indicating that this sample has poor specific surface area. It was not reported in the literature any measurements of surface area for this particular MOF. The obtained value represents essentially the external specific surface area. For rod-shape particles with 650×130 nm in average, the calculated external specific surface area is $20\ m^2/g$. The description of this calculation is presented in Appendix B.

Two reasons can be pointed for the poor specific surface area:

- the thermal treatment of spray drying may change the material;
- the degasing process may shrink the structure of this MOF preventing nitrogen to penetrate into the pores.

4.4.2.6 Thermal Analysis

To better understand the thermal behaviour of the obtained material and the hydration of the samples, TGA and DSC were performed on sample N01 in an inert atmosphere of nitrogen. The used sample was spray-dried after 72 hours of ageing time.

The obtained results are shown in Figure 4.28. The material starts to lose mass after 100°C due to the vaporization of free water adsorbed in the framework and bounded water to the MIL-88A molecule. The content of water is around 5% for this sample. Around 280°C, another mass loss of around 6% is detected and a peak in the DSC curve appears. Fumaric acid sublimates at the temperature of 287°C but has a flash point at a lower temperature of 206°C (GESTIS, 2013). This mass loss is related to the sublimation of unreacted fumaric acid and fumarate dianions from the MIL-88A molecule and collapse of the structure. The greatest mass loss occurs around 370°C and is related to an endothermic process.

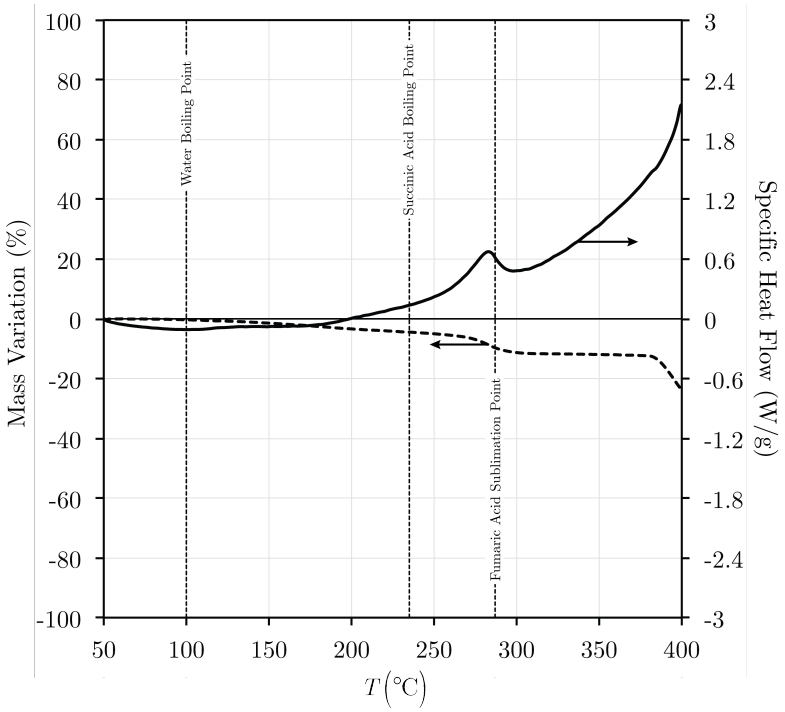


Figure 4.28. TGA and DSC results for sample N01.

Figure 4.29 shows the comparison of the TGA results of N01 samples with experimental results from Serre et al. (2004) using methanol as solvent and with an air atmosphere.

The sample from Serre et al. (2004) loses the free and bonded solvent until the temperature of 150°C. Above 200°C, mass loss related to the departure of fumarate chains from the MIL-88A framework is observed, which happens for lower temperatures when compared to the spray-dried sample N01. The sample undergoes an oxidation process and the residual solid was identified to be Fe_2O_3 by Serre et al. (2004).

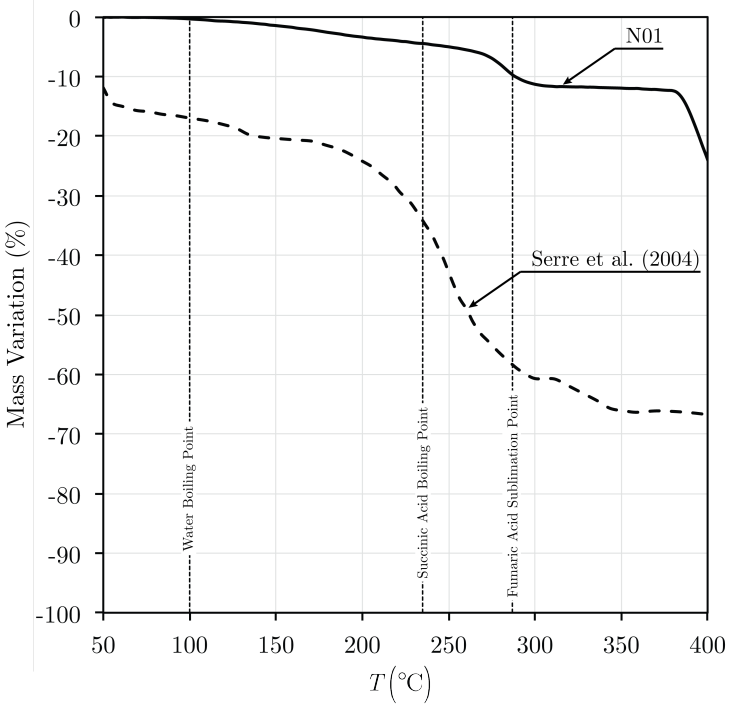


Figure 4.29. TGA results for sample N01 and results from Serre et al. (2004).

4.5 Formulation 2

The ideal synthesis of MIL-88A nanoparticles requires a significant yield, fast and controlled kinetics (Chalati et al., 2011) and an adequate control of the nucleation and growth steps. Slow kinetics can result from the competition of different equilibria between the species in solution and potential secondary precipitation processes. Available reactants in solution will be consumed to produce MIL-88A. Because of that, the equilibrium between the reactants in solution and the secondary precipitate species that were formed is shifted and the secondary precipitate species dissolve. Reactants will be again available for the reaction of MIL-88A but the kinetics is limited by the dissolution rate of the secondary precipitate species.

The study of the equilibrium of the species in solution is fundamental to understand the formation of secondary precipitation phenomena that will compete with the kinetics of crystallization of MIL-88A. It was reported by Chalati et al. (2011) that increasing pH, although increasing the kinetics of crystallization, can lead to the formation of iron oxide/hydroxide by-products which are not suitable for the

preparation of nanoparticles of MIL-88A. The formation of iron(III) hydroxide and fumaric acid precipitates were selected as probable to occur and were investigated.

4.5.1 Precipitation Model of the Instantaneous Equilibrium without Reaction

In this section, a precipitation model is used to study the equilibrium of the ionic species in solution and conditions that may lead to the precipitation of secondary and competitive species, iron(III) hydroxide and fumaric acid. This model was used to evaluate the initial condition of reactants in solution and the immediate equilibrium after mixing but before reaction and formation of MIL-88A occurs.

A map of the regions of precipitation of iron(III) hydroxide and fumaric acid when both reactants are mixed together was plotted that allows the selection of the optimal zone for the production of MIL-88A without competitive precipitations.

For simplicity of nomenclature, the chemical formula of the fumarate ion, $O_2CCH{=}CHCO_2$, was replaced with the short name "Fum".

4.5.1.1 Equilibrium of Fumaric Acid in Aqueous Solutions

The complete dissociation of fumaric acid in solution occurs in two stages:

$$H_2Fum\ (aq) \rightleftharpoons HFum^-\ (aq) + H^+\ (aq) \tag{4.4}$$

and

$$HFum^-\ (aq) \rightleftharpoons Fum^{2-}\ (aq) + H^+\ (aq) \tag{4.5}$$

At equilibrium, the respective dissociation constants are given by

$$K_{HFum^-} = \frac{\left[HFum^-\right]\left[H^+\right]}{\left[H_2Fum\right]} \tag{4.6}$$

and

$$K_{\mathrm{Fum^{2-}}} = \frac{\left[\mathrm{Fum^{2-}}\right]\left[\mathrm{H^{+}}\right]}{\left[\mathrm{HFum^{-}}\right]}. \tag{4.7}$$

Table 4.4 lists the dissociations constants of fumaric acid at different temperatures (Boily and Seward, 2005).

Table 4.4. Dissociation constants of fumaric acid for different temperatures.

$T\left(^{\circ}\mathrm{C}\right)$	$pK_{\mathrm{HFum^{-}}}$	$pK_{\mathrm{Fum^{2-}}}$
10	2.93	4.46
20	2.94	4.46
30	2.96	4.48
40	2.98	4.50
50	3.00	4.52
60	3.03	4.56
70	3.08	4.61
80	3.14	4.65
90	3.21	4.69

Both dissociations constants were fitted to a polynomial equation with less that 1% of deviation:

$$pK_{\mathrm{HFum^{-}}} = 4.06\times10^{-5}T^{2} - 7.33\times10^{-5}T + 2.94 \tag{4.8}$$

and

$$pK_{\mathrm{Fum^{2-}}} = 3.13\times10^{-5}T^{2} - 7.10\times10^{-5}T + 4.45 \tag{4.9}$$

where T is given in $^{\circ}\mathrm{C}$.

Fumaric acid has low solubility in water at room temperature. When the concentration of fumaric acid in solution is higher than the concentration of saturation, no more fumaric acid can be dissolved. The increase of the solution pH shifts the equilibrium thus increasing the solubility of the fumaric acid in solution. The overall reaction for the precipitation of fumaric acid is

$$H_2Fum\ (s) \rightleftharpoons 2H^+\ (aq)\ +\ Fum^{2-}\ (aq) \tag{4.10}$$

and the solubility product of fumaric acid is given by

$$K_{s,\,H_2Fum} = \left[H^+\right]^2 \left[Fum^{2-}\right] . \tag{4.11}$$

Table 4.5 shows the solubility and the solubility constant of fumaric acid as a function of temperature (Lange and Sinks, 1930).

Table 4.5. Solubility and solubility product of fumaric acid for different temperatures.

$T\left(°C\right)$	$S_{H_2Fum}\left(M\right)$	$pK_{s,\,H_2Fum}$
5	2.41×10^{-3}	10.3
10	2.93×10^{-3}	10.2
15	3.55×10^{-3}	10.1
20	4.30×10^{-3}	10.0
25	5.21×10^{-3}	9.91
30	6.32×10^{-3}	9.83
35	7.66×10^{-3}	9.76
40	9.29×10^{-3}	9.69
45	1.13×10^{-2}	9.63
50	1.36×10^{-2}	9.58
55	1.65×10^{-2}	9.54
60	2.01×10^{-2}	9.51
65	2.43×10^{-2}	9.50
70	2.95×10^{-2}	9.49
75	3.57×10^{-2}	9.49
80	4.33×10^{-2}	9.50

The solubility was fitted to the following expression with less than 0.1% of deviation,

$$\ln S_{H_2Fum} = 3.85\times10^{-2}T - 6.22 \tag{4.12}$$

with S_{H_2Fum} in M and T in °C. The solubility product was fitted to a polynomial expression with less than 0.5% of deviation and its dependence with temperature is given by

$$pK_{s,\,H_2Fum} = 1.71\times10^{-4}T^2 - 2.54\times10^{-2}T + 10.4 \tag{4.13}$$

with T in °C.

The dissociation of the fumarate species and precipitation of fumaric acid can be estimated by solving the mass and ionic charge balance of all the species in solution and is described in Appendix D.

To verify the dissociation constants used in the modelling of the equilibrium of fumaric acid, a titration of fumaric acid was performed at 25°C. 200 mL of a solution of fumaric acid 0.04 M was titrated with 50 mL of a solution of sodium hydroxide 0.8 M and the pH was measured. Figure 4.30 shows the measured and calculated pH as a function of the added volume of sodium hydroxide to the fumaric acid solution. It can be concluded that the equilibrium of fumarate species can be well described and the dissociations constants from Table 4.4 are valid.

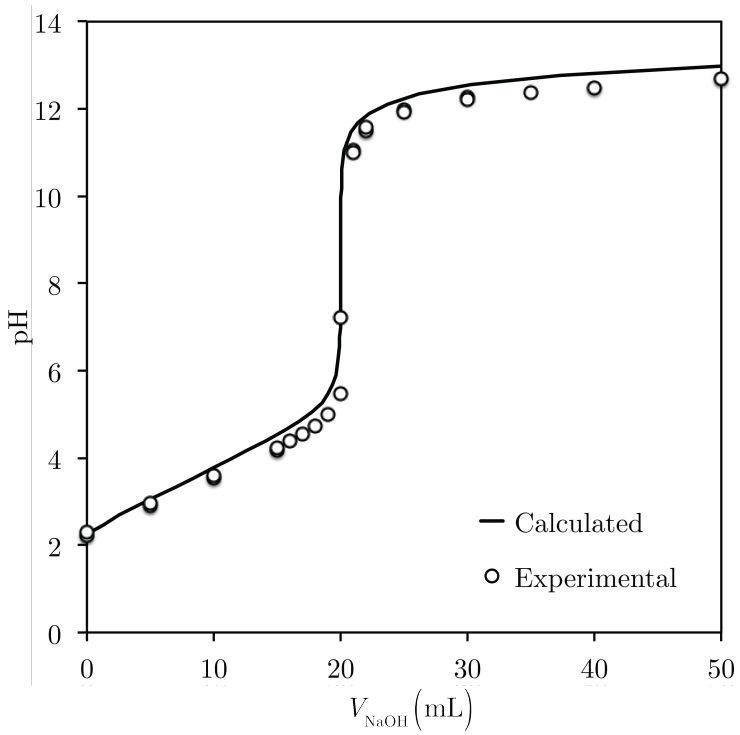


Figure 4.30. Titration of a solution of fumaric acid 0.04 M with a solution of sodium hydroxide.

Figure 4.31 shows the fumaric acid dissociation as a function of pH calculated using dissociation model. It is possible to conclude that higher pH values promote a higher

deprotonation rate of the organic linker which explains the faster kinetic of crystallization of MIL-88A observed by Chalati et al. (2011) when the pH of the reaction medium is increased above 2.7.

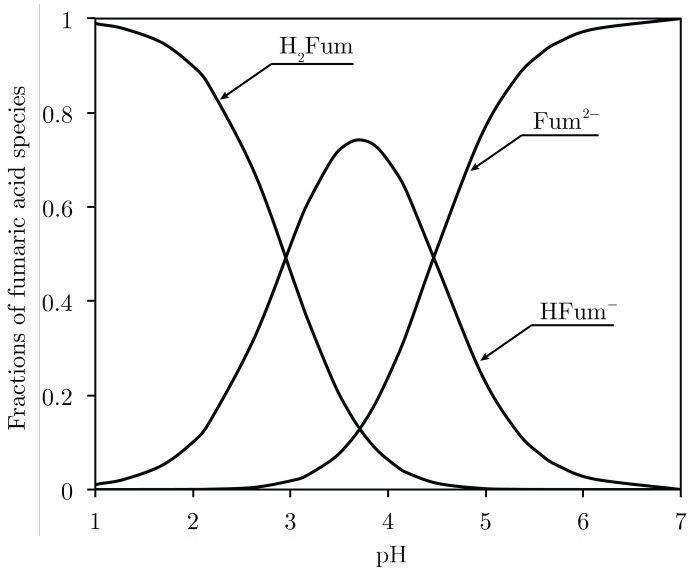


Figure 4.31. Fumaric acid dissociation as a function of pH.

4.5.1.2 Equilibrium of Iron(III) Hydroxide in Aqueous Solutions

The formation of iron(III) hydroxide precipitate with low solubility may explain the darker coloration of the initial suspension and the formation of an amorphous phase in the beginning of the reaction for Formulation 1.

When dissolved in water, iron(III) chloride is completely dissociated and undergoes hydrolysis by the association of Fe^{3+} cations with OH^- anions.

The equilibrium of iron in solution is described by

$$Fe^{3+}\ (aq) \rightleftharpoons Fe\Big(OH\Big)^{2+}\ (aq) + H^+\ (aq) \tag{4.14}$$

and

$$Fe\Big(OH\Big)^{2+}\ (aq) \rightleftharpoons Fe\Big(OH\Big)_2^{+}\ (aq) + H^+\ (aq). \tag{4.15}$$

The respective dissociation constants of the species in equilibrium are given by

$$K_{\mathrm{Fe(OH)^{2+}}} = \frac{\left[\mathrm{Fe(OH)^{2+}}\right]\left[\mathrm{H^{+}}\right]}{\left[\mathrm{Fe^{3+}}\right]} \tag{4.16}$$

and

$$K_{\mathrm{Fe(OH)_2^{+}}} = \frac{\left[\mathrm{Fe(OH)_2^{+}}\right]\left[\mathrm{H^{+}}\right]}{\left[\mathrm{Fe(OH)^{2+}}\right]} \tag{4.17}$$

and at 25°C, $K_{\mathrm{Fe(OH)^{2+}}} = 6.80\times10^{-3}$ and $K_{\mathrm{Fe(OH)_2^{+}}} = 2.60\times10^{-5}$ (Stumm and Lee, 1960).

When the solubility of iron(III) hydroxide is exceeded, precipitation occurs,

$$\mathrm{Fe(OH)_3\ (s) \rightleftharpoons Fe^{3+}\ (aq) + 3OH^{-}\ (aq).} \tag{4.18}$$

The solubility product of iron(III) hydroxide is given by

$$K_{s,\,\mathrm{Fe(OH)_3}} = \left[\mathrm{Fe^{3+}}\right]\left[\mathrm{OH^{-}}\right]^3 \tag{4.19}$$

and at 25°C, $K_{s,\,\mathrm{Fe(OH)_3}} = 6.0\times10^{-38}$ (Ghosh et al., 1966).

Despite the low solubility, iron(III) hydroxide can still be found in solution in equilibrium with the formed solid,

$$\mathrm{Fe(OH)_3\ (s) \rightleftharpoons Fe(OH)_3\ (aq)} \tag{4.20}$$

The solubility constant is given by

$$K_{d,\,\mathrm{Fe(OH)_3}} = \left[\mathrm{Fe(OH)_3}\right] \tag{4.21}$$

and at 25°C, $K_{d,\,\mathrm{Fe(OH)_3}} = 2.9\times10^{-7}$ (Stumm and Lee, 1960).

In alkaline solutions (pH>12), $Fe\left(OH\right)_4^-$ anions can be formed (Stumm and Lee, 1960),

$$Fe\left(OH\right)_3\ (s) + OH^-\ (aq) \rightleftharpoons Fe\left(OH\right)_4^-\ (aq) \tag{4.22}$$

At equilibrium, the dissociation constant is given by

$$K_{Fe(OH)_4^-} = \frac{\left[Fe\left(OH\right)_4^-\right]}{\left[OH^-\right]}. \tag{4.23}$$

and at $25°C$, $K_{Fe(OH)_4^-} \approx 10^{-5}$ (Ghosh et al., 1966; Stumm and Lee, 1960).

The equilibrium of iron(III) in solution and precipitation of iron hydroxide acid can be estimated by solving the mass and ionic charge balance of all the species in solution and is described in Appendix D. To verify the dissociation constants used in the modelling of the equilibrium of iron(III) hydroxide, different iron(III) chloride solutions were prepared and the pH was measured. Experimental pH results are well described by the dissociation/precipitation modelling with a maximum deviation of 2% (Figure 4.32).

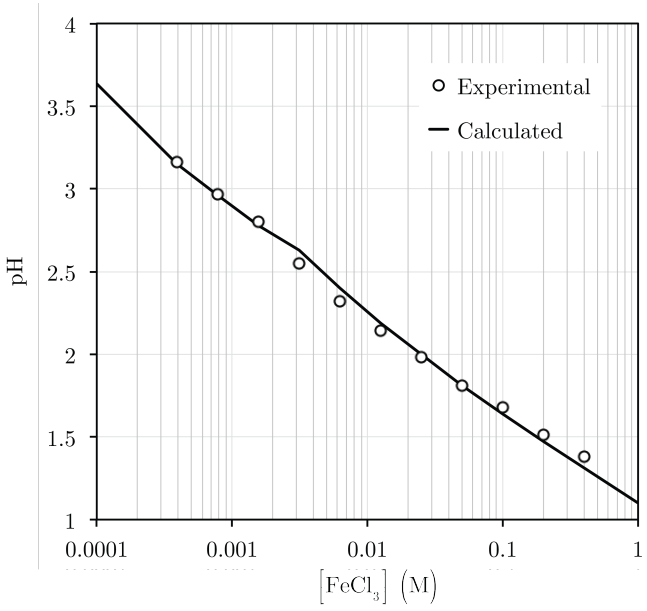


Figure 4.32. pH of solution of iron(III) chloride as a function of concentration.

Furthermore, 100 mL of a solution of iron(III) chloride 0.4 M was titrated with a solution of sodium hydroxide 0.8 M and the pH was measured and compared with calculated values. Experiments were carried out at 25°C. Figure 4.33 shows the pH as a function of the added volume of sodium hydroxide to the solution of iron(III) chloride. For higher the concentrations of sodium hydroxide in solution, other iron oxide/hydroxide can be formed (Pourbaix, 1974) which are not taken into consideration in this model and can explain the deviation from the experimental results for higher concentration of sodium hydroxide and the pH increase.

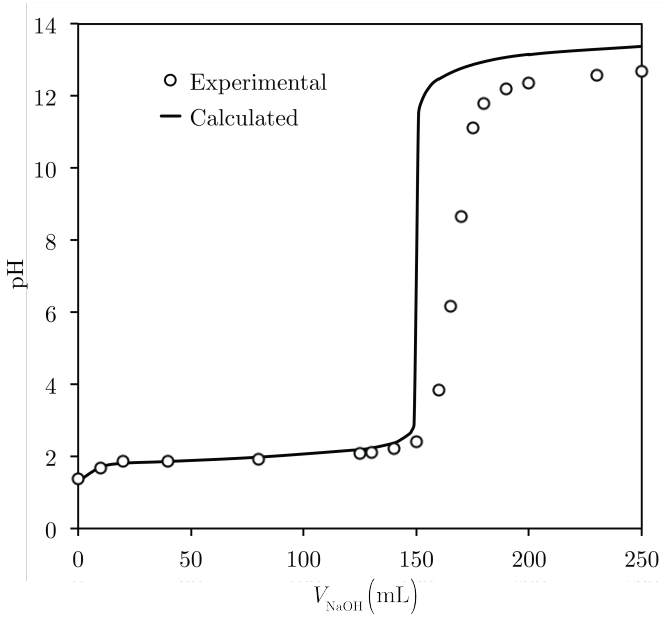


Figure 4.33. Titration of iron(III) Chloride solution with sodium hydroxide.

Higher temperatures (above 100°C), commonly used in hydrothermal synthesis and micro-wave assisted irradiation, also promote the formation of iron oxide/hydroxide secondary products and possibly Fe_2O_3 maghemite (Parsons et al., 2009). Furthermore, iron(III) hydroxide solubility decreases with the increase of temperature (Taylor et al., 1999). Figure 4.34 shows the observed effect of temperature in a solution of iron(III) chloride 0.008 M. As the temperature increases, the coloration of the solution changes from pale yellow becoming darker and brown and the pH of the solution decreases. Furthermore, the presence of particles was detected through DLS.

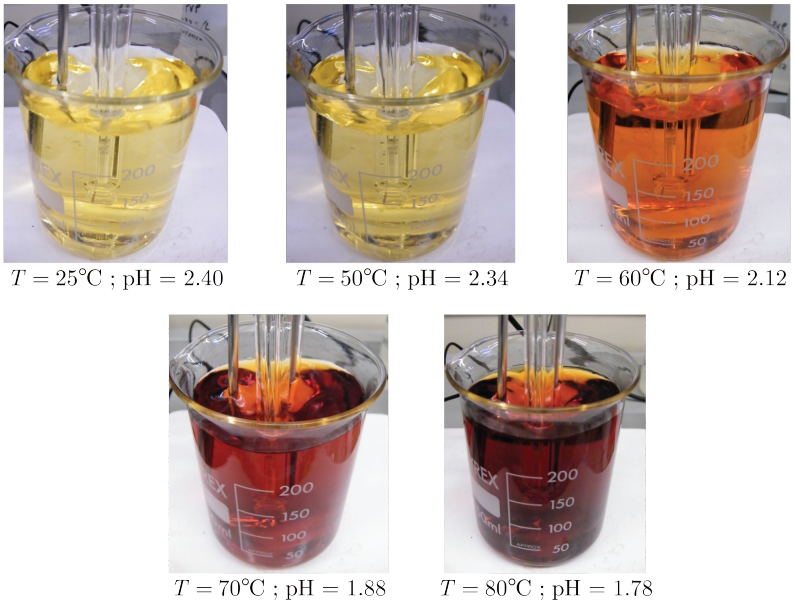


Figure 4.34. Effect of temperature on the solubility of iron(III) hydroxide in a solution of iron(III) chloride with concentration 0.008 M.

To overcome the formation of iron(III) hydroxides and oxides, lower temperatures should be preferred while producing MIL-88A.

4.5.1.3 Instantaneous Equilibrium without Formation of MIL-88A

Although faster kinetics of crystallization of MIL-88A are achieved for higher pH values by favouring the dissociation of fumaric acid, the increase of pH can also lead to faster growth rates and generate larger particles (Chalati et al., 2011). Furthermore, the increase of temperature also leads to the formation of iron oxide/hydroxide secondary products and possibly Fe_2O_3 maghemite while decreasing the solubility of iron(III) hydroxide. Room temperature of 25°C was considered to favour the precipitation of small MIL-88A particles and the following study of equilibrium will focus on that temperature.

After mixing both reactants, the immediate equilibrium without formation of MIL-88A can be estimated by solving the mass and ionic charge balance of all the species in solution. In Appendix D is described the method for solving the immediate equilibrium without formation of MIL-88A that takes into account the possibility of precipitation of iron(III) hydroxide and fumaric acid after both reactants are mixed together.

The absence of competitive precipitation processes can be achieved by tuning the pH and concentration of the reactants.

Figure 4.35 shows a map of the regions of precipitation of iron(III) hydroxide and fumaric acid when both reactants are mixed together at room temperature of 25°C. $\chi = [\mathrm{HCl}] - [\mathrm{NaOH}]$ is the difference of concentrations of hydrochloric acid added to the iron(III) chloride solution and sodium hydroxide added to fumaric acid solution.

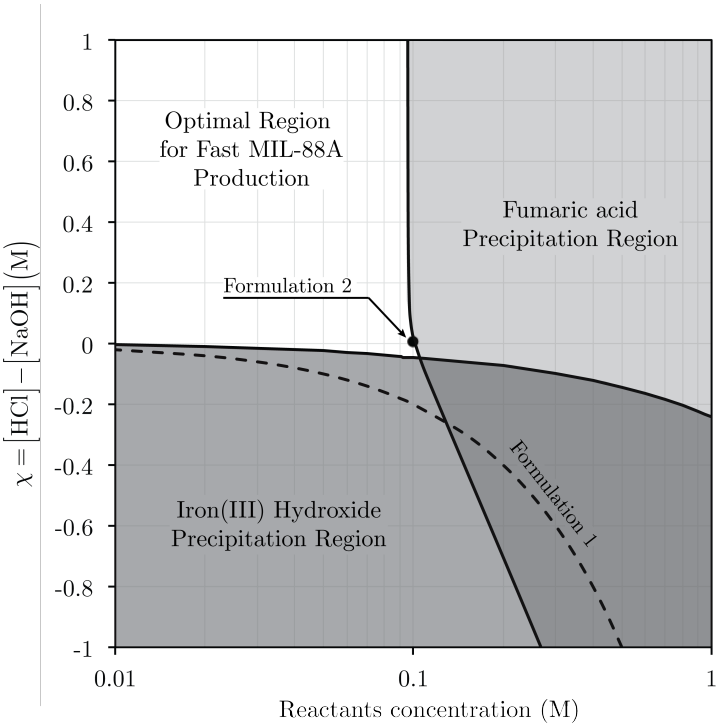


Figure 4.35. Map of fumaric acid and iron(III) hydroxide precipitation regions.

The necessary concentration of sodium hydroxide to increase the solubility of fumaric acid and ensure complete dissolution was calculated from the precipitation model and can be correlated to a polynomial expression with 2% of deviation and is given by:

- If $[\mathrm{H_2Fum}] > S_{\mathrm{H_2Fum}}$

$$[\mathrm{NaOH}]_d = 0.218[\mathrm{H_2Fum}]^2 + 1.08[\mathrm{H_2Fum}] - 0.0577\,; \tag{4.24}$$

- If $[\mathrm{H_2Fum}] < S_{\mathrm{H_2Fum}}$

$$\left[\mathrm{NaOH}\right]_d = 0 \tag{4.25}$$

where $S_{\mathrm{H_2Fum}}$ is the solubility of fumaric acid.

The concentrations of hydrochloric acid added to the iron(III) chloride solution and sodium hydroxide added to fumaric acid solution can be estimated for two different cases. If $\chi - \left[\mathrm{NaOH}\right]_d > 0$, the concentrations of hydrochloric acid and fumaric acid are calculated by

$$\begin{cases} \left[\mathrm{HCl}\right] = \chi - \left[\mathrm{NaOH}\right]_d \\ \left[\mathrm{NaOH}\right] = \left[\mathrm{NaOH}\right]_d \end{cases} \tag{4.26}$$

and if $\chi - \left[\mathrm{NaOH}\right]_d < 0$ then the concentrations of hydrochloric acid and fumaric acid are calculated by

$$\begin{cases} \left[\mathrm{HCl}\right] = 0 \\ \left[\mathrm{NaOH}\right] = -\chi \end{cases}. \tag{4.27}$$

In Figure 4.35 is also plotted the operational zone used in Formulation 1. Independently of the concentration used, the formation of iron(III) hydroxide precipitate is always probable. Likewise, for higher reactants concentrations, the precipitation of fumaric acid can also occur. For Formulation 1, the formation of MIL-88A will compete with the formation of precipitate of secondary products and only by slow dissolution processes, the crystallization of MIL-88A can achieve high conversion.

To overcome the occurrence of competitive precipitation processes, Formulation 2 was conceived and the concentration of reactants of $0.1\,\mathrm{M}$ with $\chi = 0.007$ close to the maximum possible concentration was selected (see Figure 4.35). A high concentration in the optimal zone for production of MIL-88A will promote nucleation and the formation of smaller particles.

4.5.2 Experimental Description

In this section, the composition of the reactants is described. The composition of each reactant solution and pH were tuned to overcome the occurrence of competitive precipitation processes and selected accordingly to the strategy developed in Section 4.5.1.3. The different steps of the process for this formulation are described and the three different operation modes used for the production of MIL-88A are presented.

Equal volumes ($250\,\mathrm{mL}$) of a solution of iron(III) chloride $0.1\,\mathrm{M}$ and a solution of fumaric acid $0.1\,\mathrm{M}$ were prepared. Sodium hydroxide with a concentration of $0.055\,\mathrm{M}$ was added to the solution of fumaric acid to increase the solubility. Hydrochloric acid was added to the solution of iron(III) chloride to avoid the precipitation of iron(III) hydroxide when both solutions are mixed. The pH of the solution was set to 0.98 .

For this formulation, the overall process is divided into three different steps.

- The first step consists on mixing of the two solutions of reactants. The reactants can be mixed in a vessel with a magnetic stirrer by placing one of the reactants and immediately adding the other reactant or it can be performed in the NETmix reactor by injecting both reactants following the pre-mixed inlet scheme used in Formulation 1 (see Figure 4.5). For the experiments using the NETmix reactor, a total inlet flow rate of $1.03\,\mathrm{L/min}$ was used to achieve $\mathrm{Re} = 600$ in the NETmix channels calculated assuming water physical properties at $25\,^{\circ}\mathrm{C}$. The residence time inside the NETmix reactor is $1.5\,\mathrm{s}$.
- The second step consists of a nucleation step. During this step, nucleation of MIL-88A starts to occur and the formation of particles is visible in the solution. This step has the duration of 10 minutes and is performed in a vessel with stirring induced through a magnetic stirrer. During this step, the solution can be continuously recirculated through the NETmix reactor.

- The third step consists on the dilution of the obtained solution. Agitation is stopped and 200 mL of the solution was transferred to a flask. Distilled water is added until a dilution ratio of 1:5. This step increases the mean free distance between particles from $\Delta x_{part} / L_{part} = 0.71$ to $\Delta x_{part} / L_{part} = 1.9$ and decreases the interactions between particles preventing them to agglomerate. This step also tries to overcome the coalescence growth process that was observed by Chalati et al. (2011) when water is used as solvent. If this step is not performed, particles aggregate and sediment within few hours after reaction.

Three different operation modes were tested for the production of MIL-88A: the Batch operation mode, the NETmix operation mode and the NETmix with recirculation operation mode. In the Batch operation mode, the mixing and the nucleation steps where performed in a stirred vessel. In the NETmix operation mode, mixing of reactants was performed in the NETmix reactor and the nucleation step was performed in a stirred vessel. In the NETmix with recirculation operation mode, mixing of reactants was performed in the NETmix reactor and the nucleation step was performed in a stirred vessel but the obtained solution was continuously recirculation in the NETmix reactor.

After the dilution step, the particle suspensions were centrifuged for more than 24 hours at 25°C and at a centrifugal force of 15000g. The supernatant was analysed by DLS to ensure that the presence of particles was not detected.

4.5.3 Results and Discussion

The reproducibility of each operation mode was tested by duplicating each experiment. For all operation modes, similar results were obtained in terms of particle size distribution, with the average diameter not varying more than 5 nm.

The appearance of the obtained solution after mixing both reactants changed through the different steps of Formulation 2. When reactants are mixed, a pale yellow solution was obtained. Figure 4.36a shows the coloration of a solution right after the

mixing of both reactants. With time, particles started to appear and the solution became darker with an orange coloration, which can be seen in Figure 4.36b where it is shown the coloration of a solution after 10 minutes of reaction time. The presence of small particles in suspension was detected through inspection of the solution with a laser beam. Particles suspended will diffract the light and the laser beam will become visible when crossing the medium.

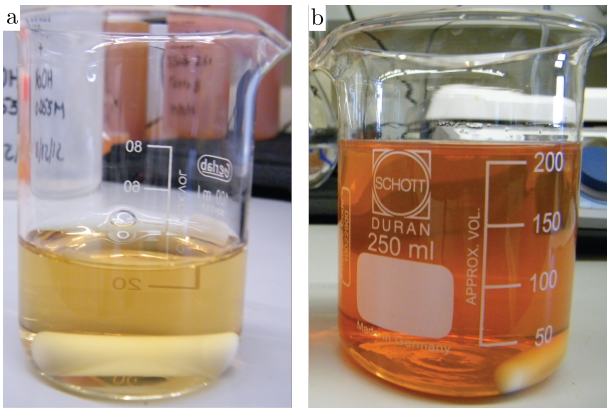


Figure 4.36. Solutions after addition of both reactants: (a) immediate addition and (b) after 10 minutes of reaction.

After the dilution step, a transparent suspension was obtained of orange-pink coloration for all the tested operation modes. With time, the suspension started to get more turbid but still transparent as shown in Figure 4.37.



Figure 4.37. MIL-88A particles suspension after dilution.

Sediments started to appear in the bottom of the flask after 72 hours of ageing showing that aggregation still occurs with time despite being delayed. Yet, the sediment could easily be resuspended with ultrasounds.

After centrifugation, a transparent gel was obtained as shown in Figure 4.38. A portion of the obtained gel was dried in an atmosphere of nitrogen for 48 hours. Wet and dried gels were used for the characterization of the product.

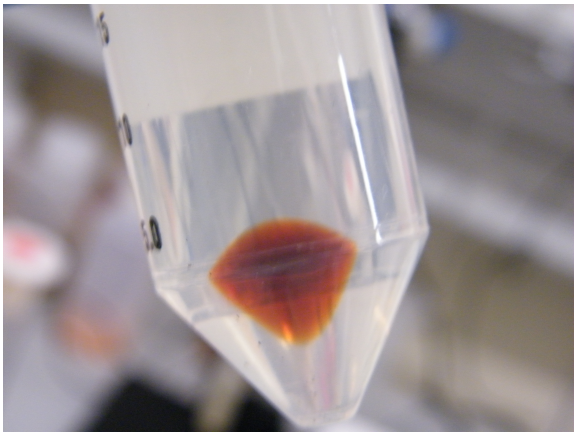


Figure 4.38. Gel obtained from centrifugation.

4.5.3.1 Iron(III) Conversion

The iron conversion for the crystallization of MIL-88A was determined for the three operation modes. For the Batch operation mode 76% of conversion was obtained, and for the NETmix operation modes, both without and with recirculation, 73% of conversion was obtained. These results are similar to the results obtained in N03 samples for Formulation 1 carried out at the same reactants concentration with a final conversion of 80%. These results seem to indicate that the final conversion is related to the chemical equilibrium of all species in solution.

4.5.3.2 XRD Analysis

XRD analysis was performed to confirm the production of MIL-88A with this formulation.

Figure 4.39 shows the XRD patterns for the Batch, and the NETmix without and with recirculation operation modes. The experimental results are compared with the simulation XRD pattern for MIL-88A in its open form due to water molecules adsorbed as determined by Mellot-Draznieks et al. (2005).

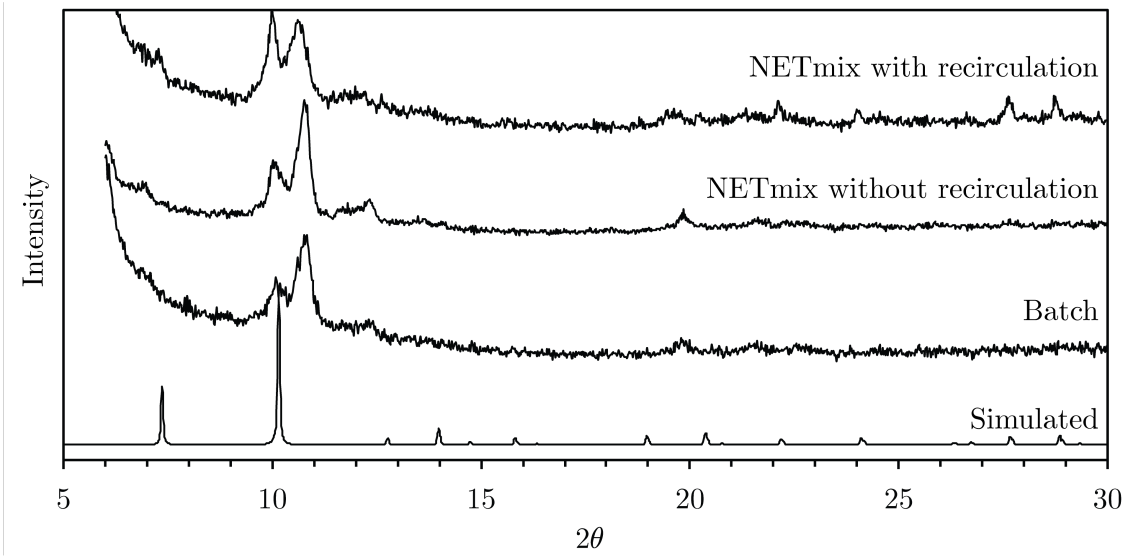


Figure 4.39. Simulated and experimental XRD patterns for Batch, NETmix without recirculation and NETmix with recirculation, operation modes.

Samples were analyzed to verify the presence of other phases but no secundary phases were detected by XRD. Sodium chloride is removed by centrifugation and no iron oxide/hydroxide species and unreacted fumaric acid were detected.

Mellot-Draznieks et al. (2005) observed that the state of hydration can strongly modify both the position and intensity of the peaks since MIL-88A is a flexible solids. The simulated XRD patterns of the closed (Serre et al., 2004) and open frameworks of MIL-88A were compared to the XRD pattern for the dry gel for the NETmix with recirculation sample (Figure 4.40). It is possible to see that the experimental results match a combination of both simulated XRD patterns. The samples must retain yet some hydrated zones but part of the sample is in its closed form of the framework.

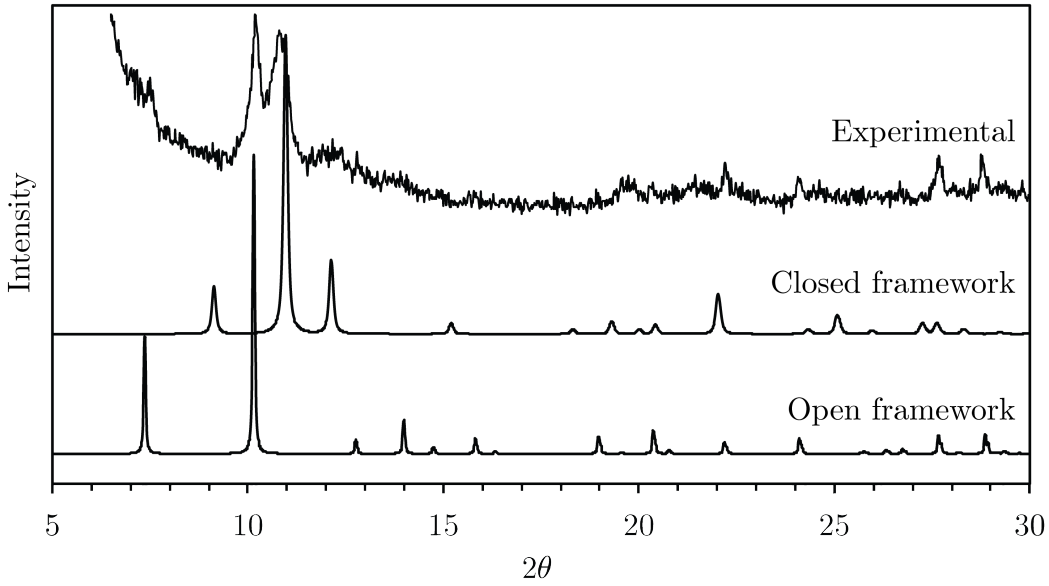


Figure 4.40. Simulated XRD patterns of closed and open frameworks and experimental XRD pattern.

4.5.3.3 Particle Size Distribution

Figure 4.41, Figure 4.42 and Figure 4.43 show the number particle size distribution for the Batch and the NETmix operating modes without and with recirculation, respectively. Measures of particle size distribution were performed after dilution, 72 hours after dilution and 2 weeks after dilution.

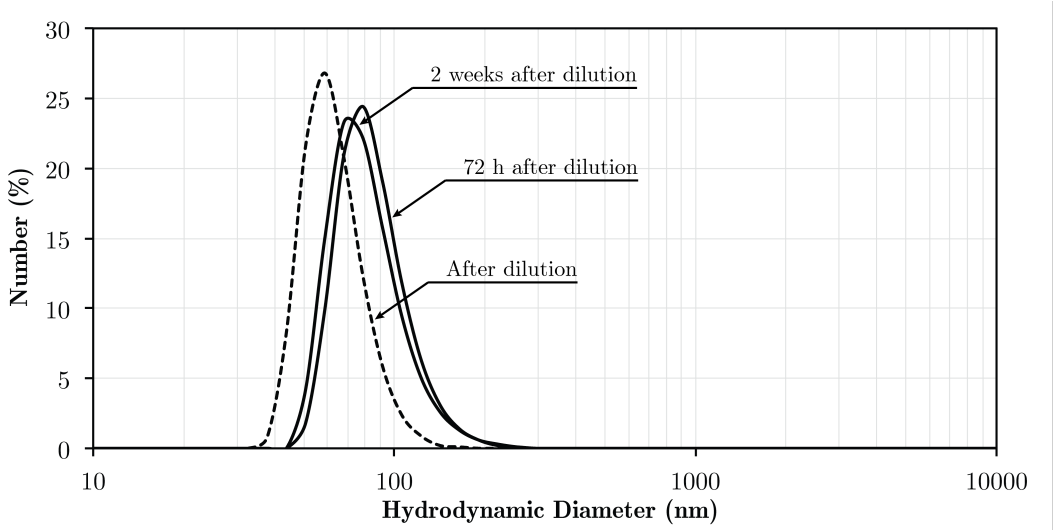


Figure 4.41. Number particle size distribution for the Batch operation mode after dilution, 72 hours after dilution and 2 weeks after dilution.

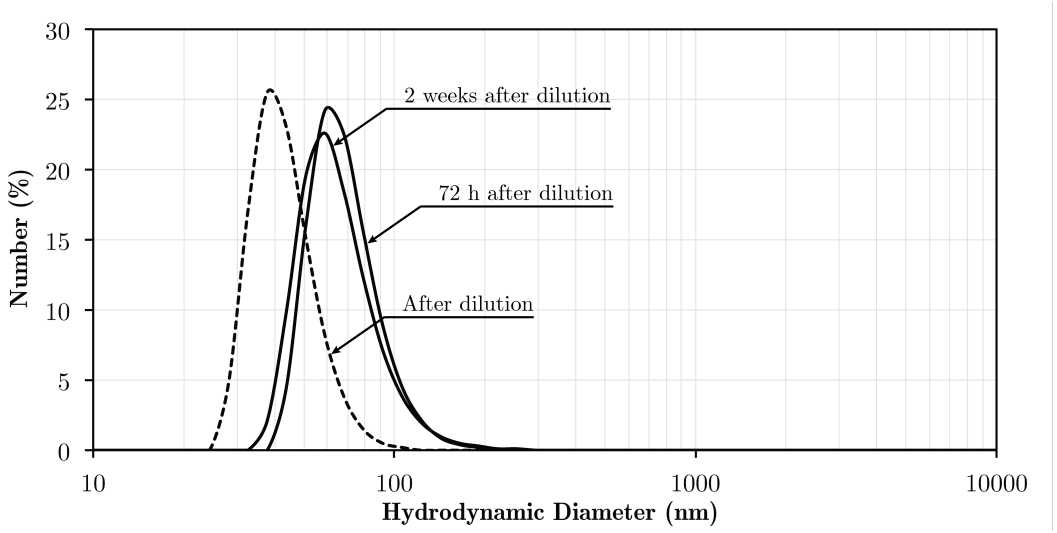


Figure 4.42. Number particle size distribution for the NETmix without recirculation operation mode after dilution, 72 hours after dilution and 2 weeks after dilution.

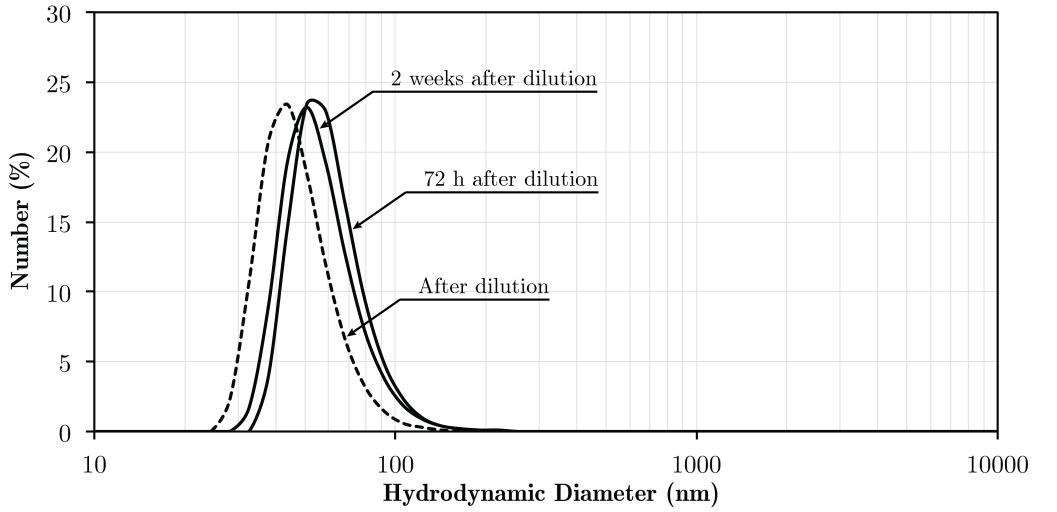


Figure 4.43. Number particle size distribution for the NETmix with recirculation operation mode after dilution, 72 hours after dilution and 2 weeks after dilution.

Particle growth after dilution is still detected by DLS but a stationary value of particle size is achieved. Although particle agglomeration and sedimentation is observed, particles can be re-suspended with the use of ultrasounds and comparable results of particle size distribution are obtained for measurements 72 h and 2 weeks afterwards.

Figure 4.44 shows the comparison of the number particle size distribution for the experiments using the Batch and the NETmix operation modes with and without recirculation for 72h after dilution.

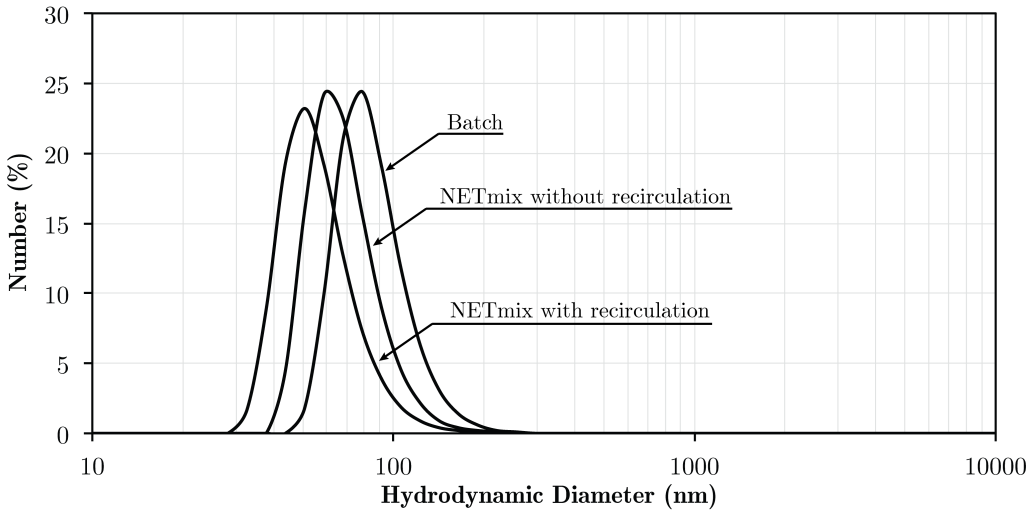


Figure 4.44. Number particle size distribution for the experiment in batch, NETmix without recirculation and NETmix with recirculation 72 hours after dilution.

It is known that nucleation can often be stimulated by agitation and an efficient mixing (Mullin, 2001). It was observed that, when NETmix reactor is used, smaller diameters are obtained. Recirculation in the NETmix reactor during the nucleation step also produced particles with smaller size.

Table 4.6 shows the average hydrodynamic diameters and an approximated calculation of the particle length as presented in Appendix B and assuming $L_{\text{part}} / D_{\text{part}} = 5$.

Table 4.6. Average hydrodynamic diameters and approximated particle length.

Sample	$\bar{D}_{h_{\text{part}}}\left(\text{nm}\right)$	$L_{\text{part}}\left(\text{nm}\right)$
Batch	94	190
NETmix without recirculation	76	150
NETmix with recirculation	64	120

4.5.3.4 Thermal Analysis

The thermal behaviour of the obtained product using the NETmix with recirculation operation mode was analysed by TGA and DSC in an inert atmosphere of nitrogen. The analysis was made for wet gel, dried gel and spray-dried powder.

Figure 4.45 shows the TGA and DSC results for a sample of wet gel after centrifugation; the main observations for this case are:

- The material starts to lose mass immediately after the beginning of the analysis due to the vaporization of water contained in the gel. Also the free water adsorbed in the framework and bounded water to the MIL-88A molecule start to vaporize around 100°C. This sample loses a high content of water of around 67% of the initial mass from water contained in the gel, free water adsorbed in the framework and bounded water to the MIL-88A molecule.
- Around 235°C, another mass loss of around 30% is detected and an endothermic peak in the DSC curve appears. This temperature is interestingly close to the succinic acid boiling point, 235°C (GESTIS, 2013). This could suggest that a hydrogenation process occurs to the fumarate chains in the framework but this hypothesis seems unrealistic since no hydrogen gas is present or released to carry out the reaction. Another hypothesis is the electrophilic addition of chlorine to the double bound of fumarate chains from the hydrochloric acid in solution creating chlorosuccinic acid with a boiling point of 236°C (GESTIS, 2013). None of the hypothesis could be confirmed.
- After 236°C no more mass loss is detected. Nevertheless, the DSC curve indicates that an endothermic reaction may be occurring.

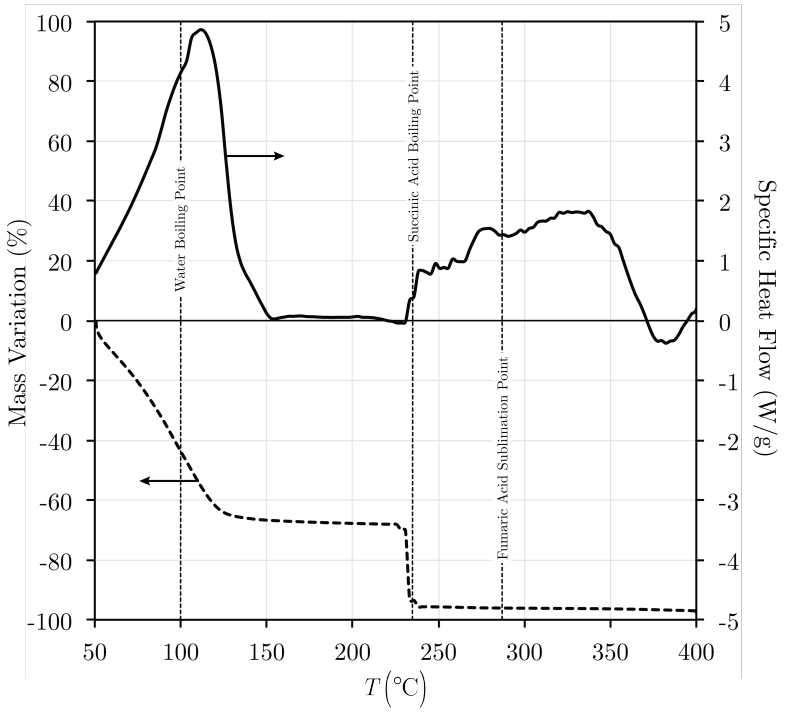


Figure 4.45. TGA and DSC results for a sample of wet gel.

Figure 4.46 shows the TGA and DSC results for a sample of dried gel, with the following main observations:

- The material starts to lose mass after 100°C due to the vaporization of free water adsorbed in the framework and bounded water to the MIL-88A molecule. The water content of this sample is around 9% and is much smaller than the water content in the wet gel sample.
- For the closed form of the framework with no adsorbed free solvent, the bounded water content corresponds to 9% of the molecule's mass and is similar to the obtained TGA value. However, it is not conclusive if the water loss corresponds only to the vaporization of bounded water in the molecule of MIL-88A. XRD results suggest that the dried gel sample still contains free water that expands the structure.
- Around 235°C, mass loss of around 30% is detected and an endothermic peak in the DSC curve appears, similarly to what happens in the wet gel sample.
- From 240°C to 310°C, an exothermic process is observed. Exothermic processes can be related to a process of recrystallization of the sample.
- Around 285°C, an endothermic process contraries the exothermic process. This endothermic process is associated with 8% of mass loss so it must be caused by the sublimation of fumaric acid molecules from the MIL-88A structure.
- From 310°C to 400°C an endothermic process occurs and a mass loss of 4% is observed.

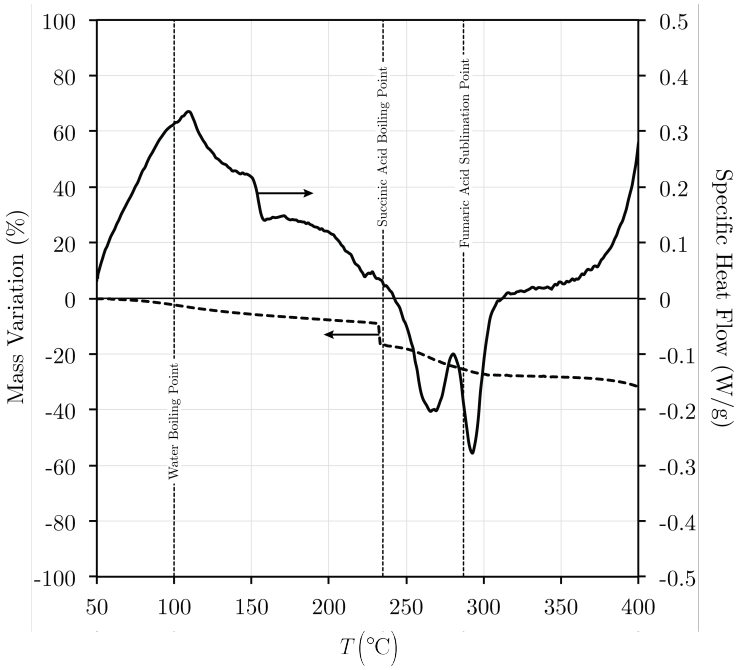


Figure 4.46. TGA and DSC results for a sample of dry gel.

Figure 4.47 shows the TGA and DSC results for a sample of spray-dried powder for which the main observations are:

- The water content of this sample is around 13% and is higher than the dried gel sample. It can be concluded that the spray drying treatment still retains free adsorbed water in the molecule.
- From 240°C to 310°C, an exothermic process is observed. Above 235°C, mass loss related to the departure of fumarate chains from the MIL-88A framework and unreacted fumaric acid is observed. The mass loss coincides with a changes in the specific heat flow that contraries the exothermic process.

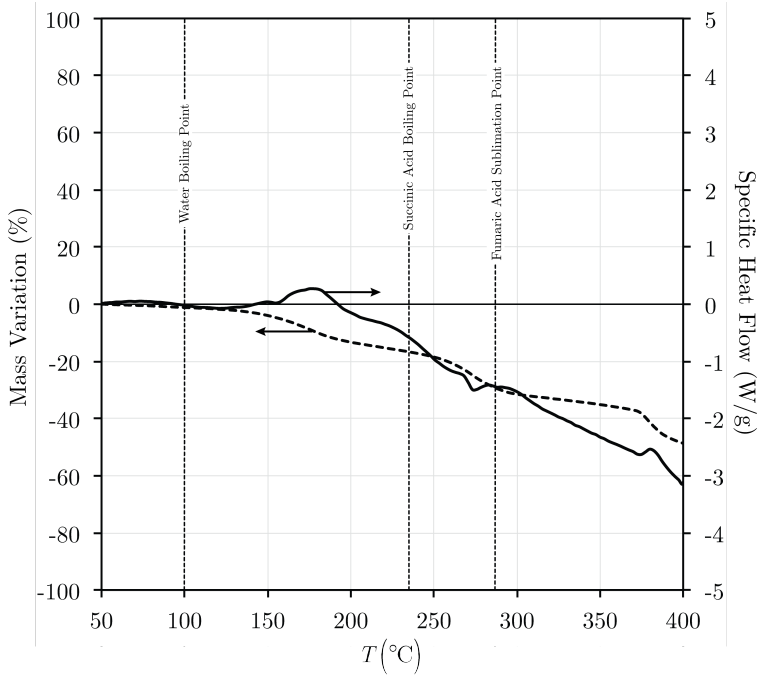


Figure 4.47. TGA and DSC results for a sample of spray-dried powder.

Figure 4.48 shows the TGA results for published data (Serre et al., 2004) using methanol as solvent and with an air atmosphere and the TGA results of samples of wet gel, dried gel and spray-dried powder.

Depending on the treatment of the sample, the degradation of the fumarate chain and vaporization of the material starts occurring between 235°C and 285°C in all the samples, which agrees with the results from Serre et al. (2004).

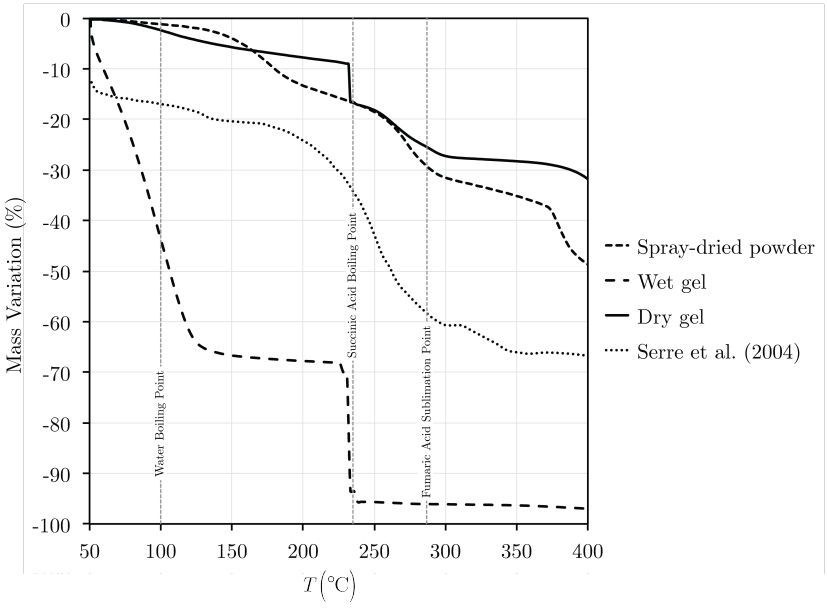


Figure 4.48. TGA results of publish data and samples of wet gel, dry gel and spray-dried powder.

4.6 Space-Time Yield Consideration

The space-time yield, STY, defined as the mass of product formed per volume of the reaction mixture and time, can used as a measure of the efficiency of the reactive process for producing MOFs. As a reference, zeolites are nowadays industrially produced with a STY in the range of 50-150 (Czaja et al., 2009). Recent efforts have resulted in scale-up procedures for the production of various MOFs with good STYs (Stock and Biswas, 2012).

For example, the mesoporous iron(III) trimesate MIL-100(Fe) is produced by hydrothermal reaction on a 10 L reactor with an industrial STY of 120 kg $m^{-3}day^{-1}$. For synthesis up-scaling to a 100 L, a STY of 300 kg $m^{-3}day^{-1}$ was even accomplished. Microporous copper trimesate KHUST-1, commercially available as Basolite C 300, is produced using continuous microwave-assisted heating synthesis with a STY of 225 kg $m^{-3}day^{-1}$ (Stock and Biswas, 2012).

Aluminium terephthalate Al-MIL-53, commercially available as Basolite A100, is produced with a STY of 160 kg $m^{-3}day^{-1}$, iron(III) benzene tricarboxilate Fe-BTC, commercially available as Basolite F300, is produced with a STY of 20 kg $m^{-3}day^{-1}$, Zinc methylimidazole ZIF-8, commercially available as Basolite Z1200, is produced with a STY of 100 kg $m^{-3}day^{-1}$ and $\left[Mg(O_2CH)_2\right]$, commercially available as Basosiv M050, is produced with a STY of 300 kg $m^{-3}day^{-1}$ (Czaja et al., 2009).

Scale-up procedures are not straightforward since the production of a given MOF may not comply with developed industrial-scale synthesis criteria. Some conditions can be suitable for the production of some MOFs and not suitable for others (Gaab et al., 2012; Stock and Biswas, 2012). Nonetheless, the optimization of some production processes for specific MOFs has been successful in achieving considerably high industrial STYs. A continuous MW-assisted synthesis of HKUST-1 using a total solvent volume of 9 L managed to achieve a high STY of 2000 kg $m^{-3}day^{-1}$ (Stock and Biswas, 2012). BASF patented a water-based synthesis method for the

production Basolite A520, an aluminium based MOF, with high STY up to $> 3600\ \mathrm{kg\ m^{-3}day^{-1}}$, in contrast with the STY of $7\ \mathrm{kg\ m^{-3}day^{-1}}$ for "state-of-art" synthesis of this MOF (Gaab et al., 2012). Furthermore, Seo et al. (2012) developed a method combined with purification steps for producing MIL-100(Fe) under hydrothermal conditions with a STY of $450\ \mathrm{kg\ m^{-3}day^{-1}}$ but suggested that the reaction time can be reduced from 12 to 3 hours without affecting the properties of the final product and a high STY up to $1700\ \mathrm{kg\ m^{-3}day^{-1}}$ can be achieved.

For the NETmix system, the STY can be estimated by

$$STY = \frac{C_{P,\max} X_P M_P}{\tau} \tag{4.28}$$

where $C_{P,\max}$ is the maximum concentration of product assuming total conversion, X_P is the conversion of the reaction, M_P is the molar mass and τ is the passage time for the total process.

For Formulation 2, the maximum theoretical concentration of MIL-88A that can be obtained is $0.017\ \mathrm{M}$. Considering that the conversion is in average 75% and for the nucleation time of 10 minutes, a high STY of $1700\ \mathrm{kg\ m^{-3}day^{-1}}$ is calculated.

The STY for this formulation is, in general, one order or magnitude higher than the reported industrial STY for other metal-organic frameworks and is of the same order of magnitude of new optimized processes while delivering nano-sized particles.

Nevertheless, the STY for this formulation is limited by the maximum reactants concentration to ensure that no competitive precipitation processes occur and by the nucleation time of the crystallization of MIL-88A. For instantaneous reactions, STY for NETmix operation could increase 2 orders of magnitude.

4.7 Conclusions

The NETmix reactor was tested to produce MIL-88A and compared with the production in a stirred tank reactor and two formulations were used.

The crystalline structure of MIL-88A was observed in all obtained results through XRD. Thermal characterization of the solids was performed. Free water adsorbed in the framework and bounded water to the MIL-88A molecule start to vaporize around 100°C. This product starts degrading above 235°C due to the volatilization of the organic ligand.

For Formulation 1, the initial mixing conditions are not crucial in order to obtain smaller particle sizes and NETmix presented no advantage. The influence of temperature and concentration were tested. As the temperature of reaction increases, crystal growth rate seems to increase more rapidly and prevail to the nucleation rate and the final dimensions of the crystals are larger. With the decrease of the reactants concentration, final particle size becomes larger. Although particles have a bigger mean free distance between them and therefore less interaction, the nucleation rate decreases and fewer nuclei are formed.

The suspension of particles presents a brown coloration right after reaction. Along the ageing time, the coloration changes from brown to pale pink. For samples that were not aged, an amorphous phase is also observed instead of MIL-88A crystals through SEM. After 72 hours, crystalline rod-shaped crystals are formed.

The formation of iron(III) hydroxide precipitate with low solubility may explain the darker coloration of the initial suspension and the formation of an amorphous phase in the beginning of the reaction for Formulation 1 and the study of the equilibrium of the species in solution is fundamental to understand the formation of secondary precipitation phenomena that will compete with the kinetics of crystallization of MIL-88A.

A precipitation model was used to study the equilibrium of the ionic species in solution and conditions that may lead to the precipitation of secondary and competitive species. The absence of competitive precipitation processes can be achieved by tuning the pH and concentration of the reactants. This procedure was applied in Formulation 2.

With this formulation, a suspension of nanoparticles is obtained of orange-pink coloration. Although particle agglomeration and sedimentation was observed, particles can be re-suspended with the use of ultrasounds and comparable results of particle size distribution are obtained for measurements 72 h and 2 weeks after dilution. It was observed that, when NETmix reactor was used, smaller diameters were obtained. Recirculation in the NETmix reactor during the nucleation step also produced particles with smaller size.

Small rod-shaped monodispersed nanoparticles of 120×25 nm are produced with Formulation 2 and the use of NETmix. The conversion into MIL-88A is high and around 75%. The STY for this formulation was calculated and is, in general, one order or magnitude higher than the reported industrial STY for other metal-organic frameworks and is of the same order of magnitude of new optimized processes while delivering nano-sized particles.

4.8 References

Boily, J.-F., Seward, T.M., 2005. Dissociation of Fumaric Acid: Spectrophotometric Investigation in Aqueous Solutions from 10 to 90 °C and Theoretical Considerations. Journal of Solution Chemistry 34, 1167-1190.

Chalati, T., Horcajada, P., Gref, R., Couvreur, P., Serre, C., 2011. Optimisation of the synthesis of MOF nanoparticles made of flexible porous iron fumarate MIL-88A. Journal of Materials Chemistry 21, 2220.

Costa, M.F.S., 2012. Development of Nanomaterials using the NETmix® Technology: Application to Production of MOFs [M.Sc], Departamento de Engenharia Química. Universidade do Porto, Porto.

Czaja, A.U., Trukhan, N., Muller, U., 2009. Industrial applications of metal-organic frameworks. Chemical Society Reviews 38, 1284-1293.

Furukawa, H., Ko, N., Go, Y.B., Aratani, N., Choi, S.B., Choi, E., Yazaydin, A.O., Snurr, R.Q., O'Keeffe, M., Kim, J., Yaghi, O.M., 2010. Ultrahigh Porosity in Metal-Organic Frameworks. Science 329, 424-428.

Gaab, M., Trukhan, N., Maurer, S., Gummaraju, R., Müller, U., 2012. The progression of Al-based metal-organic frameworks – From academic research to industrial production and applications. Microporous and Mesoporous Materials 157, 131-136.

GESTIS, 2013. GESTIS Substance Database. Institute for Occupational Safety and Health of the German Social Accident Insurance (IFA), http://gestis-en.itrust.de.

Ghosh, M.M., O'Connor, T.O., Engelbrecht, R.S., 1966. Precipitation of Iron in Aerated Ground Waters. Journal of the Sanitary Engineering Division 92, 199-213.

Horcajada, P., Chalati, T., Serre, C., Gillet, B., Sebrie, C., Baati, T., Eubank, J.F., Heurtaux, D., Clayette, P., Kreuz, C., Chang, J.S., Hwang, Y.K., Marsaud, V., Bories, P.N., Cynober, L., Gil, S., Ferey, G., Couvreur, P., Gref, R., 2010. Porous metal-organic-framework nanoscale carriers as a potential platform for drug delivery and imaging. Nature Materials 9, 172-178.

Horcajada, P., Gref, R., Baati, T., Allan, P.K., Maurin, G., Couvreur, P., Ferey, G., Morris, R.E., Serre, C., 2012. Metal-Organic Frameworks in Biomedicine. Chemical Reviews 112, 1232-1268.

Hoskins, B.F., Robson, R., 1989. Infinite polymeric frameworks consisting of three dimensionally linked rod-like segments. Journal of the American Chemical Society 111, 5962-5964.

Jacoby, M., 2008. Heading To Market With MOFs. Chemical & Engineering News 86, 13-16.

Kim, M., Cahill, J.F., Fei, H., Prather, K.A., Cohen, S.M., 2012. Postsynthetic ligand and cation exchange in robust metal-organic frameworks. J Am Chem Soc 134, 18082-18088.

Kuppler, R.J., Timmons, D.J., Fang, Q.-R., Li, J.-R., Makal, T.A., Young, M.D., Yuan, D., Zhao, D., Zhuang, W., Zhou, H.-C., 2009. Potential applications of metal-organic frameworks. Coordination Chemistry Reviews 253, 3042-3066.

Lange, N.A., Sinks, M.H., 1930. The Solubility, Specific Gravity and Index of Refraction of Aqueous Solutions of Fumaric, Maleic and i-Malic Acids. Journal of American Chemistry Society 52, 2602-2604.

Mellot-Draznieks, C., Serre, C., Surblé, S., Audebrand, N., Férey, G., 2005. Very Large Swelling in Hybrid Frameworks: A Combined Computational and Powder Diffraction Study. J Am Chem Soc 127, 16273-16278.

Mullin, J.W., 2001. Crystallization, 4 ed. Butterworth-Heinemann.

Parsons, J.G., Luna, C., Botez, C.E., Elizalde, J., Gardea-Torresdey, J.L., 2009. Microwave Assisted Synthesis of Iron(III) Oxyhydroxides/Oxides Characterized Using Transmission Electron Microscopy, X-ray Diffraction, and X-ray Absorption Spectroscopy. J Phys Chem Solids 70, 555-560.

Pourbaix, M., 1974. Atlas of Electrochemical Equilibria in Aqueous Solutions, 2 ed. National Association of Corrosion Engineers, Houston, USA.

Sanderson, K., 2007. Materials chemistry: Space invaders. Nature 448, 746-748.

Seo, Y.-K., Yoon, J.W., Lee, J.S., Lee, U.-H., Hwang, Y.K., Jun, C.-H., Horcajada, P., Serre, C., Chang, J.-S., 2012. Large Scale Fluorine-Free Synthesis of Hierarchically Porous Iron(III) Trimes- ate MIL-100(Fe) with a Zeolite MTN Topology. Microporous and Mesoporous Materials.

Serre, C., Mellot-Draznieks, C., Surblé, S., Audebrand, N., Filinchuk, Y., Férey, G., 2007. Role of Solvent-Host Interactions That Lead to Very Large Swelling of Hybrid Frameworks. Science 315, 1828-1831.

Serre, C., Millange, F., Surble, S., Ferey, G., 2004. A route to the synthesis of trivalent transition-metal porous carboxylates with trimeric secondary building units. Angew Chem Int Ed Engl 43, 6285-6289.

Sigma-Aldrich, 2013. Metal-Organic Frameworks, http://www.sigmaaldrich.com/chemistry/chemical-synthesis/metal-organic-frameworks.html.

Stock, N., Biswas, S., 2012. Synthesis of metal-organic frameworks (MOFs): routes to various MOF topologies, morphologies, and composites. Chem Rev 112, 933-969.

Stumm, W., Lee, G.F., 1960. The chemistry of aqueous iron. Schweizerische Zeitschrift für Hydrologie 22, 295-319.

Surble, S., Serre, C., Mellot-Draznieks, C., Millange, F., Ferey, G., 2006. A new isoreticular class of metal-organic-frameworks with the MIL-88 topology. Chem Commun (Camb), 284-286.

Taylor, K.C., Nasr-El-Din, H.A., Al-Alawi, M., 1999. Systematic Study of Iron Control Chemicals Used During Well Stimulation. SPE Journal 4, 19-24.

Yaghi, O.M., Li, H., Davis, C., Richardson, D., Groy, T.L., 1998. Synthetic Strategies, Structure Patterns, and Emerging Properties in the Chemistry of Modular Porous Solids. Accounts of Chemical Research 31, 474-484.

5 Final Remarks

This chapter is divided into two sections. Section 5.1 summarizes the main conclusions of the present work. Section 5.2 provides a list of suggestions for future work.

5.1 Conclusions

In Chapter 2, a simple mechanistic model for the prediction of the pressure drop was successfully developed. This model comprised a single adjustable parameter that is only dependent on the geometric configuration of the network. This model is supported and validated from experimental data of pressure drop obtained for three different NETmix reactor prototypes.

The model proposed by Laranjeira (2005) for the frequency of oscillation of the flow inside the chambers was confirmed and extended for the 2D NETmix geometry from the experimental dynamic measurements of the pressure drop. The energy performance of the NETmix reactor was determined by evaluating the power number, N_P, and Z factor for the three existing NETmix reactor prototypes. By

comparison with published data (Thakur et al., 2003), the NETmix reactor proved to be competitive with existing mixers.

A new 3D CFD model was introduced, the NETmix Unit Block model. This model enables the computation of transport properties of a more realistic representation of the NETmix geometry. The NETmix Unit Block model follows a strategy that takes advantage of the periodically nature of NETmix geometry and the expected flow pattern, thus reducing the simulation domain and delivering the necessary grid refinement to perform the 3D simulation. The simulation results were considered validated since they are in good agreement with experimental measurements of pressure drop and the dynamic behaviour of the flow inside the mixing chambers. Heat and mass studies were performed in the NETmix reactor to evaluate the enhancement on the convective heat and mass transfer coefficients when compared to the flow between parallel plates. This work suggests that heat/mass transfer rate is enhanced by the use of the NETmix reactor caused by the reduction of the boundary layers due to fluid motion perpendicular to the flow direction. Correlations for the unit cell Nusselt and Sherwood numbers were presented and can be of great use on the design of new NETmix devices.

In Chapter 3, the application of the NETmix reactor was extended to heterogeneous liquid-liquid reactions. The adiabatic heterogeneous reaction of nitration of benzene was chosen as a case study due to its relevance as a high added-value material in the polymer industry. A mathematical model was developed and it is capable to predict the formation of nitrobenzene and the raise of temperature inside the NETmix reactor for operational conditions in the range of interest of industrial operation within 15% of deviation when compared to the published experimental data of Biggs and White (1956) and Santos (2005). Due to the lack of experimental work in this topic, considerations were made for the NETmix operation conditions that have to be set and a mathematical expression was developed to calculate the minimum Reynolds number that ensures that a sufficient power per unit volume is used for mixing. This mathematical tool can be useful in the right selection of operation conditions that

could lead to small reaction times with high conversions. Assuming the considerations made in this dissertation are true, the NETmix reactor was shown to be suitable for large-scale production of nitrobenzene, delivering high degree of mixing in laminar regime with large throughputs.

The development of a new class of high added-value materials, Metal-organic frameworks (MOFs), in the NETmix reactor was introduced in this dissertation. These organic-inorganic hybrid materials are promising candidates for applications in a large number of fields related to porous materials due to their exceptionally high surface areas. In Chapter 4, the NETmix reactor was tested to produce MIL-88A and compared with the production in a stirred tank reactor. Two different formulations were used. For the first formulation, Formulation 1, the NETmix reactor presented no advantage. This was due to the formation of secondary precipitation phenomena that compete with the kinetics of crystallization of MIL-88A. To overcome that, a precipitation model was developed to study the equilibrium of the ionic species in solution and conditions that may lead to the precipitation of secondary and competitive species. Formulation 2 was conceived and the absence of competitive precipitation processes was achieved by tuning the pH and concentration of the reactants. With this formulation, a suspension of nanoparticles was obtained and although particle agglomeration and sedimentation were observed with time, particles can be easily re-suspended with the use of ultrasounds. It was observed that, when NETmix reactor was used, smaller diameters were obtained. Recirculation in the NETmix reactor during the nucleation step also produced particles with smaller size. From Formulation 2 and the use of NETmix, small rod-shaped monodispersed nanoparticles of 120×25 nm were produced that can be suitable to be used as nanocarrier for drug delivery (Horcajada et al., 2010). The conversion into MIL-88A is high and around 75% and the Space-Time Yield (STY) for this formulation is, in general, one order or magnitude higher than the reported industrial STY for other metal-organic frameworks and is of the same order of magnitude of new optimized processes while delivering nano-sized particles.

As a final remark, the main achievements of this dissertation are:

- A simple mechanistic model for the prediction of the pressure drop along the NETmix reactor was developed;
- NETmix performance in terms of power consumption was proven to be competitive when compared to other commercially available mixers;
- The NETmix Unit Block model was developed and validated;
- Heat and mass transfer enhancement were studied with the NUB model. The ;
- Development of a mathematical model for the adiabatic heterogeneous reaction of nitration of benzene in the NETmix reactor, valid for operational conditions in the range of interest of industrial operation;
- Development of a precipitation model that can be used as a tool for the fine-tuning of formulations for production of MIL-88A;
- Production of small rod-shaped monodispersed nanoparticles of MIL-88A of 120×25 nm with high conversion and high STY.

5.2 Future Work

Some suggestions of future work are presented below:

- Use of the Nusselt and Sherwood numbers correlations presented in Chapter 2 to develop a heat and mass transfer model for the whole reactor that would be used for the design of new NETmix devices for new applications.
- In this work, the mass transfer controlled regime was studied. Further work could include the study of the kinetic controlled regimes.
- Test the NETmix reactor as a photocatalytic reactor due to its mass transfer enhancement properties.
- Obtain experimental data to validate the heterogeneous benzene nitration model developed in Chapter 3.

- Further study heterogeneous systems in the NETmix reactor. Investigate, experimentally and numerically, the capability of NETmix reactor to generate high interfacial area between two immiscible fluids.
- Apply the same methodology developed in Chapter 4 for the development of different metal-organic frameworks materials.

5.3 References

Biggs, R.D., White, R.R., 1956. Rate of Nitration of Benzene With Mixed Acid. AIChE Journal 2, 26-33.

Horcajada, P., Chalati, T., Serre, C., Gillet, B., Sebrie, C., Baati, T., Eubank, J.F., Heurtaux, D., Clayette, P., Kreuz, C., Chang, J.S., Hwang, Y.K., Marsaud, V., Bories, P.N., Cynober, L., Gil, S., Ferey, G., Couvreur, P., Gref, R., 2010. Porous metal-organic-framework nanoscale carriers as a potential platform for drug delivery and imaging. Nature Materials 9, 172-178.

Laranjeira, P.E., 2005. NETmix® Static Mixer Modelling, CFD Simulation and Experimental Characterisation [Ph.D], Departamento de Engenharia Química. Universidade do Porto, Porto.

Santos, P.A.Q.O., 2005. Nitração de Compostos Aromáticos: Transferência de Massa e Reacção Química. [Ph.D]. Faculdade de Ciências e Tecnologia da Universidade de Coimbra, Porto, Portugal.

Thakur, R.K., Vial, C., Nigam, K.D.P., Nauman, E.B., Djelveh, G., 2003. Static Mixers in the Process Industries—A Review. Chemical Engineering Research and Design 81, 787-826.

A Logarithm Mean Temperature Difference

A.1 Logarithm Mean Temperature Difference

The energy balance on a differential control volume is given by

$$\dot{m}c_P \mathrm{d}T_b = h_{loc}\left(T_{wall} - T_b\right)\mathrm{d}A \tag{A.1}$$

where T_{wall} is the temperature at the wall of the parallel plates, T_b is the bulk temperature of the fluid flow and $\dot{m}$ is the mass flow rate. Equation (A.1) can be rearranged to be expressed as

$$\frac{\mathrm{d}\left(T_{wall} - T_b\right)}{\left(T_{wall} - T_b\right)} = -\frac{h_{loc}\mathrm{d}A}{\dot{m}c_P} \tag{A.2}$$

Integrating Equation (A.2), the energy balance between the inlet and outlet is given by

$$\ln\frac{\left(T_{wall,out} - T_{b,out}\right)}{\left(T_{wall,in} - T_{b,in}\right)} = -\frac{\bar{h}A_{transf}}{\dot{m}c_P} \tag{A.3}$$

Substituting Equation (A.3) in Equation (A.4),

$$\dot{Q} = \dot{m} c_P \left(T_{b,out} - T_{b,in} \right) = \overline{h} A_{transf} \Delta T_{av}, \tag{A.4}$$

it can be seen that the mean temperature difference in the unit cell is given by the logarithm mean temperature difference between the inlet and the outlet,

$$\Delta T_{av} = \Delta T_{\ln} = \frac{T_{b,out} - T_{b,in}}{\ln\left[\left(T_{wall,in} - T_{b,in} \right) / \left(T_{wall,out} - T_{b,out} \right) \right]}. \tag{A.5}$$

B Size, Surface and Distribution Calculations for MOF Particles

B.1 Mean Free Distance Between Particles

For the calculation of the mean distance between MOF particles, the rod shaped crystals were approximated to a cylinder shape as shown in Figure B.1.

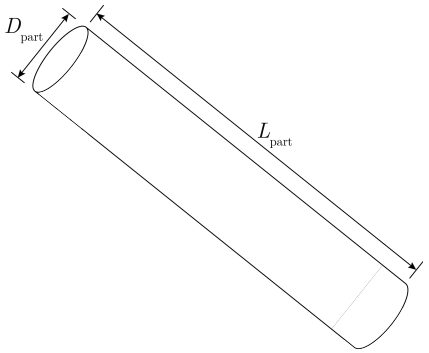


Figure B.1 Approximate geometry of the particles.

The volume of each particle is given by the volume of a cylinder,

$$V_{\text{part}} = \frac{\pi}{4} D^2_{\text{part}} L_{\text{part}} \tag{B.1}$$

where D_{part} is the diameter of the base and L_{part} is the length.

The total number of particles in solution is obtained by dividing the total volume of MOF particles by the volume of one particle and can be estimated as

$$N_{\text{part}} = \frac{m_{\text{MOF}}}{\rho_{\text{MOF}}} \frac{4\left(L_{\text{part}} / D_{\text{part}}\right)^2}{\pi L_{\text{part}}^3} \tag{B.2}$$

where ρ_{MOF} is the density of the MOF and m_{MOF} is the total mass of MOF in the suspension.

It is assumed that the total number of particles is evenly distributed in a cube with the same volume as the solution, V_{sol}. In an edge of the cube, the particles are distributed by

$$\left(N_{\text{part}}\right)^{1/3} L_{\text{part}} + \left(N_{\text{part}}\right)^{1/3} \Delta x_{\text{part}} = \left(V_{\text{sol}}\right)^{1/3} \tag{B.3}$$

where Δx is the distance between particles. The distance

$$\frac{\Delta x_{\text{part}}}{L_{\text{part}}} = \left(\frac{4}{\pi}\right)^{1/3} \left(\frac{V_{\text{sol}} \rho_{\text{MOF}}}{m_{\text{MOF}}}\right)^{1/3} \left(\frac{L_{\text{part}}}{D_{\text{part}}}\right)^{2/3} - 1 = \left(\frac{4}{\pi}\right)^{1/3} \left(\frac{\rho_{\text{MOF}}}{c_{\text{MOF}} M_{\text{MOF}}}\right)^{1/3} \left(\frac{2L_{\text{part}}}{D_{\text{part}}}\right)^{2/3} - 1 \tag{B.4}$$

where c_{MOF} is the concentration of MOF in the solution and M_{MOF} is the molar mass of MOF.

B.2 Specific External Surface Area

Specific external surface area is calculated by dividing the surface area of each particle, A_{part}, by the mass of each particle, m_{part},

$$S_{\text{ext}} = \frac{A_{\text{part}}}{m_{\text{part}}} = \frac{A_{\text{part}}}{V_{\text{part}} \rho_{\text{MOF}}} \tag{B.5}$$

The area of a cylinder calculates the surface area,

$$A_{\text{part}} = \frac{\pi D_{\text{part}}^2}{4} + \pi D_{\text{part}} L_{\text{part}} \tag{B.6}$$

Combining Equation (B.1) and Equation (B.6) with Equation (B.5), the specific external surface area is given by

$$S_{\text{ext}} = \frac{D_{\text{part}} + 4L_{\text{part}}}{D_{\text{part}} L_{\text{part}} \rho_{\text{MOF}}}. \tag{B.7}$$

B.3 Distribution of Dispersant

The distribution of dispersant in solution can be approximated by simple geometric relationships. Each molecule of dispersant was considered spherical with diameter D_{disp}.

To calculate the amount of dispersant that can be adsorbed by each particle, the surface of each MOF particle was divided into squares of area D_{disp}^2 as shown in Figure B.2.

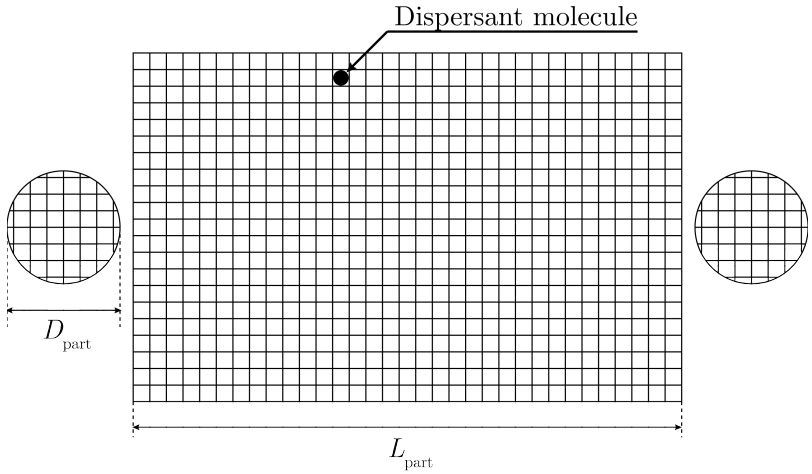


Figure B.2. Division of the surface area of a particle.

For citrate ions, a dispersant molecule diameter of 0.45 nm (López-Macipe et al., 1998) was considered. A dispersant molecule diameter of approximately 6 nm (Armstrong et al., 2004) was used for PVP based upon calculation of the radius of gyration of the PVP chain.

The theoretical maximum number of dispersant molecules, $N_{\text{disp, ads}}$, that can be adsorbed in a monolayer per particle is calculated by

$$\frac{N_{\text{disp, ads}}}{N_{\text{part}}} = \left(\pi \frac{D_{\text{part}} L_{\text{part}}}{D_{\text{disp}}^2} + \frac{\pi}{2} \frac{D_{\text{part}}^2}{D_{\text{disp}}^2} \right). \tag{B.8}$$

The remaining dispersant molecules will remain free in solution. The number of free dispersant molecules, $N_{\text{disp, free}}$, in solution is estimated by subtracting the adsorbed dispersant molecules to the total number of dispersant molecules, $N_{\text{disp, total}}$,

$$N_{\text{disp, free}} = N_{\text{disp, total}} - N_{\text{disp, ads}}. \tag{B.9}$$

The number of free dispersant per particle of MOF can be related to the total concentration of dispersant in solution, dimension of the particles of MOF and the mean free distance between particles,

$$\frac{N_{\text{disp, free}}}{N_{\text{part}}} = \frac{C_{\text{disp}} L_{\text{part}}^3 N_A}{N_{\text{part}}} \left(\frac{\Delta x}{L_{\text{part}}} \right)^3 - \frac{N_{\text{disp, ads}}}{N_{\text{part}}} \tag{B.10}$$

where C_{disp} total concentration of dispersant in solution and N_A is the Avogadro constant.

The number of dispersant molecules between two evenly distributed MOF particles, $N_{\text{disp, }\Delta x}$, is given by,

$$N_{\text{disp, }\Delta x} = \left(\frac{N_{\text{disp, free}}}{N_{\text{part}}} \right)^{1/3}. \tag{B.11}$$

B.4 Hydrodynamic Diameter

From DLS measurements it is possible to obtain the hydrodynamic diameter that is the diameter of a hard sphere that diffuses at the same rate as the real particle. The conversion to real dimensions is necessary.

The hydrodynamic diameter can be related with the particle dimensions by

$$D_{h_{\text{part}}} = L_{\text{part}} F_{\text{shape}} \left(\frac{3/2}{\left(L_{\text{part}} / D_{\text{part}} \right)^2} \right)^{1/3} \tag{B.12}$$

where F_{shape} is a shape factor. For rod shape particles, F_{shape} takes the value of 1.3 for $L_{\text{part}} / D_{\text{part}} \approx 5$ (Harding, 1995). This ratio of length and diameter of the particle is a good approximation according SEM imaging results.

B.5 References

Armstrong, J.K., Wenby, R.B., Meiselman, H.J., Fisher, T.C., 2004. The Hydrodynamic Radii of Macromolecules and Their Effect on Red Blood Cell Aggregation. Biophysical journal 87, 4259-4270.

Harding, S.E., 1995. On the hydrodynamic analysis of macromolecular conformation. Biophysical Chemistry 55, 69-93.

López-Macipe, A., Gómez-Morales, J., Rodríguez-Clemente, R., 1998. The Role of pH in the Adsorption of Citrate Ions on Hydroxyapatite. Journal of Colloid and Interface Science 200, 114-120.

C Rheological Analysis in MOF Production

C.1 Experimental Techniques

The rheological experiments were performed using a cone-and-plate Paar Physica UDS 200 Rheometer. The used cone had a diameter of 75 mm and the angle between the surface of the cone and the plate is 1°. The temperature was set to 25°C and kept constant by using a Viscotherm VT2. The reactants were kept separated in the rheometer plate to ensure that reaction only starts to occur when the cone starts rotating and acquiring data.

Rotational experiments were made with constant shear rate and the torque value was acquired along the time for 60 seconds. The viscosity was measured for three different reactants concentrations: 0.08 M, 0.16 M and 0.4 M. For each concentration, four different shear rates were used: 366 Hz, 713 Hz, 1426 Hz and 2852 Hz. A total of 12 experiments were performed.

C.2 Experimental Results

The viscosity results have similar behaviour for all the experiments. In the beginning a rapid increase is observed, a maximum value of viscosity is achieved, μ_{max}, and

after that the viscosity value decreases to what appears to be a stationary value, μ_∞. Figure C.1 shows the viscosity change after mixing as a function of time for reactants concentration of $0.4\ \mathrm{M}$ and constant shear rate of $366\ \mathrm{Hz}$.

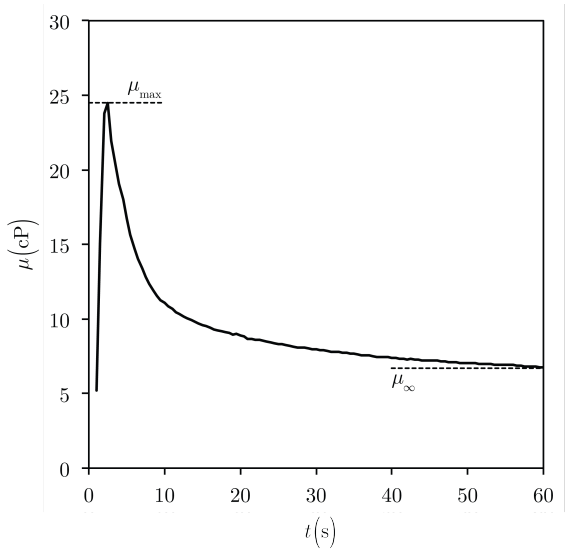


Figure C.1. Viscosity as a function of time for a reactants concentration of 0.4 M and a shear rate of 366 Hz.

Results of maximum viscosity obtained in each experiment as a function of the shear rate, $\dot{\gamma}$, are shown in Figure C.2.

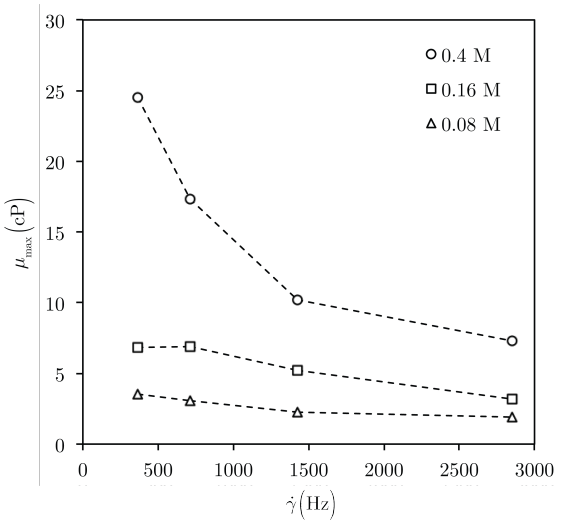


Figure C.2. Maximum viscosity of the mixture of reactants as a function of shear rate.

C.3 NETmix operation

The Reynolds number in the NETmix channels can be estimated by the viscosity of the mixture and the shear rate in the channels. This section describes the calculation of the Reynolds number for NETmix reactors with 2D configuration.

Since the depth of the prismatic channels is bigger than the width, $\omega > d$, the velocity profile was approximated to a parabolic flow profile between parallel plates,

$$v_x\left(y,z\right) = v_{\max}\left(1-\left(\frac{y}{d/2}\right)^2\right) \tag{C.1}$$

where v_x is the velocity component in the flow direction and $v_{\max}$ is the maximum velocity of the fluid, y is the width direction and z is the depth direction. The average velocity in the NETmix channel, $\overline{v}$, can be related to the maximum velocity using the mean value theorem,

$$\overline{v} = \frac{\int_{-d/2}^{d/2} v_x\left(y,z\right)\mathrm{d}y}{d} = \frac{2}{3}v_{\max} \tag{C.2}$$

Using Equation (C.1) and Equation (C.2), the shear rate in the channels of a 2D NETmix reactor is given by

$$\dot{\gamma} = \left.\frac{\mathrm{d}v_x}{\mathrm{d}y}\right|_{y=-d/2} = \frac{6\overline{v}}{d} \tag{C.3}$$

Knowing the viscosity as a function of the shear rate from the rheology studies, the necessary velocity in the NETmix channels to achieve a determined Reynolds number can be found by solving the non-linear system of equations shown in Equation (C.4).

$$\begin{cases} \dot{\gamma} = \dfrac{6\overline{v}}{d} \\ \mu_{\max} = f\left(\dot{\gamma}\right) \\ \mathrm{Re} = \dfrac{\rho d_h \overline{v}}{\mu_{\max}} \end{cases} \tag{C.4}$$

D Modelling of the Equilibrium of Fumaric Acid and Iron(III) Hydroxide in Aqueous Solutions

D.1 Equilibrium of Fumaric Acid in Aqueous Solutions

The dissociation of the fumarate species and precipitation of fumaric acid can be estimated by solving the mass and charge balance of all the species in solution.

At equilibrium, the dissociation constants are given by

$$K_{\mathrm{HFum^-}} = \frac{\left[\mathrm{HFum^-}\right]\left[\mathrm{H^+}\right]}{\left[\mathrm{H_2Fum}\right]} \tag{D.1}$$

and

$$K_{\mathrm{Fum^{2-}}} = \frac{\left[\mathrm{Fum^{2-}}\right]\left[\mathrm{H^+}\right]}{\left[\mathrm{HFum^-}\right]} \tag{D.2}$$

If the concentration of fumaric acid exceeds the solubility value precipitation occurs and the solubility product is given by,

$$K_{s,\,\mathrm{H_2Fum}} = \left[\mathrm{H^+}\right]^2\left[\mathrm{Fum^{2-}}\right] \tag{D.3}$$

The dissociation constant of water, $K_W = \left[\mathrm{H^+}\right]\left[\mathrm{OH^-}\right]$, is 10^{-14} at 25°C.

Conservation of mass and charge are considered for each situation. The mass and charge balance equations are combined with the equilibrium expressions and a single function is written as a function of the concentration of $\mathrm{H^+}$ ions. The concentration of all the other species in solution can be calculated from the concentration of $\mathrm{H^+}$.

These equations contemplate the possibility of addition of sodium hydroxide or hydrochloric acid to the medium.

D.1.1 Fumaric Acid Dissociation Without Precipitation

Sodium mass balance:

$$\left[\mathrm{Na^+}\right]_e = \left[\mathrm{NaOH}\right]_i \tag{D.4}$$

Chlorine mass balance:

$$\left[\mathrm{Cl^-}\right]_e = \left[\mathrm{HCl}\right]_i \tag{D.5}$$

Fumarate mass balance:

$$\left[\mathrm{H_2Fum}\right]_i = \left[\mathrm{H_2Fum}\right]_e + \left[\mathrm{HFum^-}\right]_e + \left[\mathrm{Fum^{2-}}\right]_e \tag{D.6}$$

Charge balance:

$$\left[\mathrm{H^+}\right]_e + \left[\mathrm{Na^+}\right]_e = \left[\mathrm{OH^-}\right]_e + \left[\mathrm{Cl^-}\right]_e + \left[\mathrm{HFum^-}\right]_e + 2\left[\mathrm{Fum^{2-}}\right]_e \tag{D.7}$$

The concentration of $\mathrm{H^+}$ ions in solution can be found by calculating the roots of Equation (D.8),

$$\left[\mathrm{H^+}\right]_e + \left[\mathrm{NaOH}\right]_i - \frac{K_W}{\left[\mathrm{H^+}\right]_e} - \left[\mathrm{HCl}\right]_i - \\ - \frac{\left[\mathrm{H_2Fum}\right]_i}{1 + \frac{K_{\mathrm{HFum^-}}}{\left[\mathrm{H^+}\right]_e} + \frac{K_{\mathrm{HFum^-}} K_{\mathrm{Fum^{2-}}}}{\left[\mathrm{H^+}\right]_e^2}} \left(\frac{K_{\mathrm{HFum^-}}}{\left[\mathrm{H^+}\right]_e} + \frac{2K_{\mathrm{HFum^-}} K_{\mathrm{Fum^{2-}}}}{\left[\mathrm{H^+}\right]_e^2} \right) = 0. \tag{D.8}$$

D.1.2 Fumaric Acid Dissociation With Precipitation

Sodium mass balance:

$$\left[\mathrm{Na^+}\right]_e = \left[\mathrm{NaOH}\right]_i \tag{D.9}$$

Chlorine mass balance:

$$\left[\mathrm{Cl^-}\right]_e = \left[\mathrm{HCl}\right]_i \tag{D.10}$$

Fumarate mass balance:

$$\left[\mathrm{H_2Fum}\right]_i = \left[\mathrm{H_2Fum}\right]_e + \left[\mathrm{HFum^-}\right]_e + \left[\mathrm{Fum^{2-}}\right]_e + \left[\mathrm{H_2Fum}\downarrow\right]_e \tag{D.11}$$

Charge Balance:

$$\left[\mathrm{H^+}\right]_e + \left[\mathrm{Na^+}\right]_e = \left[\mathrm{OH^-}\right]_e + \left[\mathrm{Cl^-}\right]_e + \left[\mathrm{HFum^-}\right]_e + 2\left[\mathrm{Fum^{2-}}\right]_e \tag{D.12}$$

The concentration of all the species in solution can be found by calculating the roots of Equation (D.13),

$$\left[\mathrm{H^+}\right]_e + \left[\mathrm{NaOH}\right]_i - \frac{K_W}{\left[\mathrm{H^+}\right]} - \left[\mathrm{HCl}\right]_i - \frac{K_{s,\,\mathrm{H_2Fum}}}{K_{\mathrm{Fum^{2-}}}\left[\mathrm{H^+}\right]_e} - \frac{K_{s,\,\mathrm{H_2Fum}}}{\left[\mathrm{H^+}\right]_e^2} = 0. \tag{D.13}$$

D.2 Equilibrium of Iron(III) Hydroxide in Aqueous Solutions

The dissociation of the iron species and precipitation of iron(III) hydroxide acid can be estimated by solving the mass and charge balance of all the species in solution.

The equilibrium constants for the iron species in solution are given by,

$$K_{\mathrm{Fe(OH)^{2+}}} = \frac{\left[\mathrm{Fe(OH)^{2+}}\right]\left[\mathrm{H^+}\right]}{\left[\mathrm{Fe^{3+}}\right]} \tag{D.14}$$

and

$$K_{\mathrm{Fe(OH)_2^+}} = \frac{\left[\mathrm{Fe(OH)_2^+}\right]\left[\mathrm{H^+}\right]}{\left[\mathrm{Fe(OH)^{2+}}\right]} \tag{D.15}$$

When the solubility of iron(III) hydroxide is exceeded, precipitation occurs and the the solubility product is given by

$$K_{s,\,\mathrm{Fe(OH)_3}} = \left[\mathrm{Fe^{3+}}\right]\left[\mathrm{OH^-}\right]^3 \tag{D.16}$$

The solubility constant for the iron(III) hydroxide in solution is given by,

$$K_{d,\,\mathrm{Fe(OH)_3}} = \left[\mathrm{Fe(OH)_3}\right] \tag{D.17}$$

In very alkaline solutions, $\mathrm{Fe(OH)_4^-}$ cations can be formed. At equilibrium, the dissociation constant is given by

$$K_{\mathrm{Fe(OH)_4^-}} = \frac{\left[\mathrm{Fe(OH)_4^-}\right]}{\left[\mathrm{OH^-}\right]} \tag{D.18}$$

Conservation of mass and charge are considered for each situation. The mass and charge balance equations are combined with the equilibrium expressions and a single

function is written as a function of the concentration of H^+ ions. The concentration of all the other species in solution can be calculated from the concentration of H^+.

These equations contemplate the possibility of addition of sodium hydroxide or hydrochloric acid to the medium.

D.2.1 Iron(III) Hydroxide Dissociation Without Precipitation

Sodium mass balance:

$$\left[Na^+\right]_e = \left[NaOH\right]_i \tag{D.19}$$

Chlorine mass balance:

$$\left[Cl^-\right]_e = \left[HCl\right]_i + 3\left[FeCl_3\right]_i \tag{D.20}$$

Iron mass balance:

$$\left[FeCl_3\right]_i = \left[Fe^{3+}\right]_e + \left[Fe\left(OH\right)^{2+}\right]_e + \left[Fe\left(OH\right)_2^{+}\right]_e \tag{D.21}$$

Charge balance:

$$\left[H^+\right]_e + \left[Na^+\right]_e + \left[Fe\left(OH\right)_2^{+}\right]_e + 2\left[Fe\left(OH\right)^{2+}\right]_e + 3\left[Fe^{3+}\right]_e = \left[OH^-\right]_e + \left[Cl^-\right]_e \tag{D.22}$$

The concentration of all the species in solution can be found by calculating the roots of Equation (D.23),

$$\begin{aligned}&\left[H^+\right]_e + \left[NaOH\right]_i - \frac{K_W}{\left[H^+\right]} - \left[HCl\right]_i - 3\left[FeCl_3\right]_i + \\ &+ \frac{\left[FeCl_3\right]_i}{1 + \dfrac{K_{Fe(OH)_2^+}}{\left[H^+\right]_e} + \dfrac{K_{Fe(OH)_2^+} K_{Fe(OH)^{2+}}}{\left[H^+\right]_e^2}} \left(3 + \frac{2K_{Fe(OH)_2^+}}{\left[H^+\right]_e} + \frac{K_{Fe(OH)_2^+} K_{Fe(OH)^{2+}}}{\left[H^+\right]_e^2}\right) = 0.\end{aligned} \tag{D.23}$$

D.2.2 Iron(III) Hydroxide Dissociation With Precipitation

Sodium mass balance:

$$\left[\mathrm{Na}^{+}\right]_e = \left[\mathrm{NaOH}\right]_i \tag{D.24}$$

Chlorine mass balance:

$$\left[\mathrm{Cl}^{-}\right]_e = \left[\mathrm{HCl}\right]_i + 3\left[\mathrm{FeCl}_3\right]_i \tag{D.25}$$

Iron mass balance:

$$\begin{aligned}\left[\mathrm{FeCl}_3\right]_i = {} & \left[\mathrm{Fe}^{3+}\right]_e + \left[\mathrm{Fe(OH)}^{2+}\right]_e + \left[\mathrm{Fe(OH)}_2^{+}\right]_e + \left[\mathrm{Fe(OH)}_3\right]_e \\ & + \left[\mathrm{Fe(OH)}_4^{-}\right]_e + \left[\mathrm{Fe(OH)}_3 \downarrow\right]_e\end{aligned} \tag{D.26}$$

Charge balance:

$$\begin{aligned}&\left[\mathrm{H}^{+}\right]_e + \left[\mathrm{Na}^{+}\right]_e + \left[\mathrm{Fe(OH)}_2^{+}\right]_e + 2\left[\mathrm{Fe(OH)}^{2+}\right]_e + 3\left[\mathrm{Fe}^{3+}\right]_e = \\ &\left[\mathrm{OH}^{-}\right]_e + \left[\mathrm{Cl}^{-}\right]_e + \left[\mathrm{Fe(OH)}_4^{-}\right]_e\end{aligned} \tag{D.27}$$

The concentration of all the species in solution can be found by calculating the roots of Equation (D.28),

$$\begin{aligned}&\left[\mathrm{H}^{+}\right]_e + \left[\mathrm{NaOH}\right]_i - \frac{K_W}{\left[\mathrm{H}^{+}\right]} - \left[\mathrm{HCl}\right]_i - 3\left[\mathrm{FeCl}_3\right]_i - \frac{K_{\mathrm{Fe(OH)}_4^-} K_W}{\left[\mathrm{H}^{+}\right]_e} + \\ &+ \frac{K_{s,\,\mathrm{Fe(OH)}_3} K_W^3}{\left[\mathrm{H}^{+}\right]_e^3}\left(3 + \frac{2K_{\mathrm{Fe(OH)}_2^+}}{\left[\mathrm{H}^{+}\right]_e} + \frac{K_{\mathrm{Fe(OH)}_2^+} K_{\mathrm{Fe(OH)}^{2+}}}{\left[\mathrm{H}^{+}\right]_e^2}\right) = 0.\end{aligned} \tag{D.28}$$

D.3 Instantaneous Equilibrium after Mixing

The initial concentration after mixing the reactants (indicated with the subscript index i) is calculated from the concentration of the reactants (indicated with the subscript index 0),

$$\left[\mathrm{FeCl_3}\right]_i = \frac{V_{\text{sol. Fe}}}{V_{\text{total}}}\left[\mathrm{FeCl_3}\right]_0 \tag{D.29}$$

$$\left[\mathrm{H_2Fum}\right]_i = \frac{V_{\text{sol. Fum}}}{V_{\text{total}}}\left[\mathrm{H_2Fum}\right]_0 \tag{D.30}$$

$$\left[\mathrm{NaOH}\right]_i = \frac{V_{\text{sol. Fum}}}{V_{\text{total}}}\left[\mathrm{NaOH}\right]_{0,\,\text{Fum}} + \frac{V_{\text{sol. Fe}}}{V_{\text{total}}}\left[\mathrm{NaOH}\right]_{0,\,\text{Fe}} \tag{D.31}$$

$$\left[\mathrm{HCl}\right]_i = \frac{V_{\text{sol. Fum}}}{V_{\text{total}}}\left[\mathrm{HCl}\right]_{0,\,\text{Fum}} + \frac{V_{\text{sol. Fe}}}{V_{\text{total}}}\left[\mathrm{HCl}\right]_{0,\,\text{Fe}} \tag{D.32}$$

where $V_{\text{sol. Fe}}$ is the volume of the concentration of the solution containing iron chloride, $V_{\text{sol. Fum}}$ is the volume of the concentration of the solution containing fumaric acid and V_{total} is the total volume after mixing.

The following situations can occur:

- Case 1: Fumaric acid and Iron(III) Hydroxide Dissociation;
- Case 2: Fumaric acid and Iron(III) Hydroxide Dissociation with Fumaric acid Precipitation;
- Case 3: Fumaric acid and Iron(III) Hydroxide Dissociation with Iron(III) Hydroxide Precipitation;
- Case 4: Fumaric acid and Iron(III) Hydroxide Dissociation with Fumaric Acid and Iron (III) Hydroxide Precipitation.

D.3.1 Case 1: Fumaric acid and Iron(III) Hydroxide Dissociation

Sodium mass balance:

$$\left[\mathrm{Na^+}\right]_e = \left[\mathrm{NaOH}\right]_i \tag{D.33}$$

Chlorine mass balance:

$$\left[\mathrm{Cl^-}\right]_e = \left[\mathrm{HCl}\right]_i + 3\left[\mathrm{FeCl_3}\right]_i \tag{D.34}$$

Fumarate mass balance:

$$\left[\mathrm{H_2Fum}\right]_i = \left[\mathrm{H_2Fum}\right]_e + \left[\mathrm{HFum^-}\right]_e + \left[\mathrm{Fum^{2-}}\right]_e \tag{D.35}$$

Iron mass balance:

$$\left[\mathrm{FeCl_3}\right]_i = \left[\mathrm{Fe^{3+}}\right]_e + \left[\mathrm{Fe(OH)^{2+}}\right]_e + \left[\mathrm{Fe(OH)_2^+}\right]_e \tag{D.36}$$

Charge balance:

$$\begin{aligned}&\left[\mathrm{H^+}\right]_e + \left[\mathrm{Na^+}\right]_e + \left[\mathrm{Fe(OH)_2^+}\right]_e + 2\left[\mathrm{Fe(OH)^{2+}}\right]_e + 3\left[\mathrm{Fe^{3+}}\right]_e = \\ &\left[\mathrm{OH^-}\right]_e + \left[\mathrm{Cl^-}\right]_e + \left[\mathrm{HFum^-}\right]_e + 2\left[\mathrm{Fum^{2-}}\right]_e\end{aligned} \tag{D.37}$$

The concentration of all the species in solution can be found by calculating the roots of Equation (D.38),

$$\begin{aligned}&\left[\mathrm{H^+}\right]_e+\left[\mathrm{NaOH}\right]_i-\frac{K_W}{\left[\mathrm{H^+}\right]}-\left[\mathrm{HCl}\right]_i-3\left[\mathrm{FeCl_3}\right]_i+\\&+\frac{\left[\mathrm{FeCl_3}\right]_i}{1+\frac{K_{\mathrm{Fe(OH)_2^+}}}{\left[\mathrm{H^+}\right]_e}+\frac{K_{\mathrm{Fe(OH)_2^+}}K_{\mathrm{Fe(OH)^{2+}}}}{\left[\mathrm{H^+}\right]_e^2}}\left(3+\frac{2K_{\mathrm{Fe(OH)_2^+}}}{\left[\mathrm{H^+}\right]_e}+\frac{K_{\mathrm{Fe(OH)_2^+}}K_{\mathrm{Fe(OH)^{2+}}}}{\left[\mathrm{H^+}\right]_e^2}\right)-\\&-\frac{\left[\mathrm{H_2Fum}\right]_i}{1+\frac{K_{\mathrm{HFum^-}}}{\left[\mathrm{H^+}\right]_e}+\frac{K_{\mathrm{HFum^-}}K_{\mathrm{Fum^{2-}}}}{\left[\mathrm{H^+}\right]_e^2}}\left(\frac{K_{\mathrm{HFum^-}}}{\left[\mathrm{H^+}\right]_e}+\frac{2K_{\mathrm{HFum^-}}K_{\mathrm{Fum^{2-}}}}{\left[\mathrm{H^+}\right]_e^2}\right)=0.\end{aligned}\tag{D.38}$$

D.3.2 Case 2: Fumaric acid and Iron(III) Hydroxide Dissociation with Fumaric acid Precipitation

Sodium mass balance:

$$\left[\mathrm{Na^+}\right]_e=\left[\mathrm{NaOH}\right]_i\tag{D.39}$$

Chlorine mass balance:

$$\left[\mathrm{Cl^-}\right]_e=\left[\mathrm{HCl}\right]_i+3\left[\mathrm{FeCl_3}\right]_i\tag{D.40}$$

Fumarate mass balance:

$$\left[\mathrm{H_2Fum}\right]_i=\left[\mathrm{H_2Fum}\right]_e+\left[\mathrm{HFum^-}\right]_e+\left[\mathrm{Fum^{2-}}\right]_e+\left[\mathrm{H_2Fum}\downarrow\right]_e\tag{D.41}$$

Iron mass balance:

$$\left[\mathrm{FeCl_3}\right]_i=\left[\mathrm{Fe^{3+}}\right]_e+\left[\mathrm{Fe(OH)^{2+}}\right]_e+\left[\mathrm{Fe(OH)_2^+}\right]_e\tag{D.42}$$

Charge Balance:

$$\begin{aligned}&\left[\mathrm{H^+}\right]_e+\left[\mathrm{Na^+}\right]_e+\left[\mathrm{Fe(OH)_2^+}\right]_e+2\left[\mathrm{Fe(OH)^{2+}}\right]_e+3\left[\mathrm{Fe^{3+}}\right]_e=\\&\left[\mathrm{OH^-}\right]_e+\left[\mathrm{Cl^-}\right]_e+\left[\mathrm{HFum^-}\right]_e+2\left[\mathrm{Fum^{2-}}\right]_e\end{aligned}\tag{D.43}$$

The concentration of all the species in solution can be found by calculating the roots of Equation (D.44),

$$\begin{aligned}&\left[\mathrm{H^+}\right]_e+\left[\mathrm{NaOH}\right]_i-\frac{K_W}{\left[\mathrm{H^+}\right]}-\left[\mathrm{HCl}\right]_i-3\left[\mathrm{FeCl_3}\right]_i+\\&+\frac{\left[\mathrm{FeCl_3}\right]_i}{1+\frac{K_{\mathrm{Fe(OH)_2^+}}}{\left[\mathrm{H^+}\right]_e}+\frac{K_{\mathrm{Fe(OH)_2^+}}K_{\mathrm{Fe(OH)^{2+}}}}{\left[\mathrm{H^+}\right]_e^2}}\left(3+\frac{2K_{\mathrm{Fe(OH)_2^+}}}{\left[\mathrm{H^+}\right]_e}+\frac{K_{\mathrm{Fe(OH)_2^+}}K_{\mathrm{Fe(OH)^{2+}}}}{\left[\mathrm{H^+}\right]_e^2}\right)-\\&-\frac{K_{s,\,\mathrm{H_2Fum}}}{K_{\mathrm{Fum^{2-}}}\left[\mathrm{H^+}\right]_e}-\frac{K_{s,\,\mathrm{H_2Fum}}}{\left[\mathrm{H^+}\right]_e^2}=0.\end{aligned}\tag{D.44}$$

D.3.3 Case 3: Fumaric acid and Iron(III) Hydroxide Dissociation with Iron(III) Hydroxide Precipitation

Sodium mass Balance:

$$\left[\mathrm{Na^+}\right]_e=\left[\mathrm{NaOH}\right]_i\tag{D.45}$$

Chloride mass balance:

$$\left[\mathrm{Cl^-}\right]_e=\left[\mathrm{HCl}\right]_i+3\left[\mathrm{FeCl_3}\right]_i\tag{D.46}$$

Fumarate mass balance:

$$\left[\mathrm{H_2Fum}\right]_i=\left[\mathrm{H_2Fum}\right]_e+\left[\mathrm{HFum^-}\right]_e+\left[\mathrm{Fum^{2-}}\right]_e\tag{D.47}$$

Iron mass balance:

$$\left[\mathrm{FeCl_3}\right]_i=\left[\mathrm{Fe^{3+}}\right]_e+\left[\mathrm{Fe(OH)^{2+}}\right]_e+\left[\mathrm{Fe(OH)_2^+}\right]_e+\left[\mathrm{Fe(OH)_3}\right]_e+\left[\mathrm{Fe(OH)_4^-}\right]_e+\left[\mathrm{Fe(OH)_3}\downarrow\right]_e\tag{D.48}$$

Charge Balance:

$$\begin{aligned}&\left[\mathrm{H^+}\right]_e+\left[\mathrm{Na^+}\right]_e+\left[\mathrm{Fe(OH)_2^+}\right]_e+2\left[\mathrm{Fe(OH)^{2+}}\right]_e+3\left[\mathrm{Fe^{3+}}\right]_e=\\&\left[\mathrm{OH^-}\right]_e+\left[\mathrm{Cl^-}\right]_e+\left[\mathrm{Fe(OH)_4^-}\right]_e+\left[\mathrm{HFum^-}\right]_e+2\left[\mathrm{Fum^{2-}}\right]_e\end{aligned}\tag{D.49}$$

The concentration of all the species in solution can be found by calculating the roots of Equation (D.50),

$$\begin{aligned}&\left[\mathrm{H^+}\right]_e+\left[\mathrm{NaOH}\right]_i-\frac{K_W}{\left[\mathrm{H^+}\right]}-\left[\mathrm{HCl}\right]_i-3\left[\mathrm{FeCl_3}\right]_i-\frac{K_{\mathrm{Fe(OH)_4^-}}K_W}{\left[\mathrm{H^+}\right]_e}+\\&+\frac{K_{s,\,\mathrm{Fe(OH)_3}}K_W^3}{\left[\mathrm{H^+}\right]_e^3}\left(3+\frac{2K_{\mathrm{Fe(OH)_2^+}}}{\left[\mathrm{H^+}\right]_e}+\frac{K_{\mathrm{Fe(OH)_2^+}}K_{\mathrm{Fe(OH)^{2+}}}}{\left[\mathrm{H^+}\right]_e^2}\right)-\\&-\frac{\left[\mathrm{H_2Fum}\right]_i}{1+\frac{K_{\mathrm{HFum^-}}}{\left[\mathrm{H^+}\right]_e}+\frac{K_{\mathrm{HFum^-}}K_{\mathrm{Fum^{2-}}}}{\left[\mathrm{H^+}\right]_e^2}}\left(\frac{K_{\mathrm{HFum^-}}}{\left[\mathrm{H^+}\right]_e}+\frac{2K_{\mathrm{HFum^-}}K_{\mathrm{Fum^{2-}}}}{\left[\mathrm{H^+}\right]_e^2}\right)=0\end{aligned}\tag{D.50}$$

D.3.4 Case 4: Fumaric acid and Iron(III) Hydroxide Dissociation with Fumaric Acid and Iron (III) Hydroxide Precipitation

Sodium mass Balance:

$$\left[\mathrm{Na^+}\right]_e=\left[\mathrm{NaOH}\right]_i\tag{D.51}$$

Chlorine mass balance:

$$\left[\mathrm{Cl^-}\right]_e=\left[\mathrm{HCl}\right]_i+3\left[\mathrm{FeCl_3}\right]_i\tag{D.52}$$

Fumarate mass balance:

$$\left[\mathrm{H_2Fum}\right]_i=\left[\mathrm{H_2Fum}\right]_e+\left[\mathrm{HFum^-}\right]_e+\left[\mathrm{Fum^{2-}}\right]_e+\left[\mathrm{H_2Fum}\downarrow\right]_e\tag{D.53}$$

Iron mass balance:

$$\begin{aligned}\left[\mathrm{FeCl_3}\right]_i = &\left[\mathrm{Fe^{3+}}\right]_e + \left[\mathrm{Fe(OH)^{2+}}\right]_e + \left[\mathrm{Fe(OH)_2^{+}}\right]_e + \\ &+\left[\mathrm{Fe(OH)_3}\right]_e + \left[\mathrm{Fe(OH)_4^{-}}\right]_e + \left[\mathrm{Fe(OH)_3\downarrow}\right]_e\end{aligned} \tag{D.54}$$

Charge Balance:

$$\begin{aligned}&\left[\mathrm{H^+}\right]_e + \left[\mathrm{Na^+}\right]_e + \left[\mathrm{Fe(OH)_2^{+}}\right]_e + 2\left[\mathrm{Fe(OH)^{2+}}\right]_e + 3\left[\mathrm{Fe^{3+}}\right]_e = \\ &\left[\mathrm{OH^-}\right]_e + \left[\mathrm{Cl^-}\right]_e + \left[\mathrm{Fe(OH)_4^{-}}\right]_e + \left[\mathrm{HFum^-}\right]_e + 2\left[\mathrm{Fum^{2-}}\right]_e\end{aligned} \tag{D.55}$$

The concentration of all the species in solution can be found by calculating the roots of Equation (D.56),

$$\begin{aligned}&\left[\mathrm{H^+}\right]_e + \left[\mathrm{NaOH}\right]_i - \frac{K_W}{\left[\mathrm{H^+}\right]} - \left[\mathrm{HCl}\right]_i - 3\left[\mathrm{FeCl_3}\right]_i - \frac{K_{\mathrm{Fe(OH)_4^-}} K_W}{\left[\mathrm{H^+}\right]_e} + \\ &+ \frac{K_{s,\,\mathrm{Fe(OH)_3}} K_W^3}{\left[\mathrm{H^+}\right]_e^3}\left(3 + \frac{2K_{\mathrm{Fe(OH)_2^+}}}{\left[\mathrm{H^+}\right]_e} + \frac{K_{\mathrm{Fe(OH)_2^+}} K_{\mathrm{Fe(OH)^{2+}}}}{\left[\mathrm{H^+}\right]_e^2}\right) - \\ &- \frac{K_{s,\,\mathrm{H_2Fum}}}{K_{\mathrm{Fum^{2-}}}\left[\mathrm{H^+}\right]_e} - \frac{K_{s,\,\mathrm{H_2Fum}}}{\left[\mathrm{H^+}\right]_e^2} = 0.\end{aligned} \tag{D.56}$$